

Organic semiconductor lasers with two-dimensional distributed feedback

Dissertation der Fakultät für Physik

der

Ludwig-Maximilians-Universität München



vorgelegt von

Stefan Riechel

aus München

München, den 11. Februar 2002

1. Gutachter : Prof. Dr. Jochen Feldmann

2. Gutachter : Prof. Dr. Khaled Karrai

Tag der mündlichen Prüfung: 15. Mai 2002

Front page:

Photograph of a mechanically flexible 2D-DFB laser made from the conjugated polymer MeLPPP. The laser is optically pumped well above the threshold for amplified spontaneous emission. The complex far-field emission pattern (blue-green) results from a large detuning between the resonance wavelength and the gain maximum.

The picture was taken in the course of the documentation for the Philip-Morris Forschungspreis 1999 awarded to Prof. Dr. J. Feldmann and Dr. U. Lemmer (Courtesy by the Philip Morris Stiftung, Fallstraße 40, D-81369 München).

Scientific publications of results presented in this work

- *A nearly diffraction limited surface emitting conjugated polymer laser utilizing a 2D photonic bandstructure*
S. Riechel, C. Kallinger, U. Lemmer, J. Feldmann, A. Gombert, V. Wittwer, and U. Scherf, Applied Physics Letters **77**, 2310 (2000).
- *Lasing modes in organic solid state distributed feedback lasers*
S. Riechel, U. Lemmer, J. Feldmann, T. Benstem, W. Kowalsky, U. Scherf, A. Gombert, and V. Wittwer, Applied Physics B **71**, 897 (2000).
- *Very compact tunable solid-state laser utilizing a thin-film organic semiconductor*
S. Riechel, U. Lemmer, J. Feldmann, S. Berleb, A. G. Mückl, W. Brütting, A. Gombert, and V. Wittwer, Optics Letters **26**, 593 (2001).
- *Conjugated Polymers: Lasing and Stimulated Emission*
U. Scherf, S. Riechel, U. Lemmer, and R. F. Mahrt, Current opinion in Solid State and Materials Science **5**, 143 (2001)
- *Picosecond amplified spontaneous emission bursts from a molecularly doped organic semiconductor*
C. Kallinger, S. Riechel, O. Holderer, U. Lemmer, J. Feldmann, S. Berleb, A. G. Mückl, W. Brütting, Journal of Applied Physics **91**, 6367 (2002)

Further publications related to this work

- *Laser aus Plastik*
C. Kallinger, A. Haugeneder, S. Riechel, U. Lemmer und J. Feldmann
Einsichten: Forschung an der Ludwig-Maximilians-Universität München **1/99**, p. 22
- *Polymer laser threshold plummets*
Opto&Laser Europe, May 1999, p. 19
- *Laserlicht aus Polymeren*
Physikalische Blätter **56**, January 2000 , p. 25
- *Polymer laser is nearly diffraction limited*
Laser Focus World, December 2000, p. 49
- *Thin-film organic laser tunes very compact DFB*
Laser Focus World, September 2001, p. 15

Contents

Zusammenfassung	1
Summary	3
1 Introduction	4
2 Fundamentals of organic semiconductor lasers	6
2.1 Organic semiconductors	6
2.1.1 Electronic and optical properties of organic semiconductors	7
2.1.2 Transport phenomena in disordered organic semiconductors.....	12
2.2 Lasing in organic semiconductors	17
2.2.1 Stimulated emission	17
2.2.2 Amplified spontaneous emission	18
2.2.3 Resonant laser structures.....	19
2.3 Distributed feedback lasers.....	20
2.3.1 Slab waveguides.....	20
2.3.2 One-dimensional distributed feedback lasers	22
2.3.3 Two-dimensional distributed feedback lasers.....	27
2.3.4 Randomly distributed feedback	29
3 Experimental techniques	32
3.1 Sample preparation and characterization.....	32
3.2 Optical experiments at high excitation density.....	33
3.2.1 Determination of the excitation density	34
3.2.2 Regeneratively amplified fs-laser system	34
3.2.3 Time-integrated emission.....	35
3.2.4 Temporally resolved emission with sub-ps resolution.....	36
3.2.5 Differential transmission spectroscopy	38

4	Materials for organic solid-state lasers	40
4.1	The conjugated polymer MeLPPP.....	40
4.1.1	Electronic, optical and transport properties of MeLPPP.....	40
4.1.2	Stimulated emission in MeLPPP.....	42
4.2	The composite molecular system Alq ₃ :DCM.....	44
4.2.1	Electronic, optical and transport properties of Alq ₃ :DCM	44
4.2.2	Stimulated emission in Alq ₃ :DCM	46
5	Lasers with one-dimensional distributed feedback	49
5.1	Fabrication of mechanically flexible organic DFB lasers	49
5.2	Characterization of the laser operation.....	51
5.3	Lateral laser modes.....	53
5.4	Wavelength tuning by variation of the film thickness.....	55
5.5	Coupling mechanism in organic solid-state DFB lasers.....	57
5.5.1	Calculation of the coupling coefficient.....	57
5.5.2	Coupling in 2 nd order DFB structures	58
5.5.3	Prediction of coupling mechanisms in 1 st order DFB structures	62
5.5.4	Implications for the design of optimized DFB lasers	63
6	Lasers with two-dimensional distributed feedback	65
6.1	Fabrication.....	65
6.2	Characterization.....	66
6.3	Laser modes of 2D-DFB lasers	68
6.3.1	Far-field identification of lasers modes	71
6.3.2	Factors favoring monomode operation	72
6.4	Photonic band structure analysis	74

7 Lasers with randomly distributed feedback	77
7.1 Sample preparation and characterization.....	78
7.2 Random laser operation.....	80
7.2.1 Variation of excitation density.....	81
7.2.2 Variation of the excitation area.....	84
8 Emission dynamics	86
8.1 Polymer lasers	86
8.1.1 ASE in slab waveguides.....	86
8.1.2 Lasing dynamics	87
8.2 Emission dynamics in Alq ₃ :DCM	92
8.2.1 Gain switching oscillations in slab waveguides.....	92
8.2.2 DFB-lasers	96
9 Devices and applications of organic solid-state lasers	98
9.1 Very compact tunable organic solid-state laser.....	98
9.2 Laser operation in the presence of electric contacts	
-- towards an organic injection laser.....	100
9.2.1 Problems associated with electrical pumping of organic lasers.....	100
9.2.2 Design of suitable structures for organic diode lasers	102
9.2.3 Optically pumped laser diodes.....	105
9.2.4 Feasibility of organic diode lasers	110
10 Outlook	112
List of abbreviations and definitions	114
Bibliography	115
Acknowledgments	130
Curriculum Vitae	132

Zusammenfassung

Die vorliegende Arbeit beinhaltet eine umfassende Untersuchung dünner organischer Halbleiterfilme hinsichtlich ihrer Einsatzmöglichkeiten in Festkörperlasern. Die einzigartige Kombination ihrer elektrischen Eigenschaften, der hohen Lumineszenzausbeute sowie der einfachen Verarbeitung eröffnet eine Vielzahl neuer Anwendungen in der Optoelektronik und ermöglicht insbesondere die Erprobung innovativer Laserresonatoren. Im Rahmen dieser Doktorarbeit wurden Laser mit räumlich verteilter Rückkopplung hergestellt und untersucht (engl.: distributed feedback, DFB). Sie bestehen aus einem dünnen organischen Halbleiterfilm der auf ein vorstrukturiertes Substrat aufgebracht wird, so dass sich ein räumlich modulierter Dünnschichtwellenleiter ausbildet. Die Lasertätigkeit wird durch Bestrahlung mit Femtosekunden-Laserpulsen angeregt und mittels zeitaufgelöster sowie zeitintegrierender Spektroskopietechniken analysiert.

Mit dem konjugierten Polymer MeLPPP und dem molekularen Verbundmaterial Alq₃:DCM kamen zwei aussichtsreiche elektrolumineszierende organische Halbleiter zum Einsatz. Ihr hoher Wirkungsquerschnitt für stimulierte Emission bewirkt eine effiziente optische Verstärkung und resultiert in einem äußerst niedrigen Schwellwert für die Beobachtung verstärkter spontaner Emission in planaren Wellenleitern. Die Bragg-Beugung in einem periodisch modulierten Wellenleiter kann ausgenutzt werden, um spektral selektive Rückkopplung zu erzielen. Unter Verwendung von geprägten Plastiksubstraten mit ein-dimensional periodischer Oberflächenmodulation wurden auf diese Weise sowohl kanten- als auch oberflächenemittierende 1D-DFB Laser realisiert. Ihre Lasertätigkeit wurde umfassend charakterisiert und modelliert. Sofern keine weiteren Vorkehrungen zur Modenselektion getroffen werden, ergibt sich ein kontinuierliches Spektrum lateraler Moden, das sich in einem verbreiterten Emissionsspektrum und einer hohen Strahldivergenz niederschlägt.

Eine erhebliche Verbesserung der Abstrahlcharakteristik wurde durch den Einsatz 2D periodisch modulierter Substrate erzielt. Die spezifischen Eigenheiten der Lichtausbreitung in einem solchen 2D photonischen Kristall führen zu monomodiger Lasertätigkeit, die sich durch eine reduzierte Laserschwelle, erhöhte Effizienz und beugungsbegrenzte Abstrahlung auszeichnet. Zudem ist die spektrale Linienbreite allein durch die Dauer des emittierten Laserpulses begrenzt. Sowohl die Ursache der monomodigen Lasertätigkeit als auch die photonische Bandstruktur bei hoher Anregung lassen sich durch ein Laue-Modell der Rückkopplung in photonischen Kristall-Lasern erklären.

Mit Hilfe einer Selbstorganisationstechnik wurden darüber hinaus Wellenleiterstrukturen mit stochastisch verteilten Streuzentren hergestellt. Lasertätigkeit mit resonanter Rückkopplung wird hierbei durch Vielfachstreuung innerhalb des Wellenleiters und die zufällige Ausbildung geschlossener optischer Pfade erreicht (Random Lasing).

Um das technologische Potential organischer Halbleiterlaser auszuloten, wurden zwei Konzepte zur elektrischen Ansteuerung untersucht. In einem hybriden Ansatz dient der organische Halbleiterlaser lediglich als durchstimmbare Festkörperstrahlquelle. Aufgrund der geringen Laserschwelle läßt sich ein äußerst kompakter Aufbau mit einem gepulsten Mikrochip Pump laser realisieren. Für die alternative Verwirklichung eines elektrisch betriebenen organischen Diodenlasers ist die Entwicklung von Strukturen essentiell, die trotz der geringen Ladungsträgerbeweglichkeit in ungeordneten organischen Halbleitern gleichzeitig geringe Laserschwellen und hohe elektrische Stromdichten ermöglichen. Im Rahmen dieser Arbeit konnte erstmalig Lasertätigkeit in Strukturen nachgewiesen werden, die für diese hohe elektrische Anregung geeignet sind.

Summary

The work at hand presents a comprehensive investigation of solid-state lasers based on thin films of a disordered organic semiconductors (OS). The high luminescence yield of OS together with their conductivity and the ease of processing them into sub-micron thick films on substrates of virtually any shape and size open vast opportunities both for the realization of novel devices and for the exploration of innovative resonator geometries. Within the course of this work optically pumped lasers with spatially distributed feedback were fabricated by deposition of a thin film of an OS on a nanopatterned substrate. Upon optical excitation with femtosecond laser pulses laser operation is observed. It is characterized using time-integrated and time-resolved spectroscopy.

As active medium two of the most promising electroluminescent organic materials were employed, namely the conjugated polymer MeLPPP and the composite molecular system Alq₃:DCM. Owing to their large gain coefficient low-threshold light-amplification by stimulated emission can be observed from slab waveguides formed by a thin layer of the OS on a planar substrate. In periodically modulated waveguides Bragg scattering gives rise to distributed feedback. Utilizing UV-embossed plastic substrates with an appropriate one-dimensional surface corrugation, edge- and surface-emitting lasers were fabricated. Excellent agreement is found between the performance of these 1D-DFB lasers and the predictions of a quantitative numerical modeling. Unless further precautions are taken these lasers operate on a continuum of lateral modes, characterized by a broad emission spectrum and a large beam divergence.

A significantly improved performance is achieved by application of a two-dimensional corrugation. The specific properties of light-propagation in the resulting 2D photonic crystal give rise to monomode laser operation, accompanied by a reduction of the laser threshold, an increased differential efficiency, and by the emission of a circularly shaped, diffraction-limited laser beam. It is demonstrated that the emission linewidth is (time-bandwidth) transform limited by the duration of the laser pulse. The mechanism leading to monomode operation at low excitation density as well as the photonic band structure at high excitation density is revealed by a Laue model for the feedback in such a 2D photonic crystal laser.

By use of a self-assembly technique waveguide structures with stochastically distributed scatter centers were fabricated. Lasing with resonant feedback is observed and attributed to the formation of random closed loop cavities (random lasing). The underlying process of recurrent light-scattering is made possible by the strong scattering, the reduced dimensionality of the waveguide geometry, and the large gain of the organic semiconductor material.

In order to explore the technological potential of organic semiconductor lasers two alternative concepts for electrical operation were examined. In a hybrid concept an OS DFB laser is merely used as a tunable solid-state laser source. Thanks to the low laser threshold a very compact setup can be realized utilizing a microchip pump laser with a repetition rate of several kilohertz. In the approach of making an organic diode laser the low mobility of disordered organic semiconductors imposes severe constraints on the device architecture. Several structures were developed and fabricated that concurrently permit large current densities and possess a low laser threshold. As a result, optically pumped lasing is for the first time demonstrated in structures that are suitable for electrical excitation.

1 Introduction

In the year 2000, A. J. Heeger, A.G. MacDiarmid and H. Shirakawa were awarded the Nobel Prize in Chemistry for “the discovery and development of conducting polymers”¹. This award traces back to 1977, when they discovered that the conductivity of conjugated polymers can be varied over the full range from insulator to metal by chemical doping^{2,3}.

Since then, remarkable progress has been made in synthesizing conjugated polymers, in understanding their properties, and in developing them for use in electronic and optical devices. Metallic polymers have become an integrate part of a variety of products including batteries, capacitors, and antistatic coatings. Besides, the class of semiconducting amorphous organic materials has proven to be particularly useful. The photosensitive layer of xerography systems and laser printers, for instance, is made from amorphous organic photoconductors. These two widespread applications clearly demonstrate some of the unique properties of disordered organic semiconductors that are not available from other materials: they do not only perform well but can also be processed and patterned by inexpensive, large-area techniques such as spincasting, ink jet printing⁴, screen printing⁵, photolithography, and micromolding⁶. Moreover, they are compatible with almost any type of substrate, including flexible ones⁷. The very same features are exploited in further optoelectronic applications that are currently pushed towards commercialization by academic and industrial research teams. Whereas organic photodetectors⁸, photovoltaic cells⁹, electrooptic modulators¹⁰, and field-effect transistors¹⁰ are still in the reasearch labs, organic light-emitting diodes (OLEDs)¹¹⁻¹³ and displays have already entered the market¹⁴. Since the demand for high-brilliance, full-color displays is rising continuously, a turnover of 500 million US-\$ in the year 2004 is predicted for OLED displays¹⁵.

Notably absent from the list of devices that can be made from disordered organic semi-conductors is the diode laser, one of the most important devices for modern technology. Appreciated for their large spectral tuning range, their high stimulated emission and their low laser threshold, organic dye molecules are conveniently employed as active laser medium for many years. Very recently, even electrically driven lasing was observed both in a liquid dye solution (electrochemiluminescence)¹⁶ and in high-quality molecular crystals of tetracene¹⁷. These breakthroughs indicate the high potential of organic materials for innovative laser sources. Even so, both of the above approaches lack the appealing inexpensive large-area fabrication techniques, the possibility of integration into thin film devices, and the mechanical flexibility of amorphous organic semiconductors.

Motivated by the rapid development of organic light-emitting diodes and their high luminescence efficiency, the development of lasers made from disordered organic semiconductors has become the focus of many investigations. To avoid complications that are associated with current injection, charge transport and electrode incorporation, it is beneficial to study stimulated emission and gain starting with excitation by photopumping. As a matter of fact, stimulated emission was first observed in a polymer solution¹⁸, and later also in diluted^{19,20} or undiluted²¹ solid films. The first attempt to achieve true lasing action from a high gain organic semiconductor material was carried out using a microcavity resonator²².

Among the various laser resonators that were later realized with organic semiconductor lasers, the concept of distributed feedback (DFB) lasers is particularly promising as it combines a low laser threshold and the compatibility with the typical OLED architecture²³⁻²⁸. Concurrently, the possibility to fabricate the DFB resonator by soft-lithography provides a very elegant way to make an all-organic laser, thus preserving the inherent mechanical flexibility of the thin-film organic semiconductor^{23,24}.

Dating back to the early 1970s²⁹, DFB lasers are a key ingredient of optical data communication and meanwhile highly developed and fairly well understood. Their outstanding importance originates from properties like a stable, tunable, single-frequency output, an extremely fast modulation capability of gigabit/s, and a good manufacturability^{30,31}. Technically, the term DFB implies a particular form of laser where feedback is induced by a uniform one-dimensional periodic modulation of the optical constants. More generally, however, it can also be used for *any* form of resonator leading to non-local, i.e. spatially distributed, feedback. Modifications of the conventional design may result in significant improvements of the laser performance. A more comprehensive control of the light-propagation, for instance, is provided if the periodic modulation is extended to two or three dimensions. The ability to tailor the propagation of light in these so-called photonic crystals enables to suppress, enhance or route spontaneous and stimulated emission and can be applied to numerous optical devices³²⁻³⁶. As an example it will be shown in this work that the performance of a conventional DFB laser can be topped in a 2D-DFB laser, simply by the use of a suitable two-dimensional periodic modulation.

Based on the examination of stimulated emission in conjugated polymers^{37,38} and on the initial demonstration of a flexible conjugated polymer laser^{23,39}, this work aims at a comprehensive investigation of organic semiconductor DFB lasers, an exploration of their potential for technological applications, and the examination of innovative resonator geometries.

Chapter 2 reviews the fundamentals of organic semiconductors, organic semiconductor lasers and DFB lasers with special emphasis on the structures utilized within the course of this work. It is followed by a description of the experimental techniques in chapter 3. Section 4 summarizes the relevant electronic and optical properties of the employed materials. Their gain spectrum and the process of stimulated emission in planar thin films is investigated. Chapter 5 presents a detailed analysis of OS lasers with one-dimensional distributed feedback. The specific material-related properties are illustrated. In Chapter 6 the superior performance of 2D-DFB lasers is demonstrated and its origin revealed in the context of the peculiar properties of photonic crystals. A complementary technique to induce non-local, resonant feedback in random cavities is introduced in section 7. The following chapter 8 deals with the dynamics of stimulated emission and lasing in plain and in composite organic semiconductors. The prospects of disordered organic semiconductors for solid-state lasers are explored in chapter 9. My thesis concludes with an outlook on the future challenges in the quest for an organic injection laser.

2 Fundamentals of organic semiconductor lasers

In this chapter the fundamental electronic, optical and transport properties of organic semiconductors are described. Furthermore the various approaches to the realization of organic solid-state lasers are introduced, followed by a description of the distributed feedback concept for thin film lasers.

2.1 Organic semiconductors

The term “semiconductor” is usually associated with crystalline *inorganic* semiconductors such as Si, GaAs or InP. The enormous success of electronic and optoelectronic devices made from these materials relies on the profound theoretical description of their physical properties and its application to the various structures. In inorganic semiconductors covalent bonding between the individual atoms leads to a periodic arrangement of the atoms in a crystalline structure. As a consequence of the periodicity and the strongly overlapping orbitals, these discrete atomic states evolve into a band structure with a well defined energy-momentum dispersion relation for electrons in the conduction band and holes (defect electrons) in the valence band. Owing to the periodicity all excitations -be they electrons, holes or Coulombically bound excitons- can be described by Bloch waves that are delocalized over the entire crystal. Controlled doping of the lattice with donor and acceptor atoms allows to modify the occupation probabilities of the various bands and determines many of the optical and transport properties of crystalline inorganic semiconductors. In strongly disordered semiconductors, such as the hydrogenated amorphous silicon (a-Si:H), the disorder induces a large number of spatially localized electron and hole states. Furthermore the scattering rate is drastically increased and the momentum is not a good quantum number as in the crystal. As a consequence, the charge mobility declines and the strength of optical transitions increases.

In an *organic* substance only the atoms within a molecule are covalently bound, whereas the intermolecular interaction is governed by comparatively weak van der Waals forces and hydrogen bonds. As a consequence, the overlap of the molecular orbitals is small, the molecules retain their identity and the properties of an organic semiconductor solid-state film are strongly influenced by the arrangement and concentration of functional groups within the contained molecules⁴⁰. Hence, the occurrence of a macroscopic conductivity implies that the molecules contain sub-units providing conductivity. Organic materials for organic electroluminescent devices can be classified into three categories according to their molecular structure: (1) organic dyes (no metal atom), (2) chelate metal complexes, and (3) conjugated polymers⁴¹. In all three categories the molecular conductivity is accomplished by conjugated π -systems formed in hydrocarbons with alternating single and double bonds. In the solid state the individual molecules can be arranged either in a crystalline or an amorphous phase. Similar to inorganic semiconductors, well defined valence and conduction bands evolve in

organic molecular crystals giving rise to a large charge mobility. In contrast, the band transport is replaced by tunneling (hopping) from molecule to molecule in disordered organic semiconductors. A common feature of all organic semiconductors is the weak dielectric constant resulting from the small intermolecular coupling. Its consequence is a high exciton binding energy of several hundred meV concurring with the formation of strongly bound, Frenkel-type excitons.

Within the course of this work representatives of two of the main classes of *disordered* organic semiconductors were used, namely the chelate metal complex tris-(8-hydroxyquinoline)-aluminum¹ (Alq₃) and secondly the conjugated polymer MeLPPP which is a comparatively large macromolecule. In both cases the molecules were randomly oriented in non-crystalline films. Not surprisingly, such semiconductors differ from their inorganic counterparts, some of the most obvious differences being the absence of an electronic band structure and a substantially lower conductivity^{40,42}. Nevertheless, disordered organic semiconductors are at least competitive for several optoelectronic applications (see Chapter 1). In the following the electronic and optical properties of organic molecules as well as some of the solid-state aspects leading to electrical conductivity will be discussed in more detail.

2.1.1 Electronic and optical properties of organic semiconductors

The conductivity of organic semiconductors are based on the presence of delocalized π -electrons in unsaturated hydrocarbon molecules. One of the most prominent representatives of this class is the benzene ring depicted in Fig. 2.1. Each carbon atom provides four valence electrons, three of whom form so-called σ -bonds with neighboring carbon or hydrogen atoms, thus defining the steric geometry of the molecule. The remaining 6 valence electrons of the 6 carbon atoms occupy p_z orbitals, which are aligned perpendicular to the plane of the σ -bonds.

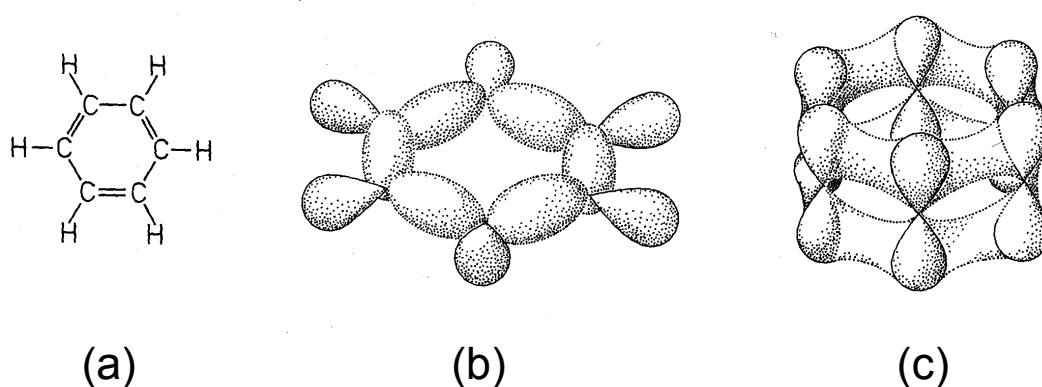


Fig. 2.1: C₆H₆ (benzene): (a) chemical structure formula, (b) spatial distribution of the σ -orbitals which are responsible for the steric configuration, (c) spatial distribution of the π -orbitals forming a delocalized π -system⁴³.

¹ Further nomenclatures include tris-(8-hydroxyquinolate)-aluminum, tris-(8-hydroxyquinolinato)-aluminum, tris-(8-hydroxyquinolato)-aluminum, and tris-(8-hydroxyquinolinato)-aluminum.

The p_z electrons from two neighboring carbons form an additional π -bond, so that the benzene ring consists of several alternating single and double bonds. In this so-called conjugated π -system π -electrons can no longer be attributed to one specific C-C bond, instead, their wavefunction is delocalized over the entire conjugated ring⁴³.

Every organic semiconductor contains a more or less extended π -system. These delocalized π -electrons are relatively weakly bound and are responsible for the semiconducting properties. Fig. 2.2 shows the chemical structure of some common materials. Whereas the chelate metal complex Alq_3 is a relatively small molecule with limited extension of the conjugated system, the conjugated polymers consist of many identical, conjugated repeat-units, called monomers. In the idealized case of a distortion-free molecule the conjugated π -system extends over the entire conjugated backbone of the polymer.

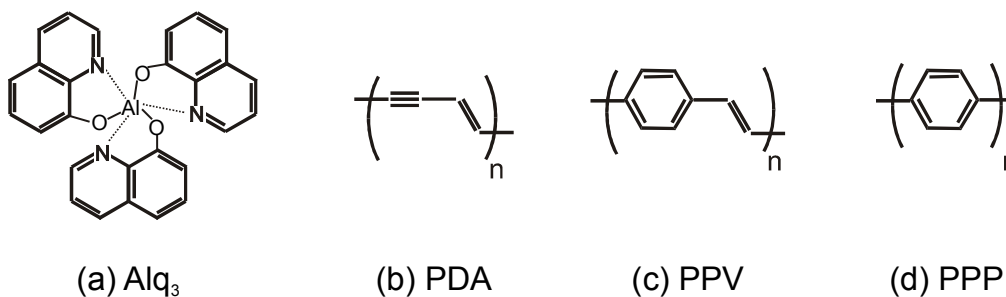


Fig. 2.2: chemical structure formula of several organic semiconductors. (a) Alq_3 , (b) polydiacetylene (PDA), (c) poly(p-phenylenevinylene) (PPV), (d) poly(p-phenylene) (PPP)

2.1.1.1 Models for organic semiconductors

Due to the complexity of the problem, quantum-chemical *ab initio* calculations of the energy-eigenstates require exceptionally high computational effort and are only possible for small molecules like Alq_3 ⁴⁴ or oligomers with a limited size, typically less than 12 monomers⁴⁵. Therefore several semi-empirical models were developed using simplified Hamiltonians for the π -electron system. These Hamiltonians differ in the number of interactions and degrees of freedom taken into account. An introduction to the nomenclature and the various methods of quantum-chemical calculations can be found in⁴⁶, recent reviews concentrating on conjugated polymers are given by Brédas⁴⁷ and Sutherland⁴⁸.

Of particular historic importance for the class conjugated polymers are the Hamiltonians introduced by Su-Schrieffer-Heeger (SSH), a one-electron theory accounting only for the electron lattice coupling, and the Hamiltonian by Pariser-Parr-Pople (PPP)^{49,50}, who explicitly consider the electron-electron correlation. Both theories predict the evolution of valence and conduction bands on single extended polymer chains. The occurrence of such bands could indeed be shown by the observation of Franz-Keldysh oscillations in a molecular crystal of polydiacetylene where the polymer strands are perfectly stretched⁵¹. Some remaining insufficiencies concerning the ordering of excited states, such as the energetic

position of triplet excitations, could be removed in a model by Abe, which includes electron-lattice as well as long-range Coulomb interaction^{52,53}.

Despite the success in the description of highly ordered polymers, the applicability of these models to conjugated polymers in a solid film is limited by defects. Incorporated defect atoms or distortions and kinks of the polymer chain interrupt the conjugation and cause a separation of the delocalized π -system into conjugated segments of finite length, behaving like individual chromophores. The distribution of the site length⁵⁴ and the orientational disorder⁵⁵⁻⁵⁷ translate into a variation of the excitation energies of the segments and thus contributes to an inhomogeneous broadening of the transition. Hence, the behavior of conjugated polymers resembles the one of separate -yet interacting- molecules with equivalent energy distribution (see Section 2.1.2).

2.1.1.2 Electronic states and excitations

A very common description of organic semiconductors is given by one-electron models neglecting electron-electron correlations. Such calculations yield molecular states which are consecutively filled with electrons. The optical properties of the molecules can be derived from the electronic structure by the use of selection rules. In the lowest electronic excitation one electron is lifted from the highest occupied molecular orbital (HOMO) to the lowest unoccupied molecular orbital (LUMO)². This $\pi^* \leftarrow \pi$ transition corresponds to a transition from the valence to the conduction band in inorganic semiconductors. It can be optically induced, typically with a photon energy E_g in the visible spectral range.

The Coulomb interaction between an electron in the LUMO and a hole in the HOMO leads to the formation of strongly bound excitons, either singlets or triplets depending on the relative spin of electron and hole. The relevant many-particle states are usually labeled according to their spin and symmetry into $n^M A_g$ and $n^M B_u$, where n is a counter for respective state, $M=2S+1$ is the multiplicity derived from the total spin S , and A_g or B_u denote the symmetry class and parity of the wavefunction (gerade, ungerade). Fig. 2.3 (b) sketches the energy levels of neutral excitations⁵⁸. In most cases the ground state is a singlet with even symmetry, denoted $1^1 A_g$. Due to the exchange correlation the binding energy E_b' of triplet excitons is higher than E_b in singlet excitons, so that the triplet $1^3 B_u$ is the lowest neutral excited state. The relative energetic position of the lowest two excited singlet states is of major importance for the optical properties of a molecule. Since the emission of a photon requires a change of parity (e.g. $1^1 A_g \leftarrow 1^1 B_u$), strong fluorescence is only observed if the state $1^1 B_u$ is located below $2^1 A_g$. In a simplified notation the wavefunction symmetry is neglected and only singlet, S_n , and triplet states, T_n , are distinguished.

² In the strict notation HOMO and LUMO refer to the energy of unfilled electronic levels *excluding* Coulomb interaction. Especially in the context of LEDs the terms HOMO and LUMO are often used as synonyms for the valence and conduction “band”. Their energetic difference is then referred to the gap detected in optical experiments, deriving from excitons, i.e. states *including* Coulomb interaction.

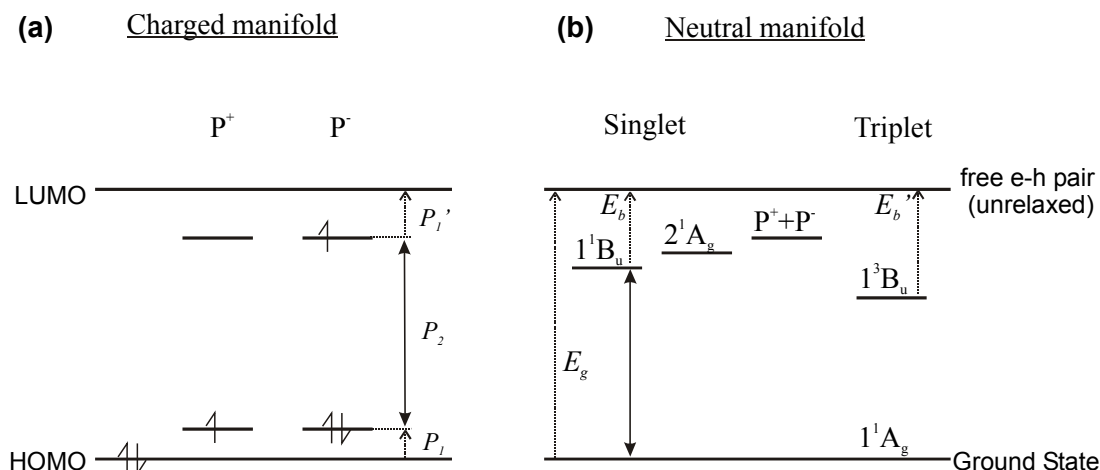


Fig. 2.3: Energy level of various excitations in organic molecules in the charged (a) and neutral (b) manifold. Adapted from⁵⁸ and⁵⁹.

Besides neutral excitations also negatively and positively charged excitations determine the properties of organic semiconductors. An excess electron on a molecule or on a polymer-segment causes a localized structural relaxation. As a consequence an anion radical is formed having two energy levels within the HOMO-LUMO gap of the neutral molecule. The lower level is filled with two electrons brought up from the HOMO, the upper level contains the excess electron (see Fig. 2.3 (a)). A similar description holds for a radical cation. In the style of inorganic semiconductors radicals on conjugated polymer chains are often referred to as polarons (P^- and P^+). The presence of polarons in a molecular system is accompanied by sub-gap ($P_2 < E_g$) optical transitions between the localized polaron states. Although its energy levels are in the gap, a polaron can move freely on its own chain, its lattice distortion moving with it. If a negative and a positive polaron meet they can form an unbound, neutral polaron pair, which, in turn, can recombine to a Coulombically bound exciton.

2.1.1.3 Electronic transitions in organic molecules

Whenever an electronic transition occurs in a molecule the nuclei are subjected to a change in Coulombic force as a result of the redistribution of electronic charge that accompanies the transition. As a consequence, electronic transitions are strongly coupled to the vibrational modes of the molecule. In the absorption (fluorescence) spectrum these vibronic transitions cause characteristic side-bands above (below) the purely electronic transition.

Fig. 2.4 (a) sketches the molecular potential energy as a function of a generalized nuclear coordinate R for the ground state S_0 and an electronically excited singlet state S_1 . The respective vibronic states are denoted by v and v' . Since the energy associated with a vibronic excitation is usually much higher than the thermal energy at room temperature, a molecule in thermal equilibrium occupies the state $S_0, v=0$.

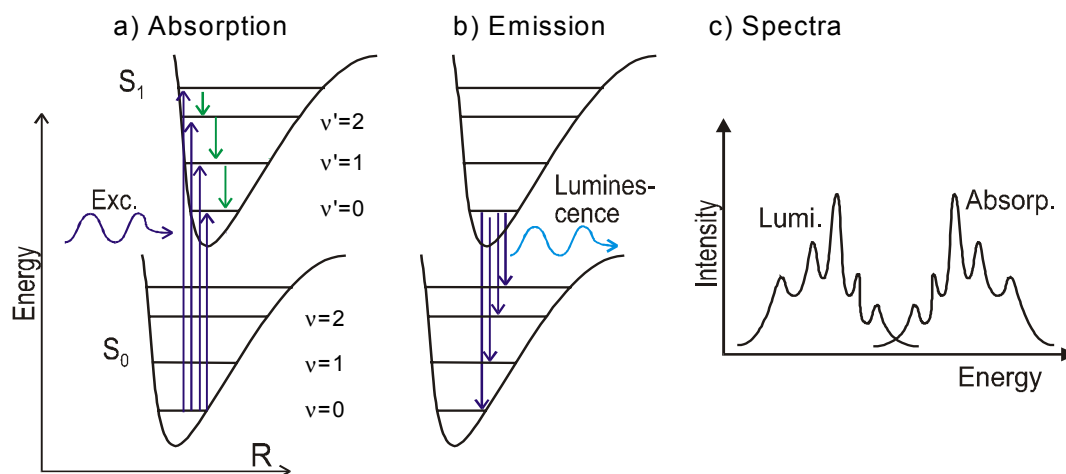


Fig. 2.4: Molecular potential energy as a function of the atomic distance. Vibronic eigenstates are denoted by v and v' . The arrows indicate vibronic transitions associated with (a) absorption and (b) emission of a photon. The corresponding absorption and luminescence spectra are sketched in (c).

Absorption of a photon of suitable energy causes a transition $S_{n,v'} \leftarrow S_{0,v}$. It is followed by a cascade of radiative and radiationless transitions. The most important transitions are summarized in Fig. 2.5. Following an excitation into a vibronically excited state S_1 a molecule quickly relaxes to the vibronic groundstate $v'=0$ by internal conversion. In a radiative transition the molecule returns to $S_{0,v}$ accompanied by spontaneous (or stimulated) emission of a photon. The resulting absorption and fluorescence spectra are sketched in Fig. 2.4 (c). In solid-state samples the vibronic structure can often not be resolved due to homogeneous and inhomogeneous broadening of the transitions. The apparent Stokes-shift between the absorption and emission maxima of the purely electronic transition is caused by intramolecular structural relaxation and intermolecular energetic dissipation (see section 2.1.2.1).

The intensity of the radiative transitions can be derived from the transition rate k_{fi} between an initial state $|i\rangle$ and a final state $|f\rangle$ as given by Fermi's golden rule (ρ_f is the density of final electronic states, $D(\omega)$ is the density of photon states at the energy ω , and H' is the Hamilton operator describing the interaction).

$$k_{fi} = \frac{2\pi}{\hbar} \rho_f D(\omega) \left| \langle \psi_f | H' | \psi_i \rangle \right|^2 \quad (2-1)$$

In application of the Born-Oppenheimer approximation the motion of electrons and nuclei can be separated, so that a vibronic state $|\epsilon v\rangle$ is described by the wavefunction $\psi_\epsilon(\mathbf{r}; \mathbf{R})\psi_v(\mathbf{R})$, where \mathbf{r} and \mathbf{R} denote the electronic and nuclear coordinates collectively. For an optical transition like one-photon absorption or emission H' is the dipole operator $H' = e\mathbf{r}$ so that equation (2-1) yields

$$k_{\epsilon'v' \leftarrow \epsilon v} \propto \left| \langle \psi_{\epsilon'}(\mathbf{r}; \mathbf{R}) | e\mathbf{r} | \psi_\epsilon(\mathbf{r}; \mathbf{R}) \rangle \right|^2 \left| \langle \psi_{v'}(\mathbf{R}) | \psi_v(\mathbf{R}) \rangle \right|^2 = \mu_{\epsilon'\epsilon} \left| \langle \psi_{v'}(\mathbf{R}) | \psi_v(\mathbf{R}) \rangle \right|^2 \quad (2-2)$$

Equation (2-2) can be used to determine the strength of radiative transitions. According to the Franck-Condon principle, radiative transitions occur ‘vertically’, i.e. within a stationary nuclear framework, and the dipole transition moment $\mu_{\epsilon'\epsilon}$ is constant. The relative intensities $k_{v'v}$ of the vibronic transitions are therefore given by the Franck-Condon factors, being the overlap integral between the vibrational wavefunctions of the nuclei in their respective electronic state: $k_{v'v} = |\langle \psi_{v'}(\mathbf{R}) | \psi_v(\mathbf{R}) \rangle|^2$.

Evaluation of $\mu_{\epsilon'\epsilon}$ yields that optical transitions require conservation of spin (singlet \leftrightarrow singlet; triplet \leftrightarrow triplet) and a change of parity (gerade \leftrightarrow ungerade). Spin-orbit coupling can additionally cause radiative singlet \leftrightarrow triplet transitions, however their transition rate is typically much lower than in spin-conserving transitions.

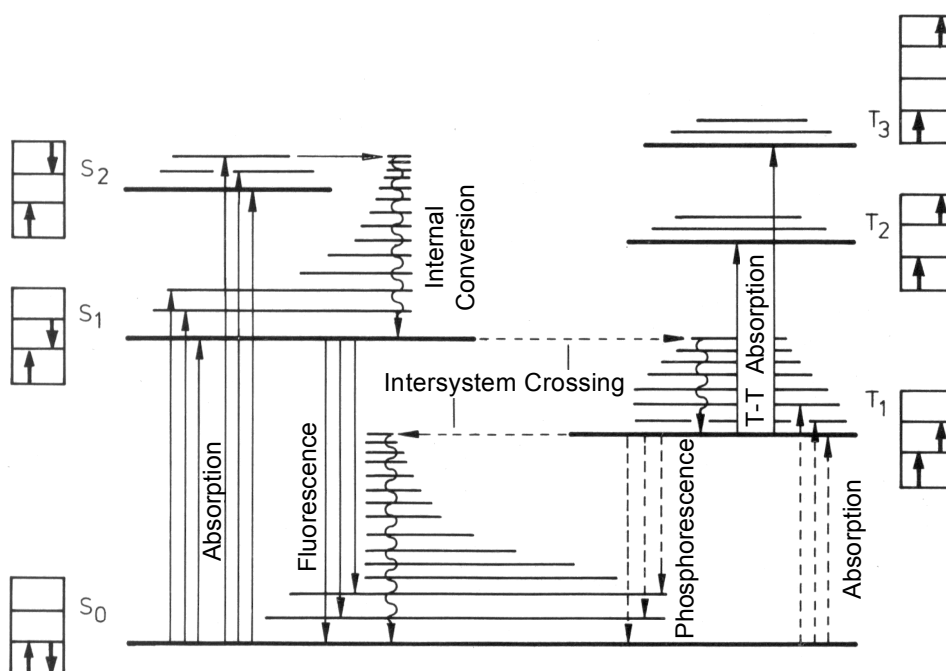


Fig. 2.5: Jablonski diagram of a typical molecule with singlet and triplet systems. Every electronic state is drawn with a number of associated vibronic states. Intersystem crossing and radiative transitions between the two systems (absorption, phosphorescence) are more or less forbidden. Internal conversion and intersystem crossing are radiationless transitions ⁴³.

2.1.2 Transport phenomena in disordered organic semiconductors

It has been suggested above that a band model with coherent transport of electrons and holes is inadequate for the description of transport phenomena in disordered organic semiconductors. Instead neutral and charged excitations are localized to molecules or segments of a conjugated polymer chain, collectively referred to as sites. Due to a variation of conjugation lengths and differing surroundings the energy of equivalent eigenstates on different sites is subject to some distribution $\rho(E)$ and electronic transitions are inhomogeneously broadened. Furthermore the sites are randomly oriented, unevenly spaced, and have only a small overlap of their wavefunctions.

The transfer of excitations in such a system can be modeled with coupled rate equations which, in turn, can be solved by numerical techniques⁶⁰⁻⁶². The temporal evolution of the probability $n_i(t)$ to find an excitation on a site i is described by

$$\frac{dn_i(t)}{dt} = \sum_j (W_{ij}n_j(t) - W_{ji}n_i(t)) + G_i(t) - \frac{n_i(t)}{\tau_{\text{rec}}} \quad (2-3)$$

Here $G_i(t)$ denotes the external generation rate (e.g. by absorption of a photon), and τ_{rec} gives the site-independent recombination rate (e.g. radiative lifetime). The dynamics of the transfer from a site i to any other site j is described by the transfer rate $W_{ji}n_i$ and is determined by the form of interaction. The hopping rate W_{ji} is separated into an intersite-distance dependency and a Boltzmann factor for jumps upward in energy

$$W_{j \leftarrow i} = F(r_{ij}) \cdot \begin{cases} 1 & : E_j < E_i \\ \exp\left(-\frac{E_j - E_i}{k_B T}\right) & : E_j > E_i \end{cases} \quad (2-4)$$

This form of energy dependence implies that the only activation energy for an upward jump is the difference of site energies. The energy for the jump is delivered by a coupling of the sites to a heat bath requiring no exact matching of the energy difference to a particular molecular vibration. The distance dependent factor $F(r_{ij})$ in (2-4) accounts for the interaction mechanism mediating the transfer process and is therefore different for neutral (dipolar) and charged (monopolar) excitations.

2.1.2.1 Energy transfer

In the transport of neutral excitations only energy, but no mass, is transferred from one site to another. The process relies on the dipole-dipole interaction of an excited donor site, an exciton or a polaron pair, with acceptor sites in its surrounding. The transfer rate for this transition depends strongly on the distance between donor and acceptor and the overlap of the donor fluorescence with the acceptor absorption. Förster found that the transfer rate is given by⁶³

$$F(r_{ij}) = \frac{1}{\tau_D} \left(\frac{R_0}{r_{ij}} \right)^6 = \frac{1}{\tau_D} \frac{1}{r_{ij}^6} \left(\frac{3}{4\pi} \int_0^\infty \frac{c^4}{n^4 \omega^4} f_D(\omega) \sigma_A(\omega) d\omega \right) \quad (2-5)$$

Here $f_D(\omega)$ and $\sigma_A(\omega)$ denote the normalized donor fluorescence spectrum and acceptor absorption spectrum respectively. If the distance between donor and acceptor is smaller than the effective Förster radius R_0 , determined by the overlap between fluorescence and emission, then the rate of dipole-dipole transfer will exceed the rate of spontaneous emission τ_D^{-1} of the donor.

In organic materials the overlap of absorption and emission is usually very large and, hence, the dipole-dipole interaction results in an energy relaxation within the density of states on a

picosecond time-scale⁶⁴. Accordingly, fluorescence is predominantly observed from the lowest sites in the DOS⁶¹. Furthermore the energy can be efficiently transferred from donor to acceptor molecules in blended systems consisting of two or more different types of molecules such as Alq₃:DCM⁶⁵.

2.1.2.2 Charge transport

The polarization energy that a charged excitation induces in its surrounding follows an $E_{pol} \propto r_{ij}^{-4}$ dependence⁶⁶. Therefore the presence of disorder and the energy-distribution $\rho(E)$ of neutral states implies that also the charged excitations will have some energetic distribution. In contrast to the case of neutral excitations the transfer of charges is accompanied by a transport of both energy and mass. Since the wavefunction overlap of donor and acceptor is small, the distance dependence of the transfer rate is determined by phonon assisted tunneling and can be approximated by an exponential, hence

$$F(r_{ij}) = f_0 \exp\left(-\frac{2}{\alpha} r_{ij}\right), \quad (2-6)$$

where α is the mean localization length and f_0 is a constant. Note that here the application of an electric field F modifies the energetic barrier $E_i - E_j$ and can thereby enhance the transition rate W_{ji} .

An evaluation of the charge carrier mobility μ based on the hopping rate W_{ji} shows a characteristic dependence on the temperature and an electric field. The exact form depends on the energy distribution $\rho(E)$. Good agreement with experimental data was shown assuming a Gaussian distribution of energetic (σ) and structural (Σ) disorder^{60,67,68}, yielding

$$\mu(F, T) = \mu_\infty \exp\left[-\left(\frac{2\sigma}{3k_B T}\right)^2 + C\left(\left(\frac{\sigma}{k_B T}\right)^2 - \Sigma^2\right)\sqrt{F}\right]. \quad (2-7)$$

As seen in equation (2-7) the field dependence of the mobility is of Poole-Frenkel form $\mu(F) = \mu_0 \exp(\beta\sqrt{F})$. Hence, the maximum unipolar current density that can be achieved when a voltage V is applied to a sample of thickness d is given by the trap free-space charge limited current (SCLC) multiplied with the Poole-Frenkel field dependence⁶⁸

$$j_{SCLC}^{PF} = \frac{9}{8} \epsilon \epsilon_0 \mu_0 \frac{V^2}{d^3} \exp[0.89 \beta \sqrt{F}]. \quad (2-8)$$

Present disordered organic semiconductors achieve room-temperature mobilities in the order of $\mu_h \approx 10^{-3} \text{ cm}^2 \text{V}^{-1} \text{s}^{-1}$ for holes and $\mu_e \approx 10^{-5} \text{ cm}^2 \text{V}^{-1} \text{s}^{-1}$ for electrons, respectively. Once more it should be noted that the comparatively low mobility is a consequence of disorder: whereas regiorandom polythiophenes show mobilities of $10^{-4} \text{ cm}^2 \text{V}^{-1} \text{s}^{-1}$, ordered regioregular poly(3-alkyl thiophene) possess a mobility of $0.1 \text{ cm}^2 \text{V}^{-1} \text{s}^{-1}$ and can even be superconducting at low temperatures⁶⁹.

2.1.2.3 Organic light-emitting diodes

The working principle of an organic light-emitting diode (OLED) is illustrated in the schematic band diagram of Fig. 2.6. Generation of light by electroluminescence requires the injection of both electrons and holes (1), their transport into the emission zone under the influence of an electric field (2), their recombination (3), and the radiative decay of the excitation generated upon electron-hole recombination (4)⁷⁰. Besides these processes a large number of rivaling electronic interactions go hand in hand with the presence and transport of neutral and charged excitations and lead to a reduced luminescence efficiency in the solid state (see e.g.^{59,70-72}). To fulfil the requirements of efficient organic light emitting diodes (OLEDs) and lasers careful optimization is required at every stage.

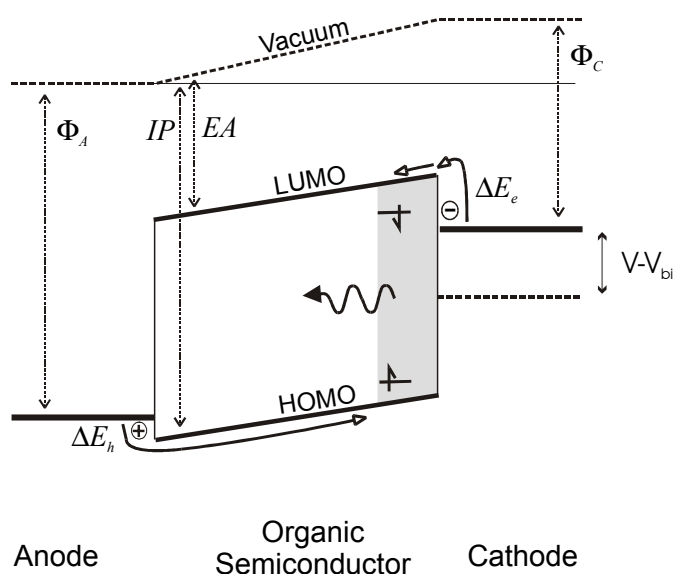


Fig. 2.6:

Schematic band diagram of a single layer OLED under forward bias using indium tin-oxide (ITO) as a hole and Ca as an electron injector. Assuming that no band-bending occurs due to accumulation of space charges the electric field is determined by the applied voltage (corrected for the built-in voltage V_{bi}) and the film thickness, typically 100 - 200 nm. According to¹³.

(1) The injection of carriers from an electrode into the HOMO or LUMO of an organic semiconductor can be described by Fowler-Nordheim tunneling through the energetic barrier caused by the mismatch (ΔE_h , ΔE_e) between the work function (Φ) of the electrode and the ionization potential (IP) or electron affinity (EA) of the organic material. In order to achieve the maximum space-charge limited current, ohmic contacts must be formed, i.e. the electrodes must be able to supply more carriers per unit time than can be transported through the dielectric. In practice, this is only possible if the height of the injection barriers does not exceed some tenths of an eV⁷⁰. The charge injection and, hence, the conductivity can also be increased by doping, either chemically^{73,74} or via field effect electrodes⁶⁹.

(2) Following the injection from electrodes, charged excitations move under the influence of an applied electric field. If the contacts are ohmic, the unipolar current is limited by screening of the applied field through space charges (equation 2-8). In this case the current does not depend on the density of injected carriers but only on the charge mobility. In bipolar devices electrons and holes are present simultaneously, leading to charge neutralization, a reduced field screening, and, consequently, a distinctly higher space charge limited current⁷⁵.

(3) The recombination of electrons and holes to Coulombically bound excitons is a bimolecular Langevin-type process. Effective recombination requires a balanced injection of electrons and holes combined with a long dwell-time of the charge carriers in the recombination zone⁷⁶. Since the limiting process is the diffusion of the carriers towards each other in their mutual Coulombic potential, the optimum recombination efficiency is reached if electron and hole current are both space charge limited. Otherwise a typical low mobility device contains significantly more polarons than excitons⁷⁷. Due to spin-statistics and the higher multiplicity of triplets, it is generally assumed that potentially emissive singlet states are generated in no more than 25% of the recombination events. Nevertheless, it has very recently been shown for a number of conjugated polymers that the ratio of singlet to triplet states can actually be distinctly larger⁷⁸.

(4) As soon as an exciton is created it may undergo intramolecular transitions as outlined in Section 2.1.1.3. Furthermore it can propagate diffusively, associated with a gradual energetic relaxation within the density of states and will, eventually, emit a photon. However the fluorescence yield, i.e. the fraction of singlet states that decay radiatively, is often not larger than 30%. The major source of excited state quenching is charge transfer from a chromophore to an impurity state, such as oxidation products with low lying LUMO state. At the high excitation densities required for laser operation, significant quenching occurs due to bimolecular exciton-exciton³⁷ or exciton-polaron⁷⁹ interaction. Furthermore excitons may re-dissociate and form non-emitting intra- or interchain polaron pairs, a process that is enhanced by the presence of an electric field⁸⁰. Last but not least, the radiationless transfer of excitation to electrodes must be taken into account. The interaction radius of these parasitic processes is enhanced by exciton diffusion.

The properties of OLEDs can be significantly improved if multilayer devices are used, allowing to optimize charge injection and transport separately for both carrier types⁸¹. Furthermore energetic barriers can be introduced which prevent excess carriers from passing through the device to the counterelectrode without recombining. This increases the dwell time of the carriers inside the recombination zone and, hence, the Langevin recombination rate. Moreover, heterostructures serve to shift the recombination zone away from the electrodes into the middle of the device and thus reduce the nonradiative quenching of excitons at the electrodes⁸². Using such a double layer device made from PPV, Tessler et al. demonstrated current densities up to 1 kA cm^{-1} under pulsed electrical excitation⁸³. At these high current densities the mobility increased drastically. Exciton densities in the order of 10^{14} cm^{-3} were obtained. Current heating was one of the most important factors limiting the efficiency of these devices⁸⁴.

2.2 Lasing in organic semiconductors

2.2.1 Stimulated emission

A prerequisite for lasing is the presence of stimulated emission, quantified by the wavelength dependent cross-section for stimulated emission $\sigma_{SE}(\lambda)$. Conjugated polymers and dyes typically show strong stimulated emission for the transition from the singlet state $S_{1,v=0}$ to vibronic sublevels of the ground state $S_{0,v}$. Due to the fast relaxation out of the vibronic levels the ground state of the optical transition is usually unpopulated, resulting in a four-level system. As light travels through an amplifying medium its intensity grows exponentially according to

$$I = I_0 \exp[(g(\lambda) - \alpha)L] \quad , \quad (2-9)$$

where I_0 is the initial intensity, g is the (power) gain coefficient, α is the loss coefficient and L is the distance traveled in the gain medium. In a four-level system the gain is related to the volume density of excited states N_{exc} via $g(\lambda) = \sigma_{SE}(\lambda) N_{exc}$. The wavelength dependence of σ_{SE} in most cases resembles the photoluminescence spectrum and is given by

$$\sigma_{SE}(\lambda) = \frac{\lambda^4 f(\lambda)}{8\pi n^2 c \tau_{rad}} \quad , \quad (2-10)$$

where $f(\lambda)$ is the normalized spectral distribution of the photoluminescence, n is the refractive index of the material c is the vacuum speed of light and τ is the radiative lifetime of the involved optical transition. Several conjugated polymers have a large cross-section for stimulated emission of some 10^{-16}cm^2 and can be used to fabricate optically pumped solid-state lasers with remarkably low threshold excitation densities in the range of 10^{17}cm^{-3} (see e.g. ⁸⁵ and references therein).

In general, the following important criteria have to be fulfilled for active materials in laser applications:

1. high luminescence efficiency
2. no spectral overlap between stimulated emission and residual or excited state absorption (neutral or charged species).
3. high mobility of electrons and holes (injection lasers only)

Regarding point 1 many conjugated polymers and dyes fulfil this criterion. If the defect density is low enough and aggregation of individual chains can be avoided PL efficiencies up to 80% can be achieved in the solid state ²². Regarding point 2 only a few basic structures seem to show the necessary spectral separation of photoinduced absorption and stimulated emission, namely some derivatives of poly(*p*-phenylene vinylene) (PPV), poly(*p*-phenylene) (PPP) and polyfluorene (PF). For future injection lasers the choice of materials is further reduced as many materials exhibit charge-induced absorption bands in the optical bandgap.

An additional degree of freedom is provided by composite guest-host systems, where the functions of charge transport and emission are undertaken by different species.

2.2.2 Amplified spontaneous emission

A good technique to characterize an organic substance as a laser material is to photopump a slab waveguide, made by deposition of a thin film of the material on a low refractive index substrate. If the pump intensity is high enough for the gain to exceed the scattering losses then spontaneously emitted photons are exponentially amplified as they travel through the waveguide (equation 2-9). Since predominantly those photons are amplified whose energy coincides with the spectral position of maximum gain the overall emission spectrum changes. A collapse of the emission spectrum, called gain narrowing, is observed as amplified spontaneous emission becomes the dominant deactivation pathway. This happens if the exponent in equation 2-9 exceeds unity, $(g(\lambda) - \alpha)L \geq 1$.

Gain narrowing in a solid conjugated polymer was first observed in 1996 in a film of MEH-PPV⁸⁶ containing strongly scattering TiO₂ particles. In the following gain narrowing was found for a large number of pure conjugated polymers, mostly derivatives of PPV, PPP or polythiophene (see e.g.⁸⁵ and references therein), as well as in films of spiro-type organic molecules⁸⁷. Owing to their small Stokes shift and the large residual self-absorption the stimulated emission is hampered in some strongly luminescent molecules. The Stokes shift can be drastically increased if the emitting species is blended into a matrix with a higher bandgap. As described above, Förster-type energy transfer leads to red-shifted optical transitions accompanied by a substantially reduced residual absorption. Using this technique gain narrowing was found for a number of strongly fluorescent dyes embedded in a conducting matrix⁸⁸ or in blends of different conjugated polymers⁸⁹. The threshold for gain narrowing occurs at excitation densities of typically 10^{17} - 10^{18} cm⁻³ corresponding to excitation energy densities of ~ 1 - 10 μ J cm⁻² in pulsed optical excitation. These values are comparatively low as a result of the high stimulated emission cross-section of organic molecules.

Subsequent to the initial observation of spectral narrowing it was proposed that the underlying mechanism was superfluorescence^{90,91} or biexcitonic emission⁹². But in the meantime detailed investigations of the emission together with quantitative modeling of the emission process have identified the mechanism to be amplified spontaneous emission (ASE)^{37,93-100}.

ASE in waveguide structures is sometimes called “mirrorless” lasing as it can have many properties of a laser such as a distinct threshold in the input-output characteristics and the emission of a concentrated, polarized, and nearly monochromatic beam. Nonetheless, the absence of resonant modes and the incoherent output distinguishes ASE from lasing.

2.2.3 Resonant laser structures

The large variety of resonator geometries that can be realized with organic materials opens a wide field of research opportunities. Fig. 2.7 features the geometries that have been explored in the past years using optical excitation. The first attempts to achieve true lasing action from a high gain organic semiconductor material inside a resonator providing positive feedback were carried out using a microcavity resonator²². Microcavity lasers (Fig. 2.7 (a)) have several attractive advantages: they are easy to fabricate, their architecture is similar to organic LEDs and they emit perpendicular to the substrate. On the other hand, the distance traveled by light on each pass through the gain region is small which results in a low roundtrip gain and relatively high threshold values¹⁰¹ unless highly reflective dielectric mirrors are used on both sides of the cavity¹⁰²⁻¹⁰⁴.

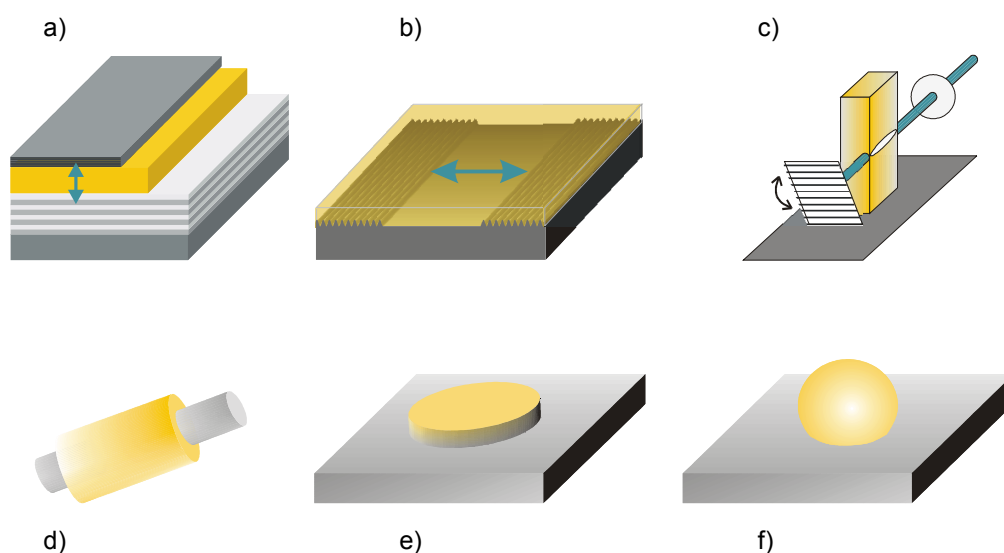


Fig. 2.7: Scheme of various resonator structures for optically pumped organic semiconductor lasers. (a) Microcavity, (b) planar waveguide with corrugated substrate (distributed Bragg reflector or distributed feedback), (c) tunable external cavity, (d) microring, (e) microdisk, (f) microdroplet (Taken from¹⁰⁵).

The problem of the small gain length and the associated low roundtrip gain can be circumvented if planar waveguides are used. A major advantage of the waveguide approach is its compatibility with the diode architecture required for electrical excitation. The simplest way to make a resonator is to break the organic film giving rise to reflections at the facets^{106,107}. Contrary to inorganic semiconductor lasers, however, breaking does not produce facets of either high quality or high reflectivity. Superior performance is achieved when the feedback is incorporated via a periodic perturbation of the waveguide (see Fig. 2.7 (b)) giving rise to Bragg scattering²³⁻²⁸. The working principle of these lasers with distributed feedback is discussed in more detail in Section 2.3.

Other interesting geometries use the whispering-gallery-modes due to total internal reflection in ring-like structures comprising microdisk, microdroplet and microring lasers (d-f)¹⁰⁸⁻¹¹³.

The large spectral width of the optical gain and the resulting tunability of organic lasers was exploited by placing the organic material inside a conventional dye laser cavity suitable for transverse pumping. A grating acts as high reflector and allows for wavelength tuning (c) ¹¹⁴⁻¹¹⁸. In the meantime the large number of publications on organic semiconductor lasers has been reviewed separately for polymer lasers ^{85,105,119-123} and lasers made from small molecules ^{28,107,124-127}.

2.3 Distributed feedback lasers

The concept of distributed feedback (DFB) lasers was introduced in the early 1970s by Kogelnik et al., who realized that laser operation can be achieved if a periodic structure is integrated within the gain region ¹²⁸. The major difference to a conventional device is that feedback is not established by *local* reflectors but by Bragg scattering due to periodically *distributed* optical inhomogeneities. Soon it was found that distributed feedback provides efficient means for narrow bandwidth, tunable laser emission ²⁹. Since then the concept has been extended to thin film waveguides ¹²⁹, distributed Bragg reflection (DBR), two-dimensional DFB ¹³⁰ and, more recently, photonic bandgap lasers ¹³¹. Subsequently the concept of distributed feedback has been applied in a vast number of diode lasers meeting virtually any demand for high-throughput optical data communication ³⁰. In the following the fundamentals of distributed feedback will be presented with special emphasis on thin film waveguide geometries.

2.3.1 Slab waveguides

Fig. 2.8 shows the schematic setup of a dielectric three-layer slab waveguide consisting of a thin film with thickness d_f that is sandwiched between substrate and cover having refractive indices of n_f , n_s and n_c , respectively. Mathematically, the propagation of light in dielectric medium is described by the Helmholtz equation for the electric field $\mathbf{E}(\mathbf{r},t)$

$$\nabla^2 \mathbf{E}(\mathbf{r},t) - \frac{n^2(\mathbf{r})}{c^2} \frac{\partial^2 \mathbf{E}(\mathbf{r},t)}{\partial t^2} = 0 \quad , \quad (2-11)$$

whose solution is of the form $\mathbf{E}(\mathbf{r},t) = \mathbf{E}_0 \exp[i(n(\mathbf{r})\mathbf{k}_0 \cdot \mathbf{r} - \omega t)]$ with the wavevector $k_0 = 2\pi/\lambda$. A determination of the waveguide modes requires solving equation 2-11 with appropriate boundary conditions.

From a simple ray model it is seen that a plane wave propagating in the film under some angle θ can be guided, provided that θ is larger than the critical angle of total internal reflection at both boundaries, implying that $n_f > n_s \geq n_c$. The second condition for waveguiding is that a standing wave pattern is formed by constructive interference of the incident wave with itself after reflection at both boundaries, yielding ¹³²

$$2k_0 n_f d_f \cos \theta_m - 2\phi_c(\theta_m) - 2\phi_s(\theta_m) = m \cdot 2\pi \quad , \quad \text{where } m = 0, 1, 2, \dots \quad (2-12)$$

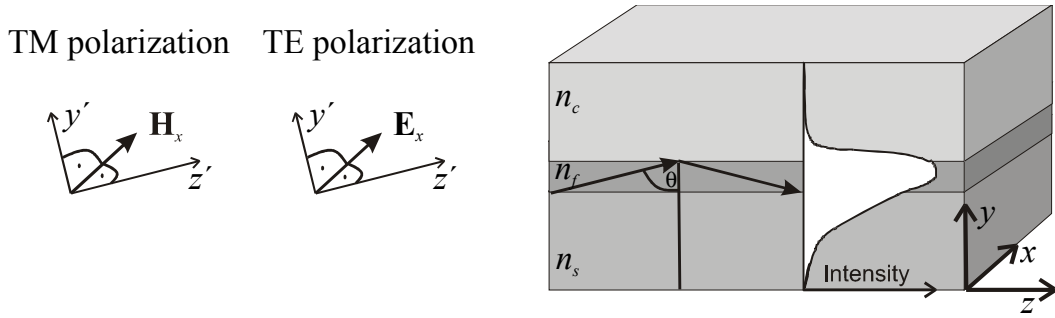


Fig. 2.8: Schematic drawing of a three layer slab waveguide. Plane waves propagating under an angle θ in the film are totally internally reflected at both boundaries. For TM waves the \mathbf{H} -vector is in the waveguide plane (in x -direction), for TE waves it is the \mathbf{E} -vector. The white-filled area sketches a typical intensity distribution in an asymmetric waveguide.

Since the phase jump ($2\phi_a$) associated with the reflection at the boundary to the adjacent layer a ($a = c, s$) depends on the polarization of the electromagnetic wave two cases have to be distinguished: TE (transversal electric) waves with the electric field vector \mathbf{E} in the waveguide plane and TM (transversal magnetic) waves with the magnetic field vector \mathbf{H} parallel to the waveguide plane. The phase jump is given by

$$\tan \phi_{a\text{TE}} = \frac{\sqrt{n_f^2 \sin^2 \theta - n_a^2}}{n_f \cos \theta} ; \quad \tan \phi_{a\text{TM}} = \frac{n_f^2}{n_a^2} \frac{\sqrt{n_f^2 \sin^2 \theta - n_a^2}}{n_f \cos \theta} . \quad (2-13)$$

According to equation 2-12 guided waves can only exist for discrete modes depending on the angle θ_m . Their intensity distribution in the y -direction results from the superposition of the plane wave propagating at angle θ_m with the reflected wave propagating at angle $(180^\circ - \theta_m)$. In the cladding layers evanescent waves are formed whose intensity falls to zero within approximately one wavelength, depending on the refractive index contrast between film and cladding layers.

The propagation of the guided wave in z -direction is entirely determined by the wavevector component³ $k_z = n_f \sin \theta_m k_0 = n_{\text{eff}} k_0$. Therefore the guided wave propagates in z -direction like a plane wave in a bulk material with refractive index n_{eff} . This is reflected in the Helmholtz equation which, apart from the constant variation $E(x, y)$, simplifies to a scalar equation

$$\frac{\partial^2 E(z, t)}{\partial z^2} + k_z^2 E(z, t) = 0 \quad \text{with a solution } E(z, t) = E_0 \exp[i(k_z z - \omega t)]. \quad (2-14)$$

All the relevant properties of guided wave propagation are therefore linked to the effective refractive index, which varies between the refractive index of the substrate and the film $n_c \leq n_s \leq n_{\text{eff}} \leq n_f$. In Fig. 2.9 (a) n_{eff} is plotted as a function of film thickness for a given wavelength in a typical organic film deposited on a glass substrate. It is seen that no guided wave is supported below a cutoff thickness and that n_{eff} is higher for TE than for TM

³ In the context of thin film lasers k_z is often called the propagation constant β .

polarization, indicating a stronger optical confinement of TE waves inside the organic film. TE waves therefore interact stronger with the gain medium, suffer less surface loss and, thus, usually have a lower laser threshold. For a given film thickness the dispersion relation $\omega(k_z)$ and the group velocity $v_{group} = d\omega/dk_z = c/n_{group}$ of the guided wave can be determined (Fig. 2.9 (b)).

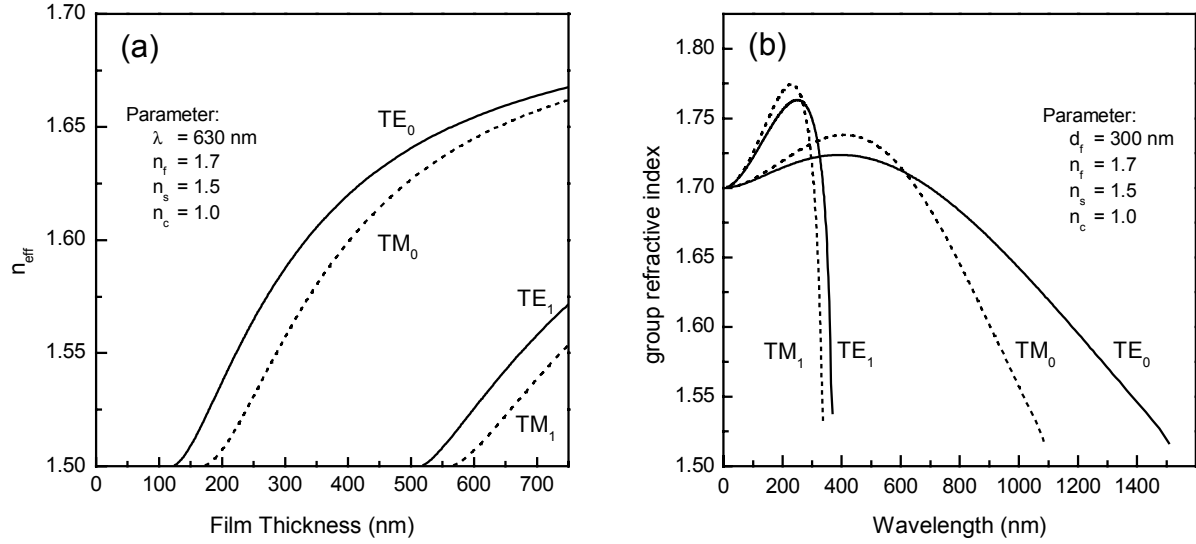


Fig. 2.9: (a) Effective refractive index as a function of film thickness d_f for a wavelength of $\lambda = 630$ nm in a typical organic film ($n_f = 1.7$) deposited on a planar glass substrate ($n_s = 1.5$). Below the cutoff thickness no guided waves are supported. (b) group refractive index of the first two TE and TM modes for a given film thickness of $d_f = 300$ nm (assuming n_f were independent of λ). No guided waves are supported above a certain cutoff wavelength.

2.3.2 One-dimensional distributed feedback lasers

2.3.2.1 Bragg scattering

Distributed feedback relies on Bragg scattering due to a periodic modulation of the complex refractive index, either in its real (n) or in its imaginary part (χ). In the special case of thin film lasers this is manifested in a modulation of the effective refractive index, $n_{eff}(z) = n_{eff}(z + \Lambda)$, or the gain coefficient, $g(z) = g(z + \Lambda)$, with the periodicity Λ . A periodic modulation of the waveguide thickness, as sketched in Fig. 2.10, perturbs the propagation of guided waves and induces coupling between otherwise independent waves. Waves propagating in the positive z -direction are partially reflected and thus coupled to waves propagating in the negative z -direction. Coupling becomes particularly strong if the reflected waves interfere constructively, which is specified by the Bragg condition. Assuming that the perturbation of n_{eff} is small the Bragg condition reads.

$$n_{eff} \Lambda = m \frac{\lambda_{Bragg}}{2} ; \quad m = 1, 2, \dots \quad (2-15)$$

Fig. 2.10 (a) shows the situation for first order distributed feedback ($m = 1$). If the Bragg condition is fulfilled with $m \geq 2$ then the lower Bragg orders will be scattered out of the waveguide. As an example a 2nd order DFB laser ($m = 2$) is sketched in Fig. 2.10 (b). It emits radiation perpendicular to the surface.

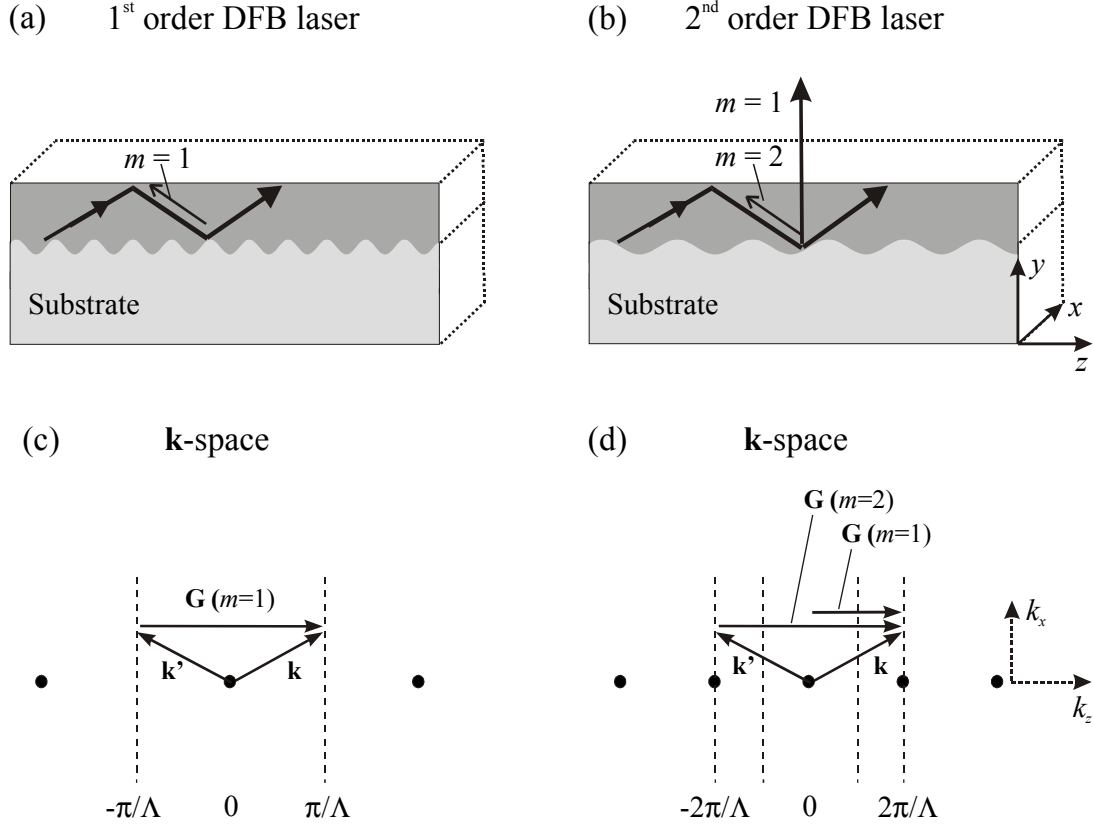


Fig. 2.10: Scheme of a DFB laser with feedback in first (a) and second (b) Bragg order. The corresponding reciprocal space is sketched in (c) and (d). The reciprocal lattice points are indicated by the black dots, the dashed lines denote the Bragg planes. Also shown is one pair of \mathbf{k} -vectors fulfilling the Laue condition.

A more general formulation of the Bragg scattering process can be given in the reciprocal space (\mathbf{k} -space). In \mathbf{k} -space the wavelength λ is replaced by the wavevector \mathbf{k} . The modulation of the waveguide is represented by a reciprocal lattice of evenly spaced lattice points, defined by the lattice vectors \mathbf{G} .

The fact that the propagation of guided waves is confined to the x - z waveguide plane is reflected in a two-dimensional extension of the reciprocal space. In this 2D \mathbf{k} -space a plane wave is described by $\mathbf{k} = \begin{pmatrix} k_x \\ k_z \end{pmatrix}$, where $|\mathbf{k}| = n_{eff} \cdot 2\pi/\lambda$. The reciprocal lattice corresponding to the waveguide modulation of Fig. 2.10 (a) and (b) is shown in Fig. 2.10 (c) and (d), respectively. The periodic waveguide modulation in z -direction generates reciprocal lattice points at $\mathbf{G} = m \mathbf{G}_0 = m \begin{pmatrix} 0 \\ 2\pi/\Lambda \end{pmatrix}$. With this notation the Bragg condition 2-15 rewrites $2k_{z,Bragg} = |\mathbf{G}|$. In analogy to the scattering of X-rays in an atomic crystal the Bragg condition can be generalized to the Laue condition¹³³.

$$2\mathbf{k} \cdot \mathbf{G} = |\mathbf{G}|^2. \quad (2-16)$$

This formulation of the feedback condition says that Bragg scattering can occur if the photon \mathbf{k} -vector is located on a Bragg plane⁴, being the perpendicular bisector of the line connecting the origin with the reciprocal lattice point \mathbf{G} . In Fig. 2.10 (c) and (d) these Bragg planes are indicated by dashed lines. A wave whose \mathbf{k} -vector is located on a Bragg plane is scattered to \mathbf{k}' and vice versa. The wavevectors of the scattered and incident wave are related via $\mathbf{k}' = \mathbf{k} - \mathbf{G}$. Note that the Laue condition is fulfilled for a continuous spectrum of plane waves all having a well defined value of k_z but continuously varying k_x . Unless further precautions are taken, a 1D-DFB laser will therefore operate simultaneously on many lateral modes.

In surface emitting lasers the output coupling is also governed by Bragg scattering. For the 2nd order DFB laser sketched in Fig. 2.10 (d) the relevant process is first order Bragg scattering ($m = 1$). The propagation direction of the radiated wave (angle φ with respect to the surface normal) is determined by phase-matching of the radiated wave and the scattered wave at the surface of the waveguide. It is governed by the relation

$$k_0 \sin \varphi = |\mathbf{k} - \mathbf{G}| . \quad (2-17)$$

2.3.2.2 Coupled wave theory

For a more detailed investigation of distributed feedback the Helmholtz equation 2-11 has to be solved in the presence of the periodic modulation. Several numerical methods have been developed, illuminating different aspects of the distributed feedback (see Section 5.5). A good qualitative understanding of DFB laser operation is provided by the coupled wave theory¹³⁴. It allows to calculate the laser threshold and the dispersion relation $\omega(k_z)$ of the photonic band structure assuming a weak⁵ *harmonic perturbation* of the propagation constant $k_z(z)$. The perturbation can affect the refractive index as well as the gain and is expressed as

$$k(z) = [n_{eff} + \Delta n \cos(|\mathbf{G}_0|z)]k_0 + i(\gamma + \Delta\gamma \cos(|\mathbf{G}_0|z)) , \quad (2-18)$$

where $\gamma = g/2$ is the field gain coefficient of the active medium. Bragg scattering is unimportant unless the Bragg condition is fulfilled. The description can therefore be restricted to k -values close to k_{Bragg} , in other words to the edges of the Brillouin zones. In the vicinity of k_{Bragg} the solution of the Helmholtz equation is approximated by a superposition of a right and left running wave with propagation constant k_{Bragg} (equation 2-19). These waves grow because of the presence of gain and they feed energy into each other due to Bragg scattering. All deviations from the exact Bragg condition as well as the growth and coupling are accounted by the prefactors $R(z)$ and $L(z)$ of the right- and left-running wave.

⁴ The Bragg plane is a x - y plane. In the two-dimensional \mathbf{k} -space the Bragg plane reduces to a line.

⁵ Weak means here that $\Delta\gamma \ll n_{eff}G$ and $\Delta n \ll n_{eff}$.

$$\begin{aligned}
E(z) &= R(z)\exp[-i k_{Bragg} z] + L(z)\exp[i k_{Bragg} z] \\
R(z) &= r_1 \exp(-i \beta z) + r_2 \exp(i \beta z) \\
L(z) &= l_1 \exp(-i \beta z) + l_2 \exp(i \beta z)
\end{aligned} \tag{2-19}$$

The propagation of the right and left running waves are determined by the complex offset propagation constant β . Its real part, $\text{Re } \beta = k - k_{Bragg}$, is the offset from the Bragg value, its imaginary part leads to an exponential rise or decay of the right/left running wave's amplitude.

With these assumptions the Helmholtz equation yields an implicit form of the photon dispersion relation $\omega(k)$

$$\begin{aligned}
\beta^2 &= (\delta + i \gamma)^2 - \kappa^2 \quad , \text{ with} \\
\delta &= \frac{n_{eff}}{c} (\omega - \omega_{Bragg}) \quad , \\
\kappa &= \frac{m |\mathbf{G}_0|}{4n_{eff}} \Delta n + \frac{1}{2} i \Delta \gamma \quad .
\end{aligned} \tag{2-20}$$

Equation 2-20 allows to determine the offset propagation constant β for given values of (1) the detuning from the Bragg frequency, δ , (2) the field gain, γ , and (3) the coupling coefficient, κ , being related to the modulation of the effective refractive index and of the gain. Depending on the choice of these parameters, β can be either purely real, purely imaginary or complex. Accordingly, three situations have to be distinguished which lead to significantly different laser properties: index coupling if κ is real ($\Delta n \neq 0$; $\Delta \gamma = 0$), gain coupling with imaginary κ ($\Delta n = 0$; $\Delta \gamma \neq 0$), and complex coupling if $\Delta n \neq 0$; $\Delta \gamma \neq 0$. The difference between these three regimes is manifested in different values of δ , β , and the threshold gain γ_{th} . Two transcendental equations relate these parameters

$$\kappa = \pm \beta / \sinh(-i \beta L) \tag{2-21}$$

$$\gamma_{th} = -i \beta \coth(-i \beta L) + i \delta \quad . \tag{2-22}$$

Fig. 2.11 shows the dispersion relation for a DFB laser with pure index and pure gain coupling in the limit of vanishing average gain γ . In the case of pure *index coupling* there is a range of frequencies around the Bragg frequency ω_{Bragg} for which β is purely imaginary. Since the corresponding waves cannot propagate in the waveguide this band of forbidden propagation is called stopband. An index coupled DFB laser will oscillate simultaneously in two modes at both sides of the stopband, at the highest density of states $D(\omega) \propto dk/d\omega$ and the lowest threshold gain. The laser threshold is given by

$$\gamma_{th} L = \left(\frac{\pi}{\kappa L} \right)^2 \tag{2-23}$$

In contrast, all frequencies are allowed in a purely *gain coupled* DFB laser, yet, there is a range of forbidden propagation constants around k_{Bragg} . The lowest laser threshold is found at the Bragg frequency with a value of $\Delta\gamma_{th} = \pi/L$.

Whether the behavior of a *complex coupled* DFB laser resembles an index or a gain coupled device depends on the relative strength and sign of the real and imaginary part of the coupling constant. Generally, it can be said that the presence of gain coupling will always lift the degeneracy of the modes and thus favor monomode operation¹³⁵.

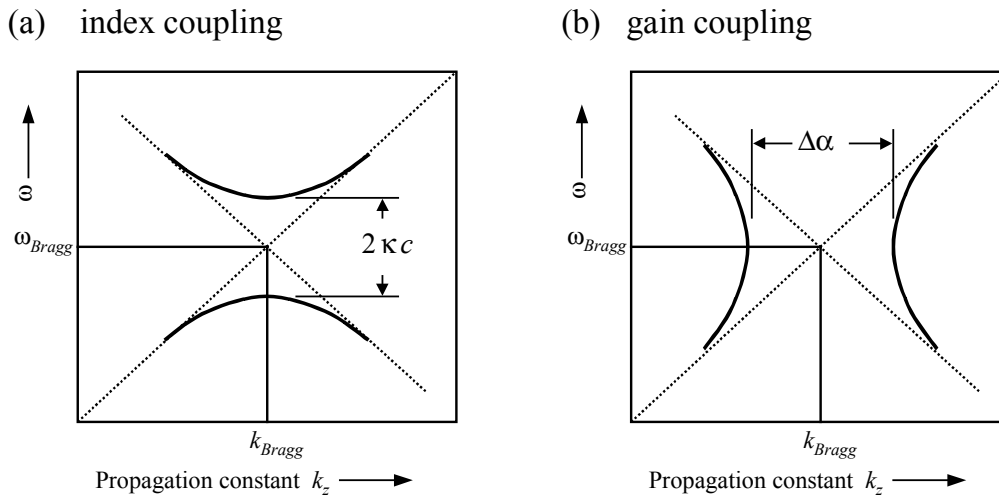


Fig. 2.11: Dispersion relation for a DFB laser with pure index modulation (a) and pure gain modulation (b). The effect of the average gain is in both cases neglected¹³⁴.

2nd order DFB lasers

The above description is valid for feedback in the 1st Bragg order. For feedback in Bragg orders $m \geq 2$, the lower orders will be scattered out of the waveguide. This effect does not only cause a constant loss for the propagating waves but also induces an additional periodic modulation of the loss. Therefore the 2nd order index grating has a similar effect like a 1st order loss modulation¹³⁶. Consequently pure index coupling is impossible for 2nd order DFB lasers and the mode degeneracy of an “index coupled” DFB lasers is lifted. Only the mode at the long wavelength side of the stopband evolves^{137,138}. In order to include the intensity losses due to surface emission, α_{Loss} , the threshold condition needs to be rewritten for 2nd order DFB lasers¹³⁹

$$g_{th}L = 2 \left(\frac{\pi}{|\kappa|L} \right)^2 + \alpha_{Loss}L . \quad (2-24)$$

Non-harmonic perturbations

As mentioned above, the coupled wave theory assumes harmonic, sinusoidal perturbations of the refractive index or gain. The Fourier spectrum of the perturbation therefore contains only one single spatial frequency $2\pi/\Lambda$. In the case of a purely harmonic perturbation the reciprocal space should therefore contain only one grating vector \mathbf{G}_0 . In contrast, the

reciprocal lattice introduced above consists of an infinite number of reciprocal lattice points, each corresponding to a different higher harmonic $m 2\pi/\Lambda$ of the modulation. Any real lattice is somewhere in between these two extremes and the waveguide perturbation contains a number of spatial harmonics. The relative strength of the corresponding Bragg scattering process scales with the respective Fourier component of the modulation. It is quantified by the corresponding coupling coefficient.

2.3.3 Two-dimensional distributed feedback lasers

2.3.3.1 Bragg scattering

The concept of distributed feedback can be extended to lasers containing a two-dimensional periodic modulation¹³⁰, named 2D-DFB lasers. Fig. 2.12 sketches a two-dimensional periodic structure and its reciprocal lattice. For a rectangular lattice with $\phi = 90^\circ$ the reciprocal lattice is also rectangular with $G_z = m 2\pi/\Lambda_z$ and $G_x = n 2\pi/\Lambda_x$. Just as in the one-dimensional case, the condition for distributed feedback is described by the Laue condition (2-16) with the reciprocal lattice vectors $\mathbf{G}_{mn} = \begin{pmatrix} G_x \\ G_z \end{pmatrix}$.

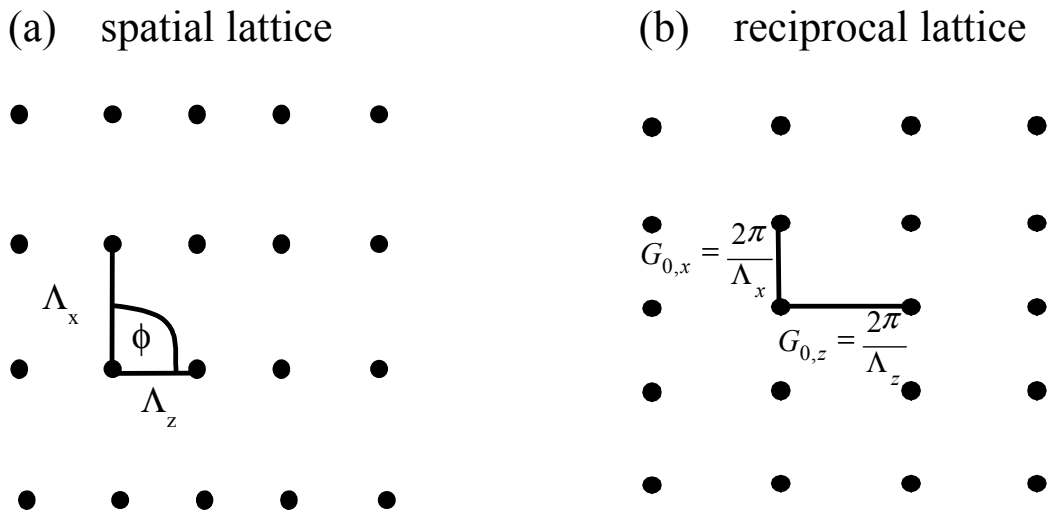


Fig. 2.12: (a) A two-dimensional rectangular lattice in real space. (b) The corresponding reciprocal lattice.

In first experiments with 2D-DFB lasers it was found that the divergence of the laser radiation could be significantly reduced with respect to 1D-DFB lasers but it was still far beyond the diffraction limit^{140,141}. Despite these early, promising results there have only been very few experimental^{130,140,141} and theoretical¹⁴²⁻¹⁴⁴ investigations until the recent renewed interest within the context of photonic crystal lasers. The first experimental demonstrations of 2D-photonic crystal lasers based on organic or inorganic materials were published more or less simultaneously with the work of the author¹⁴⁵⁻¹⁴⁹.

2.3.3.2 Coupled mode analysis

The first quantitative theoretical investigations of 2D-DFB lasers were presented in a coupled mode analysis for rectangular gratings^{142,144}. These calculations neglect interactions due to higher spatial harmonics of the modulation as well as the interaction between guided and radiation fields. It was predicted that simultaneous coupling of the guided waves to the x - and z -grating could lead to monomode laser operation in first and second Bragg order, i.e. for the wavevectors $\mathbf{k} = \begin{pmatrix} \pi/\Lambda_x \\ \pi/\Lambda_z \end{pmatrix}$ or $\mathbf{k} = \begin{pmatrix} 2\pi/\Lambda_x \\ 2\pi/\Lambda_z \end{pmatrix}$. In contrast to 1D-DFB lasers no horizontal confinement would be required. In the case of second order distributed feedback the phase of the radiation field is the same all over the surface. Hence, the divergence of the laser beam should be diffraction-limited with respect to the extension of the excited area^{144,150}. Nevertheless the proposed diffraction-limited surface emission had not been observed prior to this work.

2.3.3.3 Photonic band structure analysis

A complementary method to analyze the behavior of 2D-DFB lasers is the computation of the respective photonic band structure. For that purpose numerical techniques have been developed that account for the contributions of all possible Bragg scattering processes. The results are usually displayed as band structure diagrams $\omega(\mathbf{k})$, like the one shown in Fig. 2.13 (a) for a 2D lattice consisting of dielectric columns³⁶. According to the Bloch theorem every state of the infinitely extended reciprocal space (extended zone scheme) can be represented by a \mathbf{k} -vector within the first Brillouin zone by translation of a reciprocal lattice vector. States originally located outside the first Brillouin zone are then attributed to a higher band of the

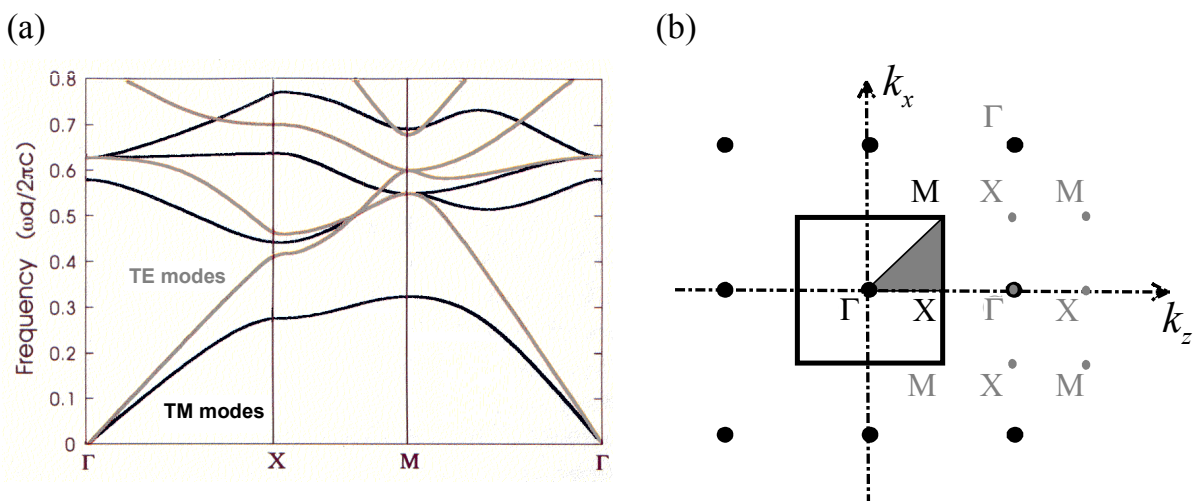


Fig. 2.13: Band structure of a two-dimensional square lattice of infinitely long dielectric columns in air³⁶. The dispersion relation of TE waves is shown in gray, TM waves are plotted black. (b) Reciprocal lattice (black dots) with the 1st Brillouin zone (square) and the irreducible Brillouin zone (gray-shaded triangle) with its high symmetry points Γ , X, and M. Gray letters indicate how some points outside the first Brillouin zone are related to the high symmetry points of the irreducible Brillouin zone by application of the Bloch theorem.

corresponding state inside the first Brillouin zone (reduced zone scheme). By means of symmetry the 1st Brillouin zone can be further diminished to the irreducible Brillouin zone shown by the shaded region in Fig. 2.13 (b).

Bragg scattering occurs if the Laue condition is fulfilled, which happens, by definition, for \mathbf{k} -vectors on the boundary of the Brillouin zones. In the case of 2D photonic crystals the border of the irreducible Brillouin zone contains all relevant states. The strongest coupling is typically expected exactly at the symmetry points. From the coupled wave analysis of 1D-DFB lasers it is known that strong Bragg scattering results in an anti-crossing of bands and the occurrence of a stopband whose width scales with the coupling strength. In the 2D photonic crystal of Fig. 2.13 the formation of a bandgap can be seen for instance by the splitting between the first and second TE and TM bands at the X-point.

It is possible to design structures having a complete photonic bandgap for all \mathbf{k} and both polarizations¹⁵¹. In such structures it is possible to suppress the spontaneous emission and modify the radiative lifetime³³⁻³⁵. The introduction of a properly designed defect state located in the photonic bandgap is a promising way to achieve lasing with an extremely low threshold and mode volume^{152,153}. On the other hand, the dielectric contrast that is needed for a complete photonic bandgap is very high and can not be reached with organic materials alone.

2.3.4 Randomly distributed feedback

The distributed feedback lasers described in the former sections rely on constructive interference of waves which are scattered at *periodically* arranged optical inhomogeneities. In contrast thereto randomly distributed feedback relies on the constructive interference of waves which are multiply scattered at *a-periodic* inhomogeneities. The resonator of such a laser is a random closed loop as sketched in Fig. 2.14. The oscillation frequency is then determined from the condition that the phase shift along the loop is a multiple of 2π .

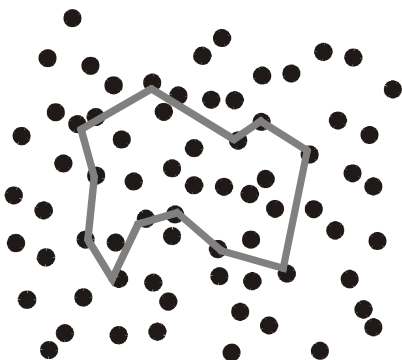


Fig. 2.14:

Schematic representation of a two-dimensional system with embedded scattering centers. If the mean free path of photons is sufficiently short recurrent light-scattering can occur efficiently and lead to random closed loop cavities.

The actual formation of such closed loops, however, requires that there is a certain probability for recurrent light-scattering, which means that a photon returns to the infinitesimal neighborhood of a place where it has been before. Although the concept is very easy it turns out that the premises for recurrent light-scattering are very strict. Therefore it was not until

recently that laser oscillation with discrete resonances¹⁵⁴⁻¹⁶⁹ as well as laser speckles¹⁷⁰ were observed in various structures exhibiting strong scattering. In some of these cases it was, however, not clear whether the observed resonances are truly due to random closed loops or rather to other forms of feedback, such as reflections at the boundaries of the active medium. Before attributing resonances in the emission spectrum to random lasing it is important to check if the behavior of the laser is in accordance with the expectations for light-propagation in strongly scattering medium.

2.3.4.1 Light propagation in strongly scattering media without gain

In a non-amplifying medium system three regimes of light-propagation have to be distinguished, depending on the wavelength and the photon's mean free path between two consecutive scattering events, l^* ¹⁷¹:

- $kl^* \gg 1$: in the regime of weak scattering light propagates diffusively. The phase of the light wave and interference effects can be neglected.
- $kl^* \approx 1$: in the presence of moderate scattering interference effects become important. If coherent light falls on such a medium, waves traveling the same path through the scattering medium, yet in the opposite direction, interfere constructively in the backscattering direction. Therefore the intensity of the backscattered light is enhanced. The photons start to be localized (regime of weak photon localization)^{172,173}.
- $kl^* < 1$: when scattering is so strong that the mean free path of light becomes smaller than a single cycle of the light wave light transport comes to a complete stop^{174,175}. A localized state is formed by interference of the trapped electromagnetic wave with itself (regime of Anderson localization⁶). The extension of the state is given by the localization length $\xi_0 \approx (2-4) \cdot l^*$ ¹⁷⁶.

In a non-amplifying, infinite *three-dimensional* system the probability for recurrent light-scattering vanishes unless $kl^* < 1$. Therefore random closed loops can only be formed in an extremely strong scattering medium. For a system with reduced dimensionality the conditions for the formation of random closed loops are less strict.

In an infinite, purely *two-dimensional*, system recurrent light-scattering can be observed irrespective of the mean free path¹⁷⁷. In terms of random lasers it is therefore especially interesting to investigate planar waveguides which confine the light to two dimensions. Admittedly, a perfectly two-dimensional system cannot be realized since some fraction of the light will always be scattered out of the waveguide. Anyway, a closed loop can still be formed by that fraction of light which remains confined in the waveguide. As a consequence, in a 2D system light can be localized with a localization length that is much larger than the wavelength.

⁶ The search for Anderson localization was also a driving force in the development of photonic crystals which can localize light if additional disorder is introduced³².

2.3.4.2 Light propagation in strongly scattering media with gain

The interplay of localization and amplification is an old and interesting topic in physical research¹⁷⁸. It is well known that optical absorption destroys photon localization because it suppresses the interference of scattered light. Contrarily, the presence of optical gain enhances coherent backscattering¹⁷⁹ and it reduces the localization length ξ to a value that is considerably lower than ξ_0 ¹⁷⁶. As a consequence, localized states can be formed in the presence of high optical gain although they are absent in the passive system¹⁶⁰. An important implication is that random closed loops are more likely formed in active than in passive structures. Varying the mean free path l^* a transition from resonant to non-resonant feedback was observed at a value of l^* being much larger than the wavelength¹⁵⁹.

In summary, two different regimes are identified, depending on the ratio of the gain length, L to the localization length ξ ¹⁸⁰:

- $L < \xi$: if the scattering is weak the localization length is larger than the extension of the gain region. In this regime scattering does not provide resonant feedback. Scattering merely increases the light path inside the material and, hence, reduces the threshold for amplified spontaneous emission. Discrete laser modes are not formed¹⁸¹. This is the classical situation of light diffusion with gain studied theoretically by Letokhov 30 years ago¹⁷⁸.
- $L \geq \xi$: for either strong disorder, a large gain, or a long gain length discrete laser peaks can be observed in the spectrum due to resonant feedback in random closed loop cavities. These random cavities are localized at a certain position so that several, spatially separated, closed loops can exist simultaneously. For increasing excitation area or gain the number of discrete laser modes increases. However, there is a maximum number of modes that can be established depending on the shape and size of the excitation area¹⁸⁰. In systems with reduced dimensionality, like e.g. optical waveguides, the localization length can be considerably larger than the wavelength of light and extended closed loop cavities can be formed^{156,165,166}. For these extended, yet localized, modes the laser threshold decreases when the excitation area is increased, now covering a larger part of the loop area. The difference between resonant and non-resonant feedback is also indicated by a differing photon statistics^{155,162,164,182,183} or an anisotropic emission¹⁶³.

3 Experimental techniques

This chapter discusses the various preparation and characterization techniques used within the course of this work. Thin films of organic semiconductors are deposited on nanopatterned substrates by casting from solution or by sublimation in high vacuum. Atomic force microscopy and transmission spectroscopy serve for the basic characterization of the film thickness and surface morphology. The properties of distributed feedback lasers are characterized according to their emission under intense optical excitation. The techniques for the transient investigation of the nonlinear optical properties of organic materials include differential transmission spectroscopy and luminescence upconversion with sub-picosecond time-resolution.

3.1 Sample preparation and characterization

All samples studied within the course of this work use a thin solid film of an organic semiconductor as active medium. The film thickness is varied in the range between 50 – 500 nm. A key issue for the optimization of the properties of organic optoelectronic devices is a well controlled film preparation and the successive fabrication of multilayers consisting of several materials with especially adapted properties. One of the major degradation mechanisms in conjugated organic materials is the cracking of double-bonds by oxidation. Therefore it is crucial to prepare organic films in dry and oxygen-free atmosphere, i.e. either in vacuum or in a glove-box filled with an inert nitrogen atmosphere.

Films of soluble conjugated polymers were prepared by the spincoating technique which is standardly used to deposit photoresists for lithography. As displayed in Fig. 3.1 (a) the substrate is covered with a solution containing the dissolved polymer. Upon revolving the sample the surplus solution is cast away with a homogeneous film remaining. The persistent solvent evaporates when the sample is stored under vacuum at elevated temperatures. The resulting film thickness depends on the molecular weight M [g/mol] of the polymer, the concentration c [mg/ml] of the solution, and the spin-frequency ω according to¹⁸⁴

$$d_f \propto M^{1/4} \omega^{1/2} c. \quad (3-1)$$

For many polymers high-quality films can be achieved if appropriate solvents are used. The conjugated polymer MeLPPP used in this work was obtained from the group of Prof. Dr. U. Scherf, presently at the University of Potsdam. It is soluble in toluene up to 60 mg/ml, allowing to fabricate homogeneous films with a thickness up to 500 nm. However, the fabrication of heterostructures is limited by the demand for orthogonal solvents, i.e. a layer that is soluble in an unpolar solvent like toluene can only be deposited on a material that is

soluble only in a polar solvent like water. Hence, the number of layers is very limited if solution processing techniques are applied.

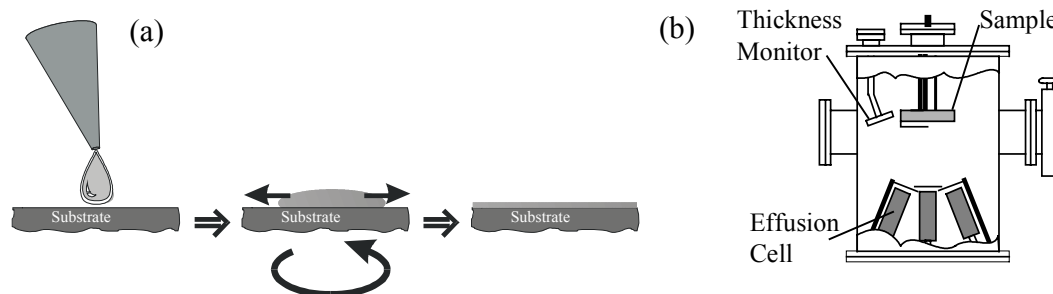


Fig. 3.1: Preparation of thin organic semiconductor films. (a) Soluble conjugated polymers are cast from solution. The final film-thickness is adjusted by the concentration and the spin frequency. (b) Setup for sublimation of small organic molecules. The film thickness is continuously monitored during sublimation¹⁸⁵.

Films consisting of small organic molecules like Alq₃ or DCM can be fabricated by sublimation in ultra high vacuum (UHV) as sketched in Fig. 3.1(b). This technique is especially well suited to fabricate heterostructures by subsequent deposition of different materials. Furthermore it is possible to deposit blends of two or more materials with a controlled composition by co-sublimation. High quality films of Alq₃:DCM were obtained independently from two different groups, namely the group of Dr. W. Brütting at the Universität Bayreuth and the group of Prof. Dr. W. Kowalsky at the Universität Braunschweig. The latter group also provided heterostructures as used in OLEDs.

Transmission, reflection and fluorescence spectra of the samples were taken using commercial spectrometers⁷. According to Beer's law the film thickness can be conveniently determined from the transmission spectrum via $T = I_T/I_0 = \exp[-\alpha d_f]$ using the absorption coefficients α . Errors due to surface reflection are eliminated accounting for the measured reflection spectrum. The surface morphology was determined with a commercial atomic force microscope (AFM) from Digital Instruments (DI Nanoscope IIIa).

3.2 Optical experiments at high excitation density

The observation of light amplification in a device of length L requires a substantial intensity gain g , so that $gL = \sigma_{SE}(\lambda) N_{\text{exc}} L \geq 1$. Given a typical cross-section for stimulated emission of order 10^{-16} cm^2 , it is readily seen that excitation densities N_{exc} exceeding 10^{16} cm^{-3} are needed. To achieve such high densities in optical experiments a laser beam is focused to a small spot. To prevent accumulated thermal heating a pulsed laser is used.

⁷ Varian Cary 50 UV-VIS Spectrometer, Varian Cary Eclipse Fluorescence Spectrometer

3.2.1 Determination of the excitation density

When using a femtosecond laser to excite a sample, the initial excitation density can be calculated from the absorbed pump pulse energy. Although the excitation density usually has an inhomogeneous distribution, a volume-averaged value is sufficient for most purposes.

The absorbed energy is calculated from the incident energy correcting for reflection and the residual transmission as measured at low excitation densities. A potential saturation of the absorption is thereby neglected, which is reasonable as long as the excitation density is substantially lower than the chromophore density. In a 300 nm thick film of MeLPPP ~ 80% of the incident light is absorbed. The exponential decrease of the excitation density within the sample is neglected. Instead, the averaged value is used. In the case of multilayers only the fraction absorbed in the *active* layer is taken into account.

The excitation volume is calculated from the film thickness and the area of the excited spot. In most experiments the laser beam is focused using a spherical lens resulting in a nearly circular spot with a typical diameter of 150 μm . The spot diameter is measured by moving a razor blade, located at the position of the sample, through the laser beam. Usually the intensity distribution is nearly Gaussian, with a spot diameter defined by 4σ . The excitation density is approximated by the constant, averaged value.

3.2.2 Regeneratively amplified fs-laser system

The pulsed laser source used in most experiments is a commercial regeneratively amplified Ti:sapphire laser emitting pulses of up to 1 mJ with a duration of less than 150 fs (FWHM) at a 1 kHz repetition rate and a center wavelength of $\lambda = 800 \text{ nm}$. Its setup is displayed in Fig. 3.2. A frequency doubled, diode pumped solid state laser (Millenia) is used to pump a Kerr-

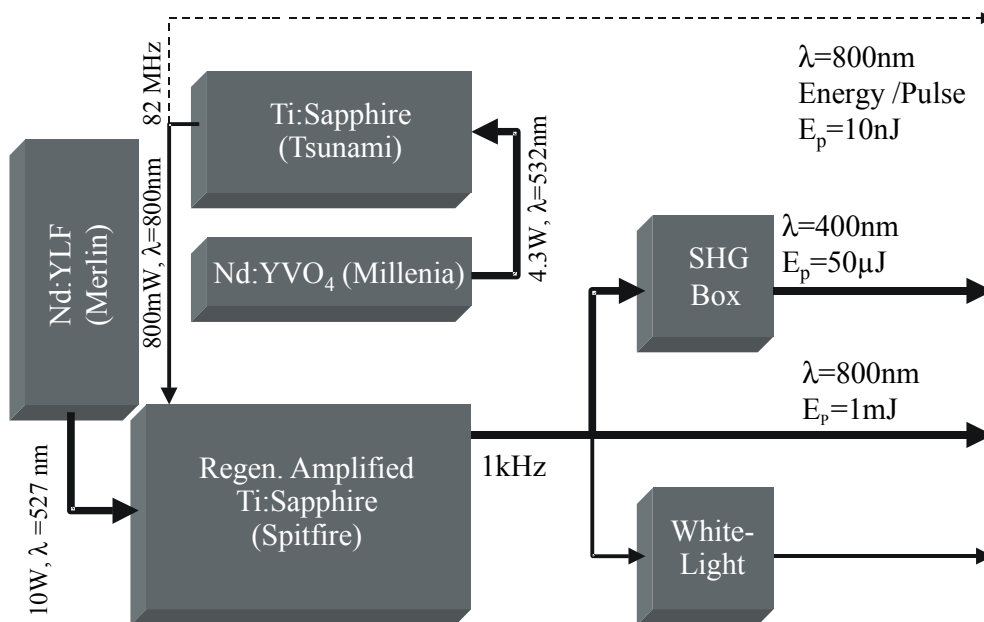


Fig. 3.2: Setup of the Spectra Physics femtosecond laser system. The core element is a regeneratively amplified Ti:sapphire laser with 1 mJ pulse energy. Its output can be used to generate the second harmonic at 400 nm and/or a white-light continuum in the visible.

lens mode-locked Ti:sapphire oscillator emitting pulses with 80 fs duration (FWHM) at a repetition rate of 82 MHz and a pulse energy $E_p \approx 10$ nJ. Its wavelength can be tuned from approx. 750 to 850 nm. If necessary, pulses of significantly higher energy can be generated in an amplification stage, where single pulses of the oscillator are amplified by a factor of 10^5 within 15-20 passes through the cavity of a regenerative amplifier (Spitfire). The core of this amplifier is another Ti:sapphire crystal which is highly pumped by a Nd:YLF laser at 1 kHz repetition rate.

The high pulse energy of up to 1 mJ is compressed in ~ 150 fs long pulses and can be used to generate femtosecond pulses in a very broad spectral range (spanning from 266 nm to 3 μm) through nonlinear optical effects. To excite organic semiconductors the second harmonic with a wavelength of 400 nm is used. Furthermore a small fraction of the beam can be used to generate a white-light continuum for differential transmission spectroscopy (see below).

3.2.3 Time-integrated emission

The emission of photoexcited organic semiconductors can be spectrally resolved using the setup of Fig. 3.3. As excitation source the frequency doubled output of the regeneratively amplified Ti:sapphire laser is used. The beam profile is shaped through adjustable diaphragms and the incident power is adjusted with a variable neutral density filter. The spot size on the sample can be adapted choosing an appropriate focusing lens. In order to prevent degradation due to photo-oxidation the samples are placed in a vacuum chamber and held under a dynamical vacuum of 10^{-4} mbar.

The emitted light is collected with achromatic doublets and focused onto the entrance slit of a 30 cm monochromator[§] with an attached Peltier-cooled CCD-array detector. Depending on the pitch of the used grating, spectral resolutions up to ~ 0.2 nm can be achieved with the described system.

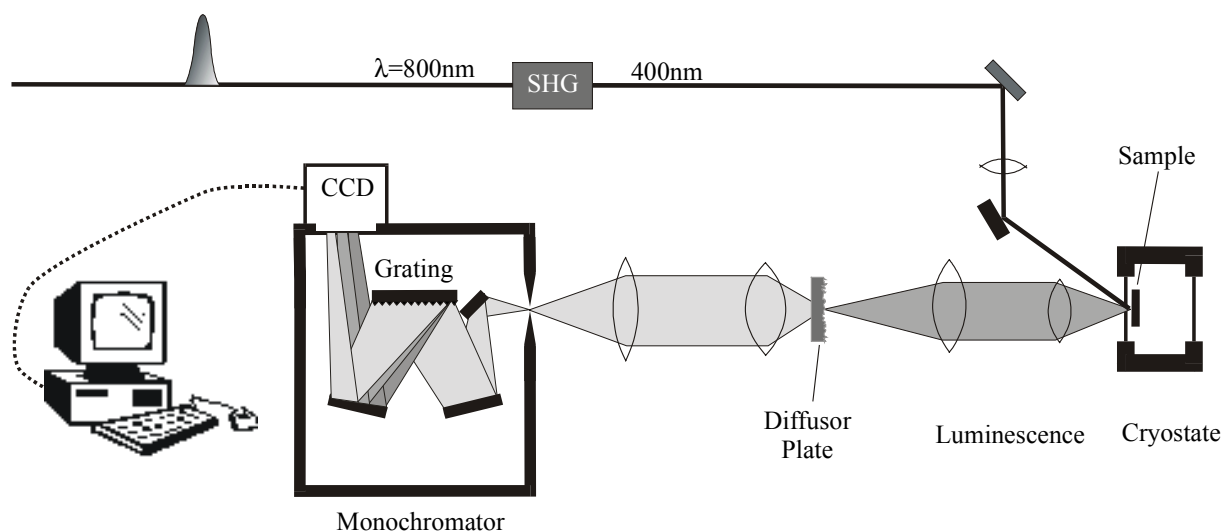


Fig. 3.3: Experimental setup for the measurement of time-integrated emission spectra.

[§] SpectraSource Instruments, model Teleris KAS0400

For the interpretation of the emission spectra it is important to know that the emission is collected perpendicular to the substrate within a cone of numerical aperture $N.A. = 0.26$. To achieve a high spectral resolution it is inevitable to illuminate the entire grating of the monochromator homogeneously. Anisotropic emission, in contrast, may cause a misinterpretation of the observed spectra. However, the emission wavelength of our surface emitting DFB lasers shows a distinct dependence on the angle relative to the surface normal. In order to determine the spectrum correctly an intermediate image of the excitation spot on the sample is created and the rough surface of a scattering plate is placed exactly at the position of the intermediate image. This acts as a point source with drastically reduced anisotropy.

3.2.4 Temporally resolved emission with sub-ps resolution

Luminescence upconversion is a powerful technique to study the temporal evolution of emission processes with a time resolution well below 1 ps. This high resolution relies on the sum-frequency generation between a femtosecond gate pulse and the luminescence light in a nonlinear optical crystal as sketched in Fig. 3.4 and Fig. 3.5. The femtosecond laser beam of the regenerative amplifier is split into two beams. A partial fraction is used to create the second harmonic and excite the sample. The resulting luminescence is focused onto a nonlinear crystal (BBO) together with the rest of the fundamental laser beam (gate beam). If the fluorescence and the gate beam overlap in space and time, the sum frequency of gate and

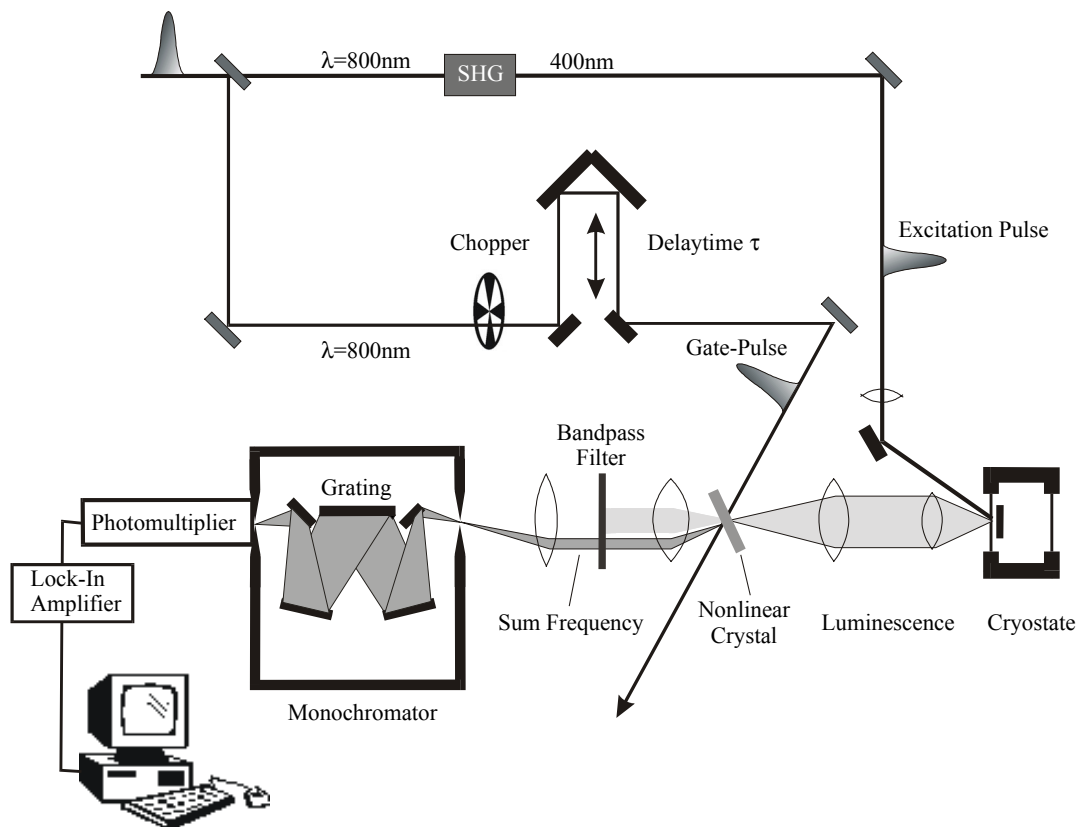


Fig. 3.4: Experimental setup for the investigation of the transient emission using the upconversion technique.

luminescence is generated. The upconverted light beam is funneled through a monochromator onto a photomultiplier tube, whereas the luminescence and the gate beam are blocked by a suitable UV-bandpass filter

The intensity of the sum frequency is determined by the convolution of the luminescence and the gate beam given by

$$I_{Sum}(\tau) \propto \int_{-\infty}^{\infty} I_{Lumi}(t + \tau) \cdot I_{Gate}(t) dt. \quad (3-2)$$

The quantity τ is the time equivalent of the length difference between the optical paths of gate and signal. For a sufficiently short gate pulse, mathematically for a δ -peak in time, the intensity of the sum frequency obeys $I_{Sum}(\tau) \propto I_{Lumi}(t = \tau)$. As illustrated in Fig. 3.5 (a) the upconversion intensity measured at a time delay τ is proportional to the intensity of the luminescence at the time $t = \tau$ after the excitation. The highest achievable time resolution of upconversion is determined by the duration of the gate pulse. Due to path length differences the actual time resolution achieved in experiments is lower. An estimate is given by the full width at half maximum of the cross correlation between the gate pulse and the excitation pulse, which is scattered from the sample surface (Fig. 3.5 (b)). A time resolution of ~ 800 fs (FWHM) is achieved, the shortest resolved exponential decay time is ~ 0.4 ps.

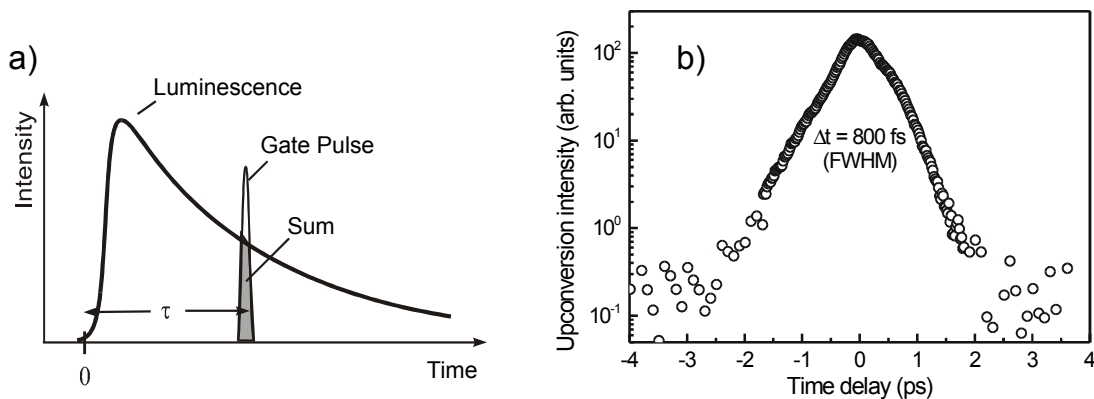


Fig. 3.5: (a) Principle of upconversion: as long as the gate beam and luminescence overlap in space and time, their sum-frequency is generated. (b) Upconversion transient of the cross correlation between the gate beam and the scattered excitation beam. A time-resolution of 800fs (FWHM) is determined.

From equation 3-2 it can be seen that the upconversion intensity is proportional to both luminescence and gate beam intensity. A large conversion efficiency even for weak signals can therefore be achieved using high gate intensities. A further condition for highly efficient conversion is a proper phase matching of luminescence and gate, so that the converted signal interferes constructively throughout the entire nonlinear crystal. Depending on the wavelength of the luminescence and the angle between gate and signal, phase matching can be accomplished by rotation of the crystal. Further improvement of the signal to noise ratio is a result of the widely used modulation technique, where every other gate pulse is blocked and the upconverted signal is evaluated using a lock-in amplifier that is synchronized at half the repetition frequency.

3.2.5 Differential transmission spectroscopy

The excited state population, and thus the gain of an active organic medium, can be examined using differential transmission spectroscopy. As shown in Fig. 3.6 the sample is excited by a femtosecond pump pulse. The transmission of the sample is probed by a second pulse which is delayed by a time τ . In order to record only transmission changes induced by the pump beam, the transmission is recorded alternately with and without pump pulse.

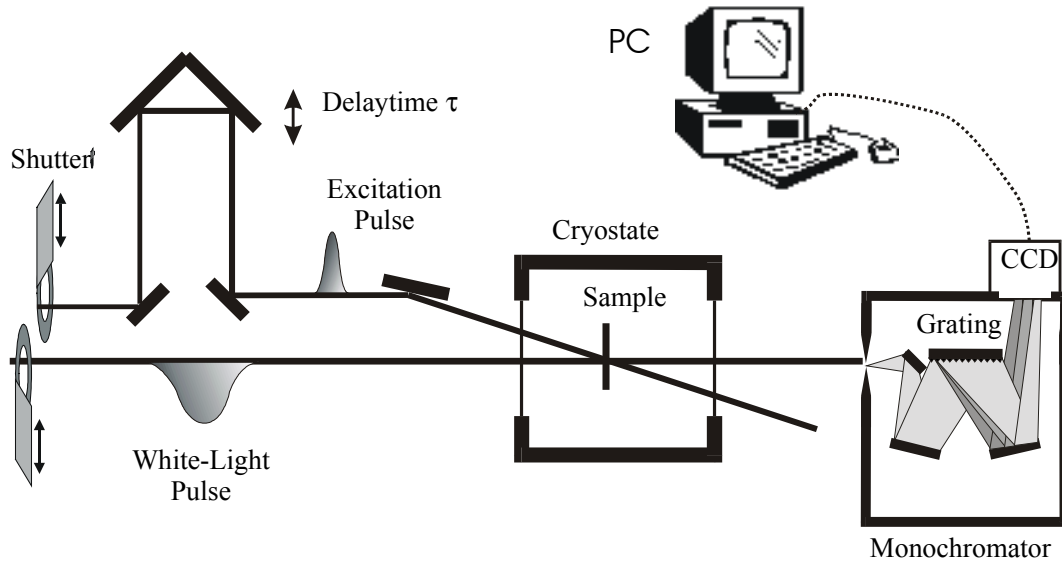


Fig. 3.6: Experimental setup for differential transmission spectroscopy.

Using Beer's law the transmission change $\Delta T(\lambda, \tau)$ can be related to changes $\Delta\alpha(\lambda, \tau)$ of the absorption coefficient $\alpha(\lambda)$ of the sample by

$$\frac{\Delta T(\lambda, \tau)}{T(\lambda)} = \frac{\exp(-(\alpha + \Delta\alpha) d_f) - \exp(-\alpha d_f)}{\exp(-\alpha d_f)} = -1 + \exp(-\Delta\alpha(\lambda, \tau) d_f). \quad (3-3)$$

A negative value of ΔT is easily attributed to photoinduced absorption. To see, whether a positive value of ΔT is due to an amplification of the incident light by stimulated emission or is merely due to the reduced ground-state absorption (bleaching), it is necessary to compute the gain factor $g(\lambda, \tau)$ by correction for the initial absorption

$$g(\lambda, t) = -(\alpha + \Delta\alpha(\lambda, \tau)) = -\alpha(\lambda) + \frac{\ln\left(\frac{\Delta T(\lambda, \tau)}{T(\lambda)} + 1\right)}{d_f}. \quad (3-4)$$

Since the gain is typically 1-2 orders of magnitude lower than the maximum absorption even comparatively low systematic errors in the measurement of α are detrimental to the determination of $g(\lambda, \tau)$.

In the experiments the probe beam is the white-light continuum (420-750 nm) generated by self-phase-modulation when focusing a small fraction of the output of the regenerative amplifier onto a sapphire plate. If it is only of interest to determine the response of the sample at one specific wavelength, the wavelength is set with an interference filter. The transmission

can then be recorded with a simple photodiode. However, if it is required to determine the response of the sample over a wide spectral range, no spectral filtering is applied. The transmission spectrum is then measured with a spectrometer and CCD detector as described above. In this case, however, it is necessary to account for the relative time delay (chirp) between the red and blue components in the white-light². At the position of the sample their relative time delay accounts for several picoseconds. To eliminate the chirp, a large number of differential transmission spectra is recorded with different time delay. The chirp is later on corrected numerically.

² By self-phase-modulation red shifted components are generated at the leading edge of the femtosecond pulse whereas the blue shifted components are produced at the falling edge¹⁸⁶.

4 Materials for organic solid-state lasers

The relevant electronic, optical and transport properties are presented for the two materials employed within the course of this work. Their suitability for lasers is demonstrated by a large cross-section for stimulated emission and the observation of low threshold amplified spontaneous emission.

4.1 The conjugated polymer MeLPPP

4.1.1 Electronic, optical and transport properties of MeLPPP

The methyl substituted ladder-type poly(*para*-phenylene), brief MeLPPP, is a very attractive π -conjugated polymer for blue-light emitting diodes¹⁸⁷ and lasers⁸⁵ due to its high luminescence quantum yield in the solid state ($\sim 30\%$), strong stimulated emission³⁷ and its large carrier mobility¹⁸⁸. Fig. 4.1 shows the structural formula of MeLPPP, its absorption and photoluminescence spectrum, and the optical constants of a solid film of MeLPPP. The absorption spectrum is dominated by the fundamental electronic transition $S_{1,v'=0} \leftarrow S_{0,v=0}$ centered at a wavelength of 456 nm and its vibronic progressions at shorter wavelengths. The photoluminescence spectrum is more or less symmetrical to the absorption exhibiting only a very small Stokes shift.

Many of the valuable properties of MeLPPP are caused by the high intra-chain order. It is reached by a stabilization of the PPP backbone against torsional displacement of the phenyl rings through covalent bridging of neighboring phenyl rings. The stiff backbone explains why the Stokes shift due to structural relaxation is negligible. At the same time the synthesis via polycondensation results in a very narrow conjugation length distribution¹⁸⁹. Only because of this weak inhomogeneous broadening it is possible to observe the prominent vibronic sidebands in absorption and emission. The average conjugation of π -electrons in MeLPPP extends over 14.5 ± 1.5 phenylene units (~ 7 monomers), corresponding to an effective conjugation length of $L_{\text{eff}} = 6.5 \pm 0.6$ nm¹⁹⁰. Given that the average molecular weight of MeLPPP is in the order of 28,000, an average polymer chain contains 35 monomer units and, hence, consists of 5 fully conjugated sites. The methyl (CH₃) substitution increases the average interchain distance to 0.6 nm and prevents interchain aggregation. This is important for a high luminescence yield. Further side chains lead to a good solubility of the polymer in unpolar solvents such as toluene.

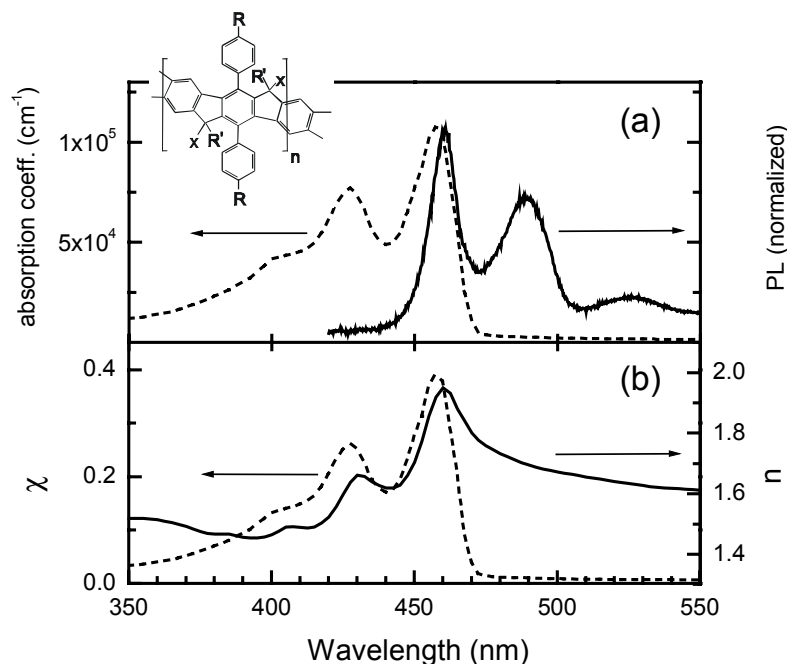


Fig. 4.1: (a) Spectrum of the absorption coefficient α and the photoluminescence of an MeLPPP film. (b) Imaginary part, $\chi = \alpha\lambda / (4\pi)$, and real part, n , of the complex refractive index for a TE mode in a solid film of MeLPPP¹⁹¹. Inset: structural formula of MeLPPP (x : CH₃, R : C₁₀H₂₁, R' : C₆H₁₃).

Fig. 4.2 summarizes the experimentally determined energy levels for various excited states of an average MeLPPP-chain¹⁰. The fundamental electronic transition from the ground state to the singlet state 1^1B_u is located at 2.72 eV (456 nm). Depending on the purity of the film, quantum yields up to 30% and excited state lifetimes around 200 ps were observed. The purely electronic transition is superimposed by a vibronic progression due to a skeletal C=C stretch-mode at an energy of ~ 180 meV¹⁹³ which causes the characteristic sidebands seen in Fig. 4.1. The exciton binding energy, defined by the energetic distance between the lowest singlet state and the transition to the continuum states of a free electron hole pair (without lattice relaxation), is in the order of 0.6-0.8 eV¹⁹⁴. However, despite the fact that MeLPPP is a molecule with exceptionally low disorder, intrachain band-like transport could not be observed¹⁹³.

Several bands of excited state absorption have been observed and attributed to transitions between the various excited states and their vibronic progressions. Nonetheless, the radiative transition from $1^1B_u, v'=0$ to $1^1A_g, v=1$, located at 2.52 eV (493 nm), does not show spectral overlap with any of the observed excited state absorption bands, neither in the charged nor in the neutral manifold. Stimulated emission can be expected to occur in this spectral range.

¹⁰ Within the first 10 ps after an excitation, spectral relaxation within the density of states occurs. Therefore the states which are observed in luminescence appear lower in energy by approx. 30-40 meV^{19,192}.

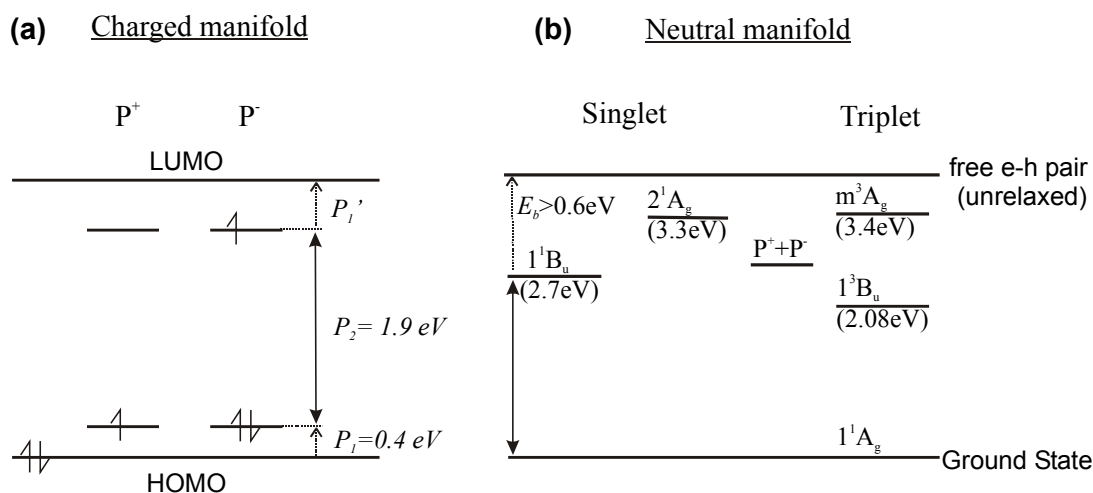


Fig. 4.2: Energy levels of various excited states of MeLPPP in the charged (a) and neutral (b) manifold. Data summarized from ¹⁹⁴ (singlet, triplet), ¹⁹⁵ (polarons), and ¹⁹⁶ (two-photon states).

Detailed investigations of the photophysics on a femtosecond timescale revealed an instantaneous onset of the fluorescence even if higher vibronic levels are excited. The loss of phase coherence and the vibronic relaxation therefore occur within 100 fs ³⁸. The vibronic relaxation may also be accompanied by an ultrafast on-chain dissociation of the exciton (formation of geminate pairs) ^{197,198}. A small spectral red-shift of the fluorescence occurs within 10 ps due to exciton diffusion¹¹ accompanied by energetic relaxation within the density of states ^{19,192}.

Another feature of the rigid backbone is a relatively high mobility of electrons and holes. From time of flight measurements a hole mobility of $\mu_h = 1 \cdot 10^{-3} \text{ cm}^2 \text{V}^{-1} \text{s}^{-1}$ was determined at an electric field of $6 \cdot 10^4 \text{ V/cm}$ ¹⁸⁸. This value is two orders of magnitude higher than in PPV. Very unusual is the fact that the interchain hopping mobility is not significantly increased for higher electric fields. Although the interpretation is still vague this might be an indication that the large conjugation length in MeLPPP is actually counterproductive for the rate of interchain hopping ²⁰⁰. The electron mobility of $\mu_e < 10^{-6} \text{ cm}^2 \text{V}^{-1} \text{s}^{-1}$ is typical for a π -conjugated polymer.

4.1.2 Stimulated emission in MeLPPP

Fig. 4.3 (a) shows emission spectra of a 300 nm thick film of MeLPPP on a glass substrate for various excitation densities. All the spectra are normalized at a wavelength of 459 nm, the spectral position of the maximum photoluminescence intensity. At the lowest shown excitation density the typical photoluminescence spectrum of MeLPPP is observed. When the excitation density is gradually increased a qualitative change of the emission spectrum is observed, dominated by an increasing relative intensity in the spectral range of the $S_{0,v=1} \leftarrow S_{1,v'=0}$ transition. The spectral narrowing is caused by amplified spontaneous

¹¹ The exciton diffusion length was determined to be 14 nm ¹⁹⁹.

emission (ASE) as discussed in Section 2.2.2. Photons emitted from the MeLPPP are coupled into the waveguide formed by the film of MeLPPP on the glass substrate. As these photons cross the photoexcited region they can be scattered out of the waveguide, be reabsorbed or cause stimulated emission. If the pump intensity is high enough for the gain to exceed the scattering losses then spontaneously emitted photons are exponentially amplified as they travel through the waveguide. Since predominantly those photons are amplified whose energy coincides with the spectral position of maximum gain the overall emission spectrum changes.

The magnitude of stimulated emission can be quantified in a differential transmission experiment. The sample is excited by an intense femtosecond pump pulse and the resulting transmission changes are monitored with a spectrally broad, time-delayed probe pulse. The gain spectrum is extracted from the differential transmission spectrum by correction for the absorption (see Section 3.2.5). Fig. 4.3 (b) shows the spectral dependence of the gain coefficient of an MeLPPP film immediately after the excitation³⁸. The magnitude of the positive contribution at 460 nm is not unquestionable since the substantial residual absorption in this spectral region implies large error bars in the determination of $g(\lambda)$ according to equation 3-4. Anyway, strong stimulated emission is observed between 485-500 nm coincident with the $S_{0,v=1} \leftarrow S_{1,v'=0}$ transition. The maximum stimulated emission cross-section ($\sigma_{SE}^{\max} \approx 1.5 \cdot 10^{-16} \text{ cm}^2$) is observed at a wavelength of 490 nm.

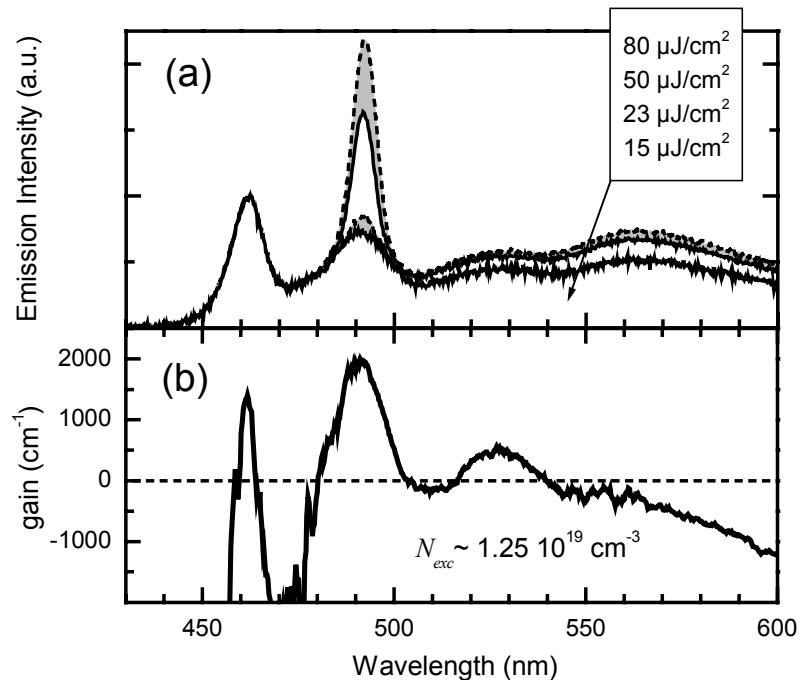


Fig. 4.3: (a) Emission spectra of a film of MeLPPP for increasing excitation density. All spectra are normalized at the wavelength where the peak of the emission spectrum occurs at low excitation density. The excitation beam is focused to a circular spot of $\sim 200 \mu\text{m}$ diameter. (b) Gain spectrum of MeLPPP measured after pulsed optical excitation at $\lambda = 400 \text{ nm}$ ³⁸.

4.2 The composite molecular system Alq₃:DCM

4.2.1 Electronic, optical and transport properties of Alq₃:DCM

The guest-host system consisting of the chelate metal complex tris-(8-hydroxyquinoline)-aluminum (Alq₃) molecularly doped with the laser dye 4-dicyanmethylene-2-methyl-6-(p-dimethylaminostyryl)-4H-pyran (DCM) is one of the most promising materials for OLED applications⁶⁵ and was also among the first organic electroluminescent materials that were used as the active material for optically pumped organic solid state lasers^{25,106,201}.

In an OLED the Alq₃ gives rise to the transport of charge carriers; in optical experiments photons with a wavelength around 400 nm are efficiently absorbed by Alq₃. DCM dissolved in various liquid organic solvents acts as a four-level system and is a commonly used laser dye having a high photostability and a large tuning range due to its broad gain spectrum²⁰². In the composite system neutral excitations are rapidly funneled from Alq₃ to the DCM-molecules (exhibiting red-shifted optical transitions) by diffusion within the Alq₃ manifold and a subsequent resonant energy transfer (Fig. 4.4 (b)). Thus the advantages of a conducting matrix -showing a rather poor luminescence- can be combined with the high luminosity of a guest dopant.

Fig. 4.4 (a) shows the absorption and fluorescence spectra of Alq₃ and DCM, respectively. As described in equation 2-5 the strong overlap of the Alq₃ emission with the DCM absorption enables an efficient Förster-type energy transfer from Alq₃ to DCM in a composite system. This is demonstrated in Fig. 4.4 (c). Although predominantly Alq₃ molecules are optically excited at a wavelength of 400 nm the major emission originates from DCM, whereas little emission is observed from Alq₃. The high efficiency of this process indicates that the energy transfer occurs on a time-scale considerably shorter than the radiative lifetime of excited states in Alq₃²⁰³. Both the maximum of the emission wavelength and the photoluminescence efficiency vary with the dopant concentration^{65,107}, reaching a maximum efficiency around 40% for a concentration of approx. 2% DCM. Due to the large Stokes shift a large part of the emission is located in the transparent spectral region making Alq₃:DCM a nearly ideal four level laser system for optically pumped solid-state applications. Fig. 4.4 (d) shows the spectral dependence of the real and imaginary part of the refractive index of an Alq₃:DCM film with a typical DCM concentration²⁰⁴. In the spectral range of DCM emission the refractive index varies between 1.7 and 1.74.

Many of the optical and charge transport properties of Alq₃ can be derived from its structural and electronic properties in the charged and neutral states, which, in turn, can be modeled using semi-empirical^{205,206} or *ab initio* calculations^{44,207,208}. In Alq₃ the central Al³⁺ ion has a distorted octahedral coordination to three quinoline ligands. Alq₃ exists in two geometrically different configurations, whereby the meridional isomer shown in the inset of Fig. 4.5 (a) is more stable and is generally the major constituent of thin films. Anyway, the coexistence of two isomers clearly favors the stability of an amorphous state, as it hinders re-crystallization.

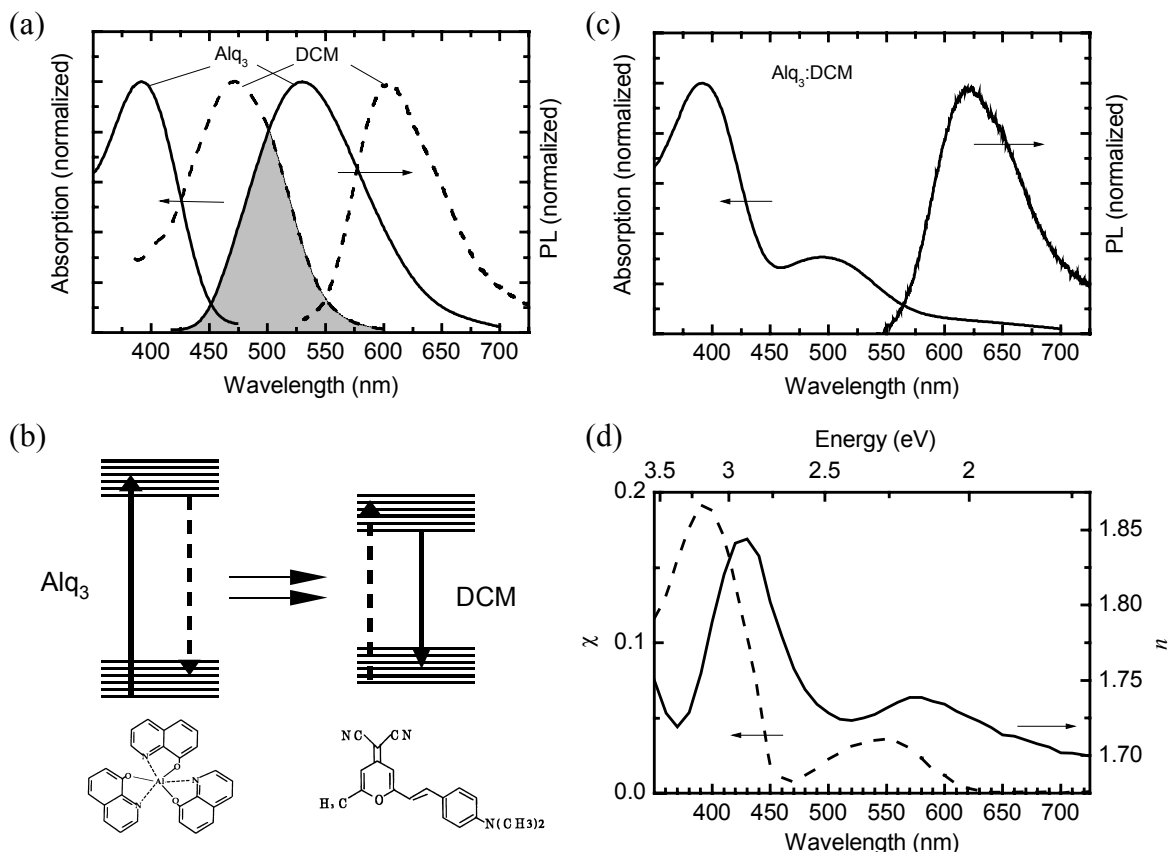


Fig. 4.4: (a) Absorption and fluorescence spectra of a solid film of Alq₃ and DCM, respectively. The overlap of the Alq₃ emission with the DCM absorption (gray shaded) results in a Förster-type energy transfer as schematically shown in (b). (c) Absorption and emission spectra of a composite Alq₃:DCM film with a DCM concentration of ~2% by weight. (d) Real (n) and imaginary part (χ) of the refractive index of an Alq₃:DCM film²⁰⁴.

The HOMO and LUMO states have a strong dipole moment and are localized on the ligands. Since the ligands are physically not equivalent HOMO and LUMO both split into three closely spaced states, each localized predominantly on one of the ligands⁴⁴. The HOMOs are localized on the phenoxide ring (O) of the quinoline, whereas the LUMOs are principally on the pyridyl side (N). Therefore the nine lowest transitions occur between the three phenoxide-like occupied orbitals and the three unoccupied pyridyl-like orbitals. The Al³⁺ ion does not contribute to the transitions. A substantial structural and energetic relaxation accompanies HOMO-LUMO transitions as well as the generation of radical anions (110 meV) or cations (90 meV).

Fig. 4.5 (b) compares the calculated transition energies and oscillator strengths with the absorption of an Alq₃ film. Good agreement between calculations and experiment is found, given that the relatively broad spectrum is explained by the large inhomogeneous broadening (125 meV) associated with the orientational disorder and the large dipole moment²⁰⁸. The relatively low fluorescence yield of 8% and the long excited state lifetime of 16 ns⁶⁵ might originate from the weak oscillator strength of the lowest singlet transition. The large Stokes shift (0.4-0.7 meV) between absorption and emission (see Fig. 4.4) is caused by structural relaxations.

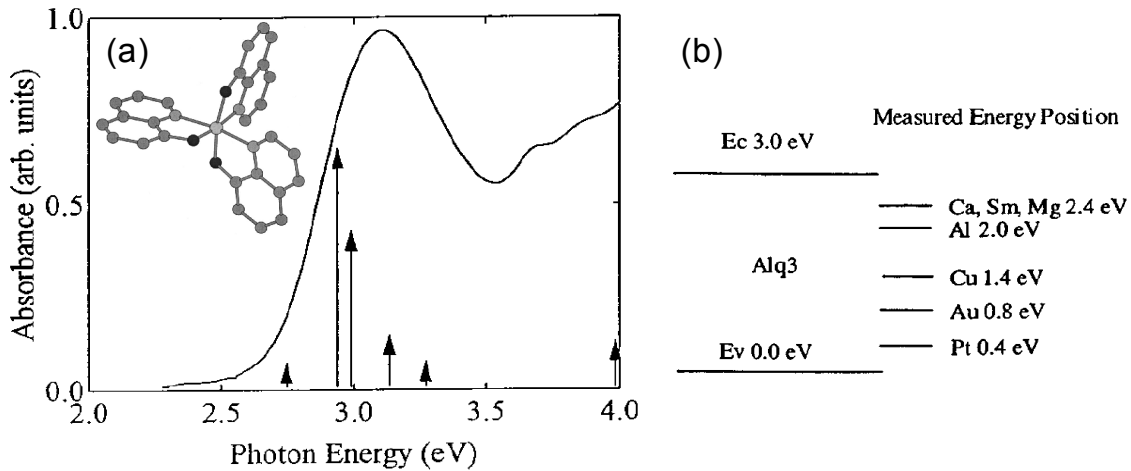


Fig. 4.5: (a) Inset: meridional isomer of Alq₃. The darker circles about the central Al represent oxygen atoms. Only one of the oxygens is opposed to a nitrogen atom, whereas in the facial isomer (not shown) all oxygens have an opposite N-atom. Main part: absorption spectrum of a solid-state film of Alq₃. The arrows represent the calculated energies and oscillator strengths. (b) Experimentally determined energy diagram for metal contacts relative to the single particle energy gap (HOMO-LUMO) of Alq₃. Taken from ²⁰⁸.

In Fig. 4.5 (b) the experimentally determined HOMO-LUMO gap is shown together with the energy levels of several contact metals. Due to the low energy barrier for injection of electrons into the LUMO and its comparatively high room temperature electron mobility Alq₃ is a good electron transporting material ($\mu_e = 8 \cdot 10^{-7} \exp(3 \cdot 10^{-3} \sqrt{F \text{ cm V}^{-1}}) \text{ cm}^2 \text{ V}^{-1} \text{ s}^{-1}$). The hole mobility is considerably lower ($\mu_h = 6 \cdot 10^{-11} \exp(9 \cdot 10^{-3} \sqrt{F \text{ cm V}^{-1}}) \text{ cm}^2 \text{ V}^{-1} \text{ s}^{-1}$) ⁶⁸.

4.2.2 Stimulated emission in Alq₃:DCM

Fig. 4.6 shows emission spectra of a 200 nm thick film of Alq₃:DCM¹² for various excitation fluences, whereby the pump beam was focused to a circular spot of $\sim 160 \mu\text{m}$ diameter. The concentration of the laser dye was adjusted to $\sim 2\%$ by weight. For low excitation conditions (pump fluence $E_{\text{pump}} \leq 52 \mu\text{J}/\text{cm}^2$) a broad emission spectrum is observed spanning from 530 nm beyond 700 nm. It can be attributed to the radiative deactivation of excited DCM molecules. Increasing the pump level to higher values ($E_{\text{pump}} > 52 \mu\text{J}/\text{cm}^2$) results in a gradual spectral narrowing of the emission band from 90 nm (FWHM) to a rather narrow band with a halfwidth of 16.5 nm centered at 628 nm. The dependence of the spectral width on the excitation energy is shown in the inset of Fig. 4.6. As in the case of conjugated polymers this narrowing of the emission spectrum can be attributed to ASE: spontaneously emitted photons propagate through the optically excited region and stimulate the collective radiative decay of further excitations. Spectral gain narrowing can be observed if ASE becomes the dominant deactivation pathway ²⁰⁹.

¹² The samples were fabricated by S. Berleb, Lehrstuhl Experimentalphysik II, Universität Bayreuth.

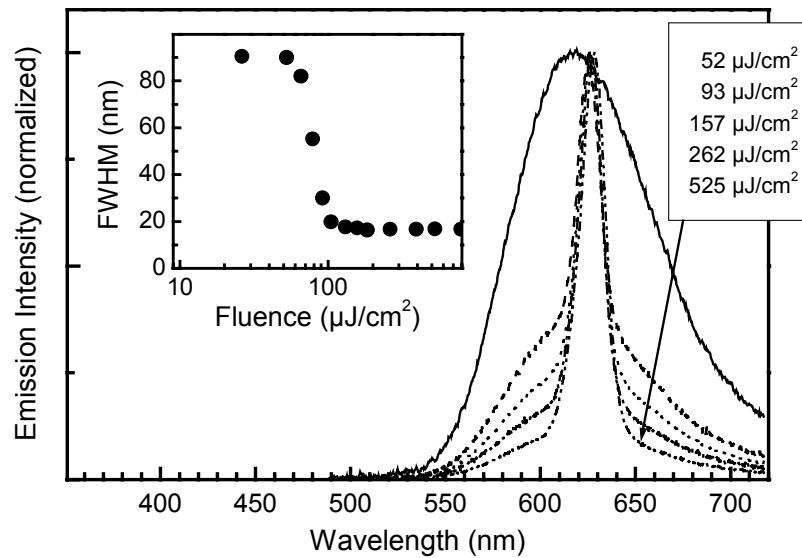


Fig. 4.6: Emission spectra of Alq₃:DCM for various excitation fluences³⁹. The inset shows the linewidth as a function of excitation fluence. Gain narrowing is observed above a fluence of 52 $\mu\text{J}/\text{cm}^2$.

To determine the spectral bandwidth of optical gain in Alq₃:DCM time dependent optical gain spectra $g(\lambda, \tau)$ were determined using differential transmission spectroscopy (see Section 3.2.5). In these measurements ASE is an unwanted effect because it leads to an ultrafast depletion of excited states. However, it has been shown that ASE is suppressed when the organic film is deposited on a glass substrate that is coated with indium tin oxide (ITO)³⁷. Therefore an Alq₃:DCM film on an ITO-coated substrate is used. As shown by equation 3-4 the gain spectrum can be extracted from the differential transmission spectrum $\Delta T(\lambda, \tau)/T(\lambda)$ by correcting for the absorption of the unexcited film. Special care is required for the proper determination of the absorption coefficient α : owing to the low DCM concentration the maximum gain arising from DCM is typically 1 to 2 orders of magnitude lower than the maximum absorption of Alq₃:DCM. Therefore even comparatively low systematic errors in the determination of the absorption coefficient can have a large effect on the calculated gain spectrum.

Fig. 4.7 shows the spectral dependence of the gain coefficient in an Alq₃:DCM film with a DCM concentration of 2% by weight corresponding to a volume density $N_{DCM} = 5 \cdot 10^{19} \text{ cm}^{-3}$ of DCM molecules in the film. The film is excited at a wavelength of 400 nm, where the predominant absorption arises from Alq₃. With a value of $2 \cdot 10^{20} \text{ cm}^{-3}$ the excitation density is four times higher than the density of DCM. It is therefore reasonable to assume that all DCM molecules will be excited after a sufficient time delay. After a time delay of $\tau = 30 \text{ ps}$ a maximum gain coefficient of 700 cm^{-1} was found at a wavelength of $\lambda = 623 \text{ nm}$. The spectral range of gain spans over 100 nm from 585 nm to 685 nm. From N_{DCM} and the maximum gain coefficient a stimulated emission cross-section of $\sigma_{SE} \approx 1.3 \cdot 10^{-17} \text{ cm}^2$ is calculated, which is in good agreement with the value reported for DCM in liquid solution²¹⁰.

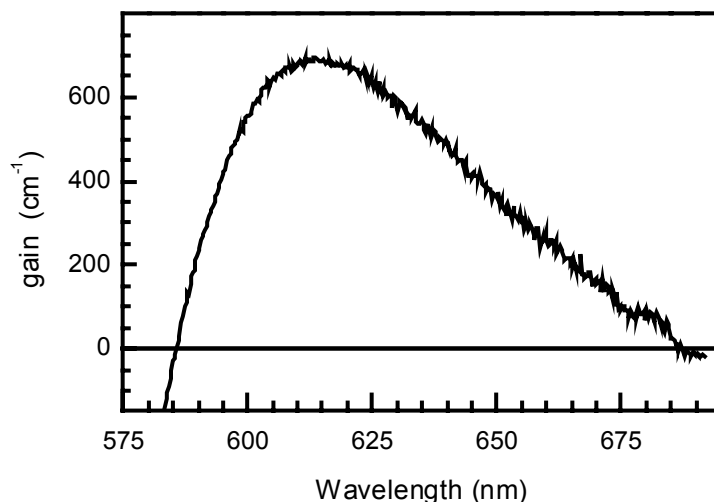


Fig. 4.7: Spectrum of the gain coefficient of an Alq₃:DCM film with a DCM concentration of ~2% by weight, measured at an excitation density of $2 \cdot 10^{20} \text{ cm}^{-3}$ in Alq₃ and a pump-probe time delay of 30 ps.

A comparison between gain- and photoluminescence spectra indicates that the gain spectrum more or less coincides with the photoluminescence at the long wavelength side. At the short wavelength side the gain spectrum is clipped by the tail of the residual absorption. At this spectral position the gain spectrum is therefore very sensitive to minor changes of the absorption coefficient. At a very high excitation density all DCM molecules are excited and the absorption can be attributed to the Alq₃ molecules alone. At lower excitation densities, however, not all DCM molecules are excited, the residual absorption is increased, and the gain spectrum is further clipped at its short wavelength side. Differences in the DCM concentrations will lead to further modifications from sample to sample. Nevertheless, the broad extension of the gain spectrum and the high absolute amount of gain demonstrate that the excellent laser properties of DCM are conserved in a solid matrix of Alq₃.

5 Lasers with one-dimensional distributed feedback

In this chapter the results concerning organic solid-state lasers with one-dimensional distributed feedback are discussed, beginning with their fabrication, their elementary characterization and an investigation of the laser modes. The fourth section demonstrates the possibility of wavelength tuning over a broad spectral range. Finally, the feedback mechanism in our structures is investigated in detail by comparison of the experimental results with the predictions of a quantitative numerical model.

5.1 Fabrication of mechanically flexible organic DFB lasers

As described in Section 2.3 thin film distributed feedback can be achieved when the effective refractive index, governing the propagation of light in waveguide structures, is periodically modulated. Such modulations, which can affect either the real or the imaginary part of n_{eff} , can be easily incorporated using corrugated substrates with a periodic height modulation. Of particular interest for organic solid-state lasers are substrates that retain the inherent advantages of organic materials like mechanical flexibility or large-area low-cost fabrication schemes. Accordingly, techniques like electron beam lithography, although approved in the fabrication of crystalline inorganic semiconductor lasers, are not desirable in case of organic semiconductor lasers. Soft-lithography techniques like embossing, imprinting or replica molding are much more attractive and have successfully been used to make surface relief substrates for organic DFB lasers^{23,211,212}.

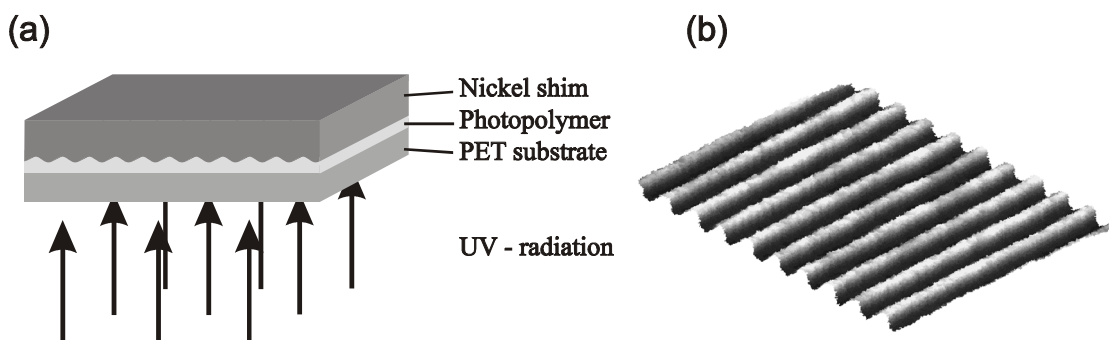


Fig. 5.1: (a) UV embossing of DFB substrates. (b) AFM image of the corrugated DFB substrate.

The templates used for DFB lasers were originally developed for antireflection coatings in solar cells at Fraunhofer Institute for Solar Energy Systems²¹³. In a holographic setup a conventional photoresist is illuminated with a periodic intensity profile of ultra-violet light. Upon development this pattern is transformed into a surface relief grating whose profile can be fine-tuned from sinusoidal to nearly square shape²¹⁴. By electroforming the pattern is then transferred to a nickel shim serving as master stamp for the soft-lithographic fabrication of

replicas. For that purpose a mechanically flexible sheet of poly (ethylen terephthalate) (PET) is covered with a transparent photopolymer and pressed onto the nickel shim. The photopolymer is cured by illumination with UV light during contact with the shim. Concurrently, the negative of the original surface relief is durably transferred onto the polyester foil (Fig. 5.1). With this technique areas as large as $(20 \text{ cm})^2$ were patterned uniformly with periodicities ranging from 200 nm to several microns.

The laser is completed by depositing a thin film (thickness $< 500 \text{ nm}$) of the active material on top of the corrugated substrate. The active layer has a higher refractive index ($n_f \sim 1.7$) than the surrounding substrate ($n_s \sim 1.45$) and air ($n_{air} = 1$). Thus a slab waveguide is formed. The modulation of n_{eff} —and hence the resulting feedback—strongly depends on the texture of the waveguide interfaces and thereby on the deposition process. Fig. 5.2 (a) displays the surface profile of a bare DFB substrate showing a modulation periodicity of $\Lambda \approx 400 \text{ nm}$ and a modulation depth of $h \approx 90 \text{ nm}$. If a 275 nm thick film of Alq_3 :DCM is deposited by co-evaporation of DCM and Alq_3 onto the substrate the film surface (Fig. 5.2 (b)) is essentially a replication of the underlying substrate. On the other hand the corrugation is almost completely leveled off through spincasting of a 250 nm thick film of MeLPPP onto the surface (Fig. 5.2 (c)).

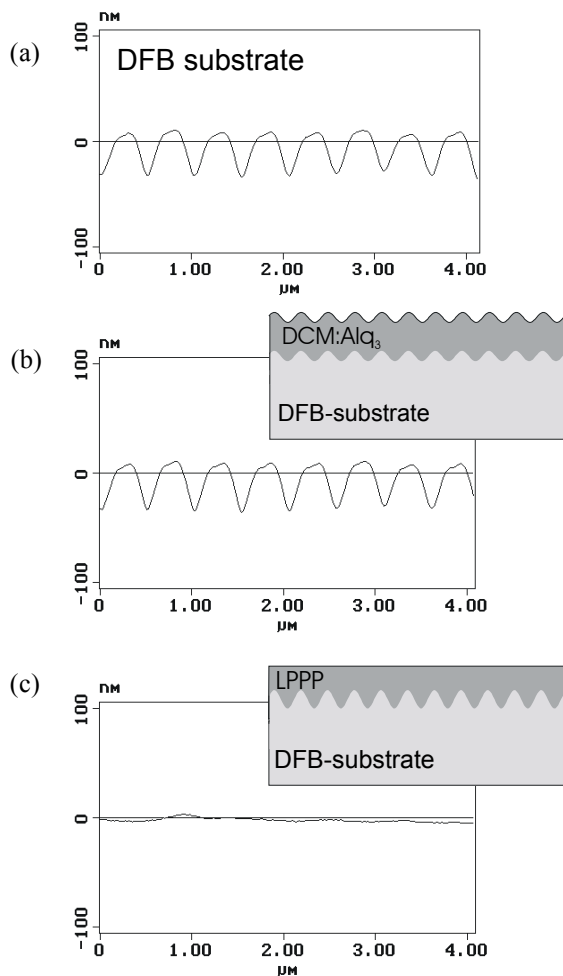


Fig. 5.2:

(a) AFM-height profile of a flexible corrugated PET substrate. The DFB-grating has a periodicity of $\Lambda = 400 \text{ nm}$. AFM height profiles after sublimation of a 275 nm thick Alq_3 :DCM film (b) and spincasting of a 250 nm LPPP film (c) are shown. The sample cross-section is sketched in the corresponding inset.

5.2 Characterization of the laser operation

Distributed feedback lasers were fabricated by sublimation of Alq₃:DCM onto corrugated substrates¹³. Depending on the modulation periodicity, Λ , the feedback condition $2n_{eff}\Lambda = m\lambda_{Bragg}$ can be fulfilled for the first, second, or a higher Bragg order m . Emission spectra below and above the laser threshold are shown in Fig. 5.3 for a first order (a) and a second order (b) DFB laser.

The first order DFB laser is based on a substrate with $\Lambda = 205$ nm and a modulation depth of 180 nm. The Alq₃:DCM film is 125 nm thick, with the DCM concentration adjusted to $\sim 2\%$. In the case of the second order DFB laser a substrate with $\Lambda = 400$ nm, a modulation depth of 90 nm and a film thickness of 180 nm are chosen. The films are thin enough to support only the lowest TE and TM modes. The samples are excited by the femtosecond pulses of the frequency doubled regenerative amplifier, focused to a circular spot of 145 μm diameter. As described above the emission is collected perpendicular to the surface and consists of a superposition of direct luminescence and waveguided light that is subsequently scattered.

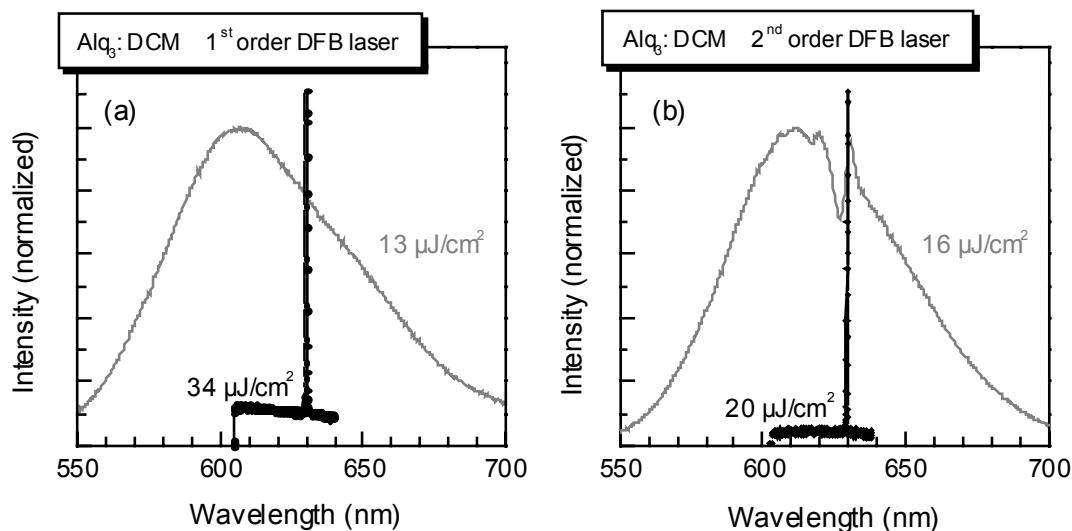


Fig. 5.3: Emission spectra of Alq₃:DCM lasers with distributed feedback in first (a) or second order (b) below (gray) and closely above the respective laser threshold. A drastic spectral narrowing is observed. Excitation power is given in units of the *absorbed* energy density (fluence).

At an excitation fluence of 13 $\mu\text{J}/\text{cm}^2$ the emission of the first order DFB laser gives a typical photoluminescence spectrum of Alq₃:DCM, spanning over more than 150 nm (Fig. 5.3 (a)). No effect of the DFB grating is seen. However, the spectrum changes drastically at a fluence of 19 $\mu\text{J}/\text{cm}^2$ ($N_{exc} = 3.1 \cdot 10^{18} \text{ cm}^{-3}$), where a narrow line emerges at a wavelength of ~ 630 nm having a width of less than 0.5 nm. At 34 $\mu\text{J}/\text{cm}^2$ this laser line dominates the spectrum, even though only that fraction of laser light is recorded which is scattered out of the waveguide (see Fig. 2.10). Fig. 5.4 displays the evolution of the intensity emitted at the laser wavelength

¹³ Samples obtained from T. Benstem, Institut für Hochfrequenztechnik, TU Braunschweig.

as a function of the pump fluence. As expected for a laser, the intensity rises linearly under low excitation, whereas a roughly exponential increase is observed closely above threshold.

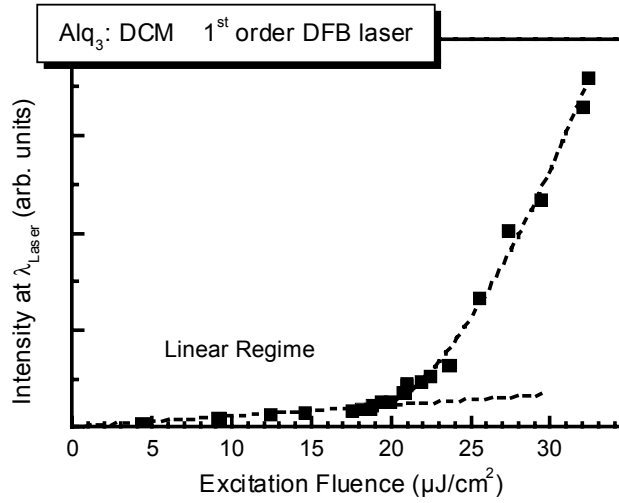


Fig. 5.4: Input–output characteristics of an Alq₃:DCM laser with 1st order distributed feedback. Above the threshold fluence (19 μJ/cm²) the intensity at the laser wavelength rises exponentially. Well above threshold the increase of intensity becomes linear again, due to gain saturation. The dashed lines are only guides to the eye.

Fig. 5.3 (b) shows the corresponding emission spectra for a DFB laser with feedback in the 2nd Bragg order. Even at low excitation densities the spectrum differs substantially from a mere photoluminescence spectrum in that there are two well pronounced dips. The stronger one, with a width of ~ 6 nm, is located at a wavelength of 626 nm, the second dip is centered at 617 nm. Keeping in mind that in a 2nd order DFB laser a substantial fraction of the waveguided light is coupled out of the surface into the detector, each dip can be attributed to a stopband, a range of wavelengths for which propagation in the waveguide is suppressed by the DFB grating. In accordance with the predictions of Section 2.3.1 the dip at the higher wavelength ($\lambda = 626$ nm) corresponds to the stopband for guided TE-polarized waves, the dip at $\lambda = 617$ nm is the stopband for TM polarized waves. When the excitation density is increased above 16 μJ/cm² ($N_{exc} = 1.8 \cdot 10^{18}$ cm⁻³, $g = 19$ cm⁻¹) the spectrum collapses to a narrow peak located at the long wavelength side of the stopband.

Passing over the laser threshold not only the spectrum but also the far-field emission changes drastically. Fig. 5.5 sketches the fan-like beam caustic observed for a 2nd order DFB laser well above the laser threshold. It is characterized by a small divergence in the direction perpendicular to the grating (z -direction) and a large divergence angle φ parallel to the grating grooves (x -direction). The physical origin of this peculiar emission pattern is investigated in Section 5.3.

It is further found that the surface emitting laser beam is strongly TE polarized, i.e. the **E**-field is aligned in the waveguide plane. Although TM polarized laser modes could be observed under very high excitation they are absent under normal operation conditions. Because of their weaker confinement TM-modes exhibit a much higher threshold. Moreover, they

couple very weakly to surface emission if dielectric gratings are used^{215,216}. Qualitatively similar results on 2nd order DFB lasers are obtained using spin-cast films of MeLPPP^{23,39}.

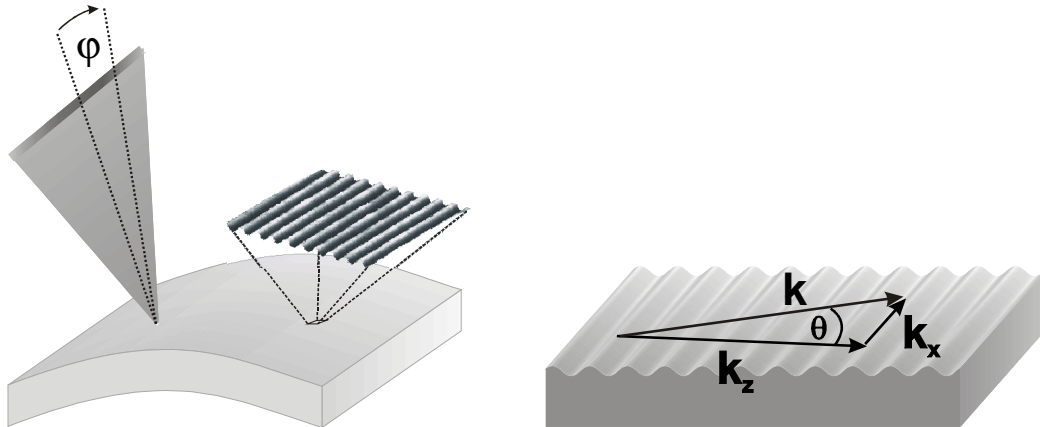


Fig. 5.5: *left*: Schematic picture of the fan-like beam caustic observed in a 2nd order surface emitting DFB laser well above threshold. The divergence in the direction parallel to the grooves is large whereas a low divergence is observed perpendicular to the grating. *right*: Scheme of the wavevector components of the laser modes in a DFB laser

5.3 Lateral laser modes

The circular shape of the excitation spot and the absence of lateral confinement lead to a situation where distributed feedback is not only provided for guided waves that propagate perpendicular to the grating but also for waves propagating at an angle θ relative to the grating vector. The right hand side of Fig. 5.5 depicts the corresponding scheme. The laser modes can be characterized by their wavevector components parallel (k_x) and perpendicular (k_z) to the grooves. The dispersion relation reads:

$$E = \frac{hc}{\lambda_0} = \frac{\hbar c}{n_{eff}} |\mathbf{k}| = \frac{\hbar c}{n_{eff}} |\mathbf{k}_x + \mathbf{k}_z| = \frac{\hbar c}{n_{eff}} \frac{k_z}{\cos \theta} \quad , \quad (5-1)$$

where k_z is determined by the Laue condition 2-16.

In the absence of lateral confinement a broad spectrum of lateral modes with continuously varying k_x for a fixed k_z is supported. This mode structure can be directly observed in the emission pattern of the 2nd order DFB-lasers. As mentioned above the laser radiation is coupled out of the waveguide by 1st order Bragg diffraction at an angle φ relative to the surface normal. The angle φ in the far-field is related to the in-plane propagation angle θ by the phase matching condition at the surface (equation 2-17). Combining 2-17 and 5-1 predicts the following angular dependence of the laser wavelength:

$$\lambda(\varphi) = n_{eff} \Lambda \sqrt{1 - \left(\frac{\sin \varphi}{n_{eff}} \right)^2} \quad . \quad (5-2)$$

The dependence of the emission spectrum on the output angle φ was measured for a 2nd order DFB laser. For that purpose a small fraction of the far-field laser emission is collected with a

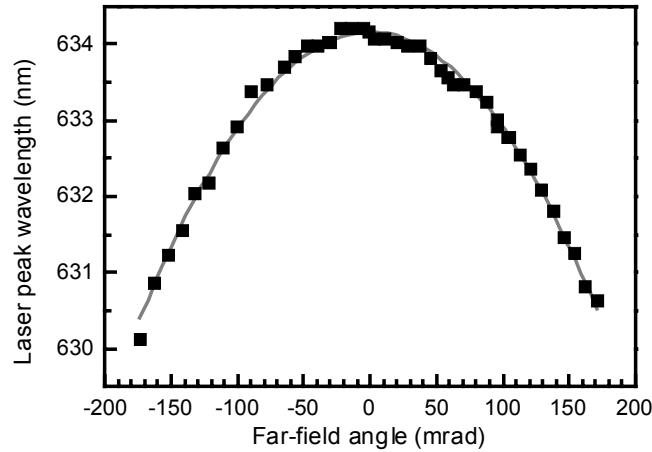


Fig. 5.6: Dependence of the emission wavelength on the far-field angle φ for a 2nd order DFB laser with a 130 nm thick Alq₃:DCM film. The full squares are the measured peak wavelengths, the solid gray line is a fit based on equation 5-2 with the fitparameter n_{eff} .

multimode fiber (core diameter 400 μm) and analyzed by a subsequent spectrometer. The fiber is placed at a distance of ~ 23.5 cm from the sample surface and is scanned along the laser fan in x -direction. In Fig. 5.6 the spectral position of the laser peak is plotted as a function of φ . As expected the laser wavelength decreases with increasing output angle. The solid gray line is a fit using equation 5-2, showing excellent agreement between the experimentally found dependence and the modeling for an effective refractive index of $n_{eff} = 1.585$.

The simultaneous oscillation of many lateral modes results in a spectral broadening of the laser line. The more lateral modes are excited at increasing pump fluence, the larger the effect should be. The angle dependency of the emission wavelength in 2nd order DFB lasers complicates a quantitative investigation of the spectral broadening. It is convenient to circumvent these experimental complications by monitoring the isotropic stray-light of a 1st order DFB laser (~ 130 nm thick Alq₃:DCM, $\Lambda = 205$ nm). Fig. 5.7 (a) shows the evolution of the normalized laser spectra for various excitation pulse energies above the laser threshold. Closely above threshold the laser spectrum is relatively narrow with a linewidth below 0.5 nm (FWHM). For increasing excitation density a gradually increasing number of lateral modes appear, evidenced by a gradually increasing intensity at the low-wavelength edge of the spectrum. Even more clearly this can be seen in Fig. 5.7 (b), where the spectral linewidth at four relative intensity levels is plotted against the excitation density. Whereas the full width at half maximum (FWHM) is more or less constant, the linewidth at 5% of the maximum intensity increases drastically with increasing excitation density. Obviously, the higher lateral modes exhibit higher laser thresholds and thus do not acquire the same intensity as the fundamental mode, but in sum they contribute significantly to the overall laser emission at high excitation densities.

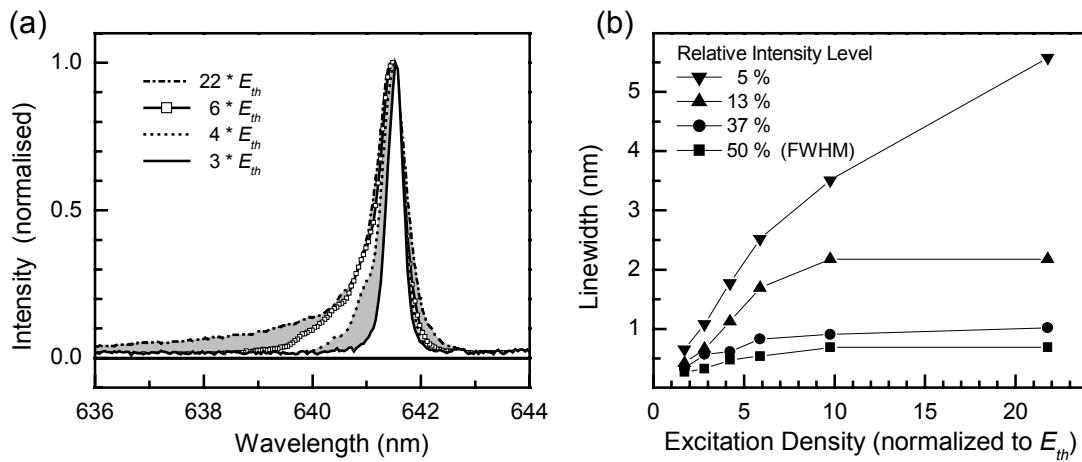


Fig. 5.7: (a) Normalized laser spectra of a 1st order Alq₃:DCM DFB laser for increasing excitation-pulse-energy, normalized to the laser threshold E_{th} . The increasing intensity at the low-wavelength side is ascribed to the evolution of lateral modes. (b) Evolution of the spectral width of the emission at various signal levels

These results show that the performance of our DFB lasers is intrinsically limited by the presence of lateral modes. Lateral modes increase the spectral width of the laser line, they increase the divergence of the output beam, and they limit each others efficiency since they all compete dynamically for the same excitation density. For an improved performance a selection of lateral modes is mandatory. In the field of inorganic DFB lasers this is conventionally achieved via horizontal confinement in a ridge waveguide with a few microns' width²¹⁷. A very elegant way of lateral mode selection without the need for additional photolithographic steps is shown in Section 6.

5.4 Wavelength tuning by variation of the film thickness

The Bragg condition $2n_{eff}\Lambda = m\lambda_{Bragg}$ suggests that tuning of the laser wavelength can be reached by a variation of either the grating periodicity Λ or of the effective refractive index of the waveguide. On the other hand it is well known that the effective refractive index of the waveguide can be varied by adjusting the film thickness (see e.g. Fig. 2.9). In order to exploit the broad optical gain spectrum of Alq₃:DCM (Fig. 4.7) a number of DFB lasers were fabricated varying the thickness of the Alq₃:DCM film from 120 nm to 435 nm¹⁴. Nanopatterned substrates with a periodicity of 400 nm and a modulation depth of 90 nm were utilized. Distributed feedback is provided by second order Bragg reflection, while the laser light is coupled out perpendicular to the film via first order Bragg diffraction.

¹⁴ These samples were prepared by S. Berleb and A. G. Mückl, Lehrstuhl Experimentalphysik II, Universität Bayreuth.

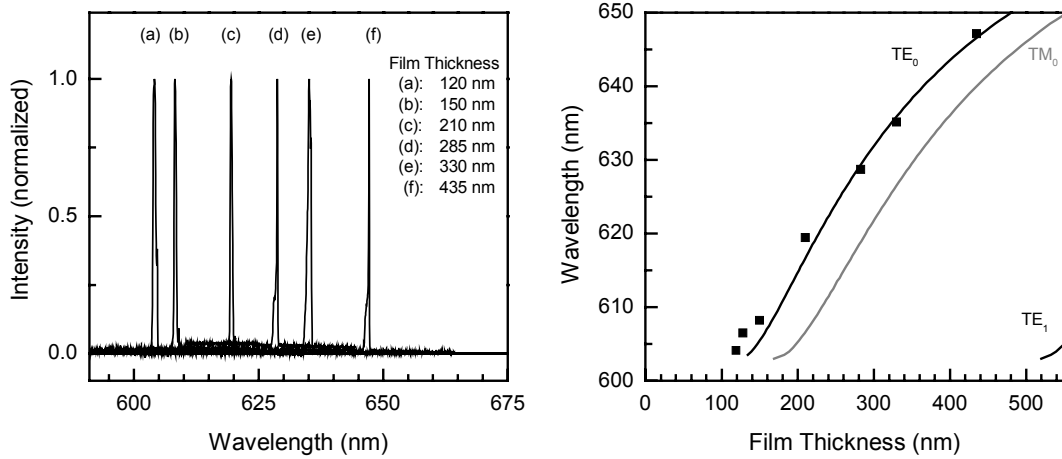


Fig. 5.8: Left: Laser spectra for a number of samples with varying thickness of the Alq₃:DCM layer. Right: Experimentally determined laser wavelengths for various film thicknesses. The solid curves are calculated assuming a planar waveguide.

The different laser spectra shown in Fig. 5.8 demonstrate that the laser wavelength can be tuned over a spectral range of $\Delta\lambda_{Las}=44$ nm from $\lambda_{Las}=604$ nm for a 120 nm thick film to $\lambda_{Las}=648$ nm for a 435 nm thick film, respectively. The experimentally determined peak positions of the laser emission are plotted versus the film thickness on the right hand side of Fig. 5.8 (squares).

Assuming that the corrugation presents only a minor modification of the waveguide the dependence of the laser wavelength on the film thickness can be calculated from equation 2-12 and 2-13. Additionally it is taken into account that the wavelength is linked to n_{eff} via the Bragg condition $\lambda_{Las} = n_{eff} \cdot \Lambda$. The solid black line shows the calculated wavelength dependency for a TE₀ mode using $n_f=1.685$ for the organic semiconductor and $n_s=1.507$ for the substrate. The experimental data points correspond very well with the calculated curve for higher film thicknesses. Only for the thinnest films a small deviation is observed. The deviations between the fit and the experimental data points are explained by the rather strong perturbation of the planar waveguide in our structure and by the simplifications of the model, neglecting the wavelength dependence of the refractive index and the shift between the laser wavelength and the exact Bragg wavelength due to the stopband.

The range of laser wavelengths being accessible with one single grating is limited by the range of film thicknesses for which laser operation is strongly favored for one single mode, typically the lowest TE polarized mode, TE₀. Whereas no guided waves are supported below $d_f \approx 110$ nm, a second allowed TE₁ mode can appear for $d_f \approx 500$ nm. Waveguide modes with TM polarization are supported above a film thicknesses of $d_f \geq 160$ nm. However, no TM laser modes are observed. This is explained by their weak dielectric confinement and the resulting higher threshold. Anyway, the further the Bragg wavelength of the TE₀ mode shifts away from the gain maximum at $\lambda \approx 630$ nm, the more important higher waveguide modes may become. Utilizing a second order DFB grating with a periodicity of 400 nm singlemode operation was obtained for wavelengths between 604 and 648 nm. Other wavelength ranges are accessible with a different grating periodicity²¹⁸.

5.5 Coupling mechanism in organic solid-state DFB lasers

The above discussion of the properties of organic semiconductor DFB lasers was based on rather intuitive models and some severe simplifications. These models can qualitatively explain the occurrence of lateral modes and the possibility of the tuning the emission wavelength by variation of the film thickness. They fail, however, to explain more subtle observations, such as the presence of a stopband clearly seen in the emission spectrum of a 2nd order DFB laser (Fig. 5.3 (b)) opposed to the absence of such a stopband in the respective 1st order structure (Fig. 5.3 (a)). To explain such effects a more detailed analysis of the coupling mechanism in organic DFB lasers is required. As a matter of fact, knowledge about the coupling coefficient κ is the starting point for the optimization of a DFB laser's performance since it determines many of its specific characteristics: whether the laser operates in a single mode or not, the far-field divergence, the optimum device length and the corresponding threshold gain, and even the laser dynamics is influenced by κ .

Attributing to the exceptional importance of the coupling coefficient, calculations of κ will be presented for the various structures used within the course of this work. Based on these calculations the performance of the corresponding laser structure is predicted with the help of the coupled mode theory presented in Section 2.3.2.2. The predicted performance is then compared with experimental investigations.

5.5.1 Calculation of the coupling coefficient

The most common approaches for the calculation of the coupling coefficient in distributed feedback lasers rely either on the original coupled mode theory¹³⁴, applicable to harmonic perturbations, or on a matrix formalism (see e.g.²¹⁹), applicable to square modulations. The calculation of radiation modes, however, is a difficult task, except for very simple structures and, hence, these theories fail to give the correct results. The matrix theory, for example, predicts a large stopband for distributed feedback in uneven orders, yet vanishing stopbands for even orders; clearly the opposite of the findings in Fig. 5.3. Therefore more elaborate numerical methods have to be applied like e.g. finite-difference time-domain simulations²²⁰ or a rigorous Floquet-matrix theory^{216,221,222}.

The calculations presented here were performed by N. Finger at the Solid-State Electronics Center, TU Wien, using a rigorous calculation of the Floquet modes including evanescent modes. The structure is approximated by a juxtaposition of rectangular regions, so that an analytic expression for the field can be given by a decomposition into discrete space harmonics (Floquet-Bloch waves). Their amplitudes are adjusted to satisfy the grating boundary conditions at the exact resonance condition. Starting from these exact solutions at the resonance, the coupling coefficients can be calculated. Coupled mode theory can then be used to determine the off-resonance laser behavior accurately for arbitrary refractive index changes.

The results of the calculation are presented in terms of the coupling coefficient

$$\kappa = \text{Re}(\kappa) + i \text{Im}(\kappa) + i \Gamma \gamma' \gamma_0, \quad (4-3)$$

where $\text{Re}(\kappa)$ and $\text{Im}(\kappa)$ represent the coupling constant in a passive structure without gain, the last term gives the additional contribution of gain coupling in an active structure. The amount of gain coupling scales with the field gain γ_0 and the confinement factor Γ of the mode inside the gain medium. The factor γ' is determined by the geometry of the DFB structure. Since the dispersion relation of a DFB laser (equation 2-20) is sensitive to κ^2 , only the relative sign of the contributions is relevant. The sign convention is chosen such that $\text{Re}(\kappa) > 0$. Therefore a positive contribution γ' of the (positive) field gain γ corresponds to an in-phase gain coupling, where the maxima of gain (or minima of loss) coincide with the maxima of the effective refractive index. In second order structures $\text{Im}(\kappa)$ has a large value deriving from the radiation losses; its negative sign indicates loss coupling.

Apart from the refractive indices and the sample geometry no material specific parameters were required in the calculations. Since the refractive indices are comparable for most organic materials and the surface morphology depends rather on the fabrication process than on the material itself. It is therefore straightforward to apply these results to future devices using a similar structure yet different materials.

5.5.2 Coupling in 2nd order DFB structures

Evaporated films

Fig. 5.9 displays the calculated Bragg wavelength and coupling constants for an evaporated film of Alq₃:DCM as a function of the film thickness. The corrugation of the substrate is assumed to be nearly sinusoidal, having a periodicity of $\Lambda = 400$ nm, a modulation depth of $h = 95$ nm, and a refractive index of $n_s = 1.5$. The surface modulation of the organic film is an exact replica of the substrate. The refractive index of Alq₃:DCM, $n_f \geq 1.75$, was taken from literature¹⁰⁷.

The qualitative dependence of the Bragg wavelength on the film thickness clearly resembles the experimentally observed dependence and the simple calculation shown in Fig. 5.8. However, the slope is considerably higher leading to a quantitative mismatch for thick films. A lower value of n_f would result in a better quantitative agreement. In retrospect, the value of $n_f = 1.75$ reported by Kozlov is clearly too high for our samples, where $n_f \approx 1.7$ seems to be a better parameter (see Fig. 4.4).

For all film thicknesses the real part of the coupling constant, κ , is in the order of several hundreds per cm, which indicates a strong index coupling component. The surface emission induces a substantial contribution of loss coupling, expressed by a negative imaginary component of κ . For films with $d_f \geq 300$ nm it is found that $\text{Im}(\kappa)/\text{Re}(\kappa) \ll 1$, such that κ becomes essentially real. In the absence of gain the dispersion relation 2-20 then predicts a

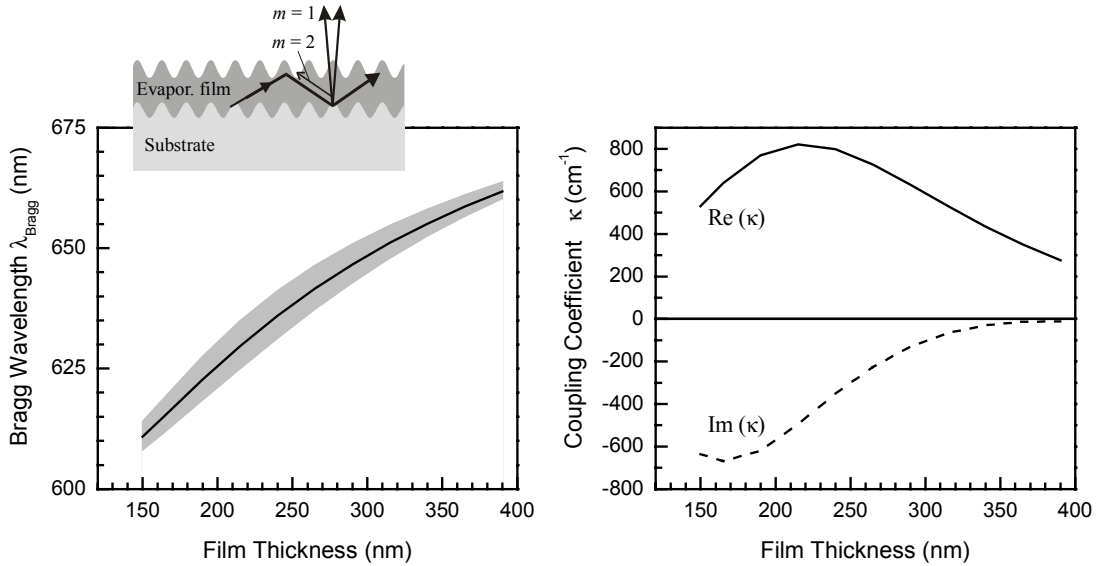


Fig. 5.9: Bragg wavelength (a) and coupling coefficients (b) for an Alq₃:DCM 2nd order DFB laser as a function of the film thickness. The gray-shaded region indicates the extension of the stopband, which is expected from Re(κ). For films thinner than ~ 250 nm a strong contribution of loss coupling by surface emission is expected. The inset shows a schematic cross-section of the device and indicates the double-lobed surface emission expected for strong loss coupling.

purely imaginary propagation constant for a broad range of frequencies with $|\omega - \omega_{\text{Bragg}}| < \kappa c/n_{\text{eff}}$. For the corresponding range of wavelengths the grating shows a strong reflectivity and propagation in the waveguide is suppressed. Due to the high strength of the coupling the stopband has a width of several nm and should be easily observable. Its position is indicated by the gray-shaded region in Fig. 5.6 (a). If d_f is decreased below 300 nm, the absolute value of Im(κ) increases strongly. Even in the absence of gain, the propagation constant β now has a real component, corresponding to a considerable transmission of the grating. Accordingly, the stopband becomes more and more obscured and, eventually, vanishes completely. The additional contribution of gain modulation is -for reasonable values of g in a photopumped structure- much lower than Im(κ) and can therefore be neglected.

From the above discussion the laser characteristics can be predicted for Alq₃:DCM lasers with different film thicknesses: a 2nd order Alq₃:DCM laser with $d_f > 300$ nm should behave like an index coupled DFB laser, showing a clear stopband and a single laser line on the long wavelength side of the stopband. The wavevector of the lasing mode is located at Re(β) = 0, that is exactly at $k_{\text{Laser}} = k_{\text{Bragg}}$. The far-field emission resulting from first order Bragg scattering should therefore be single-lobed. For decreasing d_f there is a gradual transition to gain coupling and the laser wavelength is pulled towards the center of the stopband¹³⁵. The laser operates with a wavevector Re(β) $\neq 0$ and the far-field emission should be double-lobed.

Fig. 5.10 (a) and (b) shows the emission spectra of two 2nd order Alq₃:DCM lasers with a film thickness of 210 nm and 330 nm, recorded at the respective threshold. (c) and (d) display the corresponding far-field intensity profiles of the same two samples measured with a CCD detector array. The thicker sample shows the predicted index coupling characteristics: the laser peak emerges at the long wavelength side of a well pronounced stopband. The longitudinal far-field emission profile is single lobed with a half angle radius of 3.2 mrad. This divergence corresponds to a diffraction-limited emission from a Gaussian spot with a

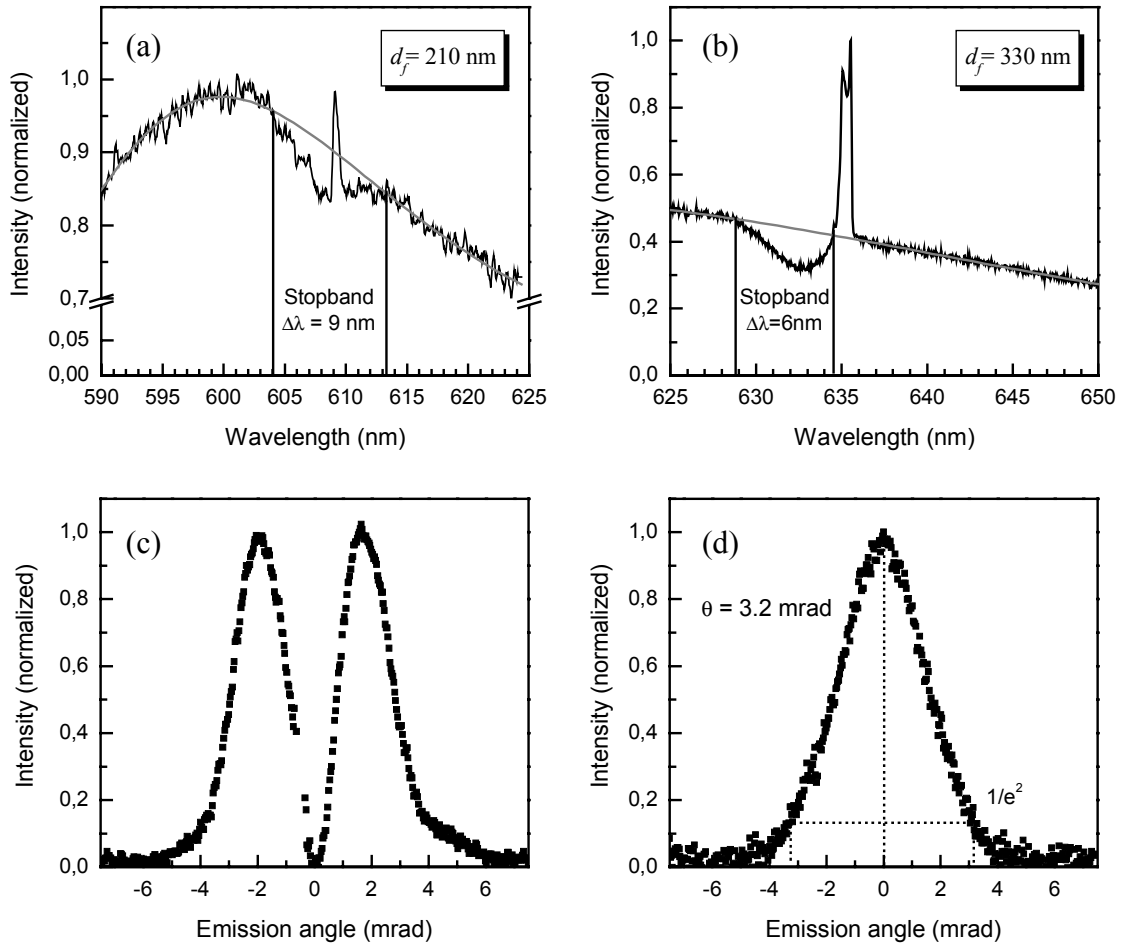


Fig. 5.10: Emission spectra for two 2nd order Alq₃:DCM lasers with a thickness of 210 nm (a) and 330 nm (b) at the respective threshold. The gray solid line indicates the form of the spectrum without grating. In the thinner sample the laser mode is found in the center of the stopband, whereas it is located on the long wavelength side of the stopband in the thicker sample. (c) and (d) show far-field irradiance profiles of the same two samples as a function of the longitudinal far-field emission angle (in *z*-direction, perpendicular to the grating grooves).

diameter of 125 μm, similar to the diameter of the excitation spot. In the thinner film the stopband is less pronounced and the laser peak emerges nearly in the center of the stopband. The far-field is double-lobed as expected for a strong imaginary contribution to the coupling coefficient.

In the experiments the laser threshold is obtained at an excitation densities in the order of $2 \cdot 10^{18} \text{ cm}^{-3}$. According to the cross-section for stimulated emission found in Section 4.2.2 ($\sigma_{SE} = 1.35 \cdot 10^{-17} \text{ cm}^2$) the intensity gain at the laser threshold is in the order of $g_{th} \approx 30 \text{ cm}^{-1}$. On the basis of the calculated coupling constants and equation 2-24 a threshold gain of 65 cm^{-1} is predicted for a 2nd order DFB laser with a 330 nm thick Alq₃:DCM film and an excitation spot diameter of 150 μm. For this comparatively thick film good agreement between experiment and modeling is found. According to the modeling the laser threshold should increase for decreasing d_f as the power loss due to outcoupling, $\alpha_{Loss} = 2|\text{Im}(\kappa)|$, increases. The experimentally observed increase of the laser threshold is less strong.

In summary, very good agreement between the modelling and the experimental observations is found for lasers made with sublimed films of Alq₃:DCM.

Spincast films

Fig. 5.11 shows the calculated Bragg wavelength and the coupling coefficients for MeLPPP DFB lasers as a function of the average film thickness of the spincast film. The substrate ($n_s = 1.475$) has a 275 nm deep sinusoidal corrugation with a periodicity of $\Lambda = 300$ nm. The upper surface of the polymer film ($n_f = 1.7$) is assumed to be flat so that the average film thickness is simply $d_f = 1/2(d_{\min} + d_{\max})$.

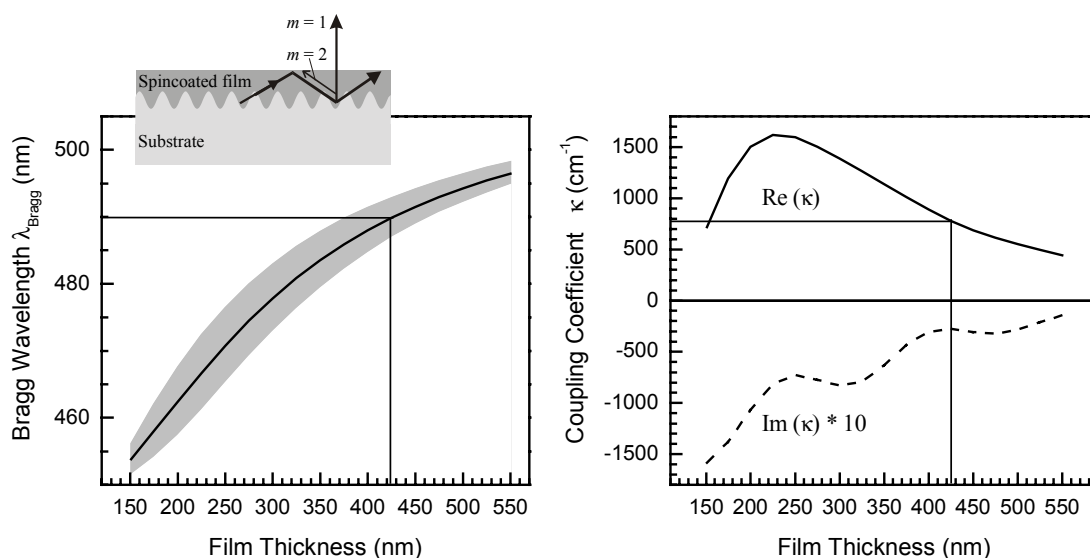


Fig. 5.11: Bragg wavelength (a) and coupling coefficients (b) for a MeLPPP 2nd order DFB laser as a function of the film thickness. For all film thicknesses the imaginary component of κ is an order of magnitude lower than the real component. Therefore the device should show a clear stopband indicated by the shaded gray region around the Bragg wavelength in (a). The inset shows a schematic cross-section of the device and indicates an irradiance profile that is characteristic for dominant index coupling.

Given the periodicity of the grating and the wavelength of maximum gain in MeLPPP, the film thickness required for laser operation is between 350 nm and 500 nm. In this range $\text{Re}(\kappa)$ is at least an order of magnitude larger than $\text{Im}(\kappa)$. As before the negative sign of $\text{Im}(\kappa)$ indicates coupling due to the surface emission. The contribution of active gain coupling in is negligible for all reasonable field gains g . DFB lasers based on MeLPPP should therefore show a behavior typical for index coupling. Due to the enormous value of $\text{Re}(\kappa)$ the stopband should be nearly 10 nm wide and, hence, span the entire gain spectrum of MeLPPP. Despite its large extension the stopband will not be highly pronounced, a fact that is indicated by the substantial value of $|\text{Im}(\kappa)| \approx 30\text{-}40 \text{ cm}^{-1}$. Furthermore the surface emission induces cavity losses, $\alpha_{\text{Loss}} = 2|\text{Im}(\kappa)|$, in the order of $60\text{-}80 \text{ cm}^{-1}$.

Fig. 5.12 shows the spectra of a DFB laser ($d_f \approx 500$ nm) below and well above threshold. The film thickness is chosen in such a way that the laser line is located close to the maximum of stimulated emission in MeLPPP. Due to the narrow emission peak of MeLPPP and the simultaneous presence of TE and TM laser modes, it is difficult to identify the position of a stopband unambiguously. To identify the stopband the spectrum below threshold is compared with a smoothed photoluminescence spectrum of a MeLPPP film on a planar glass substrate. This comparison reveals excellent agreement above a wavelength of 493 nm but significant

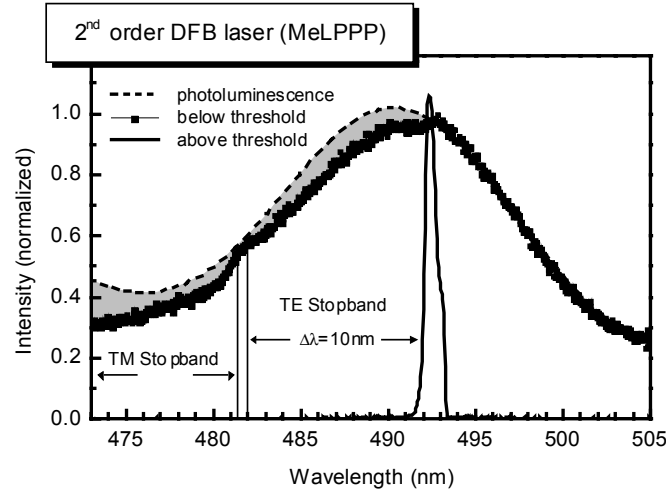


Fig. 5.12: Normalized emission spectra of a MeLPPP 2nd order DFB laser below (squares) and above the laser threshold (solid line). The dashed line indicates the photoluminescence of a planar MeLPPP film. The positions of the TE and TM stopbands are indicated.

deviations below that wavelength (gray-shaded area). These differences can be attributed to two very wide, yet weakly pronounced, stopbands; one for the TE and TM polarization, each. According to this interpretation the laser line is located at the long wavelength side of a 10 nm wide TE stopband, just as predicted by the calculation. Further evidence for index coupling comes from the single lobed far-field emission with a divergence of 2.4 mrad (similar to Fig. 6.3). When the excitation beam is focused to a circular spot with a diameter of 95 μm a threshold gain of $g_{th} \approx 100 \text{ cm}^{-1}$ ($N_{exc} \approx 7.5 \cdot 10^{18} \text{ cm}^{-3}$) is determined. This is in excellent agreement with the value of $g_{th} \approx 100\text{-}120 \text{ cm}^{-1}$ which is predicted from equation 2-24 using the calculated parameters. Hence, the experimentally found behavior can be predicted very well.

5.5.3 Prediction of coupling mechanisms in 1st order DFB structures

Fig. 5.13 shows the predicted coupling coefficients for 1st order structures of Alq₃:DCM and MeLPPP. The grating for Alq₃:DCM has a periodicity of 205 nm and a modulation depth of 175 nm, for the MeLPPP grating $\Lambda = 150 \text{ nm}$ and $h = 100 \text{ nm}$ are assumed. All further parameters are chosen as reported above. The most obvious difference to 2nd order gratings is the absence of $\text{Im}(\kappa)$ in a passive structure, which is simply due to the absence of surface emission.

In the case of *spincast films* very strong index coupling is found, whereas gain coupling is comparatively weak. For instance with a film thickness of 300 nm and a power gain of 100 cm^{-1} $\text{Re}(\kappa)/\text{Im}(\kappa) > 1000$ is found. First order DFB lasers using spincast films should therefore be strongly index coupled. However, these predictions could not be checked experimentally since no suitable 1st order DFB grating was available for MeLPPP.

In the case of evaporated films $\text{Re}(\kappa)$ is by a factor of 5 to 10 lower than in the other considered structures. This is due to the fact that the local effective refractive index is

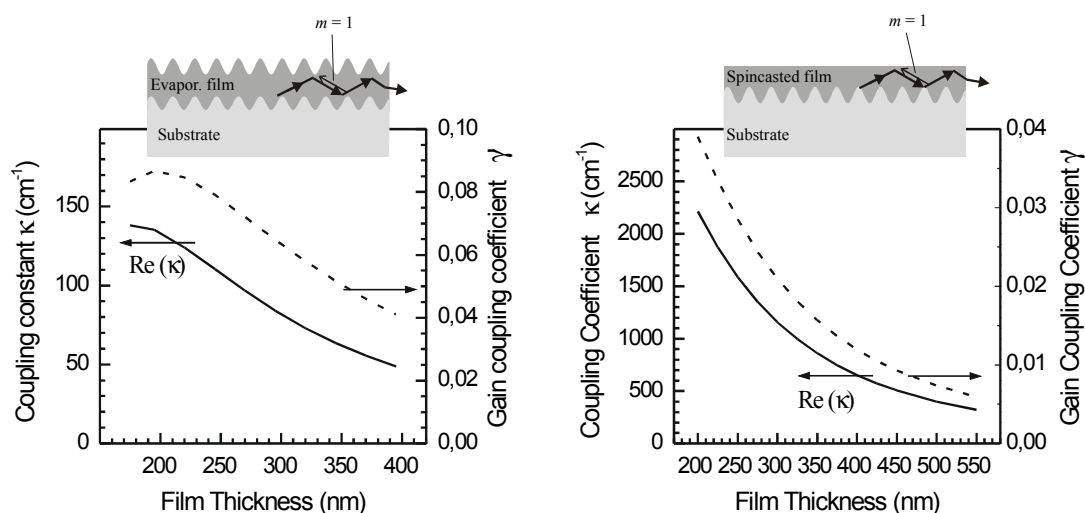


Fig. 5.13: Calculated coupling coefficients for 1st order DFB structures with either a modulated upper surface as in Alq₃:DCM (left) or a flat upper surface as expected for a spincoated MeLPPP film (right). The real part of the coupling coefficient is very weak in the Alq₃:DCM structure, resulting in a vanishing stopband width.

constant. In other words one could say that here the reflections from the upper and the lower film surface nearly cancel each other. As a consequence of the low coupling coefficient the extension of the stopband is expected to be only approx. 1 nm wide. Indeed, no stopband was observed in the Alq₃:DCM 1st order DFB laser (Fig. 5.3 (a)). Due to the low value of $\text{Re}(\kappa)$ the relative contribution of active gain coupling is the largest among the investigated structures, yet still negligible: for $d_f = 350$ nm the confinement is 84%; with a gain of 100 cm^{-1} one obtains $\text{Re}(\kappa)/\text{Im}(\kappa) \approx 30$. Concomitantly the structure behaves like a weakly index coupled laser.

5.5.4 Implications for the design of optimized DFB lasers

The coupling coefficients of various organic solid-state distributed feedback structures were calculated using an adapted Floquet matrix theory. Starting from these calculations, coupled mode theory is used to predict the performance of the various laser structures used within the course of this work. One important result is that the different surface texture of sublimed and evaporated structures gives rise to a different coupling mechanism. The transition from complex coupling to index coupling which is observed in 2nd order DFB lasers with increasing thickness of the Alq₃:DCM film, was successfully modeled. Furthermore the gain required to reach threshold can be reliably estimated. In summary, very good agreement between the predictions of the modeling and the experiments is found, even though some of the relevant material constants were not precisely known at the time the calculations were performed. Therefore these calculations are a powerful tool for the optimization of future organic DFB lasers. An example is outlined below.

Under continuous wave operation a certain longitudinal intensity distribution establishes inside the cavity of a DFB laser. This intensity distribution is a direct consequence of the

excitation profile and the coupling strength κL , being the product of the coupling coefficient and the length of the device¹³⁴. For optimum performance the optical intensity distribution inside the cavity must be properly matched to the excitation distribution. Otherwise the excitation density is locally depleted (spatial hole burning) and the output power of the device exhibits strong fluctuations. If the excitation density is homogeneously distributed over the entire length of the device, so should be the optical intensity. This condition is reached if the value of κL is adjusted to 1.25 for an index coupled laser²²³ or 1.6 for gain coupled device²²⁴, respectively. On the other hand, the Gaussian excitation density distribution in optical experiments demands for a higher κL product, most likely in the order of 5-10¹³⁴. Since an infinite DFB structure does not have a well defined device length L it is the diameter of the excitation spot which has to be adjusted.

Due to the large modulation depth of the present DFB gratings, large coupling coefficients in the order of 500-1500 cm^{-1} are obtained in most of the structures. For optical excitation with a Gaussian excitation profile this implies an optimum spot diameter in the order of 100-200 μm , which is very convenient. In electrically driven devices, however, the distribution of excitation density is homogeneous and the large coupling coefficient implies an optimum device length in the order of only 10-20 μm . Such a short device requires a very high threshold gain (see equation 2-24). Therefore lower modulation depths are favorable for future electrically driven devices resulting in a reduced coupling coefficient, an increased optimum device lengths, and finally in a drastically reduced threshold gain. Due to the absence of surface emission losses, first order structures are the most promising candidates. Whereas up to now only dielectric gratings were considered, the Floquet-Bloch calculations can be extended to structures including metallic contacts^{216,222}.

6 Lasers with two-dimensional distributed feedback

In this chapter it is shown that two-dimensional distributed feedback can give rise to monomode laser operation with diffraction-limited surface emission. Excitation high above threshold results in multimode operation and enables a direct investigation of the two-dimensional photonic band structure.

Distributed feedback resonators based on nanopatterned substrates have shown to be a very promising method to fabricate organic semiconductor thin film lasers. One of their major drawbacks, however, is the presence of lateral modes leading to multimode laser operation. As seen in the previous chapter multimode operation is unfavorable due to the associated broadening of the laser spectrum and a large divergence. In order to concentrate the emission to a spectrally narrow line and to control the emission properties, it is crucial to reduce the number of lateral modes participating in the laser operation. The conventional way is the photolithographic definition of a lateral waveguide with a width of several microns. A more elegant method for mode selection is the use of two-dimensionally (2D) nanopatterned substrates giving rise to a 2D distributed feedback (2D-DFB) or in other words a 2D photonic band structure^{140,141}. Despite the early, promising results, there have only been very few experimental and theoretical^{142-144,225} investigations until the recent renewed interest within the context of photonic crystal lasers¹⁴⁵.

6.1 Fabrication

The fabrication of the 2D-DFB lasers is very similar to the fabrication of the 1D-DFB lasers. As active laser material the conjugated polymer MeLPPP is used, which is spincoated onto a mechanically flexible, nanopatterned substrate. The major difference to the 1D-DFB laser is in the form of the surface corrugation. Whereas a 1D sinusoidal corrugation with a periodicity of $\Lambda = 300$ nm and a depth of $h = 275$ nm is used for 1D-DFB lasers, two perpendicular sinusoidal corrugations with a periodicity of $\Lambda_z = \Lambda_x = 300$ nm and a depth of $h_z = h_x = 160$ nm form the grating for the 2D-DFB laser. The maximum modulation depth is therefore similar for both structures, which is important when comparing the two structures. An AFM image of the resulting corrugation is displayed in the schematic setup of Fig. 6.1. The superior performance of our 2D-PBS lasers relies on phase locking of the modes established in the two perpendicular resonators. A particularly high grating quality is therefore compulsory, demanding that the deviation of the two periodicities Λ_z and Λ_x must not exceed the laser linewidth, a fraction of a nanometer.

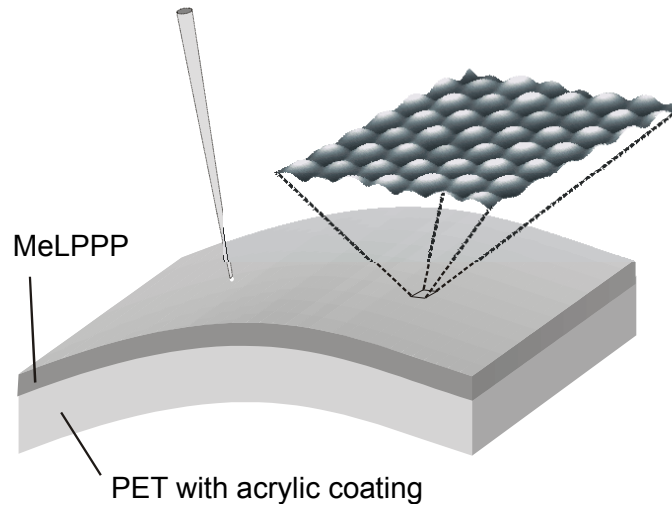


Fig. 6.1: Schematic setup of a 2D-DFB laser. A film of MeLPPP is spincast onto a flexible, nanopatterned substrate. The surface of the substrate has a two-dimensional periodic corrugation shown by the AFM image. Laser emission is observed perpendicular to the substrate.

Gratings with sufficient quality can be fabricated by the soft lithography technique described in Section 5.1. As mentioned before, the corrugation is ultimately defined by the intensity pattern applied to a photoresist. Using a holographic exposure technique highly uniform 1D sinusoidal intensity profiles can be generated. 2D patterns are achieved if the sample is rotated between two subsequent exposures.

6.2 Characterization

Fig. 6.2 presents emission spectra for two different excitation conditions corresponding to excitation densities below and well above threshold, respectively. The dashed line shows the photoluminescence observed when the sample is excited below threshold. The first vibronic transition has a slightly higher intensity than in the photoluminescence spectrum of an MeLPPP-film on a planar glass substrate (Fig. 4.1). This difference is due to the effect of the periodic modulation, which acts as a grating coupler and scatters waveguided light with a wavelength around 490 nm into the direction of the detector. The emission behavior changes drastically at a fluence of $5.6 \mu\text{J}/\text{cm}^2$. At a wavelength of 491 nm a sharp laser peak evolves. Upon further increasing the pump pulse energy the spectrum is completely dominated by the laser peak. The solid line in Fig. 6.2 shows the emission spectrum at a fluence of $8.4 \mu\text{J}/\text{cm}^2$. The measured halfwidth is 0.25 nm, limited by the spectral resolution of the setup.

It is interesting to compare these results with the findings for a laser utilizing an MeLPPP-film of the same thickness but a substrate with a purely one-dimensional periodic height modulation of the same maximum amplitude as in the 2D-case. In the inset of Fig. 6.2 the emission intensity at the laser wavelength, collected perpendicular to the substrate with a numerical aperture of 0.26, is plotted as a function of the pump fluence for a 1D and a 2D-DFB laser. The 2D-laser threshold is reduced by 30% and the differential efficiency is increased.

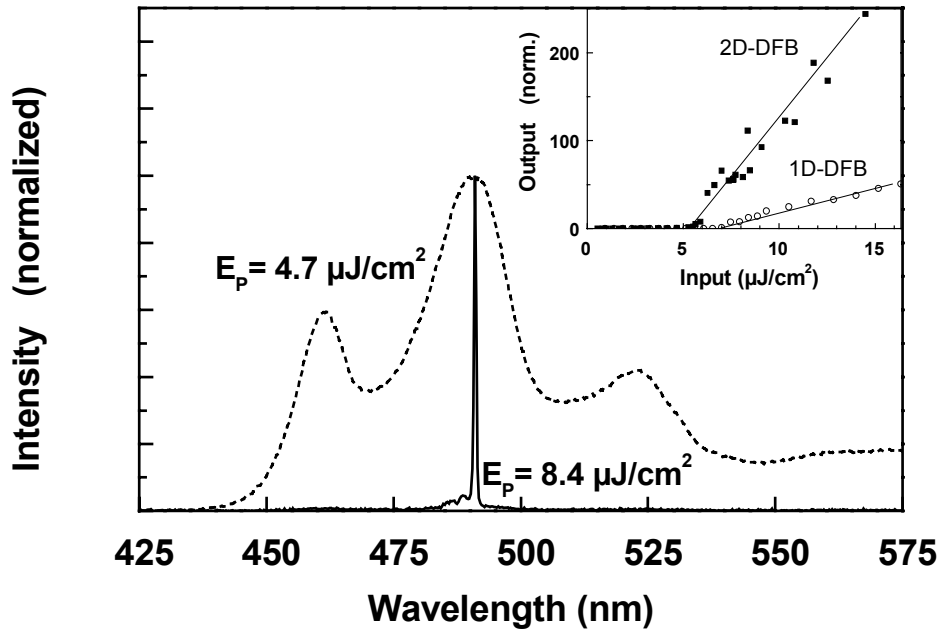


Fig. 6.2: Emission spectra of the 2D-DFB laser below (dashed line) and above the laser threshold (solid line). The spectral half-width (FWHM) of the laser line is 0.25 nm. The inset shows the radiated power at the laser wavelength –normalized to the threshold value– as a function of excitation fluence. Direct comparison with a 1D-DFB laser shows an increase of efficiency and a reduction of the laser threshold.

As the most intriguing feature the divergence of the emission is drastically reduced in the 2D laser. While a strongly polarized emission with rather high divergence parallel to the grating lines is observed in the case of 1D feedback (Fig. 5.5), highly directed unpolarized emission is achieved with the 2D structure. The inset in Fig. 6.3 shows an image of the circularly shaped far-field emission pattern of the 2D-DFB laser. The corresponding transverse irradiance profile, depicted as solid squares in Fig. 6.3, can be fitted with a Lorentzian curve (solid line). The value of 2.4 mrad for the angular radius of the far-field emission indicates diffraction-limited emission from the entire area of the excited spot ($D \approx 150 \mu\text{m}$). This clearly shows that the laser oscillates in phase over the entire excited area, i.e. the laser operates in a single, spatially extended, mode. In section 8.1.2.2 it will be shown that the emission from this coherent oscillation is not only diffraction-limited but also (time-bandwidth) transform-limited.

In contrast to the inherent multimode operation of a 1D-DFB laser without lateral confinement one single lateral modes is selected a 2D-DFB laser. Compared to a 1D-DFB laser with lateral mode selection in a ridge waveguide the horizontal extension of the 2D-DFB laser mode is much larger resulting in a distinctly lower value of the diffraction-limited divergence angle. When the diameter of the excitation spot is more and more increased filamentation of the laser mode into several independent cavities might eventually set a lower limit to the achievable divergence^{140,141}. However, no such filamentation was observed in the present experiments.

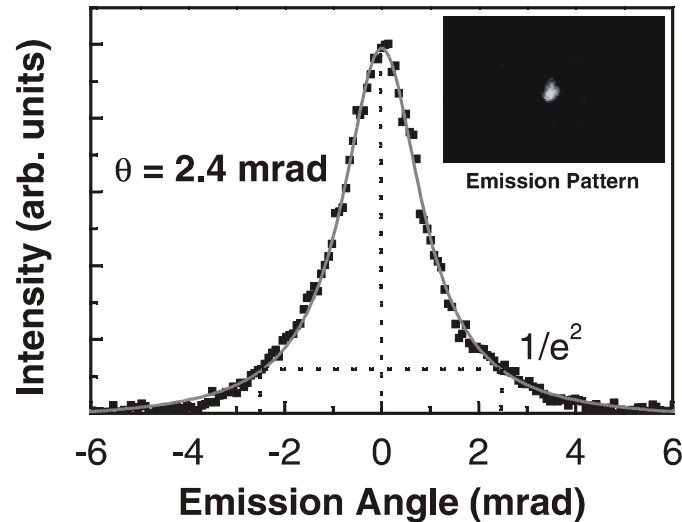


Fig. 6.3: Inset: Image of the circularly shaped far-field emission of the 2D laser in monomode operation ($E_p = 8 \mu\text{J}/\text{cm}^2$). The solid squares show the angular dependence of the corresponding transverse irradiance profile.

As shown in Fig. 6.5 (b), additional features appear in the far-field emission pattern when the excitation intensity is further increased. At approximately twice the threshold energy ($\geq 10 \mu\text{J}/\text{cm}^2$) two perpendicular laser fans are superimposed to the central low divergence spot (horizontal and vertical line in Fig. 6.5 (b)). Simultaneously the spectrum of the laser broadens to $\sim 1 \text{ nm}$ FWHM (not shown). At pump pulse energies above $37.5 \mu\text{J}/\text{cm}^2$, emission fans tilted by 45 degrees are additionally superimposed (Fig. 6.5 (c)). The spectrum of these features extends from 484 nm to 495 nm (Fig. 6.8), spanning the entire gain width of MeLPPP. These experimental findings can be explained in terms of a Laue-formulation for the feedback mechanism in the 2D photonic crystal.

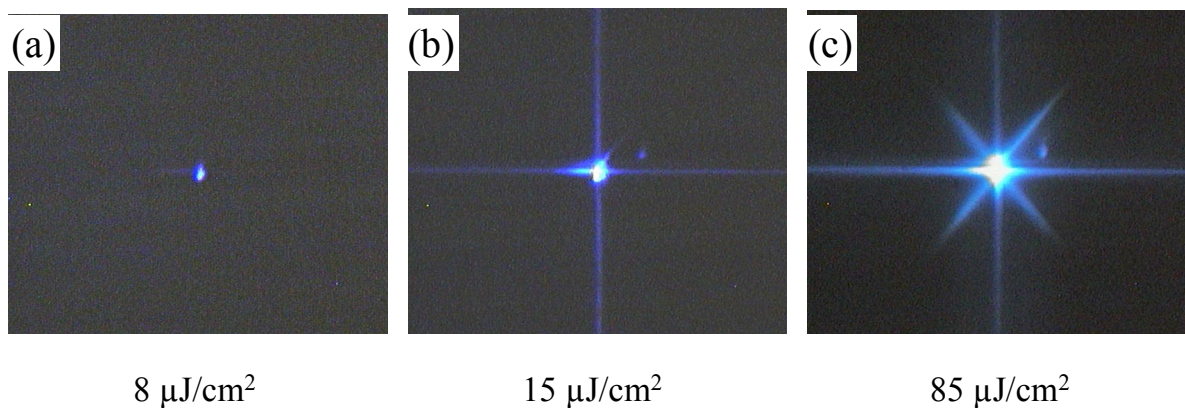


Fig. 6.4: Evolution of the far-field emission pattern of the 2D-DFB laser with increasing excitation fluence from (a) to (c) The images are (false-color) photographs of a screen placed in front of the laser.

6.3 Laser modes of 2D-DFB lasers

Since the refractive index contrast in organic 2D-DFB structures is comparatively weak, the photon dispersion relation $\omega(|\mathbf{k}|)$ is nearly linear. Therefore the laser modes can be determined in a Laue-type formulation of Bragg scattering of the 2D photonic crystal by application of the following procedure:

Elastic Bragg scattering couples waves with wavevectors \mathbf{k} , \mathbf{k}' having the same energy $E(\mathbf{k}) = E(\mathbf{k}')$. The resulting constructive interference of waves in an optically amplifying medium can lead to positive feedback and the formation of a laser mode, which is characterized by its effective propagation constant $\mathbf{K} = 1/2(\mathbf{k} + \mathbf{k}')$. In a surface emitting DFB laser some fraction of the laser light is coupled out of the surface via $k_0 \sin \varphi = |\mathbf{k} - \mathbf{G}|$. Therefore every laser mode can be identified in the far-field by its characteristic in-plane wavevector components. When all possible laser modes have been determined, one can look for the mode(s) with the lowest laser threshold.

To establish a laser mode at a given pump level, three conditions have to be fulfilled simultaneously:

- (i) The photon energy $E(\mathbf{k})$ has to be located within the spectral region of gain.
- (ii) Positive feedback requires that \mathbf{k} fulfills the Laue condition $\mathbf{k} \cdot \mathbf{G}_{mn} = 1/2 |\mathbf{G}_{mn}|^2$, with $\mathbf{G}_{mn} = \begin{pmatrix} m 2\pi/\Lambda_z \\ n 2\pi/\Lambda_x \end{pmatrix}$ being a reciprocal lattice vector. In other words \mathbf{k} and $\mathbf{k}' = \mathbf{k} - \mathbf{G}_{mn}$ have to be located on a Bragg plane of the reciprocal lattice (see e.g. ¹³³).
- (iii) The threshold gain for the specific mode has to be exceeded.

In Fig. 6.5 (a) the reciprocal lattice of the 2D-DFB structure is shown as black dots. Since the refractive index contrast induced by the modulation is rather low, one can assume that the photon dispersion is given by the $E(\mathbf{k})$ -relation of an unperturbed planar waveguide. The shaded gray ring indicates the \mathbf{k} -vectors of photons having an energy in the spectral region of optical gain in the MeLPPP-waveguide (condition (i)). The relevant Bragg planes (Bragg-lines in 2D) for the square lattice are marked by the solid green, solid/dotted red lines (condition (ii)). At the intersections of the gain region with the Bragg planes conditions (i) and (ii) are fulfilled simultaneously. The corresponding plane waves form lasing modes, provided that the modal gain is sufficiently high. The \mathbf{k} -vectors of such waves are emphasized by the thicker parts of the red and green lines.

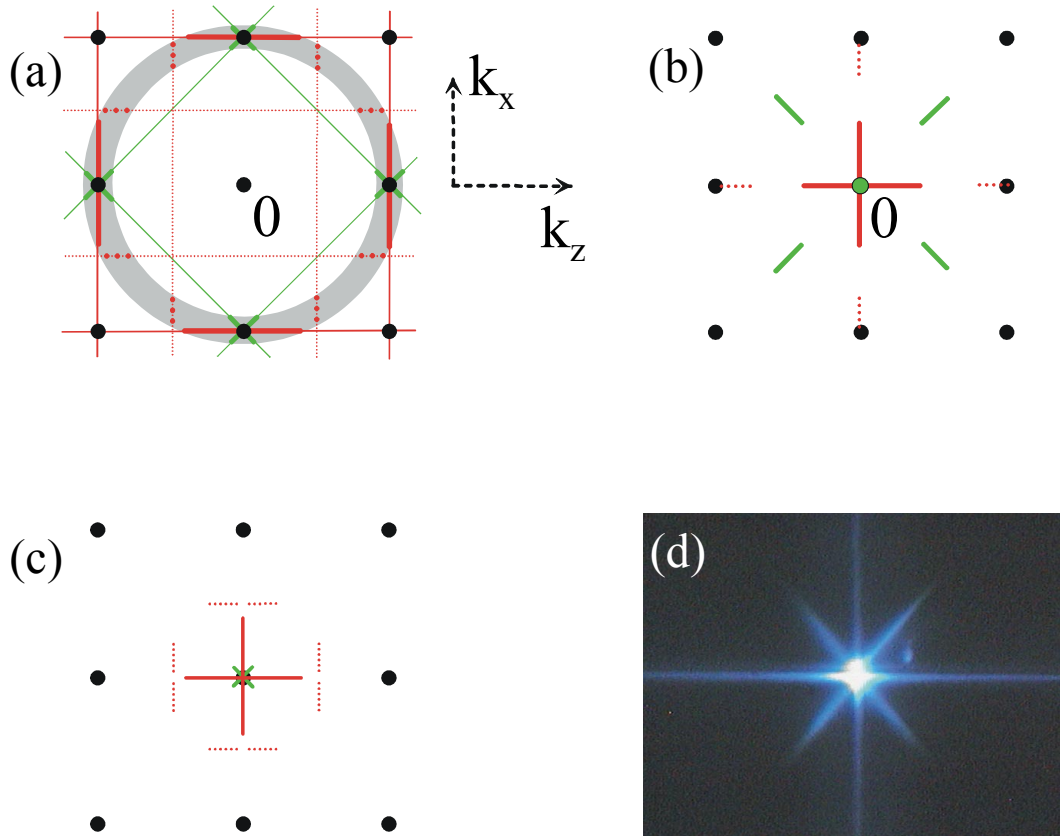


Fig. 6.5: (a) reciprocal lattice of a two-dimensional square lattice (black dots). The different lines depict the Bragg lines, the various solutions of the Laue condition (equation 2-16). The shaded area represents the \mathbf{k} -vectors of waves which can be amplified during propagation in the MeLPPP film (gain region). (b) Effective propagation vector of the modes formed by superposition of the resonant waves. (c) In-plane components $k_{0,z}$, $k_{0,x}$ of the radiated modes in the far-field. (d) Experimentally observed far-field emission pattern of the 2D laser for excitation far above threshold.

Accordingly, three contributions to in-plane positive feedback can be identified:

- Intersections of the gain region with the horizontal and vertical $\{2\ 0\}_1$ Bragg lines (solid red line) corresponding to $\mathbf{G}_{mn} = \{2\ 0\}_1$ ¹⁵.
- Intersections of the gain region with the $\{1\ 1\}_1$ Bragg-lines (solid green lines).
- Additionally, the $\{1\ 0\}_1$ Bragg-lines (dotted red lines) intersect with the gain region.

Laser modes are generally formed by the superposition of at least two coupled waves. For each of the three above mentioned contributions the corresponding effective propagation vector, given by $\mathbf{K} = 1/2(\mathbf{k} + \mathbf{k}')$, is displayed in Fig. 6.5 (b). The significance of this picture can be visualized as follows: A mode with $K_z=0$, $K_x \neq 0$ forms a standing wave pattern in z -direction which moves in x -direction with a speed determined by K_x . The higher the value of $|\mathbf{K}|$, the faster the mode is moving in the z - x -plane. If the gain region has only a limited spatial extension fast moving modes have a comparatively short dwell time in the gain region. Accordingly, the laser threshold will scale with $|\mathbf{K}|$.

¹⁵ A set of equivalent (rotation by 90°) reciprocal lattice points \mathbf{G}_{mn} is collectively addressed as $\{m\ n\}$. The corresponding Bragg-lines are denoted as $\{m\ n\}_1$

At $\mathbf{K}=0$ the situation is more complicate. This is due to the fact that at the four equivalent high symmetry points $\mathbf{G}_{mn} = \{1\ 0\}$ three Bragg lines intersect. All the corresponding waves with $\mathbf{k} = \{1\ 0\}$ are coupled to each other by single and by multiple Bragg scattering. This gives rise to a true two-dimensional optical feedback and results in an enhanced feedback for the mode formed from these four waves. The observation of a non-polarized emission, the reduced threshold and the increased efficiency are direct consequences of the true 2D laser operation.

6.3.1 Far-field identification of laser modes

A partial fraction of the intensity contained in the resonator is continuously coupled out via an additional Bragg scattering process that transfers energy from the 2D-waveguide modes to radiation modes. Based on equation 2-17 the resulting far-field emission pattern can be used to identify those lasing modes which oscillate for a given excitation condition. Considering that the relevant grating vectors are $\mathbf{G} = \{1\ 0\}$ the in-plane components of the radiated waves are represented by the pattern shown in Fig. 6.5 (c). Indeed, the far-field emission at high excitation conditions (Fig. 6.5 (d)) fits well to the pattern predicted by the analysis.

The various features of the far-field pattern can be attributed to the laser modes. In the order of appearance with increasing excitation one finds:

- for a rather broad range of excitation fluences ($5.6\ \mu\text{J}/\text{cm}^2 < E_p < 9.4\ \mu\text{J}/\text{cm}^2$) a monomode laser beam is emitted perpendicular to the substrate ($k_{0,x} = k_{0,y} = 0$), resulting from the 2D laser operation at $\mathbf{k} = \{1\ 0\}$ (see Fig. 6.4 (a)).
- the horizontal and vertical laser lines in the image of Fig. 6.4 (b) arise from waves on the $\{2\ 0\}_1$ Bragg lines.
- the diagonal laser lines appearing in Fig. 6.4 (c) originate from waves on $\{1\ 1\}_1$. The distinctly higher threshold indicates weaker coupling than for the $\{2\ 0\}_1$ Bragg lines.
- laser modes due to scattering at $\mathbf{G} = \{1\ 0\}$ are not observed. Because of their large value of $|\mathbf{K}|$ a high laser threshold is expected for these modes and condition (iii) is not fulfilled.

6.3.2 Factors favoring monomode operation

The diffraction-limited emission resulting from monomode operation is obviously a very attractive property of 2D-DFB lasers. It is therefore interesting to analyze the factors leading to monomode operation and to explore how the dynamic range of monomode emission can be extended. Three factors favoring monomode operation can be identified:

6.3.2.1 Vanishing effective propagation constant

The analysis of the 2D-laser modes (Fig. 6.5 (b)) shows that in monomode operation a standing wave pattern is formed which is stationary in space ($\mathbf{K} = 0$). The energy contained in the mode is therefore confined inside the excited region for a long time. In contrast, lateral modes have a non-vanishing effective propagation vector \mathbf{K} . Photons in these modes move out of the excited region within a couple of roundtrips through the cavity. The maximum gain length is therefore limited for lateral modes.

It is obvious that this criterion can not be responsible for mode selection in the given 2D-DFB structure. Firstly, the same argument applies to the corresponding 1D-DFB lasers where no lateral monomode operation was observed, not even at threshold. Secondly, the spectrum of lateral modes is continuous and centered around $\mathbf{K} = 0$. The effective propagation constant of lateral modes can therefore be arbitrarily small resulting in a negligible difference of the gain length. Thirdly, there is a substantial energy loss due to radiation. Radiation loss affects all modes and may well exceed losses due to the mode walk-off by some orders of magnitude. Although the effect of the vanishing effective propagation is not relevant in the present structure, it is possible to design structures where its effect is very large¹⁴².

6.3.2.2 Enhanced coupling

In the analysis of the laser modes it was found that four plane waves at $\mathbf{k} = \{1\ 0\}$ were coupled to each other by single and by multiple Bragg scattering via $\mathbf{G} = \{2\ 0\}$ and $\mathbf{G} = \{1\ 1\}$. The coupling strength is therefore higher than it is in the comparable 1D structure where only single Bragg scattering via $\mathbf{G} = \{2\ 0\}$ is possible. As a result the coupling coefficient, κ , is larger than in the 1D structure. According to equation 2-23 the threshold gain is inversely proportional to κ^2 . The enhanced coupling at the intersections of several Bragg lines therefore translates into a reduced threshold for the corresponding mode, an enhanced efficiency for this single mode, and a clear discrimination against concurring lateral modes.

The threshold reduction depends on the relative strength of the contributing Bragg scattering mechanisms. In the present structure the predominant coupling is one-dimensional via $\mathbf{G} = \{2\ 0\}$. This is seen from the fact that the emission of the 2D laser is dominated by two weakly coupled orthogonal resonators over a wide range of excitation densities (Fig. 6.4 (b)).

Cross-coupling between these two resonators is induced by $\mathbf{G} = \{1 \ 1\}$. An increased cross-coupling would enhance the discrimination of lateral modes.

Anyway, the sheer presence of Bragg scattering by $\mathbf{G} = \{1 \ 1\}$ is in contradiction to the coupled mode analysis of Toda and Han^{142,144}. They predicted that Bragg scattering by $\mathbf{G} = \{1 \ 1\}$ should not occur for TE waves in a square lattice. Two arguments are given: firstly the incidence angle with respect to the scattering plane is 45° , which is very close to the Brewster angle for low index contrast. Secondly, the scattered TE wave would have to propagate exactly parallel to the direction in which the \mathbf{E} -field of the incident wave oscillates. Whereas this does not occur in conventional structures, quantum electrodynamics predicts that it can happen in a photonic crystal²²⁶. A coupled mode analysis is obviously not sufficient to describe the behavior of 2D-DFB lasers comprehensively. More advanced simulations in the form of photonic band structure calculations are required (see Section 0).

Nevertheless, the arguments described above can help to optimize the performance of 2D-DFB lasers: larger cross coupling and, hence, a larger discrimination of the lateral modes is expected if the refractive index contrast of the modulation is enhanced. Alternatively one could select a triangular grating, where three resonators, tilted by 60° , are coupled to each other. In principle, the cross coupling contribution would also be higher in TM polarization, however, it is difficult to design a structure where the threshold is lower for TM than for TE modes.

6.3.2.3 Gain enhancement in photonic crystal lasers

The formation of photonic bandgaps in 1D- or 2D-DFB lasers is associated with a vanishing group velocity $v_{group} = d\omega/dk$ just outside the bandgap. In 1D-DFB lasers it has further been shown that the modes near the bandgap have the lowest gain threshold. According to an intuitive explanation these photons are multiply reflected, travel a very long optical path through the active region and, hence, acquire a large gain²²⁵. A more fundamental description is given by cavity quantum electrodynamics: if the gain medium is not in free space its spontaneous emission rate (equation 2-1) as well as its spectral shape will be modified by a factor proportional to the local density of photon modes $D(\omega)$ ²²⁷. A sharp peak in the density of modes will therefore enhance the spontaneous emission rate and, according to equation 2-10, also enhance the gain (see e.g.²²⁸).

In an infinite, purely 1D system the density of modes shows a van Hove singularity at all band extrema. In a finite structure the singularities are directly related to the group velocity via $D(\omega) \propto 1/v_{group}$ ²²⁷. In contrast, $D(\omega)$ does not diverge at the band extrema of a 2D periodic structure but has a step-discontinuity. A vanishing group velocity is therefore not a sufficient criterion for the observation of gain enhancement in 2D DFB-lasers. Instead, it was found for a number of structures that strong gain enhancement can occur at saddle points of the dispersion relation if the band becomes essentially flat^{227,229-232}. It is important to note that gain-enhancement, used in these distributed feedback-like bandedge lasers, does not demand

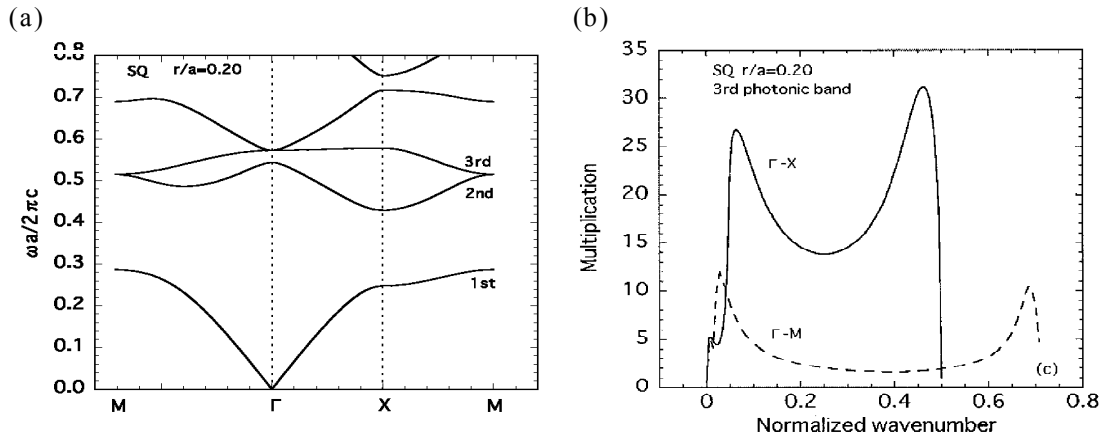


Fig. 6.6: (a) TM-band structure of a square-lattice photonic crystal, consisting of dielectric cylinders surrounded by air. The third band in Γ -X direction is exceptionally flat. (b) Direction dependence of the gain enhancement for the third band in Γ -X and Γ -M direction. (Taken from ²³² and ²³³)

for a high dielectric contrast, unlike the threshold reduction in defect-mode photonic bandgap lasers (see Section 2.3.3.3).

For a square lattice an especially large gain enhancement for TE and TM modes was predicted in the vicinity of the Γ -point of the 3rd Γ -X band ^{231,232}. Fig. 6.6 (a) shows the band structure for a square lattice of dielectric cylinders in air. The third photonic band is very flat and, consequently, a large gain enhancement is calculated. Fig. 6.6 (b) shows that the gain enhancement is anisotropic favoring modes at the Γ - and at the X-point.

Transferring the results of the band structure analysis, presented in the reduced zone scheme, to the extended zone scheme of our analysis, one finds that the 3rd band in Γ -X direction corresponds to the $\{2\ 0\}_1$ Bragg line in the vicinity of $\mathbf{k} = \{1\ 0\}$. Whereas the absolute amount of gain enhancement in the 2D structure is not necessarily higher than in an equivalent 1D structure, the directionality of the gain-enhancement is peculiar to 2D ²³². Although the structure considered by Susa has a much higher refractive index contrast, it is possible to transfer the results to the 2D-DFB laser: gain-enhancement owes to the sheer presence of a periodicity and not to the amount of the refractive index contrast.

6.4 Photonic band structure analysis

As seen in the previous section a calculation of the photonic band structure is a very powerful tool for the investigation of the behavior of 2D-DFB lasers. However, the incorporation of gain is very difficult and even the calculation of passive 3-dimensional structures demands for a high computational effort.

In a first approach the photonic band structure of our 2D-DFB lasers is calculated assuming a passive, completely two-dimensional structure with infinite extension in y -direction. The three-dimensional modulation of the waveguide is then represented by a spatial variation of the effective refractive index. Since the variation of n_{eff} is not precisely known an approximate function has to be found. The Ansatz for n_{eff} has to account for the relevant Bragg scattering processes, namely Bragg scattering by $\mathbf{G} = \{2\ 0\}$ and $\mathbf{G} = \{1\ 1\}$. The corresponding modulation of n_{eff} is a superposition of four modulations: one in x -direction, one in z -direction plus two contributions tilted by 45° . It can be written as

$$n_{eff}(x, z) = n_{eff}^0 + \Delta n^{\{2\ 0\}} [\cos(4\pi x/a) + \cos(4\pi z/a)] + \Delta n^{\{1\ 1\}} \left[\begin{array}{l} \cos\left(\frac{2\sqrt{2}\pi\sqrt{x^2 + z^2} \cos(\arctan(z/x) - \pi/4)}{a}\right) \\ + \sin\left(\frac{2\sqrt{2}\pi\sqrt{z^2 + y^2} \sin(\arctan(z/x) - \pi/4)}{a}\right) \end{array} \right] \quad (6-1)$$

A physically reasonable form of $n_{eff}(x, z)$ should somehow resemble the real corrugation of the waveguide. Varying the ratio between $\Delta n^{\{2\ 0\}}$ and $\Delta n^{\{1\ 1\}}$ it is found that a negative of the substrate corrugation (Fig. 6.1) can be obtained for $\Delta n^{\{2\ 0\}} \approx -10 \cdot \Delta n^{\{1\ 1\}}$. The absolute amount

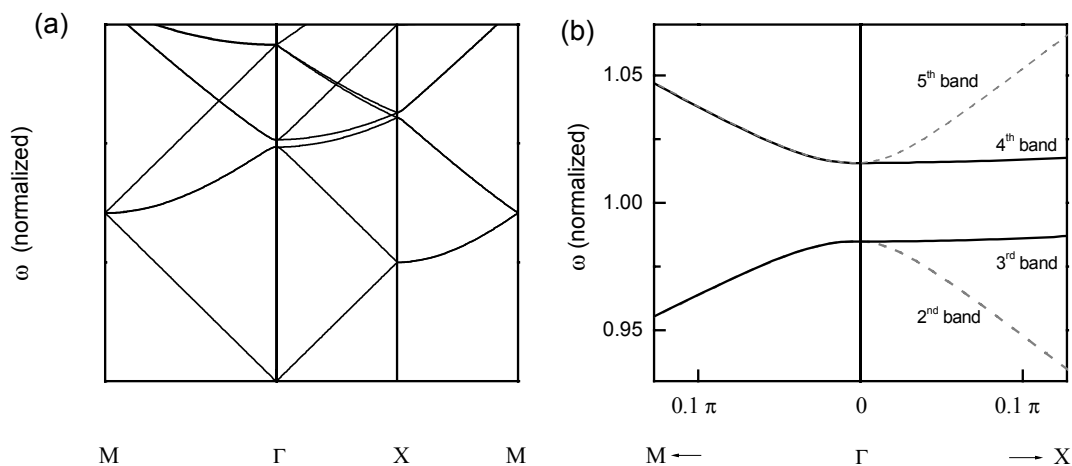


Fig. 6.7: (a) Bandstructure of the 2D photonic crystal assuming a sinusoidal variation of the refractive index. (b) Close-up of the 2nd to 5th band in the vicinity of the Γ -point. In the chosen normalization the X-point of the 1st band has the coordinates $(\pi, 0.5)$.

of $\Delta n^{\{2,0\}} \approx 0.15$ can be estimated from the coupling coefficient of a 1D-DFB laser via equation 2-20.

Fig. 6.7 shows the calculated band structure for TE polarization¹⁶ assuming $n_{eff}^0 = 1.63$, $\Delta n^{\{2,0\}} = 0.05$, $\Delta n^{\{1,1\}} = -0.005$, and $a = 600$ nm. In the calculation the values of Δn are deliberately exaggerated by a factor of 2 to 5 in order to magnify the effect. As expected a bandgap arises between the 3rd and 4th band at the Γ and at the M-point. The close-up of the band structure in the vicinity of the 2nd to 5th band at the Γ -point shows, that the 3rd band in Γ -X direction is more or less flat, the prerequisite for gain-enhancement in a photonic crystal laser. Furthermore it is seen that the slope is much steeper in the Γ -M direction than in Γ -X.

The fact that the 2D-DFB laser modes can be spatially separated in the far-field, can be used to investigate the photonic band structure of a 2D photonic crystal. In Fig. 6.8 the photonic band structure of a 2D-DFB laser is determined from spatially resolved far-field spectra. The 3rd photonic band in Γ -X direction and the 2nd to 5th band in Γ -M direction can be identified. Their dispersion relation in the vicinity of Γ can be measured with the technique introduced in section 5.3. Good qualitative agreement between the experimental data (Fig. 6.8 (c)) and the calculated bandstructure (Fig. 6.7) is observed. A more detailed analysis, however, requires a more reliable ansatz of $n_{eff}(x, z)$ or a full three-dimensional treatment of the wave propagation. Such an analysis is currently in progress.

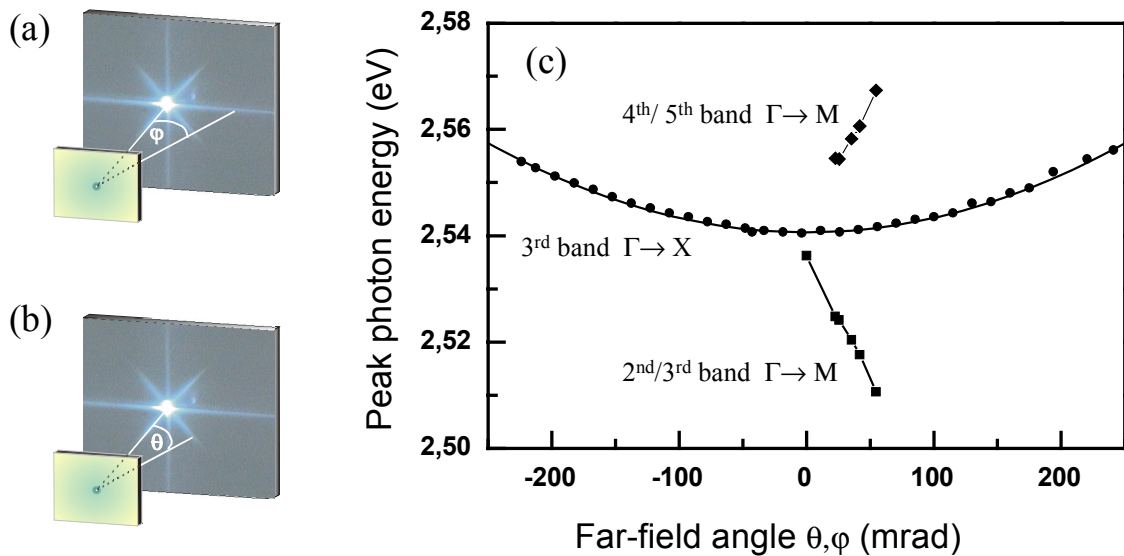


Fig. 6.8: The leaky modes of the 2D-photonic band structure can be investigated in the far-field laser emission. For that purpose laser spectra are recorded as a function of the emission angle relative to the surface normal. (a) Schematic setup for the investigation of the 3rd band in Γ -X direction, (b) 2nd to 5th band in Γ -M direction. (c) Peak position of the laser line as a function of the emission angle. The addressable frequency range of the band structure is determined by the spectral width of the polymer gain spectrum.

¹⁶ The calculation was performed with a program provided by Dr. K. Busch, Institute for Theory of Condensed Matter, University of Karlsruhe, Germany. A plane wave expansion technique is used (see e. g. ³⁶).

7 Lasers with randomly distributed feedback

Using a self-assembly technique colloidal monolayers are grown on glass substrates from an aqueous solution of monodisperse polystyrene beads. Laser emission is observed from a film of Alq₃:DCM evaporated onto these templates. Investigation of the laser emission reveals that resonant feedback occurs due to the formation of closed loop cavities in strongly scattering waveguides.

In recent years, there have been substantial efforts to study disordered media that both scatter and amplify light. When the scattering is weak, scatter centers embedded in the gain medium enhance the path of light within the active medium and result in an efficient amplification of spontaneously emitted photons (ASE)^{181,183,234-236}. Therefore it was not by chance that gain narrowing from a solid conjugated polymer film was first demonstrated in a sample containing TiO₂ particles⁸⁶. Although these samples showed a well-defined threshold and spectral narrowing, discrete laser lines indicating resonant feedback were missing. The experiments could therefore be explained by light diffusion with gain, where interference effects can be neglected and resonant feedback does not occur^{171,178,237-240}. Nevertheless the demonstration of weak localization of light^{172,173} and, in 1997, also of Anderson localization^{174,175,241} revealed that interference becomes important when the scattering strength is further increased.

In the meantime it has been discovered that lasing with resonant feedback can occur in scattering media exhibiting either exceptionally high gain¹⁶⁵⁻¹⁶⁷ or a disorder close to the value required for Anderson localization¹⁵⁵⁻¹⁶⁴. Sufficiently large scattering can be achieved, for instance, in powdered laser crystals, in mixtures of dyes with colloids¹⁶⁴, or in colloidal crystals soaked with laser dyes^{154,165-169}. In some of these cases it was, however, not clear whether the observed resonances are truly due to random closed loops or rather due to other forms of feedback such as reflections at the boundaries of the active medium.

Although theoretical predictions indicate that geometries with reduced dimensionality should allow to establish resonant feedback for a comparatively low amount of scattering (see Section 2.3.4), only few experimental studies deal with appropriate thin film waveguide structures^{156-158,165-167}. In the following random lasing in thin film waveguides containing intentionally added scatter centers is demonstrated. Resonant feedback is observed although the scattering mean free path is considerably larger than the light wavelength.

7.1 Sample preparation and characterization

The random lasers used within the course of this work are formed by evaporation of a ~ 400 nm thick Alq_3 :DCM film onto a glass substrate that is decorated with a monolayer of polystyrene beads. A cross-section of the sample is sketched in Fig. 7.1 (b). The Alq_3 :DCM film has a higher refractive index ($n_f \approx 1.7$) than the surrounding media consisting of glass ($n_s \approx 1.45$), polystyrene ($n_{PS} \approx 1.57$), and air so that a multilayer waveguide is formed which is capable to guide the light emitted from Alq_3 :DCM under optical excitation. The polystyrene beads embedded in the waveguide are densely packed and serve as scatter centers, due to the refractive index contrast between polystyrene and Alq_3 :DCM.

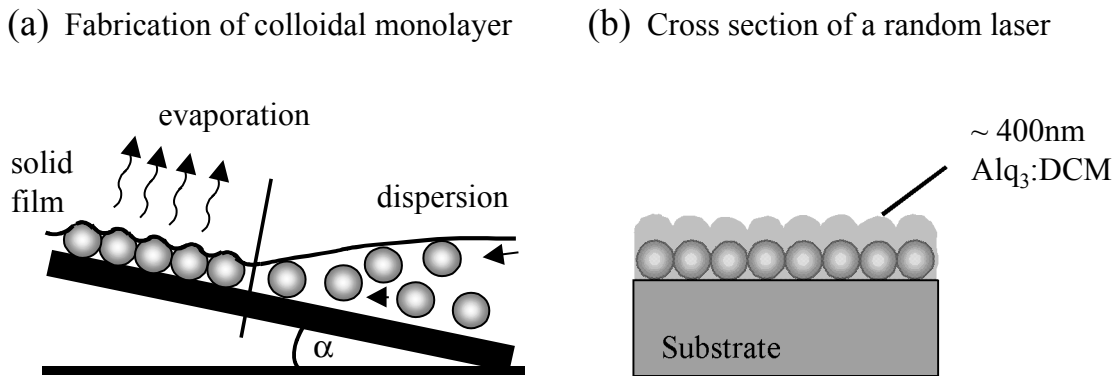


Fig. 7.1: (a) Technique for the self-assembled growth of colloidal monolayers on a glass substrate. Nucleation seeds develop at the meniscus of the drying solution due to attractive lateral capillary immersion forces. The interplay of evaporation and attractive forces determines the growth of the monolayer^{242,243}. (b) The random laser is finished by evaporation of a thin film of Alq_3 :DCM onto the colloidal monolayer.

Colloidal monolayers consisting of monodisperse, nanometer-sized polystyrene (PS) beads were fabricated²⁴⁴ using the self assembly technique sketched in Fig. 7.1. The PS beads are dispersed in an aqueous solution stabilized by negatively charged SO_4^- groups attached to the surface of the colloids. A drop of the solution containing 0.25 vol% of PS beads is spread over a hydrophilic glass substrate¹⁷ and subsequently slowly evaporated at a controlled temperature and moisture. The two-step process leading to the formation of a monolayer of hexagonally arranged colloids was investigated by Nagayama with the help of a microscope and an attached video camera^{247,248}. If the wetting of the sample is good and the sample is tilted by an angle α the solution forms a meniscus at the top edge of the sample²⁴⁹. As soon as the thickness of the remaining water film is in the order of the bead diameter attractive forces establish, the so called lateral capillary immersion forces^{243,250,251}, and pull the beads

¹⁷ Self-assembly of colloids from an aqueous solution requires a hydrophilic surface. For that reason glass substrates are placed for 60 minutes in a solution of NaOH:ethanol (1:9 by weight)²⁴⁵, rinsed with Milli-Q H_2O , and subsequently tempered at 585 °C for 330 minutes²⁴⁶.

towards each other thus forming small aggregates of PS beads. In the following the interplay of evaporation and capillary forces lead to a constant convective flow of solvent and particles towards the meniscus. The particles are attached to the seeds, and a colloidal monolayer grows.

Fig. 7.2 (a) shows a photograph from a glass substrate covered with a thin polycrystalline layer of colloids. Two extended areas with green and orange iridescence can be clearly distinguished with a well defined interface between them. The green iridescence can be identified as the Bragg reflection from a polycrystalline colloidal monolayer, the orange iridescence stems from areas where a double-layer of colloids is formed^{252,253}.

After deposition of the Alq₃:DCM film¹⁸ the surface is very rough so that the waveguide formed by the multilayer exhibits strong losses. The area relevant for random lasing is at the upper edge of the sample where many nucleation center started to grow simultaneously. Fig. 7.2 (b) shows an AFM image of a 20*20 μm² sized area. In the chosen color code the PS beads appear bright yellow on a gold/brown substrate. It is clearly seen that the colloids aggregate to small clusters, which are densely packed but well separated and randomly oriented. In the middle of the sample, where the monolayer is closed, the light-scattering is so strong that no amplified spontaneous emission was observed from the waveguide, not even at the highest available excitation densities.

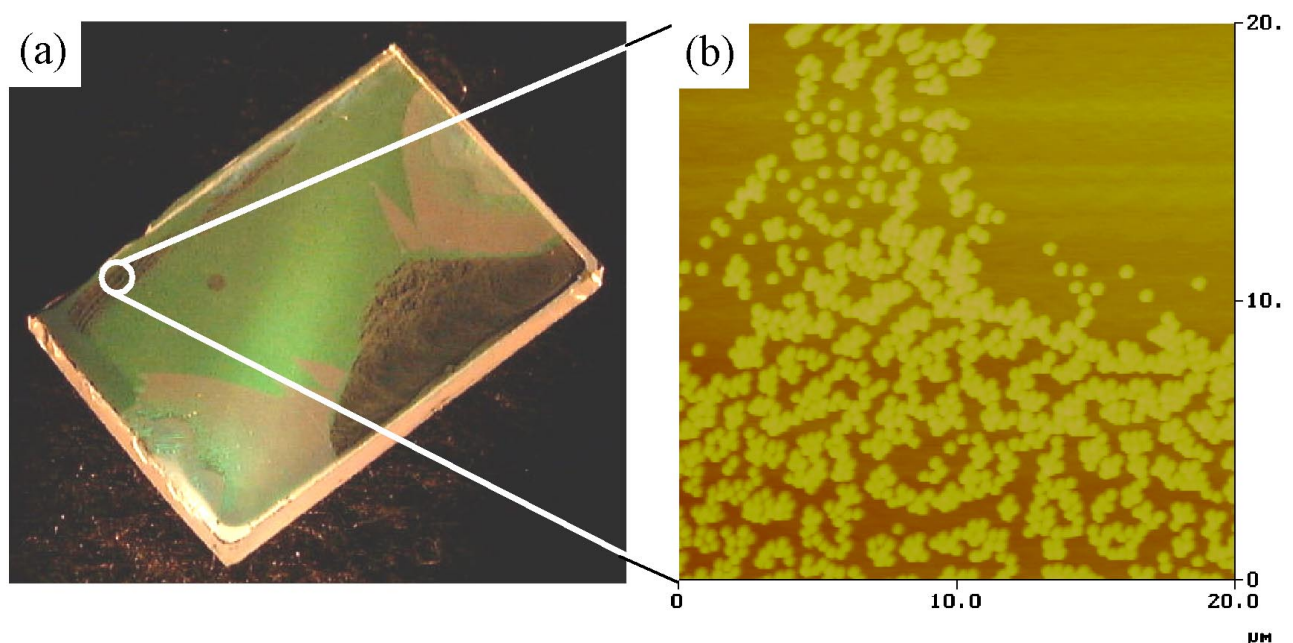


Fig. 7.2: (a) Photograph of a sample containing a colloidal monolayer that is illuminated with white-light. The monolayer is indicated by green iridescence. (b) AFM image showing the area at the top of the sample where the nucleation started. The monolayer is not (yet) closed, instead the polystyrene beads are agglomerated to well separated, densely packed clusters.

¹⁸ The Alq₃:DCM layers were made by A. G. Mückl, Lehrstuhl Experimentalphysik II, Universität Bayreuth.

7.2 Random laser operation

The fact that laser action occurs due to resonant feedback in random closed loops can be shown unambiguously by the following facts (see section 2.3.4.2): (1) strong scattering is observed. (2) Above a threshold excitation discrete peaks evolve in the emission spectrum, their spectral width being significantly smaller than the linewidth observed in ASE experiments. (3) These resonances can be attributed to localized laser modes with a well defined resonator length. Since the modes are localized the mode pattern is different at every point of the sample. From the determined length of the resonator length feedback mechanisms other than random closed loops can be excluded. (4) The number of modes increases with increasing gain or excitation area. (5) For a given excitation area there is a maximum number of modes. (6) As long as the extension of the excitation area is in the order of the resonator loop, the laser threshold decreases when the excitation area is increased.

In order to check that all of the above facts are valid in our samples emission spectra were recorded for various excitation conditions. In the first set of experiments a circular spot with a diameter of $\sim 125 \mu\text{m}$ was excited. The spot size and the location on the sample were held constant whereas the pump fluence –and hence the gain- was varied (see Fig. 7.3 (a)). In the second experiment a narrow stripe with a width of $\sim 50 \mu\text{m}$ was excited. Here the fluence was held constant whereas the length of the stripe –and hence the excitation area- was varied (see Fig. 7.3 (b)).

(a) variation of the excitation fluence

(b) variation of the excited area

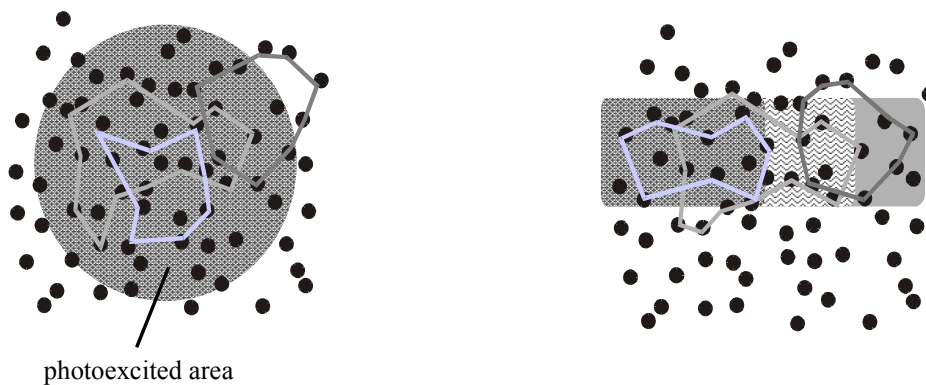


Fig. 7.3: Excitation conditions for the investigation of random lasers. The black dots represent randomly distributed scatter centers, the shaded area indicates the excitation area. Three possible random closed loop cavities are indicated for (a) a variation of excitation fluence in a fixed excitation spot and (b) a variation of the excitation area.

7.2.1 Variation of the excitation density

Fig. 7.4 shows the evolution of the emission spectrum of a random laser for increasing excitation density (from bottom to top). In this experiment the pump beam is focused to a circular spot of 125 μm diameter. The dash-dotted line shows the smooth photoluminescence of $\text{Alq}_3\text{:DCM}$ below threshold. Above an excitation fluence of $\sim 1500 \mu\text{J}/\text{cm}^2$ narrow emission lines emerge. The linewidth of these resonances is below 1 nm and is an order of magnitude lower than the spectral half-width of amplified spontaneous emission (ASE) in $\text{Alq}_3\text{:DCM}$ (see Fig. 4.6). The narrow lines are therefore attributed to laser modes formed by resonant feedback. At the wavelength of such a narrow line the emission intensity rises super-linearly with increasing excitation density, just as expected for a laser. This effect is displayed in the inset of Fig. 7.4, where the relative intensity at two wavelengths is compared for a number of excitation fluences. Whereas the intensity ratio is constant at low excitation fluences it rises steadily above a threshold value. When the excitation density is increased further above threshold more and more peaks evolve as a gradually increasing number of laser modes exceed threshold. Above a second threshold, however, the number of modes seems to saturate. A further increase of the excitation density merely results in an increasing intensity for a limited number of modes. At the same time the contrast between adjacent maxima and minima increases steadily.

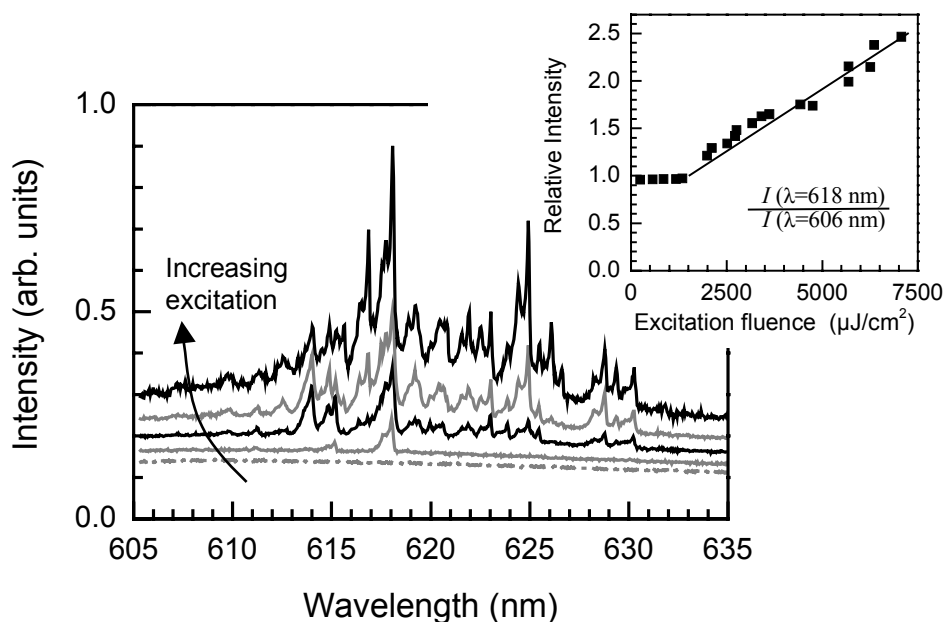


Fig. 7.4: Emission of a random laser for increasing excitation density from bottom to top (1350 - 5700 $\mu\text{J}/\text{cm}^2$). The inset shows the relative intensity at two wavelengths (strongest laser mode at $\lambda = 618 \text{ nm}$; no resonance at $\lambda = 606 \text{ nm}$) as a function of the excitation fluence.

Obviously, a limited number of resonant laser modes is sufficient to deplete the gain in the entire photopumped area and to suppress all the competing stimulated emission processes. In contrast, ASE or an infinitely growing number of modes would result in a smoothing of the emission spectrum. Since the diffusion length of the electronic excitations is negligible on the scale of the spot diameter such a behavior can only be explained if few resonant cavities cover the entire excitation spot. The roundtrip path length L_{RT} will therefore be in the order of several tens to hundred microns. From the fact that the threshold pump fluence is a factor of 100 higher than the threshold of a second order DFB laser it is immediately obvious that the resonant cavities suffer from high losses.

As will be seen in 7.2.2, a qualitatively similar behavior is found at various positions along the edge of the monolayer and also on several samples with a different thickness of the Alq₃:DCM layer. The mode pattern, however, is distinctive for each position or sample. Therefore it can be concluded that the resonances are due to simultaneous operation of several resonant cavities which are localized at distinct positions and extend over several microns.

A closer investigation of the emission spectra can reveal the path length of the resonant loops. The condition for resonant feedback is given by the fact that the phase change in a single roundtrip must be a multiple of 2π , or in other words $n_{eff}L_{RT}/\lambda = m$. A single resonator with an optical roundtrip length $n_{eff}L_{RT}$ results in a number of evenly spaced resonance frequencies c/λ . Vice versa, the optical path length of the various resonant loops contributing to the random laser operation can be determined from a Fourier transform (FT) of the emission spectrum. If the emission intensity is plotted against $1/\lambda$ in units of μm^{-1} then the conjugate variable is simply the optical pathlength in units of μm ²⁵⁴. A closed loop path with a well defined value of $n_{eff}L_{RT}$ should therefore be indicated by a peak in the FT. Well pronounced resonances in the emission spectrum typically derive from low-loss cavities where some fraction of the light travels several roundtrips through the cavity. Accordingly it should be possible to identify higher harmonics of $n_{eff}L_{RT}$ in the FT.

Fig. 7.5 shows the FT of the emission spectra belonging to the lowest and highest excitation density shown in Fig. 7.4. The discrete spacing of the FT is $11.4 \mu\text{m}$, determined by the finite width of the spectrum¹⁹. The gray dash-dotted line is the FT of the Alq₃:DCM photoluminescence. Apart from the peak at DC (only positive counts in the spectrum) no significant resonances are observed. In contrast, the FT at high excitation density contains several resonances below a pathlength of $300 \mu\text{m}$. The strong resonances below $100 \mu\text{m}$ can not be resolved due to the coarse step width. Nevertheless, there is a well resolved peak at an optical pathlength $n_{eff}L_{RT} \approx 300 \mu\text{m}$ for which two higher harmonics at $600 \mu\text{m}$ and $900 \mu\text{m}$ can be identified. Using a typical value for n_{eff} the corresponding resonator length L_{RT} is $\sim 200 \mu\text{m}$.

¹⁹ Although the discrete step resolution of the FT could be improved measuring a wider spectrum, doing so adds only redundant information. Due to the effect of the waveguide efficient amplification occurs only within a finite spectral width; here between 610 nm and 630 nm . No resonances are observed outside this range.

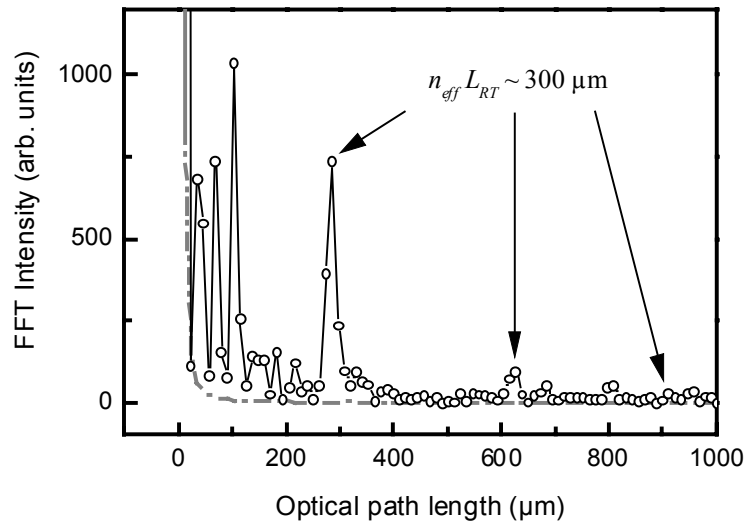


Fig. 7.5: Fourier transform of the emission spectra (plotted against $1/\lambda$) for excitation below (dash-dotted line: $1350\mu\text{J}/\text{cm}^2$) and above the laser threshold (open circles: $5700\mu\text{J}/\text{cm}^2$). A peak in the FT indicates a resonant cavity with the corresponding optical path length.

Which feedback processes could lead to a resonator length of $200\mu\text{m}$ in our structures? Fabry-Perot resonances can be excluded, since there are no reflecting surfaces separated by $100\mu\text{m}$. As seen in the previous chapters on 1D-DFB lasers the effective resonator length of a DFB laser is in the order of $100\mu\text{m}$. In this case, however, resonant feedback due to a photonic-crystal like collective reflection from the Bragg planes of a colloidal crystal can be excluded. Firstly, the Laue condition can not be fulfilled for the given bead diameter and emission wavelength, secondly, the single crystalline domains are much too small ($\leq 5\mu\text{m}$) to establish a resonator within a single domain.

The absence of conventional resonators suggests that feedback is indeed due to multiple scattering at randomly distributed scatter centers. The formation of random closed loops might be further supported by the presence of strong gain (see Section 2.3.4.2). The question is whether scattering in the given structure is strong enough to support this explanation. Unfortunately the typical experiment for the determination of the mean free path l^* , namely the measurement of the coherent backscattering cone under (nearly) normal incidence, fails in the case of waveguides whose thickness is smaller than l^* . Therefore a rough estimation is needed.

From Mie theory the scattering cross-section and the angular distribution of the scattered intensity can be calculated for a single PS bead surrounded by $\text{Alq}_3\text{:DCM}$ ²⁰. A scattering cross-section of $\sigma_{\text{Scatter}} \approx 0.013\mu\text{m}^2$ is calculated. The scattering probability for a single bead embedded in a waveguide is estimated to 0.055, determined by the ratio of σ_{Scatter} to the corresponding waveguide cross-section of $0.236\mu\text{m}^2$. Accordingly a light wave would on

²⁰ The calculations were performed with a commercial program (MQMIE 2.3, Dr. Michael Quinten, Wissenschaftlich-Technische Software).

average be scattered at every 18th PS bead. Since the beads are not densely packed (Fig. 7.2) the mean free path is certainly larger than the diameter of 18 PS beads, i.e. $l^* > 5.6 \mu\text{m} \approx 9 \lambda$. This is still lower than the critical value for resonant feedback reported by Cao¹⁵⁹. A resonator loop of 200 μm would on average consist of 35 individual scattering events, similar to the value estimated by¹⁶⁶. Obviously every scattering event causes a loss of intensity, either out of the loop or even out of the waveguide. Nevertheless, Mie calculations further predict that the angular distribution of the scattered intensity is peaked around an angle of 0° and, hence, a large fraction of the scattered light stays confined within the waveguide for a considerable number of scattering events. Keeping in mind that the gain between two consecutive, average spaced scattering events can be as large as $\exp(g_{Alq_3:DCM} \cdot l^*) \approx 1.5$ it appears reasonable that the scattering losses can be overcome.

In summary, it has been shown that our samples exhibit very strong scattering. Therefore resonant closed loop cavities are formed by multiple light-scattering, resulting in the evolution of discrete, narrow peaks in the emission spectrum at high excitation densities. From a Fourier transform loop lengths of up to 200 μm could be identified. Because of the large extension of these loops only a limited number of resonant loops can be established within a certain excitation area. To unambiguously attribute these findings to random lasing, it remains to be shown that the emission spectrum varies across the sample. Furthermore an increasing excitation area should lead to a decreasing laser threshold and an increasing number of modes.

7.2.2 Variation of the excitation area

In a second experiment the excitation density is held at a constant value, whereas the excitation area is varied (see Fig. 7.3 (b)). This is done by focusing the excitation beam to a 50 μm wide stripe whose length is varied between 200 μm and 1000 μm by razor blades. The width of the stripe is slightly smaller than the diameter of a typical loop with a circumference of 200 μm . Furthermore special care is taken to verify that the excitation density does not increase with increasing excitation area. In order to collect the emission from the entire spot, these experiments were performed with a wider monochromator entrance slit resulting in a lower spectral resolution than in the previous experiment.

Fig. 7.6 shows various emission spectra recorded at a pump fluence of 435 $\mu\text{J}/\text{cm}^2$. Below a stripe length of 300 μm a smooth photoluminescence spectrum is observed. Increasing the stripe length gradually above 300 μm a steadily increasing number of modes develops. The evolution of the mode pattern is, however, qualitatively different to the previous experiment. If the excitation *density* is varied the same modes dominate all spectra, but if the excitation *area* is increased each spectrum contains different modes. For a growing excitation area there is no saturation in the number of modes. These observations are easily explained by the fact that more and more closed loop paths are covered by the excitation spot and subsequently exceed their laser threshold (see Fig. 7.3 (b)). For an infinitely extended spot the number of

modes would be arbitrarily large resulting in a smooth spectrum whose substructure is completely leveled out¹⁶⁵.

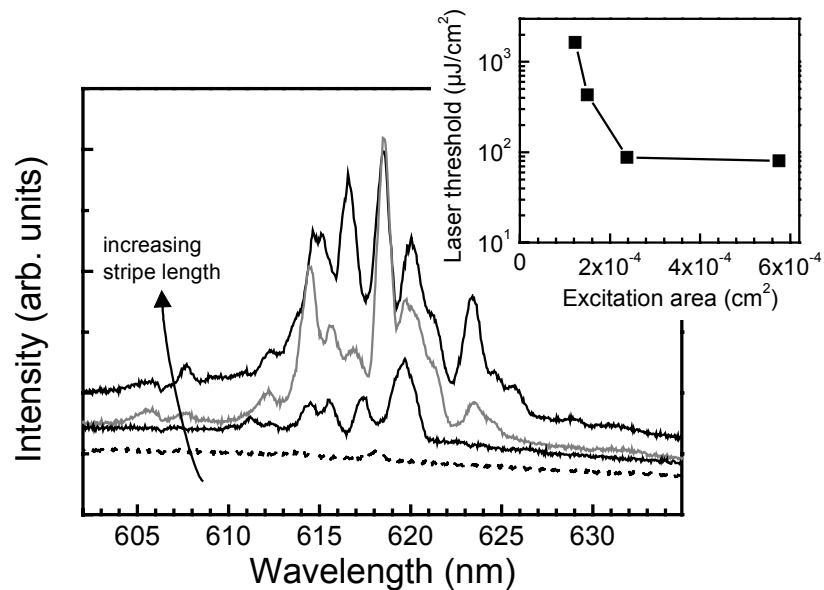


Fig. 7.6: Emission of a random laser for constant excitation density but increasing excitation area. The excited spot is a narrow stripe with $50 \mu\text{m}$ width and a length of 310, 370, 490, and $1150 \mu\text{m}$ (from bottom to top). The pump fluence is $435 \mu\text{J}/\text{cm}^2$. The inset shows the dependence of the laser threshold on the area of the excited spot.

The inset of Fig. 7.6 shows the variation of the laser threshold with increasing excitation area. As long as the excitation area is comparable to a typical loop area the laser threshold is comparatively high due to the fact that –by chance– only a fraction of a resonant loop is excited. With increasing excitation area the threshold pump fluence decreases and finally saturates if –again by chance– one random closed loop is entirely located inside the photopumped area.

8 Emission dynamics

The dynamics of amplified spontaneous emission and lasing in disordered organic semiconductors is investigated. Single-pulse transform-limited emission is demonstrated for 2D-DFB lasers made from MeLPPP. The dynamics of the composite system Alq₃:DCM is dominated by gain switching oscillations due to the interplay of energy transfer and stimulated emission. In planar waveguides oscillations with a frequency up to 0.2 THz are observed. In the corresponding DFB laser the oscillation frequency is reduced.

Despite the fact that organic semiconductor lasers have been investigated for several years, comparatively little is known about their emission dynamics^{107,201,255}. Nevertheless, a detailed understanding of the emission dynamics is important for the optimization of the laser resonator itself. The mode selection in multimode lasers, for instance, is governed by the fact that all partaking modes compete dynamically for the same gain on a ‘first come, first serve’ basis²⁵⁶.

The emission dynamics of a laser is, in nature, an interplay of the stimulated emission provided by the organic semiconductor material with the feedback governed by the laser resonator. To be able to distinguish between these two effects, first the emission dynamics of the plain material is investigated before looking at the respective DFB lasers. Alq₃:DCM is taken as a representative of the composite material blends, whereas the conjugated polymer MeLPPP stands for the genuine materials.

8.1 Polymer lasers

8.1.1 ASE in slab waveguides

Amplified spontaneous emission in thin films of a conjugated polymer has been intensively studied in the past few years. The underlying process was revealed by detailed investigations of the population and emission dynamics together with quantitative modeling of the emission process^{37,93-100}.

The most important findings in the context of lasers can be summarized as follows: after excitation with a femtosecond laser pulse the population of the emitting state rises more or less instantaneously, reaching its maximum within less than 1 ps³⁷. On a similar time-scale also the polarization of the excitation pulse is lost¹⁹⁷. Following the build-up of the population density photons are emitted spontaneously, some of which are coupled into the slab waveguide formed by the polymer-substrate/air heterostructure. Gain narrowing of the emission spectrum is observed if the excitation density is sufficiently high that the gain due to stimulated emission exceeds the losses owing to scattering.

Fig. 8.1 shows the emission transient of a 300 nm thick film of MeLPPP at a wavelength of 490 nm for various excitation densities below and above the threshold for ASE. At the lowest excitation fluence the rise and decay of the emission are mono-exponential with a decay time of $\tau \approx 25$ ps. The maximum is reached 2 ps after the excitation. Above the threshold for ASE ($\sim 23 \mu\text{J}/\text{cm}^2$) both rise and decay of the photon density are clearly bi-exponential. From the fact that all transients coincide after a time delay of ~ 15 ps, it can be concluded that all excitations exceeding the threshold value are depopulated within one single short burst of amplified spontaneous emission. Owing to the time required for the photon propagation through the excited area, the emission maximum is delayed relative to the maximum of the excitation density³⁸.

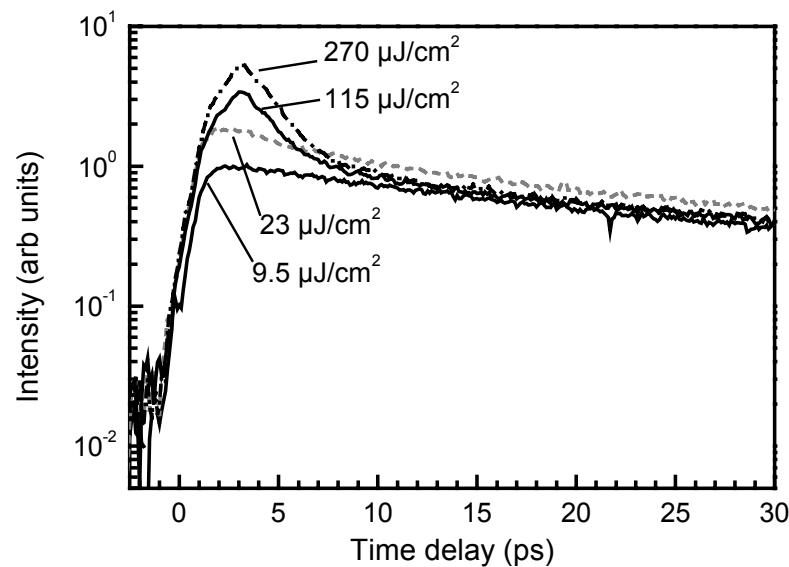


Fig. 8.1: Emission transients of a MeLPPP film ($d_f=290$ nm on a PET substrate) at the wavelength of maximum stimulated emission ($\lambda = 490$ nm).

8.1.2 Lasing dynamics

In Chapter 6 the time integrated performance of surface-emitting 1D- and 2D-DFB lasers made from MeLPPP was discussed. For 1D-DFB lasers lateral multimode operation was observed at all excitation levels exceeding threshold. The 2D-DFB lasers exhibit a lower laser threshold and show true monomode operation for a range of excitation levels close above threshold. The differences between 1D- and 2D lasers were attributed to an additional coupling mechanism in 2D-DFB lasers resulting in an enhanced coupling strength.

On the other hand, the dynamic response of a DFB laser is governed by its coupling coefficient^{139,257,258}. The build-up of intensity after pulsed excitation is governed by the modal gain coefficient²⁵⁷, whereas the trailing edge of the pulse is governed by the cavity loss coefficient, α_{Loss} . Since both the modal gain and the cavity loss vary with the coupling coefficient, the different coupling strength in 1D- and 2D-DFB lasers should be observable in

their emission dynamics. Vice versa, the coupling coefficient of a DFB laser can be determined from the emission dynamics. The magnitude of the cavity loss coefficient, for instance, can be directly related to the exponential decay time of the intensity after pulsed excitation via ¹³⁹

$$\tau_{cav}^{-1} = \frac{c}{n_{group}L} \left(2 \left(\frac{\pi}{|\kappa|L} \right)^2 + \alpha_{Loss}L \right). \quad (8-1)$$

8.1.2.1 1D-DFB lasers

Fig. 8.2 shows emission transients of a second order 1D-DFB laser for several excitation levels above the laser threshold ($\sim 7.5 \mu\text{J}/\text{cm}^2$). At the lowest excitation pump fluence the laser operates just above threshold. Therefore the corresponding net gain is quite low and the laser needs considerable time to switch on. Because of the low signal to noise ratio no significant increase of the output power can be observed earlier than 6 ps after the excitation pulse. The maximum intensity is reached after a time delay of 10 ps when the gain due to stimulated emission is at equilibrium with the output loss. Thereafter the intensity stored in the laser cavity decays exponentially with a cavity decay time of $\tau_{cav} \approx 2.0$ ps. Using equation 8-1 a loss coefficient of 31 cm^{-1} is calculated.

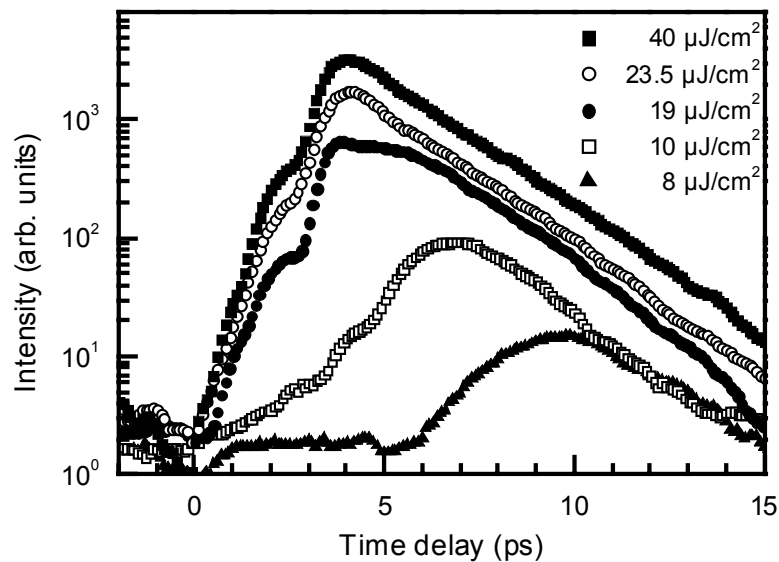


Fig. 8.2: Transient of the surface emission of a 2nd order 1D-DFB laser for various excitation densities. The sample is excited with a 150 fs long pulse at the time 0 ps. The laser threshold is reached with a fluence of $7.5 \mu\text{J}/\text{cm}^2$. The experimental noise level is at an intensity of 10^0 . Because of the low signal to noise ratio at the lowest excitation densities the transients have been smoothed with a low pass Fourier filter.

If the excitation fluence is increased beyond the threshold the emission rise time decreases significantly due to the increased gain coefficient. The decay time, on the other hand, has a constant value so that the maximum intensity is reached at earlier times. The minimum pulse width of $\Delta t = 2.3$ ps (FWHM) is observed at an excitation fluence of $40 \mu\text{J}/\text{cm}^2$.

It is worthwhile to note that in DFB lasers the maximum intensity is reached after a considerably longer time delay than in ASE experiments. In a planar waveguide there is no feedback and the photons make only one single pass through the excitation spot. With a spot diameter of $150 \mu\text{m}$ and a group refractive index of 1.75 the time required for such a single pass is only 0.87 ps. Accordingly, the maximum intensity is reached within approx. 1 ps after the maximum in the excitation density. In a DFB laser, however, it takes up to 10 ps until the maximum intensity is reached. In a simplistic picture, one can assume that photons are multiply reflected during their way through the DFB resonator²²⁵. As a full roundtrip through the cavity would take ~ 1.7 ps, the time delay of 10 ps corresponds to 5 to 6 full cavity roundtrips.

A peculiar phenomenon of the laser kinetics are the superimposed oscillations with a period of ~ 2 ps. Most clearly they are seen in the leading edge of the transients at high excitation densities. Whereas oscillations with a period of the cavity roundtrip time are observed in the onset of lasers with reflecting facets²⁵⁹ such oscillations are unusual for DFB lasers without reflecting facets. As it can be ruled out that the oscillations are merely experimental artifacts²¹ they are most likely caused by photon propagation effects: photon propagation is not properly accounted by the conventional rate equation model of DFB laser dynamics. A detailed modeling of the emission dynamics of organic semiconductor photonic crystal lasers is still in progress²².

8.1.2.2 2D-DFB lasers

Fig. 8.3 shows emission transients for a 2D-DFB laser at several excitation densities above the laser threshold of $5.6 \mu\text{J}/\text{cm}^2$. The qualitative behavior is similar to the 1D-DFB laser. Nevertheless, there are some substantial differences. It was noted above that the laser threshold of the 2D-DFB laser is lower. Therefore it is not surprising that the peak emission of the 2D laser is higher and occurs at earlier times if both devices are excited at comparable excitation densities. At comparable excitation densities the 2D-laser is simply driven further above its threshold than the 1D analogy and exhibits a higher net gain. Surprisingly, however,

²¹ The oscillations are present in the raw data and not result of the Fourier filter. Reflections in the light-path of excitation and gate pulse can be ruled out because of the absence of oscillations in the measurement of the cross-correlation (Fig. 3.5) and ASE (Fig. 8.1). Reflection of the excitation pulse from the backside of the sample contain only $\sim 1\%$ of the incident intensity and unlikely to cause such strong effects.

²² In cooperation with A. Klaedte and Prof. O. Hess, DLR Stuttgart. Preliminary results on the photonic band-structure are published in²²⁰.

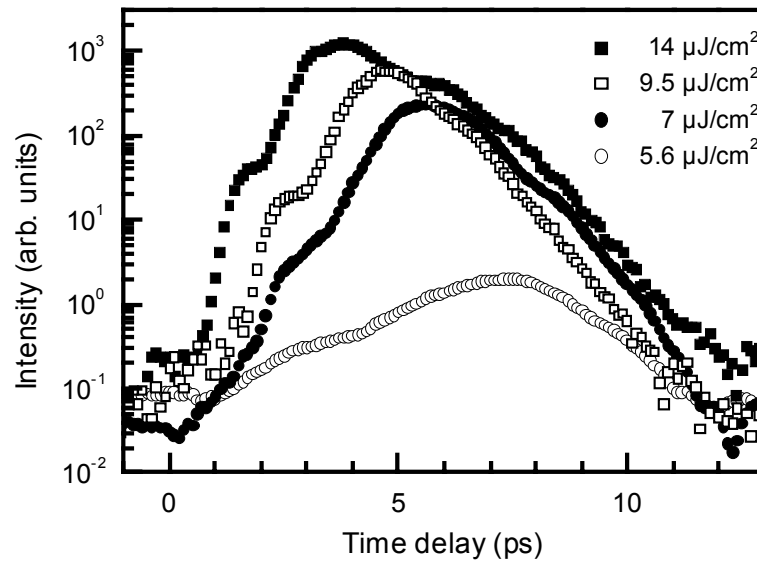


Fig. 8.3: Emission transients of a 2D-DFB laser for various excitation densities. The laser threshold is approx. at $5.6 \mu\text{J}/\text{cm}^2$. The lowest two transients are smoothed by a low-pass Fourier filter, the original noise level is at an intensity of 10^{-1} .

the same is true if both devices are driven by the same amount above their laser threshold. This is demonstrated by Fig. 8.4 where the emission of a 1D- and a 2D-DFB laser are compared when both are excited at a pump fluence of $E_p \approx 1.25 E_{th}$: the 2D-laser switches on faster, although its material gain, g , and its excess gain, $g-g_{th}$, are lower than in the 1D-laser. Another intriguing observation is that the decay of the intensity occurs with a decay time of $\tau_{cav} \approx 0.9 \text{ ps}$, i.e. on a distinctly faster time-scale than in the 1D laser²³. Radiation loss coefficients of 65 cm^{-1} (2D-DFB) and 31 cm^{-1} (1D-DFB) are calculated from equation 8-1. Hence, one arrives at the peculiar conclusion that the 2D-DFB laser has the lower laser threshold, although it suffers higher losses.

The seeming contradictions are explained by the feedback mechanism of the 2D-DFB laser. The additional Bragg scattering process mentioned in Chapter 0 results in an enhanced coupling coefficient. Higher coupling reduces the laser threshold according to equation 2-23. In the language of photonic crystal lasers, the threshold reduction owes to gain enhancement for the mode at the high-symmetry point. Following the argument of Kovac et al.²⁵⁷ the enhanced gain, in turn, results in a faster dynamic build-up of intensity than in any other laser mode. As a consequence, the entire inversion is depleted before other (lateral) modes with a lower modal gain can evolve. Thus the dynamic evolution of the photon density helps to establish and stabilize monomode operation in 2D-DFB lasers.

²³ Owing to the fast rise and decay, the oscillations are highly pronounced and the decay is not truly singly exponential.

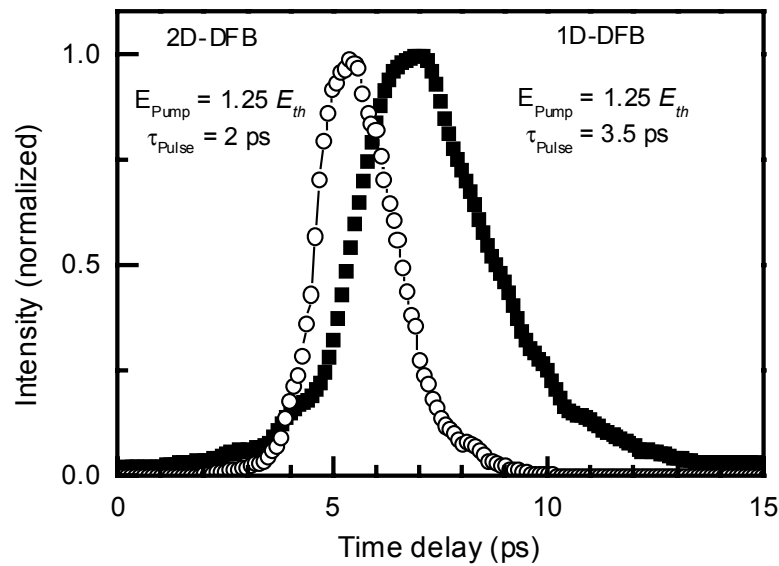


Fig. 8.4: Normalized emission transients for a 1D- and a 2D-DFB laser at a pump fluence of $1.25 E_{th}$. As shown in chapter 0 the 2D-DFB laser operates in a single mode, in contrast to the 1D-DFB laser.

The pulses emitted by the 2D-DFB laser in monomode operation are as short as $\Delta t = 1.9$ ps. The transform-limited linewidth²⁴ calculated from the cavity lifetime is 0.21 nm, which coincides almost exactly with the measured spectral half-width of the 2D-DFB laser. In multimode operation the pulse duration rises slightly to $\Delta t \approx 2.3$ ps. Thanks to the superior performance of distributed feedback lasers, the pulse duration is shorter than in lasers made from the same material yet with a conventional two-mirror cavity²⁶⁰.

Briefly, a surface-emitting 2D-DFB laser generates a pulsed, diffraction-limited laser beam with transform-limited picosecond pulses.

²⁴ the transform-limited spectral linewidth (FWHM) of an excited state with lifetime τ is given by $\Delta\omega = 1/\tau$.

8.2 Emission dynamics in Alq₃:DCM

The high excitation density dynamics of the emission process in the composite system Alq₃:DCM is strongly influenced by the energy transfer from the initially photoexcited Alq₃ to the DCM molecules. It was found that the onset of amplified spontaneous emission from DCM molecules is time delayed due to the preceding energy transfer. For higher excitation densities the interplay between filling of the emitting states and the collective stimulated emission leads to ultrafast oscillations, both in the transient population and in the emission³⁹. Since the energy transfer is the basis for an understanding of the laser dynamics the relevant experiments are briefly reviewed. Thereafter it will be shown that the ASE dynamics can be simulated with a spatio-temporal rate equation model. The emission dynamics of Alq₃:DCM lasers is investigated experimentally and interpreted with the help of the consolidated findings for ASE.

8.2.1 Gain switching oscillations in slab waveguides

In Fig. 4.6 it was shown that the emission spectrum of thin films of Alq₃:DCM exhibit significant gain narrowing at high excitation densities. To study the dynamics of the excited state population and of the emission two complementary time-resolved techniques are employed: Pump-probe transients monitor the excited state population of the DCM-molecules while emission transients are measured with a temporal resolution of ~ 2 ps using an optical Kerr gate setup containing a CS₂-cell⁹³. A comparison of the pump-probe transients measured at the spectral position of stimulated emission in DCM ($\lambda_{probe} = 635$ nm) and a direct time resolved measurement of the DCM-emission detected at 630 nm for the same excitation conditions are shown in Fig. 8.5. The pump-probe data are shown on the left hand side while the transient emission is depicted on the right hand side.

Just above the threshold for ASE, at an excitation fluence of $93 \mu\text{J}/\text{cm}^2$, the population of the DCM molecules rises slowly and reaches a maximum after approximately 20 ps²⁵. While the (non-amplified) spontaneous emission of DCM is below the detection limit of the time-resolved emission measurements an emission-burst due to ASE is observed in the temporal window between 15 to 35 ps after the initial excitation. At higher pumping levels the threshold for the emission of an ASE-burst is reached at earlier times. This is clearly seen in the emission transients on the right hand side of Fig. 8.5. The time delay between the pump pulse and the onset for the (first) burst of ASE decreases with increasing pump pulse energy. For higher excitation densities ASE leads to a significant ultrafast depopulation of the DCM molecules. This can be seen directly in the pump-probe transients on the left-hand side. For increasing excitation densities a maximum is reached more and more rapidly followed by a picosecond depopulation due to ASE.

²⁵ In accordance with the values found in ultrafast studies of Foerster-type excitation transfer in blends of conjugated polymers²⁶¹⁻²⁶³.

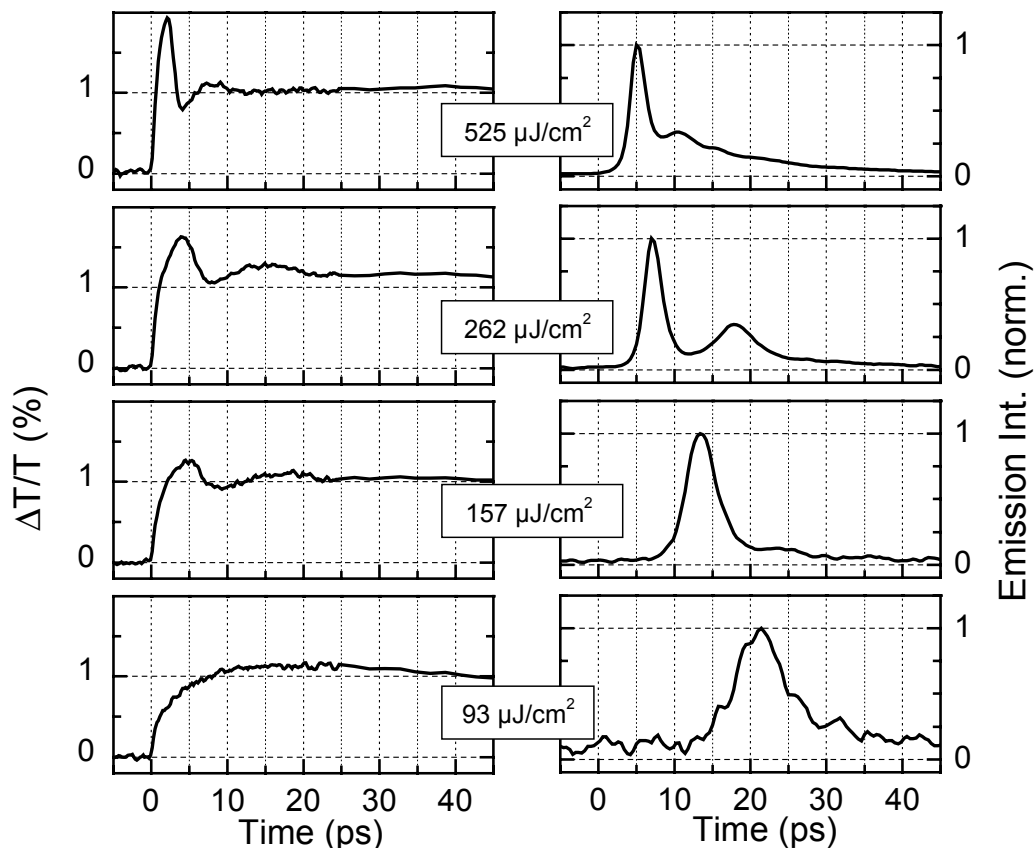


Fig. 8.5: Left: Pump-probe transients of Alq₃:DCM for various excitation levels. The pump pulse has a wavelength of 400 nm while the probe pulse is spectrally located at 635 nm. At this wavelength optical amplification due to stimulated emission by DCM-molecules is observed. Right: Emission transients at 630 nm after photoexcitation at 400 nm. The transients are measured with the technique of optical Kerr-gating. The zero of the time-axis is defined by the leading edge of the emission at the highest excitation density. Taken from ³⁹.

At a pump fluence of $262 \mu\text{J}/\text{cm}^2$ the first burst of ASE is terminated after less than 10 ps, i.e. well before all excitations are transferred from Alq₃ to DCM. After depopulation of the DCM states by the first ASE burst the DCM manifold can be populated a second time to a value above the threshold for ASE. A second, weaker, ASE-burst can evolve and is observed with a time delay of ~ 10 ps after the first burst. With increasing excitation intensity the time delay between the bursts decreases; the oscillation frequency rises to approx. 0.2 THz.

The pump pulse energy dependent delay of the emission burst and the oscillatory transient is similar to the relaxation oscillations which are observed during the switch-on processes in a variety of lasers ²⁰⁹. In typical laser relaxation oscillation, the filling of the emitting states through continuous pumping and their depopulation due to stimulated emission compete with each other, leading to an oscillatory behavior of both the inversion and the density of emitted photons. In this case the situation is related, but qualitatively different, since neither a resonator is present nor is there a continuous pumping scheme. The series of emission bursts is mainly determined by the temporal evolution of the gain in the material given by the density of excited DCM molecules. This density is determined by the competition between

“pumping” by energy transfer from excited Alq₃ molecules and depopulation by ASE. Additionally, the geometry of the photoexcited area affects the dynamics.

For a quantitative understanding of the experimental results numerical simulations of the emission dynamics in this composite system using a model that accounts for the dynamics of the spatially dependent densities of excited states in the two molecular species and the photon density. For any given position (x,y) in the excited area, a spatio-temporal system of coupled rate equations has to be solved. A system of rate equations is adapted that has been previously used to describe ASE in conjugated polymer films³⁷. The effect of photon propagation is explicitly included in this model.

First the evolution of the density of excited states $N_{Alq}(x,y)$ in Alq₃ is considered. Following pulsed excitation, the density of excited states in Alq₃ decays due to intrinsic deactivation processes or via energy transfer to DCM. The corresponding equation reads

$$\frac{\partial N_{Alq}}{\partial t} = - \left(\tau_{Alq}^{-1} + \frac{(N_{DCM}^{\max} - N_{DCM})}{N_{DCM}^{\max}} \tau_{transfer}^{-1} \right) N_{Alq} , \quad (8-2)$$

where τ_{Alq} denotes the excited state lifetime in Alq₃ and $\tau_{transfer}$ is the time constant for the excitation transfer from Alq₃ to DCM. At low excitation conditions the density of excited DCM molecules, N_{DCM} , is always distinctly lower than the total density of DCM molecules in the film, N_{DCM}^{\max} . The energy transfer then has a simple exponential time dependence²⁶. At high pumping levels, however, a considerable part of the DCM molecules is excited. Assuming that there is no energy transfer from Alq₃ to *excited* DCM molecules the transfer rate decreases with increasing ratio N_{DCM}/N_{DCM}^{\max} . This effect is considered by the prefactor of $\tau_{transfer}$. The corresponding rate equation for the density N_{DCM} of excited DCM molecules reads:

$$\frac{\partial N_{DCM}}{\partial t} = \frac{(N_{DCM}^{\max} - N_{DCM})}{N_{DCM}^{\max}} \tau_{transfer}^{-1} N_{Alq} - \tau_{DCM}^{-1} N_{DCM} - \frac{c}{n_{group}} \int \sigma_{SE} N_{DCM} M d\lambda d\varphi . \quad (8-3)$$

The last term on the right hand side describes the process of stimulated emission. It couples the local excitation density N_{DCM} with $M(x,y,\varphi,\lambda,t)$ being the number of photons per volume, per propagation angle in direction $\vec{u}(\varphi)$, and per wavelength λ . σ_{SE} is the (wavelength dependent) cross-section for stimulated emission in DCM. The rate equation for the photon density $M(x,y,\varphi,\lambda,t)$ is then given by

$$\frac{\partial M}{\partial t} = - \frac{c}{n_{group}} \vec{u}(\varphi) \nabla_{x,y} M + \Gamma_{sp} \tau_{spont}^{-1} \frac{1}{2\pi} f(\lambda) N_{DCM} + \frac{c}{n_{group}} \sigma_{SE} N_{DCM} M , \quad (8-4)$$

where the first term on the right side describes the photon propagation in the direction $\vec{u}(\varphi)$, the second term considers the spontaneous emission, and the last term describes stimulated

²⁶ A simple Förster transfer would cause a $1/r^6$ -dependence of the transfer rate on the distance between the (immobile) molecules (equation 2-5). However, at room temperature the excitons in Alq₃ are mobile. As the exciton diffusion length of 20 nm exceeds the typical Foerster radius⁶⁵, a constant transfer rate appears more realistic²⁶¹.

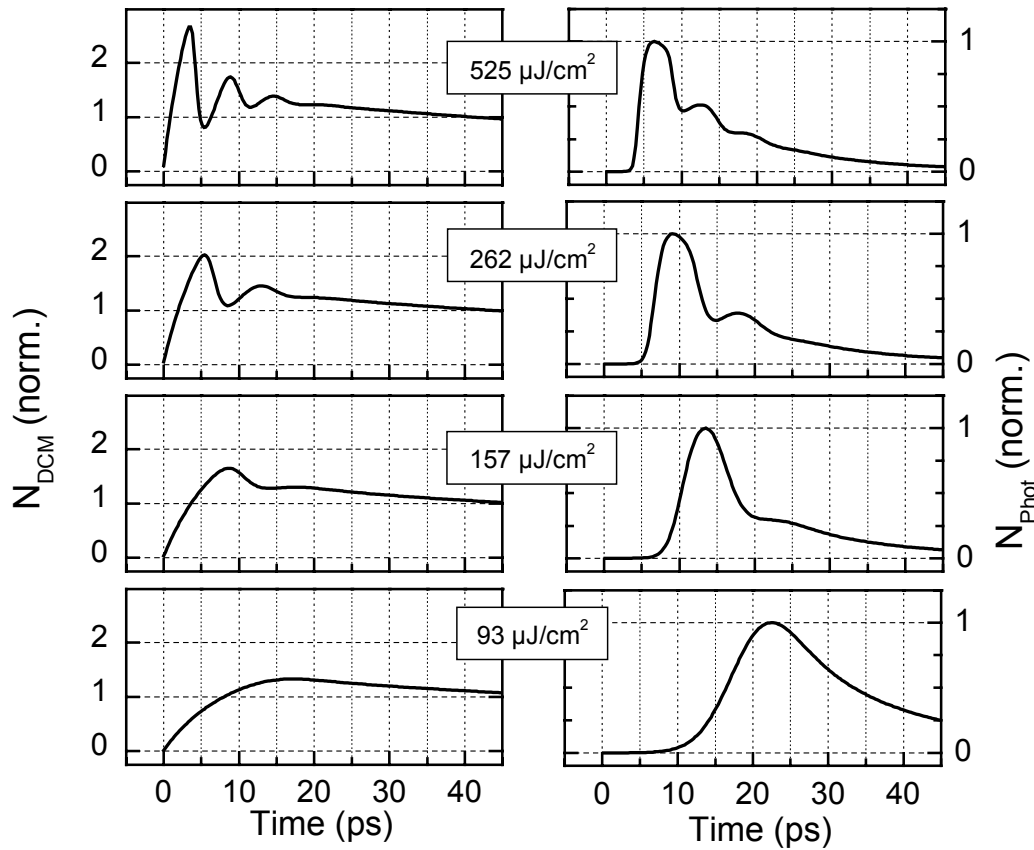


Fig. 8.6: Left: Calculated transient population of the DCM-molecules. Right: Calculated total transient number of emitted photons. A system of rate equations as described in the text is used to model the excitation and emission dynamics in Alq₃:DCM.

emission. Γ_{sp} is the probability that a spontaneously emitted photon is coupled into the waveguide and $f(\lambda)$ is the normalized lineshape function of the spontaneous emission from DCM.

In the calculation the lifetime τ_{DCM} of DCM has been set to 4 ns²¹⁰ while the nonradiative lifetime was assumed to be 1 ns in order to match a lifetime of 800 ps as measured in time resolved emission measurements at low excitation levels. The transfer time was adjusted to $\tau_{transfer} = 9.5$ ps so that pump probe transients below the ASE threshold could be fitted. Using these parameters and taking into account the excitation conditions, both the transient population as well as the total number of emitted photons can be calculated. The numerical data are shown in Fig. 8.6.

All main experimental observations are reproduced by the calculated curves. ASE sets in when the pumping level exceeds a threshold value. It leads to a burst of stimulated emission and a rapid depopulation of the excited states. For the lowest pump level (93 $\mu\text{J}/\text{cm}^2$) ASE only depopulates a small part of the excited states while the emission transient is already dominated by the ASE-burst. The calculated curves clearly reflect the increasing relevance of ASE for higher intensities. If the decreasing transfer rate due to filling of the DCM states is included in the calculation the oscillatory behavior of the population and the emission can be well reproduced. In contrast, the simulated transients do not match the experiment if the effect of state filling is ignored. In that case the frequency of the simulated oscillations is distinctly

higher than in the experiment. Hence, filling of the acceptor states prolongs the resonant energy transfer in Alq₃:DCM at high excitation densities.

In conclusion, the organic composite semiconductor Alq₃:DCM shows an unusual collective emission behavior under high excitation conditions. The energy transfer from photoexcited Alq₃ to DCM leads to a pumping level dependent delay between a femtosecond pump pulse and the amplified spontaneous emission. At high excitation densities the interplay between the energy transfer and ASE generates a series of picosecond emission bursts, similar to the relaxation oscillations in conventional lasers. Simultaneously the excitation transfer is slowed down by filling of the DCM states.

8.2.2 DFB-lasers

The time-integrated operation of Alq₃:DCM lasers was characterized in detail in section 5.2. Fig. 8.7 shows the emission transient of a 2nd order DFB laser with a film thickness of 180 nm²⁷. Similar to the case of ASE on a planar substrate the laser output shows a classic gain-switched characteristic which consists of a single optical pulse at low excitation fluence and multiple relaxation oscillation peaks at high excitation density²⁶⁴. Due to the slightly larger excitation spot diameter ($\sim 200 \mu\text{m}$) the threshold fluence is lower than in the experiments above ($E_p \approx 15 \mu\text{J}/\text{cm}^2$), corresponding to a threshold gain of merely $g_{th} \approx 22 \text{ cm}^{-1}$ ($N_{exc} \approx 1.9 \cdot 10^{18} \text{ cm}^{-3}$). Together with the time delay owing to the excitation transfer from Alq₃ to DCM this results in a comparatively long pulse peak delay up to 160 ps. The combination of the slow rise time and a cavity decay time of $\tau_{cav} \approx 7.5 \text{ ps}$ yields rather long pulses up to $\Delta t \approx 30 \text{ ps}$ (FWHM).

As the excitation density is increased, the delay time falls below 25 ps and the pulse duration decreases to $\Delta t \approx 5 \text{ ps}$. Therefore the first emission burst terminates before the excitation transfer is entirely completed and laser oscillation evolves one more time. For increasing excitation fluence up to four peaks are observed. Simultaneously the oscillation frequency, determined by the inverse of the separation between the first two oscillation peaks, increases from 8 GHz up to 45 GHz as shown in the inset of Fig. 8.7.

Large and by, the dynamic evolution of the laser emission is an analogue of the ASE in a planar waveguide. The most important difference between the two is the slower timescale of the laser dynamics. The reasons for the slower dynamics of the laser are similar to the case of MeLPPP. Owing to the feedback the threshold material gain is considerably lower in a DFB laser. Therefore the photons have to travel a longer optical path before significant amplification occurs; the laser needs a comparatively long time to switch on. Secondly, the cavity lifetime is increased, slowing down the decay of the photon density. As long as the photon density is large the repeated build-up of an excess population is prevented. The cavity lifetime therefore sets an upper limit to the relaxation oscillation frequency²⁶⁵. Last but not

²⁷ Fabricated by T. Benstem, Institut für Hochfrequenztechnik, TU-Braunschweig.

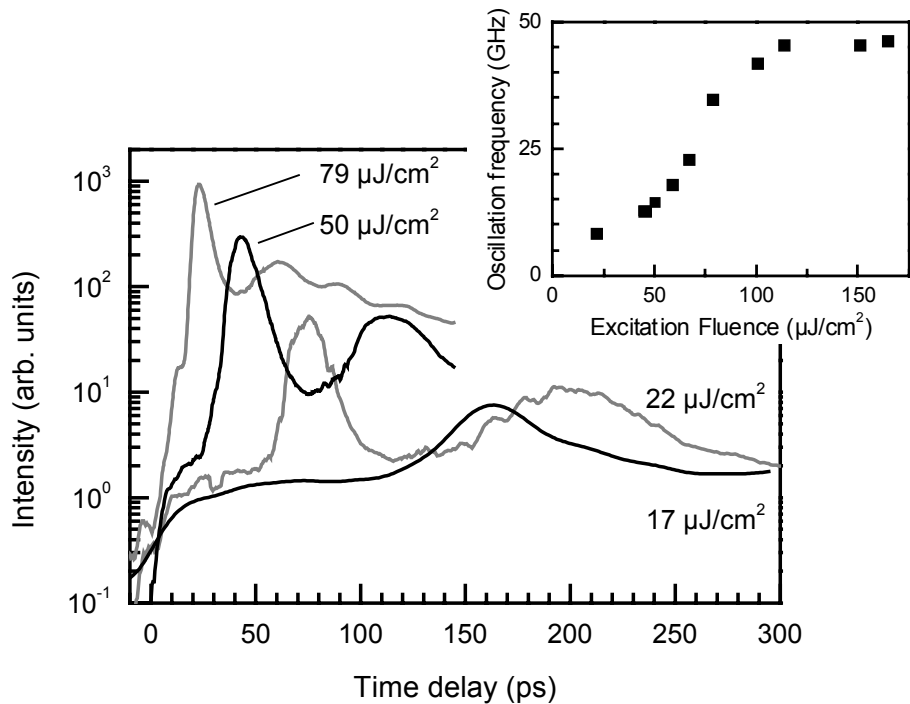


Fig. 8.7: Transient of the surface emission from a 2nd order 1D-DFB laser for various excitation densities. The sample is excited with a 150 fs long pulse at the time 0 ps. The transients are smoothed with a low pass Fourier filter, the experimental noise level is at an intensity of 10^{-1} . Inset: Variation of the oscillation frequency with increasing excitation fluence.

least, the excitation transfer is prolonged. In the transient at $22 \mu\text{J}/\text{cm}^2$, for example, the first emission burst is not terminated earlier than 90 ps after the pulsed excitation. The evolution of a second emission burst after 200 ps clearly indicates that a considerable energy transfer occurs later than 90 ps after the excitation pulse. With an exponential energy transfer, having a time constant of 9.5 ps, such a behavior cannot be explained.

In summary, the kinetics of laser emission in composite materials is dominated by the energy transfer process. Depending on the pump level single or multiple-pulse emission can be achieved.

9 Devices and applications of organic solid-state lasers

Two alternative concepts for the realization of electrically operated organic solid-state lasers are investigated. Firstly, the tunability of the organic solid-state material is exploited in a hybrid design using a compact external pump source. Secondly, the advances towards direct electrical pumping of organic semiconductor diode lasers are described. For the first time optically pumped lasing is demonstrated in a diode laser structure. Future challenges are discussed.

Owing to their low laser threshold and the large spectral tuning range organic semiconductor lasers have great potential for many applications, e.g. for laser-based analytical techniques. Furthermore the inherent mechanical flexibility together with the availability of large-area fabrication techniques might eliminate the need for mechanic scanning procedures in laser survey, data storage or sensor applications. Anyway, electrically driven laser operation in combination with a compact design will be required for any of these applications. In principle, two alternative concepts exist which take advantage of the exceptionally high gain provided by organic semiconductors. In the first concept the organic DFB laser is merely used as a tunable solid-state laser, which is optically pumped by a compact primary laser. Secondly, the rapid development of organic light-emitting diodes and their high efficiency motivate work towards direct electrical operation of organic injection lasers. Their promises, challenges and recent advances towards their realization are discussed.

9.1 Very compact tunable organic solid-state laser

In chapter 5.4 it has been demonstrated that spectrally narrow surface emission can be obtained from second order 1D-DFB lasers using flexible, nanopatterned substrates covered with an organic semiconductor. By variation of the thickness of an Alq₃:DCM layer tuning of the emission wavelength over 44 nm can be achieved. In these experiments –and also in the experiments reported by other groups- the organic film is pumped by a rather bulky and expensive laser system²⁸. Such lasers are well suited for basic studies of the laser properties, however, they do not take advantage of the low laser threshold in organic semiconductor lasers. For most applications much more compact and inexpensive pump-lasers are desirable.

The low laser threshold resulting from the distributed feedback concept and the high gain allow the realization of a very compact and, in principle, widely tunable all solid state laser. For this purpose a diode pumped passively Q-switched Nd³⁺:YAG laser with an integrated frequency tripler (Uniphase NanoUV-355) is used as pumping source. The inset of Fig. 9.1

²⁸ Typical laser systems include frequency-doubled or –tripled Nd³⁺:YAG lasers, Nitrogen lasers and the various models of complex femtosecond laser systems.

shows a scheme of the laser configuration. The pump laser produces sub-nanosecond pulses with a pulse energy of ~ 100 nJ at a wavelength of 355 nm and a 10.8 kHz repetition rate. Due to its laser wavelength and its short pulse duration this laser is optimally suited to pump Alq_3 and accumulate a very large population in the DCM dopant molecules. Since the microchip laser furthermore produces a high-quality beam, exhibiting narrow beam diameter and divergence, the organic laser can be pumped without need of intermediate focussing optics. Accordingly the whole optical arrangement has a length of only ~ 10 cm and a volume of ~ 70 cm^3 .

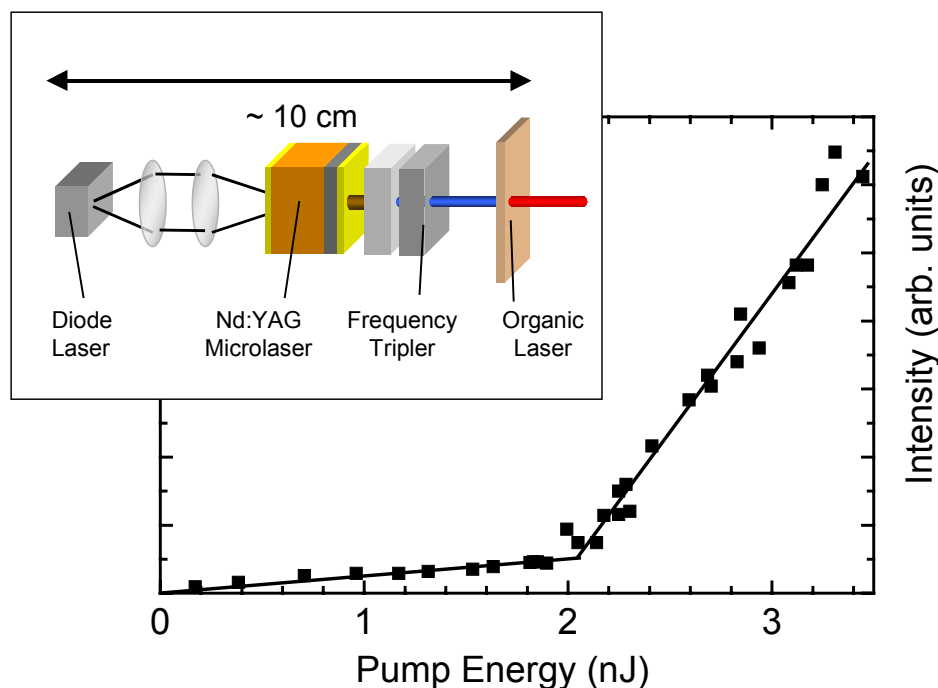


Fig. 9.1: The inset shows the scheme of the very compact all solid state laser using the organic semiconductor film as active medium. The pump source is a commercially available diode-pumped, self-pulsating, frequency tripled Nd:YAG-microchip laser (Uniphase NanoUV-355). The organic semiconductor laser can be placed directly in front of the pump laser. Thus the total length of this very compact solid state "dye" laser is less than 10 cm. The main part of the figure shows the input-output characteristics at the laser wavelength when the beam is focused to a 125 μm diameter spot.

Fig. 9.1 shows the input-output characteristics of a laser utilizing a 300 nm thick Alq_3 :DCM film. The observed laser threshold amounts to $E_P = 2$ nJ when the pump laser is focussed to an excitation spot with a diameter of 125 μm . The threshold pump energy is by a factor of 50 lower than the maximum pulse energy provided by the compact pump laser. In ambient atmosphere the durability of the organic laser is limited to some 10^5 pulses. However, the lifetime is increased by several orders of magnitude by placing the organic sample in vacuum. Similar results could be achieved by a proper sealing of the active medium. It was mentioned above that the incorporation of the dye into a solid matrix reduces the fluorescence yield as excited states are quenched. Here, the very same process has a positive effect. The repetition rate of conventional dye lasers working with a liquid dye solution is limited by the build-up of a long-lived triplet state population and its parasitic absorption. In the solid state triplets are

rapidly quenched so that a repetition rate 10.8 kHz is easily achieved. Compared to commercial dye lasers without circulating dye solution this is an increase by a factor of 1000.

So far, different laser wavelengths were reached by a variation of the film thickness in different samples. The maximum tuning range is limited by the range of film thicknesses giving rise to monomode laser operation. The use of a tapered grating with spatially varying periodicity Λ and/or an evaporated film with a thickness gradient can provide a possibility for continuous tuning of the laser wavelength over the entire gain spectrum on one and the same substrate.

9.2 Laser operation in the presence of electric contacts -- towards an organic injection laser

Can electrically pumped lasers be made from disordered organic semiconductors? That is a question that many have been asking^{120,123,126,127,266,267}. Yet, despite the fact that the typical answer is 'probably yes', no one has yet made a diode laser from disordered organic semiconductors. The challenges are threefold: firstly, stimulated emission under electrical excitation has not yet been observed, secondly, the incorporation of electric contacts into a laser structure imposes additional losses thus raising the laser threshold and, thirdly, separately optimized structures for OLEDs and optically pumped lasers are mutually unfortunate. Two milestones on the way towards an organic injection laser are therefore the demonstration of stimulated emission under electrical excitation and of optically induced lasing in the presence of electric contacts.

The major aim of the experiments reported in this chapter is to study the influence of electric contacts on the performance of optically pumped organic semiconductor lasers. Following a discussion of the problems associated with electrical pumping of organic semiconductor lasers, the feasibility of several concepts for the incorporation of electric contacts is investigated. Some of the most favorable structures for organic diode lasers are implicated using the promising organic semiconductors Alq₃:DCM and MeLPPP. Under optical excitation laser operation is demonstrated. The respective laser thresholds are compared quantitatively and implications for organic injection lasers are discussed.

9.2.1 Problems associated with electrical pumping of organic lasers

9.2.1.1 Stimulated emission under electrical excitation

Optimistic estimates predict that the threshold current density required for lasing action in organic semiconductor lasers be in the order of 100 A/cm²^{120,126}. However, despite the fact that current densities of several hundred A/cm² have been demonstrated in a number of materials^{83,268,269}, stimulated emission was not observed.

In the first place, of course, the sustainable current densities are restricted by the low carrier mobility and by current heating⁸⁴. Therefore 1 kA/cm² is presently the upper limit for the current density. Even for such high current densities the exciton density is only in the order of 10¹⁴ cm⁻³, three to four orders of magnitude below the density of charges⁸³. The singlet exciton density is often limited by unbalanced injection of electrons and holes, the slow Langevin-type formation of excitons, the statistical generation of singlet and triplet excitons, and exciton quenching through charges, excitons or the electric field (see chapter 2.1.2.3). Most importantly, however, in several materials the emission from singlet excitons is masked by excited state or charge absorption. For instance, a spectral overlap of the charge absorption with the band of stimulated emission was found for Alq₃:DCM2²⁶⁸ and some derivatives of PPV^{77,83,270}. In combination with the unfavorably high ratio between charged and neutral excitations in low-mobility materials, charge-induced absorption inhibits net stimulated emission under electrical excitation.

These drawbacks indicate that a systematic search for suitable transport and emitter materials is necessary to realize an organic injection laser. First promising results thereof are the absence of overlap between stimulated emission and charge-induced absorption in certain derivatives of PPV^{269,271}. Alternatively, the use of short electrical pulses, in combination with emitters whose lifetime is longer than the decay time of charge-induced absorption, should simultaneously result in a high density of excitons and a negligible density of charges²⁶⁷. This happens, however, at the expense of a comparatively low stimulated emission cross-section in long-lived emitters (see equation 2-10).

9.2.1.2 Optical loss induced by contact layers

The typical design of an OLED consists of a semitransparent anode, usually ITO, one or more layers of an organic semiconductor, and a cathode, usually a low-workfunction metal (see Fig. 2.6). At first sight it appears straightforward to incorporate the electric contacts into some of the low-threshold resonator geometries developed for optically pumped organic lasers (see Fig. 2.7). Specifically microcavities and waveguide structures like DFB or DBR, containing an organic film with a few hundred nanometers thickness, appear almost predestinated to make an organic diode laser. At closer investigation, however, the situation becomes more complex due to the notable absorption of the contact materials in the visible spectral range: following equation 2-9 the condition for the threshold gain is $g_{th} \approx 1/L + \alpha$. In dielectric structures the losses can be negligible so that g_{th} is entirely determined by the length of the amplifying medium. If, however, the losses become substantial, as in the presence of contacts, the dominant factor is $g_{th} \geq \alpha$.

Particularly severe restrictions result from the incorporation of metallic contacts. At a metal electrode the transverse electric fields vanish decaying within a skin depth of a few nanometers. If a metal cathode is used as one of the mirrors in a microcavity, the threshold is at least an order of magnitude higher than in the case of two dielectric mirrors (double-DBR microcavity)¹⁰². In a waveguide design the mode penetrates approximately 0.2-0.5 μm into

the cladding layer. When metals are used as contact layers they induce drastic waveguide losses unless cladding layers with a thickness exceeding $0.2 \mu\text{m}$ are introduced^{120,123}. In this case, however, the overall device thickness exceeds $0.5 \mu\text{m}$ which presents a serious problem to the electrical properties of the diode; at least if semiconducting organic materials are used. Highly conducting cladding layers or different electrode materials might be a solution. Unfortunately, many of the materials that are currently used as charge injection and transport layers in highly efficient heterostructure OLEDs are not qualified for cladding layers: they either have a higher refractive index than the organic semiconductor or possess strong absorption bands in the spectral range of stimulated emission. Among these materials are e.g. the highly doped, metallic polymers like polyaniline (PANI), polypyrrole or PEDOT:PSS¹²⁰.

Similar problems arise with alternative electrodes such as ITO. In contrast to metals ITO has a dielectric characteristic in the visible spectral range, exhibiting a higher refractive index ($n_{ITO} \approx 2$) than most organic semiconductors. In conventional OLEDs the ITO layer is $0.1\text{-}0.2 \mu\text{m}$ thick so that a large fraction of the optical mode is allocated in the ITO layer. Although the transparency of ITO can be optimized while keeping the resistivity sufficiently low²⁷², ITO does always have some residual absorption and, hence, increases the threshold for stimulated emission drastically^{37,273}.

9.2.2 Design of suitable structures for organic diode lasers

Suitable structures for organic diode lasers must be integral to a low loss laser resonator and be able to support very high bipolar current densities. At the present time the strongest electroluminescence is achieved in diode structures where the organic semiconductor (OS) is sandwiched between two electrodes²⁹.

Due to the low mobility of disordered organic semiconductors, the current flow through an OS is space charge limited. Child's law (equation 2-8) predicts that the (unipolar) current density through the organic layer scales with the film thickness, d_f , according to $J_{SCLC} \propto d_f^{-3}$. In 500 nm thick films up to 300 A/cm^2 were obtained using 200 ns pulses of 150 V ¹²³. To obtain a current density in the kA/cm^2 range, d_f should not exceed 200 nm ⁸³, similar to half a wavelength of light in the organic medium, $\lambda/2n_f$. The optimum thickness of the organic semiconductor layer will be in the order of $100\text{-}200 \text{ nm}$. Since the best diode will most probably be a heterostructure, consisting of an emitter layer surrounded by electron and hole transport layers, the thickness of the electron-hole recombination zone, d_{rec} , is much lower than that.

The problem for the optical design of an organic semiconductor laser is to minimize losses arising from the contact layers, while maintaining an excellent diode structure. Thin organic

²⁹ Nevertheless, the recent discovery of ambipolar organic light-emitting field-effect transistors²⁷⁴ might give more flexibility in the design of future devices: in contrast to an OLED a bipolar FET structure has all of its electric contacts on one and the same side of the organic layer.

films are compatible with either slab waveguide lasers³⁰ or microcavities. Optical losses arise from the penetration of the electric field of the laser mode into the absorbing electrodes. The potential anode materials are either ITO or a semitransparent film of a high workfunction metal like Pt or Au. Cathodes typically consist of low-workfunction metals or metal alloys, such as Al, Ag, Mg/Ag, or LiF/Al. A recent breakthrough in the development of OLEDs proved that ITO covered with a 5 nm thick transparent layer of bathocuproine can serve as efficient electron injecting electrode^{126,275}. Hence, both electrodes can be fabricated either from either a metal or ITO.

The most favorable design will have (in order of relevance):

- (i) a small overlap of the mode with the absorbing electrodes;
- (ii) as thin as possible a film of the OS;
- (iii) a large confinement, Γ , of the mode within the recombination zone.

Fig. 9.2 shows the cross-sections of several potential organic diode laser architectures together with the corresponding optical mode profile, given by transversal distribution of the electromagnetic intensity $|\mathbf{E}_z|^2$. The structures (a)-(g) represent potential waveguide designs while (h) corresponds to a $\lambda/2$ microcavity with two DBR mirrors. In a waveguide the evanescent field penetrates up to half a wavelength into the claddings so that -in the best case- the intensity is restricted to a layer with a thickness of $\sim \lambda/n_f$ ³¹. In the structures (a)-(d) the guided mode is essentially confined within the diode (including electrodes), whereas it extends well beyond the electrodes in (e)-(h).

Fig. 9.2 (a) shows a waveguide with two metal electrodes. Waveguide losses below 100 cm^{-1} require that the OS have a thickness of $d_f \geq \lambda/n_f$. In the case of MeLPPP ($\lambda = 490 \text{ nm}$; $n_f = 1.7$) this implies $d_f \approx 300 \text{ nm}$, too thick for an excellent OLED. Fig. 9.2 (b) is the design of a typical OLED consisting of a metal and a *thick* ITO contact ($d_{ITO} \approx 100 \text{ nm}$). A waveguide is formed irrespective of the thickness of the OS, thus allowing to optimize the diode setup independently. The mode pattern is slightly different if the ITO layer is at the interface to the substrate (standard diode) or to the air (inverted diode). Irrespective of the small difference, in both cases the largest fraction of light is guided in the ITO layer resulting in large waveguide losses. The losses in the ITO electrode can be strongly reduced if the ITO layer is made thin enough, say $\sim 20 \text{ nm}$ thick (structures (c) and (e)). Whereas the inverted diode requires a minimum thickness of the OS to form a low-loss waveguide, the standard diode can be arbitrarily thin. This happens, however, at the cost of a lower confinement of the mode in the OS and a larger overlap with ITO.

³⁰ For DFB and DBR waveguide lasers also the grating must be considered. See Chapter 9.2.3.1.

³¹ In the following discussion the OS is considered as a homogeneous medium with a constant refractive index. Nevertheless, the confinement factor of the mode in the emitter layer as well as the total waveguide thickness can be optimized if the refractive index of the emitter layer is increased¹⁰⁶, e.g. by doping with TiO_x nanoparticles²⁷⁶.

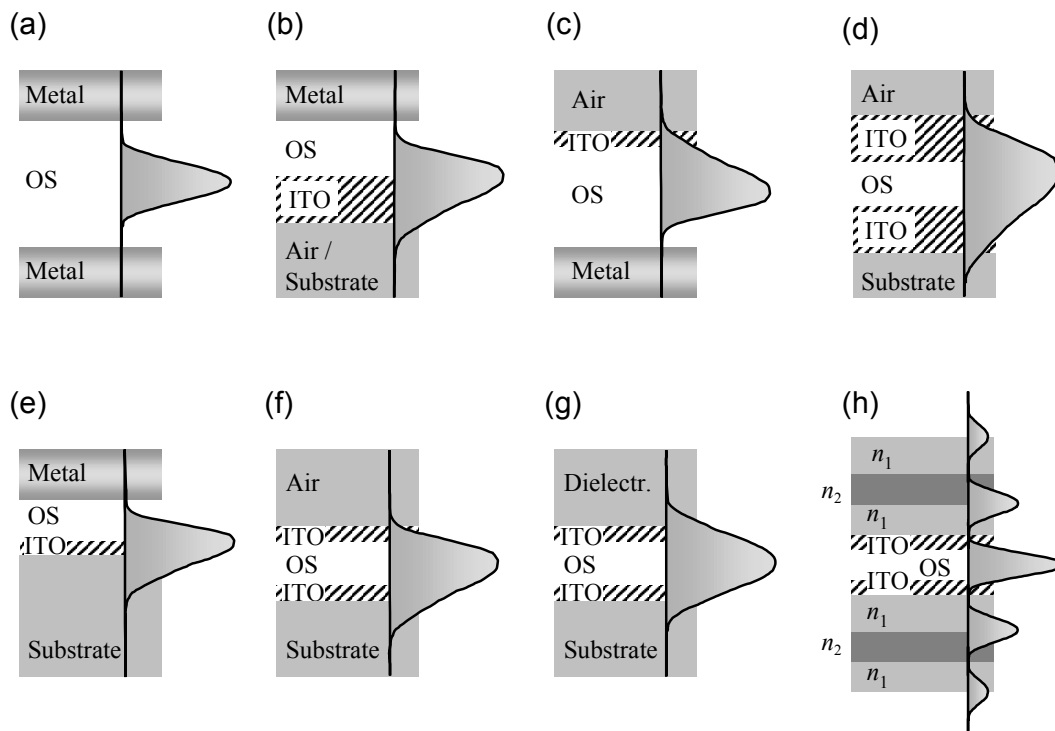


Fig. 9.2: Schematic cross-sections of several potential architectures for organic diode laser. The resulting optical mode profile is indicated by the gray-shaded area. (a)-(g) are designs for slab-waveguides, whereas (h) is a microcavity with two dielectric mirrors. In (a)-(d) the mode is essentially confined within the diode (including electrodes), whereas the mode extends well beyond the electrodes in (e)-(h). The contact electrodes can be either made from two metals (a), using an ITO anode and a metallic cathode (b), (c), (e), or with ITO for both electrodes (d),(f)-(h).

The structures in Fig. 9.2 (d) and (f)-(h) use ITO for both anode and cathode. Whereas *thick* ITO layers (d) induce significant optical losses in a multimode waveguide, *thin* ITO layers allow to fabricate waveguides with optical losses below 30 cm^{-1} ¹²⁶ without restrictions on d_f . Using a dielectric upper cladding (g) it would even be possible to fabricate a symmetric waveguide and to optimize the confinement factor of the mode in the recombination zone.

Last but not least, the use of ITO in anode and cathode renders double-DBR microcavities possible (Fig. 9.2 (h)) –today’s lowest threshold organic semiconductor lasers¹⁰⁴. By proper design of the DBR stacks the overlap of the optical mode with the ITO layers can be minimized. Furthermore the thickness of the entire diode $\lambda/2n_f$ would be in the order of 150-200 nm, the optimum thickness for OLEDs.

Which of the above structures will be the best for electrically pumped organic diode lasers depends on the choice of the materials. Apart from (b) and (d) all of the structures in Fig. 9.2 exhibit moderate optical losses in to the electrodes. Criterion (i) can therefore be fulfilled. Assuming that it is more important to optimize the electrical properties of the diode than to maximize the mode confinement³², the most suitable waveguide design is most probably the one of Fig. 9.2 (g), followed by (f), (e), (c), and (a).

³² According to equation 2-8 threshold current and voltage are related by $V_{th} \propto j_{th}^{1/2} d_f^{1/2}$. A reduction of the film thickness by a factor 2 reduces the mode confinement Γ also by approx. a factor of 2. Consequently, the

9.2.3 Optically pumped laser diodes

9.2.3.1 Preparation and investigation of DFB lasers with electric contacts

Second order DFB lasers were prepared based on the two promising organic semiconductor materials MeLPPP and Alq₃:DCM. Distributed feedback is induced by means of corrugated polyester substrates as described in Chapter 5.5.2. For both organic semiconductors several of the above mentioned concepts were realized applying different electrode materials. Since the lasers are surface emitting, at least one of the contacts is semitransparent. In order to address the influence of each contact layer separately, the samples are subdivided in four regions: the OS is either sandwiched between both electrodes (i), is in contact with one of the electrodes (ii), (iii), or does not have any of the electrodes (iv). Each of the four resulting structures has its specific effective refractive index for the guided electromagnetic wave. Accordingly, for one and the same film thickness and grating periodicity, the laser wavelength is different in every structure. In order to exploit the maximum gain of the material it is therefore necessary to optimize the thickness of the OS separately for every structure, especially if the gain spectrum is as narrow as in the case of MeLPPP. Calculations of the mode profile help to determine the appropriate range of film thicknesses³³.

An important difference between the two materials stems from the different texture of the upper surface. Whereas it is flat in the case of the spincoated polymer film the surface of the evaporated Alq₃:DCM is a replication of the substrate. If metallic electrodes are used this difference strongly affects the mode profile. Fig. 9.3 sketches the corresponding cross-sections.

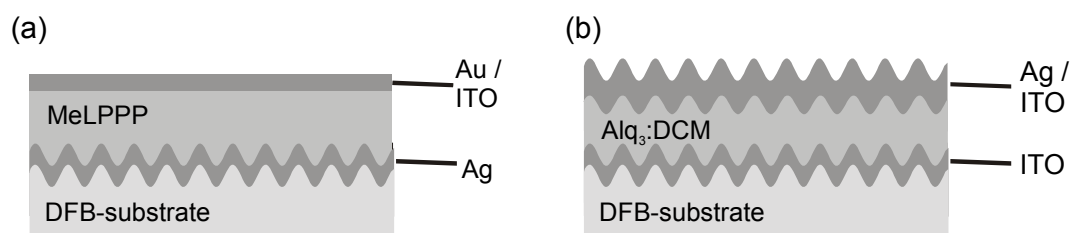


Fig. 9.3: Schematic cross-section of DFB laser diodes made from MeLPPP (a) and Alq₃:DCM (b), respectively.

It is desirable to compare the laser operation in the various design concepts quantitatively, regardless of the respective laser wavelength³⁴. For that reason it is beneficial to plot the emission intensity at the laser wavelength against the optically induced material gain. Differences in the laser threshold can then directly be attributed to a different waveguide loss

threshold material gain rises by a factor of 2, demanding for a higher current. Nevertheless, the thinner structure easily provides the enhanced current and the threshold voltage even drops by a factor of 2.

³³ I would like to thank Martin Reufer for performing extensive mode profile calculations.

³⁴ In principle, the emission wavelength can be adjusted choosing an appropriate grating pitch.

or to the mode confinement factor. This procedure allows to extrapolate the results of optical experiments to the corresponding electrical experiments.

Optically induced laser operation was investigated using the standard setup described in section 3.2.3. The samples were excited with femtosecond laser pulses ($\lambda = 400$ nm) focused to a circular spot with a diameter of 95 μm . In both materials the excitation beam entered the sample through the semitransparent anode, i.e. samples based on MeLPPP were illuminated from the top, Alq₃:DCM based samples through the substrate. Emission spectra were recorded through the anode for various excitation pulse energies ranging from well below threshold to more than twice the threshold of the respective sample. From the incident pump fluence the averaged excitation density in the active area is calculated (section 3.2.1) and converted into an averaged material gain at the laser wavelength by use of the spectrally varying stimulated emission cross-section.

In the case of MeLPPP the assumption of a linear dependence between excitation density and gain is reasonable since the chromophore density is the same for absorption and emission. On the other hand the determination of the material gain is troublesome for Alq₃:DCM at high excitation densities. Firstly, the excitation density in Alq₃ (c) can be much higher than the density of DCM molecules (N_{DCM}^{max}), secondly, the DCM population does not rise instantaneously so that laser operation might start before the excitation transfer is complete (see chapter 8.2). A reasonable functional dependence of the gain should be linear at low N_{Alq} and saturate to the maximum value ($g_{\text{max}}(\lambda) = \sigma_{SE}(\lambda)N_{DCM}^{\text{max}}$) for high N_{Alq} . Lacking a more profound description the following dependence is assumed

$$g_{\text{mat}}(\lambda) = \sigma_{SE}(\lambda)N_{DCM}^{\text{max}} \cdot \left[1 - \exp\left(-\frac{\sigma_{SE}(\lambda)N_{Alq}}{\sigma_{SE}(\lambda)N_{DCM}^{\text{max}}}\right) \right]. \quad (9-1)$$

9.2.3.2 DFB lasers based on MeLPPP

The MeLPPP DFB lasers are based on a grating with a periodicity of $\Lambda = 300$ nm and a modulation depth of $h \approx 275$ nm. Together with the narrow gain spectrum of MeLPPP this determines the available range of film thicknesses via $n_{\text{eff}}(d)$ and the Bragg condition 2-15. It is found that the Bragg wavelength coincides with the gain maximum for $d_{\text{min}} \geq 285$ nm³⁵, which is in the order of λ/n . For the time being, no other than metallic cathodes have been reported for OLEDs made from soluble conjugated polymers; only metallic cathodes are therefore considered. Consequently, (a), (c) and (e) are the most promising structures among the potential architectures shown of Fig. 9.2.

Three different samples are compared: sample A is a MeLPPP laser *without* contacts, sample B and C have two electrodes, each. Due to its low workfunction and the weak absorption at $\lambda = 490$ nm, Ag is chosen as cathode material. The anode is a thin semitransparent film, either

³⁵ Minimum thickness of the OS film; the average film thickness is $d_f = 1/2(d_{\text{min}} + h)$.

20 nm ITO (sample B) or 6.5 nm Au (sample C). Since the absorption is distinctly higher for the anode than for the cathode an inverse diode scheme is chosen thus minimizing the overlap of the optical mode with the anode. The film thickness was separately optimized for every structure in order to match the laser wavelength with the gain maximum of MeLPPP. Table 9-1 summarizes the parameters of the three relevant structures.

Sample	Substrate	Cathode	d_{min}	Anode	Cladding	λ_{Laser}	g_{th}
A	PET	-	240 nm	-	Air	492.4 nm	130 cm^{-1}
B	PET	Ag, 150 nm	285 nm	ITO, 20 nm	Air	493.2 nm	135 cm^{-1}
C	PET	Ag, 150 nm	350 nm	Au, 6.5 nm	Air	490.8 nm	650 cm^{-1}

Table 9-1: Overview of the MeLPPP DFB laser structures.

Above a threshold excitation density optically pumped lasing is observed in the samples A-C, characterized by a distinct laser threshold and highly directed, TE-polarized surface emission. Above threshold the emission spectrum collapses to a narrow line at a wavelength of 492.4 nm, 493.2 nm and 490.8 nm for sample A, B, and C, respectively. Fig. 9.4 shows a double logarithmic plot of the input output characteristics of the samples, exhibiting the typical S-shape: for low gain the intensity rises linearly, followed by an exponential increase closely above threshold, which, eventually, levels off to above the saturation intensity.

Without electric contacts (sample A) the laser threshold is reached at a material gain of 130 cm^{-1} . Increasing the gain by a factor of two the intensity at the laser wavelength rises by a factor of 10^3 . Surprisingly sample B has almost exactly the same threshold gain (135 cm^{-1}). In

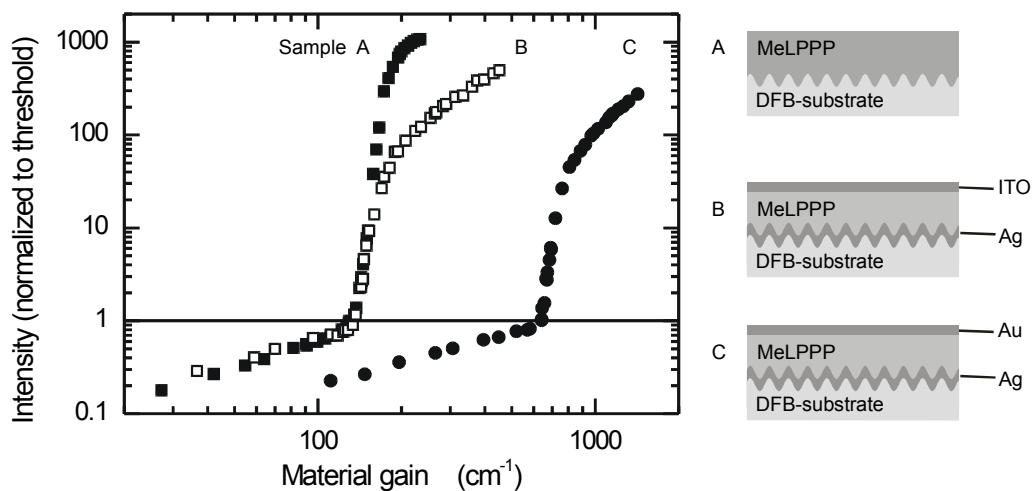


Fig. 9.4: 2nd order MeLPPP DFB lasers with electric contacts. Double logarithmic plot of the emitted intensity at the laser wavelength against the optically induced material gain in the active layer. All curves are normalized to the intensity at the laser threshold. On the right hand side the schematic cross-section of the samples A, B and C is shown.

contrast thereto sample C requires a five times higher threshold gain of $\sim 650 \text{ cm}^{-1}$ making the structure irrelevant for electrical excitation³⁶.

With regard to the realization of an organic diode laser it is very promising to see that, firstly, OS lasers work at all in the presence of electric contacts and that, secondly, the laser threshold is not substantially increased. However, with a minimum MeLPPP thickness of 285 nm, the active layer is clearly too thick to support sufficiently high current densities.

To reveal whether the low waveguide losses of sample B are peculiar to thick MeLPPP layers it is valuable to investigate the influence of anode and cathode separately. For a sample having only a Ag contact³⁷ the threshold gain is reduced to 90 cm^{-1} , whereas it increases to 160 cm^{-1} in a sample where only the ITO contact is present³⁸. The underlying effects seem to compensate each other if both contacts are present. The threshold reduction in the presence of a Ag cladding is most likely due to an enhanced coupling³⁹ which tends to reduce the threshold gain of a DFB laser (equation 2-24). Since the same reduction should also be valid in the presence of both contacts, it has to be concluded that the ITO contact increases the threshold gain by approximately $30\text{-}40 \text{ cm}^{-1}$. The increase of threshold is partly due to absorption in the ITO and to a reduced confinement factor of the mode in the MeLPPP layer. Both mechanisms will be slightly enhanced if the thickness of the MeLPPP is reduced, or the build-up is changed from an inverse diode to a standard diode.

In conclusion, surface emitting DFB diode-laser structures with moderate waveguide losses can be realized with the conjugated polymer MeLPPP.

9.2.3.3 DFB lasers based on Alq₃:DCM

The Alq₃:DCM lasers are based on gratings with a periodicity of 400 nm and a modulation depth of 90 nm. Due to the broad gain spectrum of Alq₃:DCM, lasing is possible for a wide range of film thicknesses (see Fig. 5.8). Furthermore metallic and dielectric electrodes are available so that, in principle, all the structures of Fig. 9.2 can be realized. The structures (e) and (f) are of particular interest since they allow the use of separately optimized OLED heterostructures.

Several samples were prepared in a standard diode setup, whereby either Ag, or a thin film of ITO⁴⁰ is used for the cathode. The anode is made of either ITO or Au⁴¹. Optimized OLEDs

³⁶ On the other hand, textured metallic microcavities are highly interesting for the study of photonic bandgap effects²⁷⁷⁻²⁷⁹.

³⁷ $d_{min} = 350 \text{ nm}$

³⁸ $d_{min} = 285 \text{ nm}$

³⁹ Enhanced coupling is indicated by a much stronger pronounced stopband and by a stronger iridescence of the DFB grating.

⁴⁰ In a real OLED, electron injection from ITO into Alq₃ requires an intermediate 5 nm thick BCP layer^{126,275}, which is omitted for simplicity.

⁴¹ All samples were made by T. Benstem at the Institut für Hochfrequenztechnik, TU Braunschweig.

consist of a three layer heterostructure, using an Alq₃:DCM emitter layer embedded between a Starburst amine hole transport layer and the undoped Alq₃ as electron transport layer^{280,281}. Sample D contains such an optimized heterostructure with a total thickness of 180 nm. In sample E the same heterostructure is embedded between two ITO electrodes. In all other samples the OS consists only of Alq₃:DCM, whose thickness is either 180 nm, 300 nm or 350 nm. Table 9-2 summarizes the build-up of the investigated structures.

Sample	Substrate	Cathode	d_f	Anode	Cladding	λ_{Laser}	g_{th}
D	PET	-	Starburst, 40 nm Alq ₃ :DCM, 100nm Alq ₃ , 40 nm	-	Air	640.5 nm	150 cm ⁻¹
E	PET	ITO, 20 nm	same as D	ITO, 20 nm	Air	654 nm	256 cm ⁻¹
F	PET	ITO, 20 nm	Alq ₃ :DCM, 180 nm	ITO, 20 nm	Air	644 nm	142 cm ⁻¹
G	PET	-	Alq ₃ :DCM, 300 nm	-	Air	643 nm	44 cm ⁻¹
H	PET	ITO, 20 nm	Alq ₃ :DCM, 300 nm	Ag, 150 nm	-	644 nm	261 cm ⁻¹
I	PET	Au, 6 nm	Alq ₃ :DCM, 350 nm	Ag, 150 nm	-	-	-

Table 9-2: Overview of the Alq₃:DCM DFB laser structures.

Under intense optical excitation laser operation was observed from the samples D-H but not from sample I. In accordance with the results of section 5.2 laser operation is evidenced by a drastic narrowing of the emission spectrum, the emission of a TE-polarized, highly directed laser beam, by the observation of laser speckles, and by a distinct laser threshold. Fig. 9.5 displays the input-output characteristics of the samples D-H as a function of the optically induced averaged material gain⁴². As with MeLPPP, all curves show the characteristic S-shape.

The lowest threshold gain is observed for sample G ($g_{mat} = 45 \text{ cm}^{-1}$), having a 300 nm thick active layer of Alq₃:DCM and no electric contacts. If the same film is embedded in a standard diode (sample H) the threshold gain rises drastically to 260 cm^{-1} , the highest value among the samples. In contrast to the case of MeLPPP a conventional diode structure with one metal contact is obviously not the best choice for evaporated films of Alq₃:DCM. The 'Kozlov'-type structure with two ITO contacts (sample F) does not only have a thinner OS layer but also a distinctly lower threshold material gain of $\sim 150 \text{ cm}^{-1}$. The waveguide losses induced by the two ITO contacts can be estimated to $\sim 100 \text{ cm}^{-1}$ ⁴³. Most probably these substantial losses, being three times larger than the value reported by Kozlov in planar waveguides¹²⁶, can be reduced by optimization of the ITO composition and by use of a lower grating modulation.

⁴² The material gain is calculated from the excitation density in Alq₃ as described in 9.2.3.1.

⁴³ Comparison of samples D and E having the same total thickness.

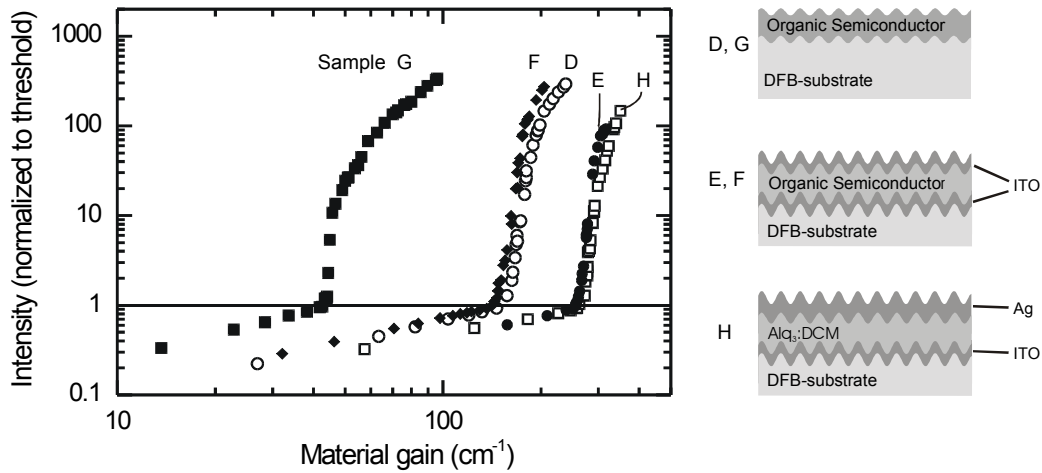


Fig. 9.5: Input-output characteristics for Alq₃:DCM 2nd order DFB lasers with electric contact layers. All intensities are normalized to the respective threshold value. The schematic cross-section of the samples D, E, F, and G (see table 9-2) is shown on the right hand side.

Under electrical operation the excitation distribution is very different than in optical experiments. Most importantly, excitons are not generated throughout the entire organic semiconductor but merely in a thin recombination zone. As a consequence, the overlap of the optical mode with the emitting layer is much lower than in the samples above. Furthermore the emitter is embedded between hole and electron transport layers. Both effects are addressed in the samples D and E containing an optimized double heterostructure. For sample D (without contacts) a threshold of 150 cm⁻¹ is found, with two ITO contacts the threshold gain rises to 255 cm⁻¹ (sample E). This already indicates that the threshold gain depends strongly on the thickness of the emitter layer. In fact, it is found that the threshold gain is -as a good approximation- inversely proportional to the thickness of the active layer and, hence, to the mode confinement Γ ⁴⁴. As the recombination zone is most probably much smaller than 100 nm, the value of 250 cm⁻¹ is still an optimistic guess for the threshold material gain of the corresponding -hypothetical- electrically pumped Alq₃:DCM DFB laser.

9.2.4 Feasibility of organic diode lasers

From the above measurements the threshold current of a -hypothetical- electrically driven organic semiconductor laser can be estimated. Assuming that there are no optical losses due to charged excitations, thermal heating or other parasitic losses the electric current is given by equation 9-2: a threshold density of singlet excitons (N_{th}^{el}) must be supplied into the recombination zone (thickness, d_{rec}) within the lifetime of the exciton (recombination time, τ_{rec}). An important factor is the electroluminescence quantum yield η_{el} which is the fraction

⁴⁴ Compare e.g. samples E and F $\left(\frac{180 \text{ nm}}{100 \text{ nm}} \approx \left(\frac{142 \text{ cm}^{-1}}{255 \text{ cm}^{-1}} \right)^{-1} \approx 1.8 \right)$ or G and D $\left(\frac{300 \text{ nm}}{100 \text{ nm}} \approx \left(\frac{44 \text{ cm}^{-1}}{150 \text{ cm}^{-1}} \right)^{-1} \approx 3 \right)$.

of photons generated per electron passing through the sample. Transferring the excitation density from optical to electrical experiments the different mode confinement factors (Γ^{opt} and Γ^{el}) must be accounted for. With the help of the stimulated emission cross-section the threshold current can then be expressed in terms of the threshold material gain determined from an optical experiment (equation 9-3)

$$j_{th} = \frac{d_{rec} e}{\eta_{el} \tau_{rec}} N_{th}^{el} \quad (9-2)$$

$$= \frac{d_{rec} e}{\eta_{el} \tau_{rec}} \frac{\Gamma^{opt}}{\Gamma^{el}} N_{th}^{opt} = \frac{d_{rec} e}{\eta_{el} \tau_{rec}} \frac{\Gamma^{opt}}{\Gamma^{el}} \frac{g_{th}^{opt}}{\sigma_{SE}} \quad (9-3)$$

With the help of equation 9-3 one can estimate the threshold current for the structures considered above. With the parameters of the best samples made from MeLPPP and Alq₃:DCM one obtains:

1. Sample B, a MeLPPP with a film thickness of 285 nm:
using $g_{th}^{opt} = 135 \text{ cm}^{-1}$, $d_{rec} = 50 \text{ nm}$, $\sigma_{SE} = 1.5 \cdot 10^{-16} \text{ cm}^2$, $\eta_{el} = 0.25$, $\tau_{rec} = 100 \text{ ps}$, and $\Gamma^{opt}/\Gamma^{el} = 6$ the required current density is $j_{th} \approx 170 \text{ kA/cm}^2$.
2. Sample E, an optimized diode with a 100 nm thick layer of Alq₃:DCM:
using $g_{th}^{opt} = 250 \text{ cm}^{-1}$, $d_{rec} = 50 \text{ nm}$, $\sigma_{SE} = 1.35 \cdot 10^{-17} \text{ cm}^2$, $\eta_{el} = 0.25$, $\tau_{rec} = 1 \text{ ns}$, and $\Gamma^{opt}/\Gamma^{el} = 2$ the required current density is $j_{th} \approx 120 \text{ kA/cm}^2$.

Although both examples are very optimistic, the required current density is at least two orders of magnitude higher than the values achieved in high-performance OLEDs. Where is the potential for future improvement? Restricted by the electrode-induced losses, careful optical design might eventually reduce the threshold gain by one order of magnitude; certainly not sufficient to make an injection laser. A solution will therefore require the application of optimized materials with a higher mobility and, possibly, narrowband emitters having a high stimulated emission and a long lifetime simultaneously.

10 Outlook

In the present work the properties of organic semiconductor lasers have been studied laying special emphasis on the exploration of novel thin film photonic crystal resonators exhibiting distributed feedback in one or two dimensions. It has been shown that optically pumped lasers can actually be fabricated with comparatively little technological effort and still show an outstanding performance, indicated by narrow divergence, diffraction-limited surface emission, and the generation of transform-limited picosecond pulses. The results of this work suggest a number of further investigations concerning basic research of photonic crystals as well as issues related to materials science and potential technological applications of organic semiconductors.

So far the investigation of 2D-DFB lasers was limited to square gratings with comparatively low, nearly sinusoidal variations of the effective refractive index. A special feature of square gratings is that all the resulting 2D laser modes have a one-dimensional analogue resulting in a low suppression of the corresponding lateral modes. However, the fabrication technique allows to produce nearly arbitrary two-dimensional gratings with adjustable aspect ratio of the fundamental modulations. It is therefore straightforward to proceed to gratings with different symmetry. Triangular gratings, for instance, will allow to establish 2D laser modes that have no 1D analogue. Such a laser should result in singlemode operation for a much broader range of excitation densities. Another promising modification is to use gratings with increased dielectric contrast and, hence, to increase the photonic bandgap until it spans the entire emission spectrum of a narrow-band emitter. Preliminary results have shown that the same happens if the substrate is metallized before the organic semiconductor is deposited.

Further exciting opportunities arise from the combination of the periodically nano-patterned substrates with the self-assembly technique developed for colloids. The former can serve as a template to grow highly ordered colloidal monolayers. As the colloid can, in principle, contain a large variety of materials including dyes, nanocrystals or metal nanoparticles, all these particles can be arranged in a well defined lattice.

More application related aspects concern the optimization of organic semiconductor lasers as compact solid-state laser sources. For that purpose, of course, the diffraction-limited emission of a single mode 2D-DFB laser is very appealing. A similar effect can be achieved with 1D-DFB lasers if a horizontal waveguide is defined, which could be directly included in the embossing process²⁸². Furthermore it is worthwhile to optimize the coupling strength of the grating. With the present gratings both the coupling and the radiation loss are high, demanding for a small excitation spot and therefore a high threshold gain. With a lower coupling strength device length can be increased and the threshold gain can be significantly reduced. Doing so it should be possible to reduce the threshold pump pulse energy to a value that can be achieved with pulsed GaN diode lasers focused to a narrow stripe. An even more compact design and significantly higher repetition rates would become possible.

Currently, tuning of the emission wavelength is achieved by a variation of the film thickness. The use of samples with a thickness gradient will allow to tune the laser wavelength continuously by simply moving the excitation spot on the sample. In addition, tapered gratings with spatially varying periodicity will serve to extend the tuning range over the entire gain spectrum of the organic semiconductor. If the emitter is dispersed in a liquid crystal the wavelength tuning could eventually even be induced by an electric field.

Probably the most ambitious task is the realization of an injection laser based on disordered organic semiconductors. Despite the rapid progress of OLEDs and optically pumped lasers stimulated emission under electrical excitation has yet to be observed, the two major obstacles being electrode and charge-induced absorption. The development of transparent cathodes together with an optimization of waveguide or microcavity structure might eventually reduce the required laser threshold by an order of magnitude. A completely different approach towards an injection laser makes use of light-emitting field-effect transistors as recently demonstrated with organic molecular crystals²⁷⁴. Their employment essentially eliminates the problem of electrode absorption. Even so, this technique is still in its very early stage. Besides that, a number of materials issues need to be addressed. The careful design of heterostructures allows to combine the best available electron and hole conductors with efficient emitter layers. In OLEDs consisting of molecular semiconductors the use of heterostructures is comparatively sophisticated, whereas it has only just begun with conjugated polymers²⁸³. First and foremost there is a dire need for better electron transporting materials to achieve balanced current transport on a high level, to shift the recombination zone away from the cathode, and to increase the exciton generation rate. As the low mobility of disordered organic semiconductors is directly correlated to their disorder, the use of higher mobilities in oriented regio-regular polymers might offer routes for solving this problem. Simultaneously, crossing of the polymer chains and the lasing mode polarization is a possible way to diminish the effect of charge-induced absorption. Secondly, long lived emitters will allow to accumulate excitations over a long time and thus reach a high excitation density with comparatively low current. To maintain a reasonably high stimulated emission cross-section, narrow-band emitters such as rare-earth atoms seem well suited. Also spiro-type molecules⁸⁷ or core-shell nanoparticles might be an alternative²⁸⁴. Furthermore the materials have to be thoroughly selected to avoid spectral overlap of charge-induced absorption with the band of stimulated emission. This calls for electric-pump optical-probe experiments to study the optical properties of light-emitting diodes under intense electrical excitation.

As soon as organic semiconductor lasers are ultimately realized they have great potential for a number of applications. Their large spectral tuning range in the visible opens possibilities for laser-based analytical techniques. Furthermore the inherent mechanical flexibility together with the availability of large-area fabrication techniques might eliminate the need for mechanic scanning procedures in laser survey, data storage or sensor applications.

In conclusion, disordered organic semiconductors are an exciting playground for the exploration of innovative concepts and devices.

List of abbreviations and definitions

OS	(disordered) organic semiconductor
ASE	amplified spontaneous emission
DFB	distributed feedback
FWHM	full width at half maximum
AFM	atomic force microscope
MeLPPP	methyl substituted ladder-type poly(<i>para</i> -phenylene)
Alq ₃	tris-(8-hydroxyquinoline)-aluminum
DCM	4-dicyanmethylene-2-methyl-6-(<i>p</i> -dimethylaminostyryl)-4H-pyran
λ	wavelength [nm]
ω	angular frequency [s^{-1}]
ν	index for vibrational mode
σ_{SE}	cross-section for stimulated emission [cm^2]
N	excitation density [cm^{-3}]
n	real part of refractive index
χ	imaginary part of refractive index
n_{eff}	effective refractive index
Λ	grating periodicity [nm]
d_f	film thickness [nm]
γ	field gain coefficient [cm^{-1}]
g	($=2\gamma$) power gain coefficient [cm^{-1}]
Γ	mode confinement factor
α	power absorption coefficient [cm^{-1}]
k, \mathbf{k}	wavenumber, wavevector
\mathbf{G}	reciprocal lattice vector
κ	coupling coefficient [cm^{-1}]
μ	mobility [$cm^2 V^{-1} s^{-1}$]
j	current density [A/cm^2]

Bibliography

- ¹ A. J. Heeger, *Semiconducting and Metallic Polymers: The Fourth Generation of Polymeric Materials--Nobel Lecture, December 8, 2000*, J. Phys. Chem. B **105**, 8475 (2001).
- ² C. K. Chiang, C. R. Fincher, Jr., Y. W. Park, et al., *Electrical conductivity in doped polyacetylene*, Phys. Rev. Lett. **39**, 1098 (1977).
- ³ H. Shirakawa, E. Louis, A. G. MacDiarmid, et al., Chem. Comm., 578 (1977).
- ⁴ T. Hebner, C. Wu, D. Marcy, et al., *Ink-jet printing of doped polymers for organic light emitting devices*, Appl. Phys. Lett. **72**, 519 (1998).
- ⁵ F. Pschenitzha and J. Sturm, *Three-color organic light-emitting diodes patterned by masked dye diffusion*, Appl. Phys. Lett. **74**, 1913 (1999).
- ⁶ J. A. Rogers, Z. Bao, and L. Dhar, *Fabrication of patterned electroluminescent polymers that emit in geometries with feature sizes into the submicron range*, Appl. Phys. Lett. **73**, 294 (1998).
- ⁷ G. Gustafsson, Y. Cao, G. M. Treacy, et al., *Flexible light-emitting diodes made from soluble conducting polymers*, Nature **357**, 477 (1992).
- ⁸ G. Yu, J. Wang, J. McElvain, and A. J. Heeger, *Large-area, full-color image sensors made with semiconducting polymers*, Adv. Mater. **10**, 1431 (1998).
- ⁹ N. S. Sariciftci, *Polymeric photovoltaic materials*, Current Opinion in Solid State & Materials Science **4**, 373 (1999).
- ¹⁰ J. H. Burroughes, C. A. Jones, and R. H. Friend, *New semiconductor device physics in polymer diodes and transistors*, Nature **335**, 137 (1988).
- ¹¹ C. W. Tang and S. A. VanSlyke, *Organic electroluminescent diodes*, Appl. Phys. Lett. **51**, 913 (1987).
- ¹² J. H. Burroughes, D. D. C. Bradley, A. R. Brown, et al., *Light-emitting diodes based on conjugated polymers*, Nature **347**, 539 (1990).
- ¹³ R. H. Friend, R. W. Gymer, A. B. Holmes, et al., *Electroluminescence in conjugated polymers*, Nature **397**, 121 (1999).
- ¹⁴ Pioneer, *Introduction of a Monochrome 256x64 OLED Display for car stereos* (1999).
- ¹⁵ S. Resources, *Long Term Forecast: Organic Light-Emitting Diode Displays* (www.stanfordresources.com, 2000).
- ¹⁶ T. Horiuchi, O. Niwa, and N. Hatakenaka, *Evidence for laser action driven by electrochemiluminescence*, Nature **394**, 659 (1998).
- ¹⁷ J. H. Schön, C. Kloc, A. Dodabalapur, and B. Batlogg, *An Organic Solid State Injection Laser*, Science **289**, 5999 (2000).
- ¹⁸ D. Moses, *High quantum efficiency luminescence from a conducting polymer in solution: a novel polymer laser dye*, Appl. Phys. Lett. **60**, 3215 (1992).

- 19 T. Pauck, R. Hennig, M. Perner, et al., *Femtosecond dynamics of stimulated emission and photoinduced absorption in a PPP-type ladder polymer*, Chem. Phys. Lett. **244**, 171 (1995).
- 20 M. Yan, L. J. Rothberg, E. W. Kwock, and T. M. Miller, *Interchain excitations in conjugated polymers*, Phys. Rev. Lett. **75**, 1992 (1995).
- 21 M. Yan, L. J. Rothberg, F. Papadimitrakopoulos, et al., *Spatially indirect excitons as primary photoexcitations in conjugated polymers*, Phys. Rev. Lett. **72**, 1104 (1994).
- 22 N. Tessler, G. J. Denton, and R. H. Friend, *Lasing from conjugated-polymer microcavities*, Nature **382**, 695 (1996).
- 23 C. Kallinger, M. Hilmer, A. Haugeneder, et al., *A flexible conjugated polymer laser*, Adv. Mater. **10**, 920 (1998).
- 24 M. Berggren, A. Dodabalapur, R. E. Slusher, et al., *Organic solid-state lasers with imprinted gratings on plastic substrates*, Appl. Phys. Lett. **72**, 410 (1998).
- 25 M. Berggren, A. Dodabalapur, and R. E. Slusher, *Stimulated emission and lasing in dye-doped organic thin films with Forster transfer*, Appl. Phys. Lett. **71**, 2230 (1997).
- 26 M. D. McGehee, M. A. Diaz-Garcia, F. Hide, et al., *Semiconducting polymer distributed feedback lasers*, Appl. Phys. Lett. **72**, 1536 (1998).
- 27 M. Berggren, A. Dodabalapur, R. E. Slusher, et al., *Organic lasers based on lithographically defined photonic-bandgap resonators*, Electron. Lett. **34**, 90 (1998).
- 28 A. Dodabalapur, M. Berggren, R. E. Slusher, et al., *Resonators and materials for organic lasers based on energy transfer*, IEEE J. Sel. Top. Quant. Electron. **4**, 67 (1998).
- 29 C. V. Shank, J. E. Bjorkholm, and H. Kogelnik, *Tunable distributed-feedback dye laser*, Appl. Phys. Lett. **18**, 395 (1971).
- 30 J. Carroll, J. Whiteaway, and D. Plumb, *Distributed feedback semiconductor lasers* (The Institution of Electrical Engineers, London, 1998).
- 31 M.-C. Amann and J. Buus, *Tunable laser diodes* (Artech House, Norwood, 1998).
- 32 S. John, *Strong Localization of Photons in Certain Disordered Dielectric Superlattices*, Phys. Rev. Lett. **58**, 2486 (1987).
- 33 E. Yablonovitch, *Inhibited Spontaneous Emission in Solid-State Physics and Electronics*, Phys. Rev. Lett. **58**, 2059 (1987).
- 34 E. M. Purcell, *Spontaneous emission probabilities at radio frequencies*, Phys. Rev. **69** (1946).
- 35 J. M. Gérard, B. Sermage, B. Gayral, et al., *Enhanced Spontaneous Emission by Quantum Boxes in a Monolithic Optical Microcavity*, Phys. Rev. Lett. **81**, 1110 (1998).
- 36 J. D. Joannopoulos, R. D. Meade, and J. N. Winn, *Photonic Crystals: Molding the Flow of Light* (Princeton University Press, Princeton, 1995).
- 37 A. Haugeneder, M. Neges, C. Kallinger, et al., *Nonlinear emission and recombination in conjugated polymer waveguides*, J. Appl. Phys. **85**, 1124 (1999).
- 38 A. Haugeneder, *Femtosekunden-Spektroskopie an organischen optoelektronischen Bauelementen*, Dissertation der Fakultät für Physik, Ludwig-Maximilians Universität, München (1999)

- 39 C. Kallinger, *Nanostrukturierte optoelektronische Bauelemente aus organischen Materialien*, Dissertation der Fakultät für Physik, Ludwig-Maximilians-Universität, München (1999)
- 40 H. Baessler, in *Primary Photoexcitations in Conjugated Polymers: Molecular versus Semiconductor Band Model*, edited by N. S. Sariciftci (World Scientific Publishing Company, Singapore, 1997).
- 41 Y. Hamada, in *Primary Photoexcitation in Conjugated Polymers: Molecular Exciton versus Semiconductor Band Model*, edited by N. S. Sariciftci (World Scientific, Singapore, 1997).
- 42 B. Schweitzer and H. Baessler, *Excitons in conjugated polymers*, Synth. Met. **109**, 1 (2000).
- 43 H. Haken and H. C. Wolf, *Molekülphysik und Quantenchemie* (Springer, Berlin, 1998).
- 44 A. Curioni, M. Boero, and W. Andreoni, *Alq₃: ab initio calculations of its structural and electronic properties in neutral and charged states*, Chem. Phys. Lett. **294**, 263 (1998).
- 45 P. Brocorens, E. Zojer, J. Cornil, et al., *Theoretical characterization of phenylene-based oligomers, polymers, and dendrimers*, Synth. Met. **100**, 141 (1999).
- 46 W. Atkins and R. S. Friedmann, *Molecular Quantum Mechanics* (Oxford University Press, Oxford, 1997).
- 47 J. L. Brédas, *Electronic Structure and Optical Properties of Conducting and Semiconducting Conjugated Oligomers and Polymers: An Overview of the Quantum-Mechanical Approaches*, Synth. Met. **84**, 3 (1997).
- 48 B. Sutherland, *Survey of exactly solved models for conducting polymers*, Synth. Met. **84**, 11 (1997).
- 49 R. Pariser and R. G. Parr, J. Chem. Phys. **21**, 767 (1953).
- 50 J. A. Pople, Trans. Faraday Soc. **49**, 1375 (1953).
- 51 G. Weiser, *Stark effect of one-dimensional Wannier excitons in polydiacetylene single crystals*, Phys. Rev. B **45**, 14076 (1992).
- 52 S. Abe, M. Schreiber, W. P. Su, and J. Yu, *Excitons and nonlinear optical spectra in conjugated polymers*, Phys. Rev. B **45**, 9432 (1992).
- 53 S. Abe, in *Primary photoexcitations in conjugated polymers: Molecular Exciton versus Semiconductor Band Model*, edited by N. S. Sariciftci (World Scientific, Singapore, 1997), p. 115.
- 54 U. Rauscher, H. Bässler, D. D. C. Bradley, and M. Hennecke, *Exciton versus band description of the absorption and luminescence spectra in poly(p-phenylenevinylene)*, Phys. Rev. B **42**, 9830 (1990).
- 55 R. H. Young, *Dipolar lattice model of disorder in random media. Analytical evaluation of the Gaussian disorder model*, Philisoph. Mag. B **72**, 435 (1995).
- 56 D. H. Dunlap, P. E. Parris, and V. M. Kenkre, *Charge-Dipole Model for the Universal Field Dependence of Mobilities in Molecularly Doped Polymers*, Phys. Rev. Lett. **77**, 542 (1996).

- 57 S. V. Novikov, D. H. Dunlap, V. M. Kenkre, et al., *Essential Role of Correlations in Governing Charge Transport in Disordered Organic Materials*, Phys. Rev. Lett. **81**, 4472 (1998).
- 58 Z. G. Soos, M. H. Hennessy, and D. Mukhopadhyay, in *Primary Photoexcitations in Conjugated Polymers: Molecular versus Semiconductor Band Model*, edited by N. S. Sariciftci (World Scientific Publishing Company, Singapore, 1997).
- 59 J. Kalinowski, in *Organic Electroluminescent Materials and Devices*, edited by S. Miyata and H. S. Nalwa (Gordon and Breach, Amsterdam, 1997).
- 60 H. Bässler, *Charge Transport in Disordered Organic Photoconductors*, phys. stat. sol. (b) **175**, 16 (1993).
- 61 M. Scheidler, U. Lemmer, R. Kersting, et al., *Monte Carlo study of picosecond exciton relaxation and dissociation in poly(phenylenevinylene)*, Phys. Rev. B **54**, 5536 (1996).
- 62 U. Lemmer and E. O. Göbel, in *Primary Photoexcitation in Conjugated Polymers: Molecular versus Semiconductor Band Model*, edited by N. S. Sariciftci (World Scientific, Singapore, 1997), p. 211.
- 63 T. Förster, *Zwischenmolekulare Energiewanderung und Fluoreszenz*, Annalen der Physik **6** (1948).
- 64 R. Kersting, U. Lemmer, R. F. Mahrt, et al., *Femtosecond energy relaxation in pi-conjugated polymers*, Phys. Rev. Lett. **70**, 3820 (1993).
- 65 C. W. Tang, S. A. VanSlyke, and C. H. Chen, *Electroluminescence of doped organic thin films*, J. Appl. Phys. **65**, 3610 (1989).
- 66 H. Bassler, *Charge transport in disordered organic photoconductors. A Monte Carlo simulation study*, Physica Status Solidi B **175**, 15 (1993).
- 67 D. Hertel, H. Bässler, U. Scherf, and H. H. Horhold, *Charge carrier transport in conjugated polymers*, J. Chem. Phys. **110**, 9214 (1999).
- 68 W. Brütting, S. Berleb, and A. G. Mückl, *Device physics of organic light-emitting diodes based on molecular materials*, Organic Electron. **2**, 1 (2001).
- 69 J. H. Schön, A. Dodabalapur, Z. Bao, et al., *Gate-induced superconductivity in a solution-processed organic polymer film*, Nature **410**, 189 (2001).
- 70 H. Bässler, *Injection, transport and recombination of charge carriers in organic light-emitting diodes*, Polymers for Advanced Technologies **9**, 402 (1998).
- 71 M. Pope and C. E. Swenberg, *Electronic Processes in Organic Solids*, Ann. Rev. Phys. Chem. **35**, 613 (1984).
- 72 R. H. Friend, G. J. Denton, J. J. M. Halls, et al., *Electronic excitations in luminescent conjugated polymers*, Sol. Stat. Comm. **102**, 249 (1997).
- 73 X. Zhou, M. Pfeiffer, J. Blochwitz, et al., *Very-low-operating -voltage organic light-emitting diodes using a p-doped amorphous hole injection layer*, Appl. Phys. Lett. **78**, 410 (2001).
- 74 A. Nollau, M. Pfeiffer, T. Fritz, and K. Leo, *Controlled n-type doping of a molecular organic semiconductor*, J. Appl. Phys. **87**, 4340 (2000).
- 75 P. W. M. Blom and M. J. M. de Jong, *Electrical Characterization of Polymer Light-Emitting Diodes*, IEEE J. Sel. Top. Quant. Electron. **4**, 105 (1998).

- 76 U. Albrecht and H. Bassler, *Efficiency of charge recombination in organic light emitting diodes*, Chem. Phys. **199**, 207 (1995).
- 77 N. Tessler, D. J. Pinner, V. Cleave, et al., *Pulsed excitation of low-mobility light-emitting diodes: Implication for organic lasers*, Appl. Phys. Lett. **74**, 2764 (1999).
- 78 M. Wohlgenannt, K. Tandon, S. Mazumdar, et al., *Formation cross-sections of singlet and triplet excitons in π -conjugated polymers*, Nature **409**, 494 (2001).
- 79 E. J. W. List, C. H. Kim, W. Graupner, et al., *Nonradiative quenching of singlet excitons by polarons in π -conjugated polymers*, Synth. Met. **119**, 511 (2001).
- 80 A. Haugeneder, U. Lemmer, and U. Scherf, *Exciton dissociation dynamics in a conjugated polymer containing aggregate states*, Chem. Phys. Lett. **351**, 354 (2002).
- 81 A. R. Brown, D. D. C. Bradley, J. H. Burroughes, et al., *Poly(*p*-phenylenevinylene) light-emitting diodes: enhanced electroluminescent efficiency through charge carrier confinement*, Appl. Phys. Lett. **61**, 2793 (1992).
- 82 A. R. Brown, N. C. Greenham, J. H. Burroughes, et al., *Electroluminescence from multilayer conjugated polymer devices: spatial control of exciton formation and emission*, Chem. Phys. Lett. **200**, 46 (1992).
- 83 N. Tessler, N. T. Harrison, and R. H. Friend, *High peak brightness polymer light-emitting diodes*, Adv. Mater. **10**, 64 (1998).
- 84 N. Tessler, N. T. Harrison, D. S. Thomas, and R. H. Friend, *Current heating in polymer light emitting diodes*, Appl. Phys. Lett. **73**, 732 (1998).
- 85 U. Scherf, S. Riechel, U. Lemmer, and R. F. Mahrt, *Conjugated polymers: lasing and stimulated emission*, Current Opinion in Solid State and Materials Science **5**, 143 (2001).
- 86 F. Hide, B. J. Schwartz, M. A. Diaz-Garcia, and A. J. Heeger, *Laser emission from solutions and films containing semiconducting polymer and titanium dioxide nanocrystals*, Chem. Phys. Lett. **256**, 424 (1996).
- 87 N. Johansson, J. Salbeck, J. Bauer, et al., *Solid-state amplified spontaneous emission in some spiro-type molecules: a new concept for the design of solid state lasing model*, Adv. Mater. **10**, 1136 (1998).
- 88 M. Berggren, A. Dodabalapur, R. E. Slusher, and Z. Bao, *Light amplification in organic thin films using cascade energy transfer*, Nature **389**, 466 (1997).
- 89 R. Gupta, M. Stevenson, A. Dogariu, et al., *Low-threshold amplified spontaneous emission in blends of conjugated polymers*, Appl. Phys. Lett. **73**, 3492 (1998).
- 90 S. V. Frolov, M. Ozaki, W. Gellermann, et al., *Mirrorless lasing in conducting polymer poly(2,5-dioctyloxy-*p*-phenylenevinylene) films*, Jpn. J. Appl. Phys. **35**, L1371 (1996).
- 91 S. V. Frolov, W. Gellermann, M. Ozaki, et al., *Cooperative emission in π -conjugated polymer thin films*, Phys. Rev. Lett. **78**, 729 (1997).
- 92 G. H. Gelinck, J. M. Warman, M. Remmers, and D. Neher, *Narrow-band emissions from conjugated-polymer films*, Chem. Phys. Lett. **265**, 320 (1997).
- 93 A. Haugeneder, M. Hilmer, C. Kallinger, et al., *Mechanism of gain narrowing in conjugated polymer thin films*, Appl. Phys. B **66**, 389 (1998).

- 94 D. Vinh, T. Vu, and B. J. Schwartz, *Ultrafast intensity-dependent stimulated emission in conjugated polymers: the mechanism for line-narrowing*, Chem. Phys. Lett. **288**, 576 (1998).
- 95 S. Stagira, M. Nisoli, G. Cerullo, et al., *The role of amplified spontaneous emission in the ultrafast relaxation dynamics of polymer films*, Chem. Phys. Lett. **289**, 205 (1998).
- 96 M. Nisoli, S. Stagira, M. Zavelani Rossi, et al., *Ultrafast light-emission processes in poly(para-phenylene)-type ladder polymer films*, Phys. Rev. B **59**, 11328 (1999).
- 97 M. D. McGehee, R. Gupta, S. Veenstra, et al., *Amplified spontaneous emission from photopumped films of a conjugated polymer*, Phys. Rev. B **58**, 7035 (1998).
- 98 B. Schweitzer, G. Wegmann, H. Giessen, et al., *The optical gain mechanism in solid conjugated polymers*, Appl. Phys. Lett. **72**, 2933 (1998).
- 99 G. Wegmann, B. Schweitzer, D. Hertel, et al., *The dynamics of gain-narrowing in a ladder-type pi-conjugated polymer*, Chem. Phys. Lett. **312**, 376 (1999).
- 100 B. Schweitzer, G. Wegmann, D. Hertel, et al., *Spontaneous and stimulated emission from a ladder-type conjugated polymer*, Phys. Rev. B **59**, 4112 (1999).
- 101 M. A. Diaz-Garcia, F. Hide, B. J. Schwartz, et al., *Plastic lasers: semiconducting polymers as a new class of solid-state laser materials*, Synth. Met. **84**, 455 (1996).
- 102 S. E. Burns, G. Denton, N. Tessler, et al., *High finesse organic microcavities*, Optical Materials **9**, 18 (1998).
- 103 A. Schulzgen, C. Spiegelberg, M. M. Morrell, et al., *Near diffraction-limited laser emission from a polymer in a high finesse planar cavity*, Appl. Phys. Lett. **72**, 269 (1998).
- 104 T. Granlund, M. Theander, M. Berggren, et al., *A polythiophene microcavity laser*, Chem. Phys. Lett. **288**, 879 (1998).
- 105 U. Lemmer, C. Kallinger, and J. Feldmann, *Laserlicht aus Polymeren*, Phys. Bl. **56**, 25 (2000).
- 106 V. G. Kozlov, V. Bulovic, P. E. Burrows, and S. R. Forrest, *Laser action in organic semiconductor waveguide and double-heterostructure devices*, Nature **389**, 362 (1997).
- 107 V. G. Kozlov, V. Bulovic, P. E. Burrows, et al., *Study of lasing action based on Forster energy transfer in optically pumped organic semiconductor thin films*, J. Appl. Phys. **84**, 4096 (1998).
- 108 S. V. Frolov, M. Shkunov, Z. V. Vardeny, and K. Yoshino, *Ring microlasers from conducting polymers*, Phys. Rev. B **56**, R4363 (1997).
- 109 S. V. Frolov, A. Fujii, D. Chinn, et al., *Cylindrical microlasers and light emitting devices from conducting polymers*, Appl. Phys. Lett. **72**, 2811 (1998).
- 110 S. V. Frolov, Z. V. Vardeny, and K. Yoshino, *Plastic microring lasers on fibers and wires*, Appl. Phys. Lett. **72**, 1802 (1998).
- 111 S. V. Frolov, A. Fujii, D. Chinn, et al., *Microlasers and micro-LEDs from disubstituted polyacetylene*, Adv. Mater. **10**, 869 (1998).
- 112 Y. Kawabe, C. Spiegelberg, A. Schulzgen, et al., *Whispering-gallery-mode microring laser using a conjugated polymer*, Appl. Phys. Lett. **72**, 141 (1998).
- 113 M. Berggren, A. Dodabalapur, Z. Bao, and R. E. Slusher, *Solid-state droplet laser made from an organic blend with a conjugated polymer emitter*, Adv. Mater. **9**, 968 (1997).

- 114 N. D. Kumar, J. D. Bhawalkar, P. N. Prasad, et al., *Solid-state tunable cavity lasing in a poly(para-phenylene vinylene) derivative alternating block co-polymer*, Appl. Phys. Lett. **71**, 999 (1997).
- 115 D. N. Kumar, J. D. Bhawalkar, and P. N. Prasad, *Solid-state cavity lasing from poly(p-phenylene vinylene)-silica nanocomposite bulk*, Applied Optics **37**, 510 (1998).
- 116 H. Giessen, G. Wegmann, D. Hertel, and R. F. Mahrt, *A tunable blue-green laser from a solid conjugated polymer*, Physica Status Solidi B **206**, 437 (1998).
- 117 G. Wegmann, H. Giessen, D. Hertel, and R. F. Mahrt, *Blue-green laser emission from a solid conjugated polymer*, Sol. Stat. Comm. **104**, 759 (1997).
- 118 G. Wegmann, H. Giessen, A. Greiner, and R. F. Mahrt, *Laser emission from a solid conjugated polymer: gain, tunability, and coherence*, Phys. Rev. B **57**, R4218 (1998).
- 119 U. Lemmer, *Stimulated emission and lasing in conjugated polymers*, Polymers for Advanced Technologies **9**, 476 (1998).
- 120 M. D. McGehee and A. J. Heeger, *Semiconducting (conjugated) polymers as materials for solid-state lasers*, Adv. Mater. **12**, 1655 (2000).
- 121 S. V. Frolov, M. Shkunov, A. Fujii, et al., *Lasing and stimulated emission in pi-conjugated polymers*, IEEE J. Quant. Electron. **36**, 2 (2000).
- 122 G. Kranzelbinder and G. Leising, *Organic solid-state lasers*, Reports on Progress in Physics **63**, 729 (2000).
- 123 N. Tessler, *Lasers based on semiconducting organic materials*, Adv. Mater. **11**, 363 (1999).
- 124 A. Dodabalapur, E. A. Chandross, M. Berggren, and R. E. Slusher, *Organic Solid-State lasers: Past and Future*, Science **277**, 1787 (1997).
- 125 M. Berggren, A. Dodabalapur, R. E. Slusher, and Z. Bao, *Organic lasers based on Foerster transfer*, Synth. Met. **91**, 65 (1997).
- 126 V. G. Kozlov, G. Parthasarathy, P. E. Burrows, et al., *Structures for organic diode lasers and optical properties of organic semiconductors under intense optical and electrical excitations*, IEEE J. Quant. Electron. **36**, 18 (2000).
- 127 V. G. Kozlov and S. R. Forrest, *Lasing action in organic semiconductor thin films*, Current Opinion in Solid State & Materials Science **4**, 203 (1999).
- 128 H. Kogelnik and C. V. Shank, *Stimulated emission in a periodic structure*, Appl. Phys. Lett. **18**, 152 (1971).
- 129 J. E. Bjorkholm and C. V. Shank, *Distributed-feedback lasers in thin-film optical waveguides*, IEEE J. Quant. Electron. **QE-8**, 833 (1972).
- 130 S. Wang and S. Sheem, *Two-dimensional distributed-feedback lasers and their applications*, Appl. Phys. Lett. **22**, 460 (1973).
- 131 J. O'Brien, O. Painter, R. Lee, et al., *Lasers incorporating 2D photonic bandgap mirrors*, Electron. Lett. **32**, 2243 (1996).
- 132 H. Fouckhardt, *Photonik* (Teubner, Stuttgart, 1994).
- 133 N. W. Ashcroft and N. D. Mermin, *Solid State Physics* (Saunders College, Philadelphia, 1976).

- 134 H. Kogelnik and C. V. Shank, *Coupled-wave theory of distributed feedback lasers*, J. Appl. Phys. **453**, 2327 (1972).
- 135 E. Kapon, A. Hardy, and A. Katzir, *The Effect of Complex Coupling Coefficients on Distributed Feedback Lasers*, IEEE J. Quant. Electron. **18**, 66 (1982).
- 136 R. G. Baets, K. David, and G. Morthier, *On the distinctive features of gain coupled DFB lasers and DFB lasers with second-order grating*, IEEE J. Quant. Electron. **29**, 1792 (1993).
- 137 W. Streifer, D. R. Scifres, and R. D. Burnham, *Coupled Wave Analysis of DFB and DBR Lasers*, IEEE J. Quant. Electron. **13**, 134 (1977).
- 138 T. Makino and J. Glinski, *Effects of radiation loss on the performance of second-order DFB semiconductor lasers*, IEEE J. Quant. Electron. **24**, 73 (1988).
- 139 S. R. Chinn, *Relaxation Oscillations in Distributed Feedback Lasers*, Optics Commun. **19**, 208 (1976).
- 140 L. I. Luk'yanova, V. N. Luk'yanov, N. V. Shelkov, and S. D. Yakubovich, *Thin-film laser with a two-dimensional diffraction grating*, Sov. J. Quantum Electron. **9**, 496 (1979).
- 141 V. A. Sychugov, A. V. Tishchenko, and A. A. Khakimov, *Two-dimensional periodic structures in thin-film lasers*, Sov. J. Quantum Electron. **12**, 27 (1982).
- 142 M. Toda, *Proposed Cross Grating Single-Mode Laser*, IEEE J. Quant. Electron. **28**, 1653 (1992).
- 143 D. L. Bullock, C. Shih, and R. S. Margulies, *Photonic band structure investigation of two-dimensional Bragg reflector mirrors for semiconductor laser mode control*, J. Opt. Soc. Am. B **10**, 399 (1993).
- 144 H. Han and J. J. Coleman, *Two-Dimensional Rectangular Lattice Distributed Feedback Lasers: A Coupled-Mode Analysis of TE Guided Modes*, IEEE J. Quant. Electron. **31**, 1947 (1995).
- 145 B. G. Levi, *Lasing Demonstrated in Tiny Cavities Made with Photonic Crystals*, Physics Today, 20 (1999).
- 146 M. Meier, A. Mekis, A. Dodabalapur, et al., *Laser action from two-dimensional distributed feedback in photonic crystals*, Appl. Phys. Lett. **74**, 7 (1999).
- 147 M. Imada, S. Noda, A. Chutinan, et al., *Coherent two-dimensional lasing action in surface-emitting laser with triangular-lattice photonic crystal structure*, Appl. Phys. Lett. **75**, 3316 (1999).
- 148 K. Inoue, M. Sasada, J. Kawamata, et al., *A Two-Dimensional Photonic Crystal Laser*, Jpn. J. Appl. Phys. **38**, L157 (1999).
- 149 S. Riechel, C. Kallinger, U. Lemmer, et al., *A flexible conjugated polymer laser using 2D distributed feedback*, in *Conference on Lasers and Electro-Optics*, OSA Technical Digest (Optical Society of America, Washington DC, 1999), p. 465.
- 150 V. N. Luk'yanov, A. T. Semenov, N. V. Shelkov, and S. D. Yakubovich, *Lasers with distributed feedback (review)*, Sov. J. Quantum Electron. **5**, 1293 (1975).
- 151 K. M. Ho, C. T. Chan, and C. M. Soukoulis, *Existence of a Photonic Gap in Periodic Dielectric Structures*, Phys. Rev. Lett. **65**, 3152 (1990).

- 152 H. Hirayama, T. Hamano, and Y. Aoyagi, *Novel spontaneous emission control using 3-dimensional photonic bandgap crystal cavity*, Mater. Science & Engin. B **51**, 99 (1998).
- 153 O. Painter, R. K. Lee, A. Scherer, et al., *Two-dimensional photonic band-gap defect mode laser*, Science **284**, 1819 (1999).
- 154 J. Martorell and N. M. Lawandy, *Distributed feedback oscillation in ordered colloidal suspensions of polystyrene microspheres*, Optics Commun. **78**, 169 (1990).
- 155 C. Gouedard, D. Husson, C. Sauteret, et al., *Generation of spatially incoherent short pulses in laser-pumped neodymium stoichiometric crystals and powders*, J. Opt. Soc. Am. B **10**, 2358 (1993).
- 156 H. Cao, Y. G. Zhao, H. C. Ong, et al., *Ultraviolet lasing in resonators formed by scattering in semiconductor polycrystalline films*, Appl. Phys. Lett. **73**, 3656 (1998).
- 157 H. Cao, Y. G. Zhao, X. Liu, et al., *Effect of external feedback on lasing in random media*, Appl. Phys. Lett. **75**, 1213 (1999).
- 158 H. Cao, Y. G. Zhao, S. T. Ho, et al., *Random laser action in semiconductor powder*, Phys. Rev. Lett. **82**, 2278 (1999).
- 159 H. Cao, J. Y. Xu, S. H. Chang, and S. T. Ho, *Transition from amplified spontaneous emission to laser action in strongly scattering media*, Phys. Rev. E **61**, 1985 (2000).
- 160 H. Cao, J. Y. Xu, D. Z. Zhang, et al., *Spatial Confinement of Laser Light in Active Random Media*, Phys. Rev. Lett. **84**, 5584 (2000).
- 161 H. Cao, J. Y. Xu, E. W. Seelig, and R. P. H. Chang, *Micro-laser made of disordered media*, Appl. Phys. Lett. **76**, 2997 (2000).
- 162 H. Cao, Y. Ling, J. Y. Xu, et al., *Photon Statistics of Random Lasers with Resonant Feedback*, Phys. Rev. Lett. **86**, 4524 (2001).
- 163 R. K. Thareja and A. Mitra, *Random laser action in ZnO*, Applied Physics B **71**, 181 (2000).
- 164 G. Zacharakis, N. A. Papadogiannis, G. Filippidis, and T. G. Papazoglou, *Photon statistics of laserlike emission from polymeric scattering gain media*, Opt. Lett. **25**, 923 (2000).
- 165 S. V. Frolov, Z. V. Vardeny, K. Yoshino, et al., *Stimulated emission in high-gain organic media*, Phys. Rev. B **59**, R5284 (1999).
- 166 R. C. Polson, J. D. Huang, and Z. V. Vardeny, *Random lasers in π -conjugated polymer films*, Synth. Met. **1119**, 7 (2001).
- 167 R. C. Polson, A. Chipouline, and Z. V. Vardeny, *Random Lasing in π -Conjugated Films and Infiltrated Opals*, Adv. Mater. **13**, 760 (2001).
- 168 S. V. Frolov, Z. V. Vardeny, A. A. Zakhidov, and R. H. Baughman, *Laser-like emission in opal photonic crystals*, Optics Commun. **162**, 241 (1999).
- 169 K. Yoshino, S. Tatsukara, Y. Kawagishi, et al., *Amplified spontaneous emission and lasing in conducting polymers and fluorescent dyes in opals as photonic crystals*, Appl. Phys. Lett. **74**, 2590 (1999).
- 170 D. S. Wiersma and A. Lagendijk, *Interference effects in multiple-light scattering with gain*, Physica A **241**, 82 (1997).
- 171 D. S. Wiersma and A. Lagendijk, *Light diffusion with gain and random lasers*, Phys. Rev. E **54**, 4256 (1996).

- 172 M. P. Albada and A. Lagendijk, *Observation of weak localization of light in a random medium*, Phys. Rev. Lett. **55**, 2692 (1985).
- 173 P. E. Wolf and G. Maret, *Weak localization and coherent backscattering of photons in disordered media*, Phys. Rev. Lett. **66**, 2696 (1985).
- 174 D. S. Wiersma, P. Bartolini, A. Lagendijk, and R. Righini, *Localization of light in a disordered medium*, Nature **390**, 671 (1997).
- 175 D. S. Wiersma, J. G. Rivas, P. Bartolini, et al., *Localization or classical diffusion of light?*, Nature (scientific correspondence) **398**, 206 (1999).
- 176 Z.-Q. Zhang, *Light amplification and localization in randomly layered media with gain*, Phys. Rev. B **52**, 7960 (1995).
- 177 P. Sheng, *Introduction to wave scattering, Localization, and Mesoscopic Phenomena* (Academic, San Diego, 1995).
- 178 V. S. Letokhov, *Generation of light by a scattering medium with negative resonance absorption*, Soviet Physics JETP **26** (1968).
- 179 D. S. Wiersma, M. P. van Albada, and A. Lagendijk, *Coherent Backscattering of Light from Amplifying Random Media*, Phys. Rev. Lett. **75**, 1739 (1995).
- 180 X. Jiang and C. M. Soukoulis, *Time Dependent Theory for Random Lasers*, Phys. Rev. Lett. **85**, 70 (2000).
- 181 N. M. Lawandy, A. M. Balachandran, A. S. L. Gomes, and E. Sauvain, *Laser action in strongly scattering media*, Nature **368**, 436 (1994).
- 182 G. A. Berger, A. Z. Genack, and M. Kempe, *Dynamics of stimulated emission from random media*, Phys. Rev. E **56**, 6118 (1997).
- 183 M. Siddique, R. R. Alfano, G. A. Berger, et al., *Time-resolved studies of stimulated emission from colloidal dye solutions*, Opt. Lett. **21**, 450 (1996).
- 184 D. W. Schubert, *Spin coating as a method for polymer molecular weight determination*, Polymer Bulletin **38**, 177 (1997).
- 185 A. Böhler, *Organische Elektrolumineszenz-Displays*, Fakultät für Maschinenbau und Elektrotechnik, Technische Universität Braunschweig, Braunschweig (1998)
- 186 W. Zinth and H.-J. Körner, *Physik III: Quantenphänomene und Aufbau der Atome* (Oldenbourg Verlag, München, 1994).
- 187 S. Tasch, A. Niko, G. Leising, and U. Scherf, *Highly efficient electroluminescence of new wide band gap ladder-type poly(para-phenylenes)*, Appl. Phys. Lett. **68**, 1090 (1996).
- 188 D. Hertel, U. Scherf, and H. Bassler, *Charge carrier mobility in a ladder-type conjugated polymer*, Adv. Mater. **10**, 1119 (1998).
- 189 U. Scherf and K. Müllen, *A Soluble Ladder Polymer via Bridging of Functionalized Poly(p-phenylene)-Precursors*, Makromol. Chem. Rapid Commun. **12**, 489 (1991).
- 190 S. Barth, H. Bassler, U. Scherf, and K. Mullen, *Photoconduction in thin films of a ladder-type poly-para-phenylene*, Chem. Phys. Lett. **288**, 147 (1998).
- 191 J. Sturm, S. Tasch, A. Niko, et al., *Optical anisotropy in thin films of a blue electroluminescent conjugated polymer*, Thin Solid Films **298**, 138 (1997).

- ¹⁹² G. Lanzani, S. De Silvestri, G. Cerullo, et al., in *Semiconducting Polymers-Chemistry, Physics and Engineering*, edited by G. Hadziionannou and P. van Hutten (Wiley-VCH, Weinheim, 1999), p. 235.
- ¹⁹³ M. G. Harrison, S. Moller, G. Weiser, et al., *Electro-optical studies of a soluble conjugated polymer with particularly low intrachain disorder*, Phys. Rev. B **60**, 8650 (1999).
- ¹⁹⁴ D. Hertel, S. Setayesh, H. Nothofer, et al., *Phosphorescence in Conjugated Poly(para-phenylene)-Derivatives*, Adv. Mater. **13**, 65 (2001).
- ¹⁹⁵ M. Wohlgenannt, W. Graupner, G. Leising, and Z. V. Vardeny, *Photogeneration and recombination processes of neutral and charged excitations in films of a ladder-type poly(para-phenylene)*, Phys. Rev. B **60**, 5321 (1999).
- ¹⁹⁶ M. G. Harrison, G. Urbasch, R. F. Mahrt, et al., *Two-photon fluorescence and femtosecond two-photon absorption studies of MeLPPP, a ladder-type poly(phenylene) with low intra-chain disorder*, Chem. Phys. Lett. **313**, 755 (1999).
- ¹⁹⁷ J. G. Mueller, U. Lemmer, U. Scherf, and J. Feldmann, *Precursor states for charge carrier generation in conjugated polymers probed by ultrafast spectroscopy*, Phys. Rev. Lett. (submitted), (2001).
- ¹⁹⁸ V. I. Arkhipov, E. V. Emelianova, and H. Bassler, *Hot exciton dissociation in a conjugated polymer*, Phys. Rev. Lett. **82**, 1321 (1999).
- ¹⁹⁹ A. Haugeneder, M. Neges, C. Kallinger, et al., *Exciton diffusion and dissociation in conjugated polymer/fullerene blends and heterostructures*, Phys. Rev. B **59**, 15346 (1999).
- ²⁰⁰ D. Hertel, H. Bässler, U. Scherf, and H. H. Hörhold, *Charge carrier transport in conjugated polymers*, J. Appl. Phys. **110**, 9214 (1999).
- ²⁰¹ V. Bulovic, V. G. Kozlov, V. B. Khalfin, and S. R. Forrest, *Transform-limited, narrow-linewidth lasing action in organic semiconductor microcavities*, Science **279**, 553 (1998).
- ²⁰² P. R. Hammond, *Laser dye DCM, its spectral properties, synthesis and comparison with other dyes in the red*, Optics Commun. **29**, 331 (1979).
- ²⁰³ A. D. Walser, I. Sokolik, R. Priestley, and R. Dorsinville, *Dynamics of photoexcited states and charge carriers in organic thin films: Alq/sub 3/*, Appl. Phys. Lett. **69**, 1677 (1996).
- ²⁰⁴ T. Benstem, Institut für Hochfrequenztechnik, TU-Braunschweig, Personal Communication (2002).
- ²⁰⁵ P. E. Burrows, Z. Shen, V. Bulovic, et al., *Relationship between electroluminescence and current transport in organic heterojunction light-emitting devices*, J. Appl. Phys. **79**, 7991 (1996).
- ²⁰⁶ W. Stampor, J. Kalinowski, G. Marconi, et al., *Electroabsorption study of excited states in tris 8-hydroxyquinoline aluminum complex*, Chem. Phys. Lett. **283**, 373 (1998).
- ²⁰⁷ A. Curioni, W. Andreoni, R. Treusch, et al., *Atom-resolved electronic spectra for Alq₃ from theory and experiment*, Appl. Phys. Lett. **72**, 1575 (1998).
- ²⁰⁸ R. L. Martin, J. D. Kress, I. H. Campbell, and D. L. Smith, *Molecular and solid-state properties of tris-(8-hydroxyquinolate)-aluminum*, Phys. Rev. B **61**, 15804 (2000).
- ²⁰⁹ A. E. Siegman, *Lasers* (University Science Books, Mill Valley, CA, USA, 1986).

- 210 U. Brackmann, *Lambdachrome Laser Dyes* (Lambda Physik, Goettingen, 2000).
- 211 M. Berggren, A. Dodabalapur, and R. E. Slusher, *Organic solid-state lasers with imprinted gratings on plastic substrates*, Appl. Phys. Lett. **72**, 410 (1998).
- 212 J. A. Rogers, M. Meier, and A. Dodabalapur, *Using printing and molding techniques to produce distributed feedback and Bragg reflector resonators for plastic lasers*, Appl. Phys. Lett. **73**, 1766 (1998).
- 213 A. Gombert, W. Glaubitt, K. Rose, et al., *Subwavelength-structured antireflective surfaces on glass*, Thin Solid Films **351**, 73 (1999).
- 214 C. Zanke, A. Gombert, A. Erdmann, and M. Weiss, *Fine-tuned profile simulation of holographically exposed photoresist gratings*, Optics Commun. **154**, 109 (1998).
- 215 W. Streifer, D. R. Scifres, and R. D. Burnham, *TM-mode coupling coefficients in guided wave distributed feedback lasers*, IEEE J. Quant. Electron. **12**, 74 (1976).
- 216 N. Finger, W. Schrenk, and E. Gornik, *Analysis of TM-Polarized DFB Laser Structures with Metal Surface Gratings*, IEEE J. Quant. Electron. **36**, 780 (2000).
- 217 T. P. Lee, C. A. Burrus, B. I. Miller, and R. A. Logan, *$Al_xGa_{1-x}As$ double heterostructure rib-waveguide injection laser*, IEEE J. Quant. Electron. **11**, 432 (1975).
- 218 G. A. Turnbull, T. F. Krauss, W. L. Barnes, and I. D. W. Samuel, *Tuneable distributed feedback lasing in MEH-PPV films*, Synth. Met. **121**, 1757 (2001).
- 219 F. K. Kneubühl and M. W. Sigrist, *Laser* (Teubner, Stuttgart, 1999).
- 220 A. Klaedtke, S. Scholz, and O. Hess, *Far-Field Pattern and Mode Structure of Photonic-Crystal -Based Planar Distributed Feedback Laser Structures*, Proceedings of the SPIE **4283**, 462 (2001).
- 221 R. J. Noll and S. H. Macomber, *Analysis of Grating Surface Emitting Lasers*, IEEE J. Quant. Electron. **26**, 456 (1990).
- 222 N. Finger and E. Gornik, *Analysis of Metallized-Grating Coupled Twin-Waveguide Structures*, IEEE J. Quant. Electron. **35**, 832 (1999).
- 223 H. Soda, Y. Kotaki, H. Sudo, et al., *Stability in single longitudinal mode operation in GaInAsP/InP phase-adjusted DFB lasers*, IEEE J. Quant. Electron. **23**, 804 (1987).
- 224 N. Susa, IEEE J. Quant. Electron. **33**, 2255 (1997).
- 225 J. P. Dowling, M. Scalora, M. J. Bloemer, and C. M. Bowden, *The photonic band edge laser: A new approach to gain enhancement*, J. Appl. Phys. **75**, 1896 (1993).
- 226 K. Gyeong-II and N. M. Lawandy, *Quantum electrodynamics in photonic crystals*, Optics Commun. **118**, 388 (1995).
- 227 A. Mekis, M. Meier, A. Dodabalapur, et al., *Lasing mechanism in two-dimensional photonic crystal lasers*, Appl. Phys. A **A69**, 111 (1999).
- 228 J. P. Dowling and C. M. Bowden, *Atomic emission rates in inhomogeneous media with applications to photonic band structures*, Phys. Rev. A **46**, 612 (1992).
- 229 T. Suzuki, P. K. L. Yu, D. R. Smith, and S. Schultz, *Experimental and theoretical study of dipole emission in the two-dimensional photonic band structure of the square lattice with dielectric cylinders*, J. Appl. Phys. **79**, 582 (1996).
- 230 S. Nojima, *Enhancement of Optical Gain in Two-Dimensional Photonic Crystals with Active Lattice Points*, Jpn. J. Appl. Phys. **37**, L565 (1998).

- 231 K. Sakoda, *Enhanced light amplification due to group-velocity anomaly peculiar to two- and three-dimensional photonic crystals*, Optics Express **4**, 167 (1999).
- 232 N. Susa, *Threshold gain and gain-enhancement due to distributed -feedback in two-dimensional photonic-crystal lasers*, J. Appl. Phys. **89**, 815 (2001).
- 233 N. Susa, *Threshold Gain due to Distributed-Feedback in Two-Dimensional Triangular- and Square-Lattice Photonic Crystals Lasers*, Jpn. J. Appl. Phys. **40**, 142 (2001).
- 234 M. A. Noginov, H. J. Caulfield, N. E. Noginova, and P. Venkateswarlu, *Line narrowing in the dye solution with scattering centers*, Optics Commun. **118**, 430 (1995).
- 235 M. Siddique, L. Yang, Q. Z. Wang, and R. R. Alfano, *Mirrorless laser action from optically pumped dye-treated animal tissues*, Optics Commun. **117**, 475 (1995).
- 236 R. M. Balachandran, D. P. Pacheco, and N. M. Lawandy, *Laser action in polymeric gain media containing scattering particles*, Applied Optics **35**, 640 (1996).
- 237 S. John and P. Gendi, *Theory of lasing in a multiple-scattering medium*, Phys. Rev. A (Atomic, Molecular, and Optical Physics) **54**, 3642 (1996).
- 238 R. M. Balachandran and N. M. Lawandy, *Understanding bichromatic emission from scattering gain media*, Opt. Lett. **21**, 1603 (1996).
- 239 R. M. Balachandran, N. M. Lawandy, and J. A. Moon, *Theory of laser action in scattering gain media*, Opt. Lett. **22**, 319 (1997).
- 240 G. van Soest, M. Tomita, and A. Lagendijk, *Amplifying volume in scattering media*, Opt. Lett. **24**, 306 (1999).
- 241 P. W. Anderson, *Absence of diffusion in certain random lattices*, Phys. Rev. **109** (1958).
- 242 N. D. Denkov, O. D. Velev, P. A. Kralchevsky, et al., *Two-dimensional crystallization*, Nature **361**, 26 (1993).
- 243 N. D. Denkov, O. D. Velev, P. A. Kralchevsky, et al., *Mechanism of formation of two-dimensional crystals from latex particles on substrates*, Langmuir **8**, 3183 (1992).
- 244 C. Klingler-Deiseroth, *Selbstorganisierende photonische Kristalle für neuartige Halbleiterlaser*, Diplomarbeit, Lehrstuhl für Photonik und Optoelektronik, LMU München, München (2000).
- 245 Z. Yang and H. Yu, *Preserving a globular protein shape on glass slides: a self-assembled monolayer approach*, Adv. Mater. **9**, 426 (1997).
- 246 S. P. Zhdanov, L. S. Kosheleva and T. I. Titova, *IR study of hydroxylated silica*, Langmuir **3**, 960 (1987).
- 247 K. Nagayama, *Fabrication of two-dimensional colloidal arrays*, Phase Transitions **45**, 185 (1993).
- 248 C. D. Dushkin, H. Yoshimura, and K. Nagayama, *Nucleation and growth of two-dimensional colloidal crystals*, Chem. Phys. Lett. **204**, 455 (1993).
- 249 A. S. Dimitrov and K. Nagayama, *Steady-state unidirectional convective assembling of fine particles into two-dimensional arrays*, Chem. Phys. Lett. **243**, 462 (1995).
- 250 P. A. Kralchevsky and K. Nagayama, *Capillary forces between colloidal particles*, Langmuir **10**, 23 (1994).

- 251 P. A. Kralchevsky, N. D. Denkov, V. N. Paunov, et al., *Formation of two-dimensional colloid crystals in liquid films under the action of capillary forces*, Journal of Physics: Condensed Matter **6**, A395 (1994).
- 252 C. D. Dushkin, K. Nagayama, T. Miwa, and P. A. Kralchevsky, *Colored multilayers from transparent submicrometer spheres*, Langmuir **9**, 3695 (1993).
- 253 A. S. Dimitrov, F. T. Miwa, and K. Nagayama, *A comparison between the optical properties of amorphous and crystalline monolayers of silica particles*, Langmuir **15**, 5257 (1999).
- 254 D. Hofstetter and R. L. Thornton, *Loss measurements on semiconductor lasers by Fourier analysis of the emission spectra*, Appl. Phys. Lett. **72**, 404 (1998).
- 255 S. Stagira, M. Zavelani Rossi, M. Nisoli, et al., *Single-mode picosecond blue laser emission from a solid conjugated polymer*, Appl. Phys. Lett. **73**, 2860 (1998).
- 256 A. Mecozzi, P. Spano, and G. P. Agrawal, *Transient Multimode Dynamics in Nearly Single-Mode Lasers*, IEEE J. Quant. Electron. **27**, 332 (1991).
- 257 J. Kovac, H. Schmidt, C. Kaden, et al., *Picosecond laser dynamics of gain-coupled and index-coupled InGaAs/InGaAlAs quantum well distributed feedback lasers*, Appl. Phys. Lett. **67**, 816 (1995).
- 258 T. K. Sudoh, M. Funabashi, Y. Nakano, et al., *Dynamics of Gain-Switching Operation in Gain-Coupled Distributed-Feedback Semiconductor Lasers with Absorptive Grating*, IEEE J. Sel. Top. Quant. Electron. **1**, 583 (1995).
- 259 C. Lingk, Lehrstuhl für Photonik und Optoelektronik, LMU München, Personal communication (2001).
- 260 S. Stagira, M. Zavelani-Rossi, M. Nisoli, et al., *Single-mode picosecond blue laser emission from a solid conjugated polymer*, Appl. Phys. Lett. **73**, 2860 (1998).
- 261 U. Lemmer, A. Ochse, M. Deussen, et al., *Energy transfer in molecularly doped conjugated polymers*, Synth. Met. **78**, 289 (1996).
- 262 G. Cerullo, M. Nisoli, S. Stagira, et al., *Ultrafast energy-transfer dynamics in a blend of electroluminescent conjugated polymers*, Chem. Phys. Lett. **288**, 561 (1998).
- 263 A. Dogariu, R. Gupta, A. J. Heeger, and H. Wang, *Time-resolved Forster energy transfer in polymer blends*, Synth. Met. **100**, 95 (1999).
- 264 J. Lin, J. K. Gamelin, K. Y. Lau, et al., *Ultrafast (up to 39 GHz) relaxation oscillation of vertical cavity surface emitting laser*, Appl. Phys. Lett. **60**, 15 (1992).
- 265 A. Yariv, *Quantum Electronics* (John Wiley & sons, New York, 1988).
- 266 N. Tessler and R. H. Friend, *Polymer LEDs as laser media?*, Synth. Met. **102**, 1122 (1999).
- 267 N. Tessler, D. J. Pinner, V. Cleave, et al., *Properties of light emitting organic materials within the context of future electrically pumped lasers*, Synth. Met. **115**, 57 (2000).
- 268 V. G. Kozlov, P. E. Burrows, G. Parthasarathy, and S. R. Forrest, *Optical properties of molecular organic semiconductor thin films under intense electrical excitation*, Appl. Phys. Lett. **74**, 1057 (1999).
- 269 I. H. Campbell, D. L. Smith, C. J. Neef, and J. P. Ferraris, *Charge transport in polymer light-emitting diodes at high current density*, Appl. Phys. Lett. **75**, 841 (1999).

- 270 M. Redecker and H. Bassler, *Optical detection of charge carriers in organic light-emitting diodes*, Appl. Phys. Lett. **69**, 70 (1996).
- 271 I. H. Campbell, D. L. Smith, C. J. Neef, and J. P. Ferraris, *Optical properties of single carrier polymer diodes under high electrical injection*, Appl. Phys. Lett. **78**, 270 (2001).
- 272 K. L. Chopra, S. Major, and D. K. Pandya, *Transparent conductors-a status review*, Thin Solid Films **102** (1983).
- 273 M. A. Diaz Garcia, F. Hide, B. J. Schwartz, et al., *"Plastic" lasers: comparison of gain narrowing with a soluble semiconducting polymer in waveguides and microcavities*, Appl. Phys. Lett. **70**, 3191 (1997).
- 274 J. H. Schön, A. Dodabalapur, C. Kloc, and B. Batlogg, *A Light-Emitting Field-Effect Transistor*, Science **290**, 963 (2000).
- 275 G. Parthasarathy, C. Adachi, P. E. Burrows, and S. R. Forrest, *High-efficiency transparent organic light-emitting devices*, Appl. Phys. Lett. **76**, 2128 (2000).
- 276 P. K. H. Ho, D. S. Thomas, R. H. Friend, and N. Tessler, *All-polymer optoelectronic devices*, Science **285**, 233 (1999).
- 277 M. G. Salt and W. L. Barnes, *Photonic band gaps in guided modes of textured metallic microcavities*, Optics Commun. **166**, 151 (1999).
- 278 M. G. Salt and W. L. Barnes, *Flat photonic bands in guided modes of textured metallic microcavities*, Phys. Rev. B **61**, 11125 (2000).
- 279 M. G. Salt, W. C. Tan, and W. L. Barnes, *Photonic band gaps and flat band edges in periodically textured metallic microcavities*, Appl. Phys. Lett. **77**, 193 (2000).
- 280 W. Kowalsky, T. Benstem, A. Böhrer, et al., *Improved lifetime and efficiency of organic light emitting diodes for applications in displays*, Proceedings of the SPIE **3621**, 103 (1999).
- 281 C. Giebeler, H. Antoniadis, D. D. C. Bradley, and Y. Shirota, *Space-charge-limited charge injection from indium tin oxide into a starburst amine and its implications for organic light-emitting diodes*, Appl. Phys. Lett. **72**, 2448 (1998).
- 282 P. Yang, G. Wirnsberger, H. C. Huang, et al., *Mirrorless Lasing from Mesostructured Waveguides Patterned by Soft Lithography*, Science **287**, 465 (2000).
- 283 D. C. Müller, T. Braig, H. Nothofer, et al., *Efficient Blue Organic Light-Emitting Diodes with Graded Hole-Transport Layers*, Chem. Phys. Chem. **1**, 207 (2000).
- 284 V. I. Klimov, A. A. Mikhailovsky, S. Xu, et al., *Optical gain and stimulated emission in nanocrystal quantum dots*, Science **290**, 314 (2000).

Acknowledgments

An dieser Stelle möchte ich all denjenigen danken, die zum Gelingen dieser Arbeit direkt oder indirekt beigetragen haben:

- *Prof. Dr. Jochen Feldmann* danke ich für die Möglichkeit diese interessante und vielseitige Arbeit an seinem Lehrstuhl durchführen zu können. Er hat die technischen und finanziellen Möglichkeiten bereitgestellt und mich von Anfang an in jeglicher Hinsicht unterstützt und gefördert. Durch seine erstklassigen Anregungen und die konstruktive Kritik habe ich viel gelernt. Entscheidende Impulse zu dieser Arbeit lieferte nicht zuletzt seine Idee vom flexiblen Plastiklaser.
- *Prof. Dr. Khaled Karrai* für die Übernahme des Koreferats und sein Interesse an dieser Arbeit.
- *Dr. Uli Lemmer*, dem Chef der Polymergruppe, danke ich für die höchst kompetente Betreuung in seiner unkomplizierten und lockeren Art. Von seinem immensen Wissen im Bereich organischer Halbleiter und seinem guten Gespür für die optimale Verwertung der Ergebnisse habe immer wieder profitiert. Genauso wie die Tür zu seinem Zimmer war auch er selbst stets offen für ein kurzes Gespräch über dies und das; weit über die pure Physik hinaus. Nicht zuletzt deswegen hat die Arbeit immer Spaß gemacht.
- *Dr. Christian Kallinger*, meinem Vorgänger im Bereich der Polymerlaser, danke ich für die prima Einführung ins Business der organischen Halbleiterlaser. Von seiner guten Selbstorganisation und seiner Freude daran, neue Dinge auszuprobieren, kann man sich wirklich eine Menge abschauen.
- Bei *Dr. Andreas Haugeneder* und *Dr. Martin Perner* bedanke ich mich für die umfassende Einführung in den Umgang mit dem Verstärkersystem.
- Ein großes Dankeschön gebührt meinen engsten Mitstreitern bei der Bewältigung der alltäglichen großen und kleinen Probleme im Sommerfeldkeller: *Jürgen Müller* für seine täglichen Ermunterungen und seinen furchtlosen Umgang mit (laut Spectra-Handbuch) fest zementierten Komponenten sowie *Christoph Lingk*, der noch jedes Computerprogramm (und auch unser Sofa) zum Laufen bekommen hat. Die Zeit mit Euch zusammen war ein besonderes Highlight.
- Gedankt sei auch den weiteren Diplomanden und Doktoranden der Polymergruppe, die stark zum Gelingen dieser Doktorarbeit beigetragen haben. *Carmen Klingler-Deiseroth* insbesondere für die Herstellung der Kolloid-Monolagen, *Gerhard Wörle* für seinen unermüdlichen Einsatz an der Glovebox und *Olaf Holderer* für seine gutes Händchen bei der Aufkonversion. *Martin Reufer* danke ich für seine tatkräftige Unterstützung bei den Diodenlaser-Experimenten und *Jana Crewett* für die Rechnungen zur photonischen Bandstruktur.

Eine interdisziplinäre Arbeit wie diese lebt natürlich von der Kooperation mit kompetenten Partnern. Ein besonderer Dank für die fruchtbare Zusammenarbeit gilt daher:

- *Prof. Dr. U. Scherf* (Uni Potsdam) für die stets reichlich vorhandenen konjugierten Polymere,
- *Dr. A. Gombert* und *Dr. V. Wittwer* vom Fraunhofer Institut für Solare Energiesysteme in Freiburg für die geprägten Substrate,
- *T. Benstem* und *Prof. Dr. W. Kowalsky* (TU Braunschweig) für den intensiven Erfahrungsaustausch und die Herstellung der verschiedensten Aufdampfschichten,
- *S. Berleb*, *A. G. Mückl* und *Dr. W. Brütting* (Universität Bayreuth) für die Alq₃:DCM Aufdampfschichten,
- sowie *D. C. Müller* und *Prof. Dr. K. Meerholz* für die Anregungen zur Herstellung von OLEDs.

Für Unterstützung in theoretischen Aspekten meiner Arbeit danke ich:

- *Dr. N. Finger* (ehemals TU Wien) für seine ausführlichen Rechnungen und Erläuterungen zum Kopplungsmechanismus in DFB Lasern,
- *Dr. K. Busch* für sein Programm zur Berechnung zweidimensionaler photonischer Bandstrukturen,
- sowie *Andreas Klaedtke* und *Dr. Ortwin Hess* (DLR Stuttgart) für die vorbereitenden Rechnungen zur Laserdynamik.

Desweiteren möchte ich einer Reihe von Personen danken, die mich während der Zeit am Lehrstuhl rat- und tatkräftig unterstützt haben: *Prof. Dr. Jürgen Köhler* für seine hilfreichen Tips zur Spektroskopie. Den Assistenten am LS Feldmann, namentlich *Dr. Mingyuan Gao*, *Dr. Nancy Hecker*, *Prof. Dr. Gero von Plessen* und *Dr. Wolfgang Spirkl* für viele Diskussionen und Tips. *Prof. Dr. Martin Koch* zudem für die Vermittlung der Braunschweiger Kooperation. *Werner Stadler*, *Stefan Niedermaier* und *Christian Holopirek* danke ich für die ausgezeichnete Unterstützung in sämtlichen technischen Belangen, *Margit Kohler* und *Anna Helfrich* für die kompetente Betreuung des Chemielabors, sowie *Maria Kaldewey*, *Ingetraud Krella*, *Gerlinde Adam* und *Irmgard Beier* für die Organisation im Sekretariat. Ein Dank für die guten Tips bei den großen und kleinen Tücken mit Hard- und Software geht an unsere "Knowledgebase" *Dr. Andreas Timinger*, *Dr. Carsten Sönnichsen*, *Gunnar Raschke* und *Clemens Hofmann*. Vielen Dank auch an all die anderen nicht namentlich genannten Mitglieder des LS Feldmann, die immer bereit waren zu helfen und die zum guten Klima beträchtlich beigetragen haben. Es hat wirklich Spaß gemacht.

Zum Schluß möchte ich auch denjenigen Danke sagen, ohne die ich nie so weit gekommen wäre. Vor allem danke ich natürlich meiner Dani für ihre Liebe und ihre Geduld mit mir. Deine guten Ratschläge, Dein Erzählen und Zuhören, Deine Ermutigung und Dein Gebet bedeuten mir sehr viel. Meinen Eltern danke ich für ihre dauerhafte ideelle und finanzielle Unterstützung während meiner gesamten Ausbildung und für das sorgfältige Korrekturlesen des Manuskripts. Jesus für die Hoffnung in meinem Leben.

